A Measurement of the Interference Structure Function, R_{LT}, for the $^{12}C(e,e'p)$ Reaction in the Quasielastic Region.

by

Maurik Willem Holtrop
Bachelors of Science
University of New Hampshire
(1987)

Submitted to the Department of
PHYSICS
in partial fulfillment of the requirements
for the degree of
DOCTOR OF PHILOSOPHY
at the
MASSACHUSETTS INSTITUTE OF TECHNOLOGY
June 1995

Signature of Author
Department of Physics
May 1995

Certified by
Professor William Bertozzi
Thesis Supervisor

Accepted by
Professor George F. Koster
Chair of the Physics Graduate Committee

A Measurement of the Interference Structure Function, R_{LT}, for the $^{12}C(e,e'p)$ Reaction in the Quasielastic Region.

by
Maurik Willem Holtrop

Submitted to the Department of Physics
on May 5, 1995, in partial fulfillment of
the requirements for the degree of
Doctor of Philosophy

Abstract

The coincidence cross-section and the interference structure function, R_{LT}, were measured for quasielastic electron scattering from the ^{12}C nucleus at an energy transfer, ω, of 110 MeV and a momentum transfer, q, of 404 MeV/c. The experiment was performed in the North Hall of the Bates Linear Accelerator Center in March 1991, using the prototype OOPS spectrometer to detect protons and the ELSSY spectrometer to detect electrons. The beam energy was 576 MeV, the electron scattering angle was 44°, and the proton scattering angles were 42.9° and 64.7°. The central outgoing electron momentum was 464 MeV/c, and the proton momentum varied over the range of 310 to 480 MeV/c to cover a range in missing energy from $E_m = 0$ to 65 MeV. The proton angle with respect to the q vector was about 11°.

This thesis describes the details of the experimental setup, including the two spectrometers and their detector packages, and the data acquisition electronics and software. New measurements for the optical properties of both spectrometers are presented, and the normalizations and efficiency corrections are discussed. The analysis of the data was performed using a two dimensional method that sorts the data in (E_m, P_m) bins. This data was radiatively corrected in this two dimensional plane before being projected onto the missing energy axis.

In the both the measured cross-sections and the R_{LT} structure function, a peak can be identified at a missing energy of 18 MeV, which is associated with proton knockout from the p-shell. A broader peak is seen at missing energies between 28 and 50 MeV corresponding to s-shell knockout. The R_{LT} structure function is consistent with zero for missing energies above 50 MeV. The integrated strengths of the peaks are compared with a factorized Distorted Wave Impulse Approximation, and an HF-RPA calculation with a spectroscopic function to model the s-shell energy dependence. The DWIA calculation agrees with the extracted R_{LT} value, but over estimates the cross-sections for the p and s-shell. The HF-RPA calculation describes the s-shell shape, but over estimates the strength by a factor of 3.

Thesis Supervisor: William Bertozzi
Title: Professor of Physics, Laboratory for Nuclear Science

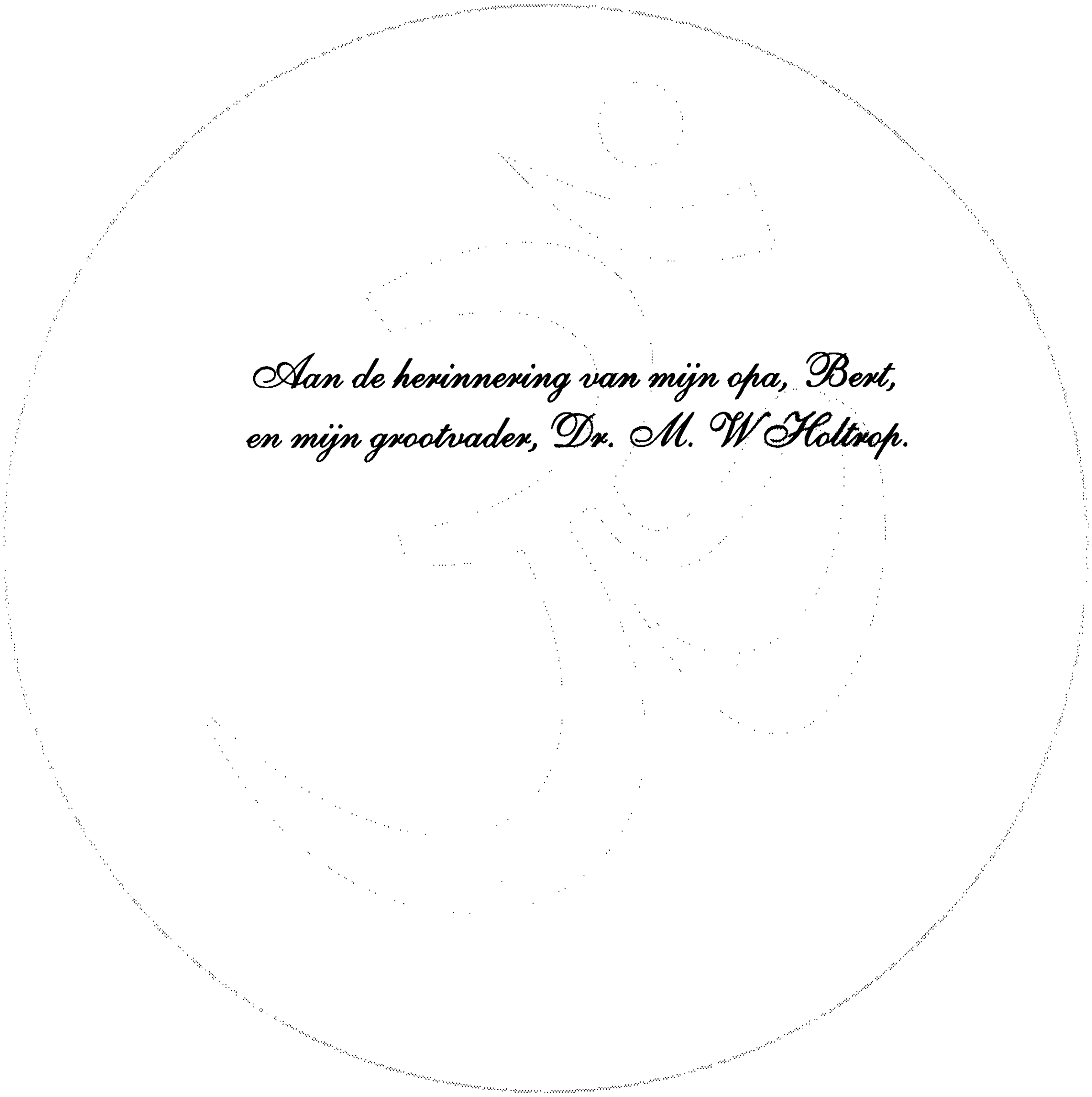

Aan de herinnering van mijn opa, Bert,
en mijn grootvader, Dr. M. W Holtrop.

Contents

TABLE OF FIGURES

Table of Tables

A Measurement of the Interference Structure Function, R_{LT}, for the ^{12}C(e,e'p) Reaction in the Quasielastic Region.

by

Maurik Willem Holtrop

Submitted to the Department of Physics
on May 5, 1995, in partial fulfillment of
the requirements for the degree of
Doctor of Philosophy

Abstract

The coincidence cross-section and the interference structure function, R_{LT}, were measured for quasielastic electron scattering from the ^{12}C nucleus at an energy transfer, ω, of 110 MeV and a momentum transfer, q, of 404 MeV/c. The experiment was performed in the North Hall of the Bates Linear Accelerator Center in March 1991, using the prototype OOPS spectrometer to detect protons and the ELSSY spectrometer to detect electrons. The beam energy was 576 MeV, the electron scattering angle was 44°, and the proton scattering angles were 42.9° and 64.7°. The central outgoing electron momentum was 464 MeV/c, and the proton momentum varied over the range of 310 to 480 MeV/c to cover a range in missing energy from $E_m = 0$ to 65 MeV. The proton angle with respect to the q vector was about 11°.

This thesis describes the details of the experimental setup, including the two spectrometers and their detector packages, and the data acquisition electronics and software. New measurements for the optical properties of both spectrometers are presented, and the normalizations and efficiency corrections are discussed. The analysis of the data was performed using a two dimensional method that sorts the data in (E_m, P_m) bins. This data was radiatively corrected in this two dimensional plane before being projected onto the missing energy axis.

In the both the measured cross-sections and the R_{LT} structure function, a peak can be identified at a missing energy of 18 MeV, which is associated with proton knockout from the p-shell. A broader peak is seen at missing energies between 28 and 50 MeV corresponding to s-shell knockout. The R_{LT} structure function is consistent with zero for missing energies above 50 MeV. The integrated strengths of the peaks are compared with a factorized Distorted Wave Impulse Approximation, and an HF-RPA calculation with a spectroscopic function to model the s-shell energy dependence. The DWIA calculation agrees with the extracted R_{LT} value, but over estimates the cross-sections for the p and s-shell. The HF-RPA calculation describes the s-shell shape, but over estimates the strength by a factor of 3.

Thesis Supervisor: William Bertozzi
Title: Professor of Physics, Laboratory for Nuclear Science

Chapter 1 Introduction.

This thesis will present the results of an electrodisintegration experiment on ^{12}C to measure the R_{LT} structure function and coincidence cross-section. The kinematics were for the quasi-elastic region, with a momentum transfer q of about 400 MeV/c and an energy transfer ω of about 100 MeV. The scattering angles were 44° for the electron arm and 42.9° and 64.7° for the proton arm. This experiment was performed at the Bates Linear Accelerator Center in February and March of 1991 with a beam energy of 576 MeV. It was among the first experiments performed with the Out Of Plane Spectrometer (OOPS), which is a compact, light weight spectrometer designed[1] to be capable of taking data out of the scattering plane defined by the beam and the electron arm. A prototype OOPS was used for which the prototype detector package was built by the MIT group.[2] Optics studies performed for this experiment demonstrated that the OOPS meets the design goals.[3] Previous optics studies for the Energy Loss Spectrometer System (ELSSY)[4] were also improved upon by a separate study. In the process of this investigation many of the components of a nuclear physics experiment were developed, including the electronic read out system, the data acquisition logic and the computer codes for the data acquisition and data analysis. This thesis will present each of these components in the following chapters.

This experiment follows a series of other experiments on the carbon nucleus that were designed to study multi-hadron processes at high energy and momentum transfer ($q \geq 400$ MeV/c, $\omega \geq 100$ MeV/c.) Only the first of this series of experiments separated structure functions (R_L and R_T), the other experiments involved measurements of the cross-section and studied its behavior in various kinematical regions and as a function of missing energy (excitation energy). The previous experiments were:

---

[1] S. M. Dolfini *et al., Nuclear Instruments and Methods* (1993)

[2] To be published

[3] J. Mandeville and the OOPS collaboration, *Nuclear Instruments and Methods* (1993)

[4] M. Holtrop *et al.*, **The ELSSY Matrix Elements**, *BATES Internal Report*, (1992)

- Quasielastic Longitudinal-Transverse separation of the cross-section at q = 400 MeV/c and ω = 120 MeV/c.[5]
- Dip region measurement at q = 400 MeV/c and ω = 275 MeV.[6]
- Two Δ measurements, at q = 400 MeV/c and ω = 275 MeV, and q = 473 MeV/c and ω = 382 MeV.[7]
- Quasielastic measurement at q = 585 MeV/c and ω = 210 MeV, q = 775 MeV/c and ω = 355 MeV, and q = 827 MeV/c and ω = 325 MeV.[8]
- Quasielastic measurement at high momentum transfer, q = 1000 MeV/c and ω = 330 MeV and ω = 475 MeV.[9]
- ^{12}C(e,e'p) and ^{12}C(e,e'd) at q = 913 MeV/c and ω = 235 MeV.[10]

This experiment was part of a set of three that were performed sequentially in the North Hall Experimental area. The other two experiments were

- Quasielastic R_l/R_T separation on the Deuteron at q = 400 MeV/c and ω = 100 MeV.[11]
- Quasielastic R_{LT} separation on the Deuteron at q = 400 MeV/c and ω = 100 MeV.[12]

The advantage of performing similar experiments back to back was clear in being able to share many of the calibrations required for an accurate measurement, reducing the amount of beam time needed. We were able to share beam energy calibrations, efficiency calibrations, rate corrections and spectrometer optics calibrations. Unfortunately there was still a limited amount of beam time, which reduced the amount of time devoted to some calibrations that could have improved the overall accuracy of this experiment. Also, the geometry of the North Hall was too restrictive to allow the proton arm to go much beyond 64°, which limited the kinematics for the R_{LT} separation.

This chapter will give an overview of electron scattering in general and exclusive electron scattering in more detail. Chapter 2 will explain the experimental setup and data

---

[5] P. Ulmer *et al., Phys. Rev. Lett.* **59**, 2259 (1987)
[6] R. Lourie *et al., Phys. Rev. Lett.* **56**, 2364 (1986)
[7] H. Baghaei *et al., Phys. Rev.* **C39**, 177 (1989)
[8] L. Weinstein *et al., Phys. Rev. Lett.* **64**, 1646 (1990)
[9] J. Morrison, *Ph.D. Thesis,* MIT, unpublished. (1993)
[10] S. Penn, *Ph.D. Thesis,* MIT, unpublished. (1993)
[11] D. Jordan, *Ph.D. Thesis,* MIT, unpublished. (1994)
[12] T. McIlvain, *Ph.D. Thesis,* MIT, unpublished. (1995)

acquisition. Chapter 3 will focus on the data analysis and the software, chapter 4 will describe the normalizations, and finally chapter 5 will present the results and discuss them. Some of the details of the analysis are relegated to appendices, or referenced to other publications.

1.1 Electron Scattering.

Electron scattering is one of the means of exploring the nucleus, and has proven itself to be very useful in this endeavor. In an electron scattering experiment the accelerator accelerates the electrons to a known energy and this beam is then projected onto a target composed of material containing the nucleus of interest. A spectrometer then detects scattered particles at a particular momentum and angle. In a *single arm* experiment the detected particle is the scattered electron, and when in this process the final nuclear state is not unique, it is an *inclusive* experiment. If the scattered electron is detected at the same time with another particle, the experiment is a *coincidence* experiment. Most of the time experiments like these distinguish a unique final state, which makes them *exclusive* experiments. Often *single arm* scattering is *inclusive* and *coincidence* scattering is *exclusive* but this is not always the case.

Some of the key features of electron scattering are:

- Electron scattering interactions are calculable with quantum electro-dynamics (QED), which is well known and yields accurate predictions. This allows one to probe the details of the nuclear current, J_μ , and extract detailed information about the nuclear structure. This stands in contrast with proton or pion scattering where the interaction is dominated by the strong force, which is not well understood.
- The electromagnetic interaction is relatively weak, which allows the interaction to be described with the one-photon exchange approximation for the lighter nuclei ($Z\alpha << 1$). It also means that the mean free path of the virtual photon is large and thus it can probe the entire nuclear volume. Hadronic probes on the other hand interact strongly, and consequently they mostly sample the nuclear surface; also they cannot be described by a single boson exchange. The disadvantage of the weakness of the electromagnetic force is that the cross-sections are much smaller than for hadron scattering, and as a result the experiments take longer.

- It is possible to vary the momentum transferred to the target ($\vec{q}^2$) independently of the energy that is transferred (ω), with the constraint that the virtual photon that is exchanged is space-like ($\vec{q}^2 \geq \omega^2$). This allows the momentum distribution of specific transition matrix elements to be mapped out. A Fourier transform of that map can be used to derive the spatial distribution of the charge and current density of the nucleus. This is not possible for real photon absorption experiments, which have the constraint that the photon is massless and thus $\vec{q}^2 = \omega^2$.
- It is possible to vary the polarization of the exchanged virtual photon from longitudinal (along the direction of the momentum) to transverse (perpendicular to the direction of the momentum). The longitudinal photon interacts with the charge density, while the transverse photon interacts with the current density. This allows for a more detailed extraction of the nuclear structure, expressed mathematically in structure functions.This will be discussed in section 1.2 and section 1.3.2.
- The analysis and interpretation of electron scattering is complicated by the process of radiation of the electron in the presence of the target nuclei. Although this process is well understood, the unfolding of the radiative tail poses a difficult question. This problem was manageable for single arm experiments, but for coincidence experiments it has only recently been fully investigated. Section 3.6 will describe the details of this procedure. The problem of radiative corrections gets worse at higher energies and momentum transfers, and at some point ($P_{final} > M_{proton}$) the radiating of the ejected proton also has to be taken into account.
- The first generation of electron accelerators provided a pulsed beam with a duty factor of about 1%. Since many experiments need to limit the peak beam current to obtain an acceptable signal to noise ratio, or to prevent damage to the target, experiments can take 100 times longer than would be the case with a continuous beam. This disadvantage is alleviated by the onset of continuous beam accelerators like CEBAF, AMPS at NIKHEF, the Mainz microtron, and the Bates stretcher ring, where the beam is on the target continuously. This is essential for many coincidence experiments at high momentum transfer.

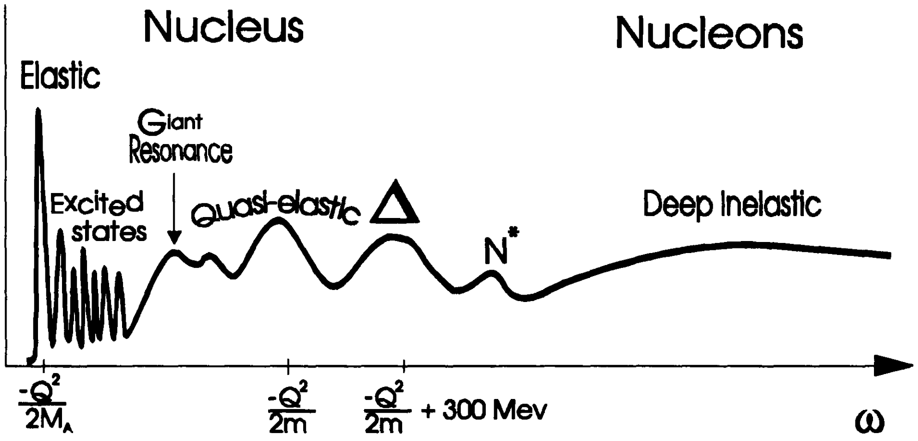

Figure 1.1 A generic single arm inclusive electron scattering spectrum.

1.2 Single Arm Electron Scattering.

A generic inclusive (e,e') spectrum showing the cross-section as a function of ω for a fixed value of $Q^2 = \omega^2 - q^2$, is presented in figure 1.1. Different regions of this spectrum can be distinguished and associated with various distinct physical processes. With increasing energy loss, the first feature in the graph is the elastic peak, at $\omega = -Q^2/2M_A$, the recoil energy of the nuclear mass, where the nucleus remains in the ground state. Next are the excited states, a number of sharp peaks that correspond to various excitations of bound nuclear states. Then comes a set of broader bumps that are caused by the excitation of collective modes, called "the giant resonances." Next is the broad quasielastic peak, located at, $\omega \cong -Q^2 / 2m$ where the virtual photon is absorbed on a single nucleon with mass *m*, which is subsequently emitted from the nucleus. The kinematics of this nucleon are close to that of a free particle with momentum p_i. The width of the peak arises from the distribution of this momentum, according to $(\vec{q} + \vec{p}_i)^2 / 2m$. The next peaks are the delta resonance and other resonant excitations, which correspond to the excitation of a nucleon to the Δ and other particle excitations. Between the quasielastic peak and the delta peak is a region called the "dip region", which has received much interest. Beyond these peaks is a large region called Deep Inelastic Scattering, where scattering from individual constituent quarks becomes visible.

In the one photon approximation the cross-section for single arm electron scattering can be written as:

$$\frac{d^3\sigma}{dk'\,d\Omega_{k'}}=\frac{4\pi\sigma_M}{M_A}\left\{\frac{q_\mu^4}{q^4}R_L(\vec{q},\omega)+\left(\frac{q_\mu^2}{2q^2}+\tan^2\left(\frac{\theta_e}{2}\right)\right)R_T(\vec{q},\omega)\right\} \tag{1.1}$$

where R_L and R_T are the longitudinal and transverse structure functions, M_A is the mass of the target nucleus, k', $\Omega_{k'}$ and θ_e are the momentum, solid angle and scattering angle of the detected electron, q_μ is the four vector $(\vec{q},\omega)$, and σ_M is given by:

$$\sigma_M=\frac{\alpha^2\cos^2\left(\frac{\theta_e}{2}\right)}{4k_0^2\sin^4\left(\frac{\theta_e}{2}\right)} \tag{1.2}$$

where $\alpha \cong 1/137$ is the fine structure constant, and k_0 is the incident electron momentum.

1.2.1 Quasielastic (e,e') Scattering

To first order quasielastic scattering can be approximated as scattering from free non-interacting nucleons in the nucleus. The assumption made (the impulse approximation) is that a virtual photon with energy and momentum $(\omega,\vec{q})$ is absorbed on a single nucleon with momentum $\vec{p}_i$ and this nucleon is ejected from the nucleus without interacting with any of the other nucleons. Thus in this kinematical regime the nucleus would look like a collection of Z protons and N neutrons. Figure 1.2 shows that the cross-section of the quasielastic peak approximately scales with A for light nuclei where N ≈ Z. Keeping with this model the relationship between ω and q can be derived

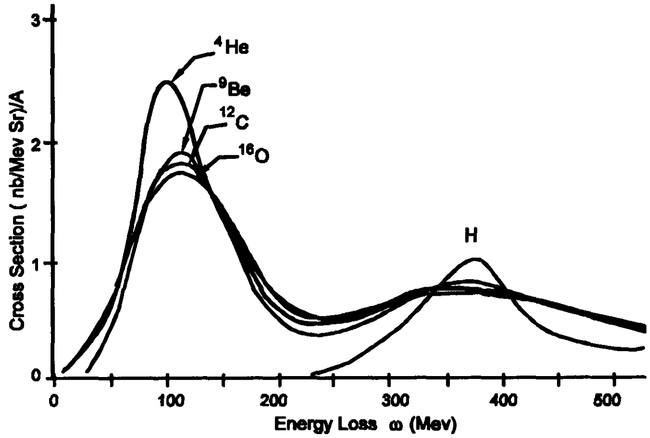

Figure 1.2 Inclusive cross-section per nucleon for a range of light nuclei[13].

---

[13] J. S. O'Connell *et al., Phys. Rev. Lett.,* ***53,*** 1627 (1984); *Phys Rev,* ***C35,*** 1063 (1987)

from energy conservation:

$$\omega = \frac{(\vec{q}+\vec{p}_i)^2}{2M_N} - \left(\frac{\vec{p}_i^2}{2M_N} - \bar{\varepsilon}\right) = \frac{\vec{q}^2}{2M_N} + \frac{\vec{q}\cdot\vec{p}_i}{M_N} + \bar{\varepsilon} \qquad \textbf{(1.3)}$$

where $\bar{\varepsilon}$ is a small energy shift which represents the difference in the final and initial state interactions and the energy dependence of the nucleon-nucleus potential.[14]

The non-interacting Fermi gas model provides a simple but reasonable description of non-separated single arm quasielastic scattering data. In this model the nuclei populate momentum space uniformly up to the Fermi momentum, given by:

$$k_f = (6\pi^2\rho)^{1/3} = \left(6\pi^2\frac{\rho_0}{4}\right)^{1/3} \qquad \textbf{(1.4)}$$

where ρ is the density of identical particles and ρ_0 is the average nuclear density, which takes into account the spin-isospin symmetry. Nuclei heavier than Nickel have a density that is close to the value for infinite nuclear matter with density $\rho_0 \approx 0.17\ \text{fm}^{-3}$, this gives a value for the Fermi momentum of $k_f \approx 270$ MeV/*c*. The Fermi energy is then given by $\varepsilon_f = k_f^2 / 2M_N \approx 39\text{Mev}$.

This model was used by Whitney, *et al.*[15], using calculations by E. Moniz, to fit data from a wide range of nuclei, from Lithium to Lead. The only variables that were fit were k_f and $\bar{\varepsilon}$. It can be noted that $\bar{\varepsilon}$ was found to be close to that of estimates from simple shell model calculations. These data and the fit are presented in Figure 1.3. The quasielastic peaks are reasonably well reproduced by this simple model, but this agreement is slightly deceiving. It was found by De Forest[16] that when the more realistic harmonic oscillator momentum densities are used, with center-of-mass motion corrections and using experimental separation energies, the good agreement can only be achieved when final-state interactions are taken into account. The model also ignored relativistic effects. This complicates the simple picture of the non-interacting Fermi gas.

---

[14] K. Y. Horikawa, F. Lenz and N. C. Mukhopadhyay, *Phys. Rev.* **C22** 1680 (1980)

[15] R. R. Whitney, I. Sick, J. R. Ficenec, R. D. Kephart, and W. P. Trower, *Phys. Rev,* **C9** 2230 (1974).

[16] T. De Forest, Jr. , in "Effets Mésoniques dans les Noyoux et Diffusion d'Electrons à Energy Intermédiaire", Saclay, CEA DPHN p. 223, (1975) as noted in S. Frullani and J. Mougey, *Advances in Nuclear Physics Vol 14,* ed. by J. W. Negele and E. Vogt, Plenum Press, New York (1984)

Experiments on ^{12}C [17], ^{40}Ca [18], ^{56}Fe [19] separating the longitudinal and transverse response functions found that the reduced longitudinal response function was about 40% low compared to the Fermi-gas calculations, and the reduced transverse response function was slightly high. This further indicates the discrepancies of the Fermi-gas model.

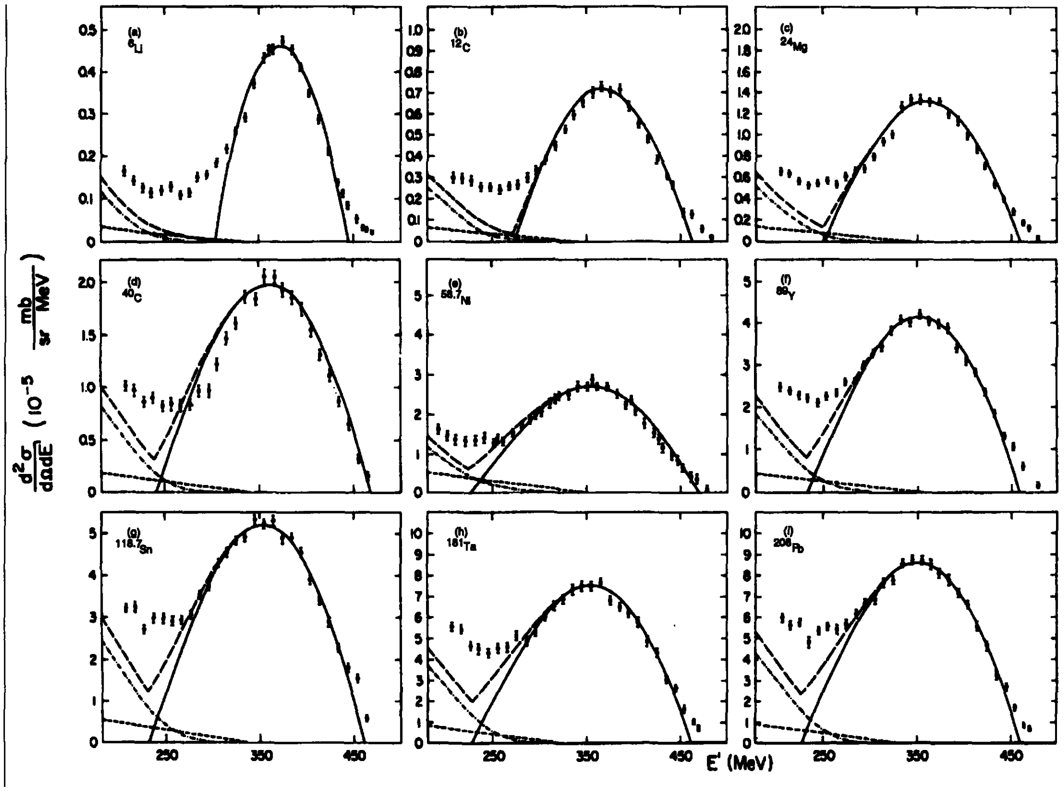

Figure 1.3 Quasielastic (e,e') data for a range of nuclei. (from Whitney, et al.)

1.3 Coincidence Electron Scattering.

In a coincidence electron scattering experiment the scattered electron is detected at the same time as a knocked out particle. By doing so the experimenter is able to select a particular final state, and thus make an *exclusive* measurement, which

---

[17] J. M. Finn, R. W. Lourie, B. H. Cottman, *Phys. Rev. Lett* **49**, 1016 (1982)
[18] P. Barreau *et al.*, *Nucl. Phys.* **A402**, 515 (1983)
[19] R. Altemus *et al.*, *Phys. Rev. Lett.* **44**, 965 (1980)

allows for a more detailed study of the reaction mechanism. In this way the experiment can be designed to be sensitive to a particular part of the theory, for instance the final state interactions, and hopefully shed light on its accuracy.

The underlying formalism for coincidence scattering reactions is more complicated than that for single arm reactions. The next three sections will define the conventions used in this work, and occasionally alternative definitions will be shown.

1.3.1 Kinematics

Although it seems that the kinematics of a coincidence reaction would be fairly straightforward, there are some intricacies, which will be highlighted in this section. The formalism used is the same as that by T. W. Donnelly,[20] and follows the conventions of Bjorken and Drell,[21] but with the metric for four-vectors defined so that $g_{00} = -1$, all other diagonal elements are 1, and the off diagonal elements are all zero.

The incident electron 4-momentum, on the electron side of the reaction, is defined by $K^{\mu} = (E_b, \vec{k})$ and the scattered electron 4-momentum by $K'^{\mu} = (E_f, \vec{k}')$. Since only highly relativistic electrons with a momentum much larger than the electron mass are considered (extreme relativistic limit, ERL), the electron mass can be neglected so that $|\vec{k}| = E_b$ and $|\vec{k}'| = E_f$. On the hadron side of the reaction we have $P_A^{\mu} \equiv (M_A, 0)$ in the laboratory frame, since the target nucleus is at rest, and $P_B^{\mu} \equiv (E_B, \vec{p}_B)$ and $P_N^{\mu} \equiv (E_N, \vec{p}_N)$ for the recoiling residual nucleus and the knocked-out particle respectively. Since these particles are *on-shell* they obey the relationships $E_B = \sqrt{\vec{p}_B^{\,2} + M_B^2}$ and $E_N = \sqrt{\vec{p}_N^{\,2} + M_N^2}$. The 4-momentum transferred to the nucleus is then given by:

$$Q^{\mu} \equiv (\omega, \vec{q}) = K^{\mu} - K'^{\mu} = P_N^{\mu} + P_B^{\mu} - P_A^{\mu} \tag{1.5}$$

---

[20] T. W. Donnelly, *Nucl. Phys.* **A555**, (1993) and "Polarization in Lepton-induced Reactions" presented at the NATO Advanced Study Institute on Perspectives in the Structure of Hadronic Systems, Dronten, The Netherlands, 1993

[21] J. D. Bjorken and S. D. Drell, "Relativistic Quantum Mechanics," McGraw-Hill, New York (1964)

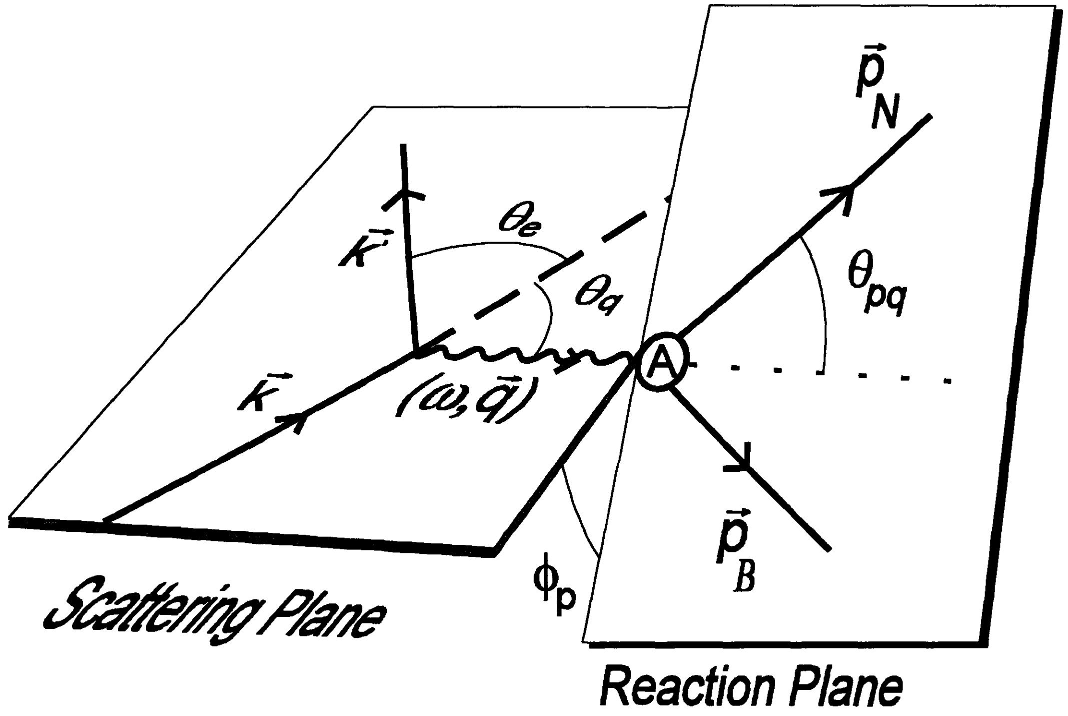

Figure 1.4 Kinematics of the (e,e'p) reaction. The angle ϕ_p determines the angle between the reaction plane and the scattering plane. When this is 0 or π the scattering is in-plane, otherwise it is out-of-plane. One often also defines an angle θ_p (not indicated here), which is the angle between $\vec{p}_N$ and $\vec{k}$ in the scattering plane.

with the magnitude $Q^2 \equiv Q^\mu Q_\mu = \omega^2 - \vec{q}^2 \le 0$. The geometry of these vectors is shown in figure 1.4.

Some useful quantities can be defined for the analysis of this problem. One defines the missing momentum as:

$$\vec{p}_m \equiv \vec{p}_N - \vec{q}. \tag{1.6}$$

Sometimes one also sees a definition of missing momentum that is the negative of that given here. The quantity P_m is the absolute value of $\vec{p}_m$, and is sometimes assigned a sign. The convention for the sign of P_m is different in different situations. When parallel kinematics are used, where $\theta_{pq} = 0$, the sign is often defined as positive for parallel and negative for anti-parallel, which again depends on the convention for $\vec{p}_m$. On the other hand when perpendicular kinematics are used, where $\vec{p}_m \perp \vec{q}$, the sign for P_m is positive when $\theta_p \leq \theta_q$, and negative when $\theta_p < \theta_q$. Again this is an arbitrary choice. In this work, P_m is not assigned a sign, unless specificly noted.

From momentum conservation it is possible to write $\vec{p}_m = -\vec{p}_B$. In the plane wave impulse approximation (PWIA) , see section 1.3.2 , this can be equated with the initial momentum of the struck particle, $\vec{p}_i = \vec{p}_m = -\vec{p}_B$.

There are a few different ways in which the excitation of the system can be defined. What is usually called the missing energy is defined by:

$$\begin{aligned} E_m &= M_N + M_B - M_A \\ &= E_N - T_N + E_B - T_B - M_A \\ &= \omega - T_N - T_B \end{aligned} \tag{1.7}$$

where in the last step the energy conservation equation, $M_A + \omega = E_N + E_B$, was used. Notice that for this equation the recoil mass, M_B, includes the excitation energy of the recoiling nucleus, and it also includes all energies associated with unobserved particles in the final state (e.g. two particle knockout). If one defines $E_B^0 = \sqrt{\vec{p}_B^2 + M_B^{0^2}}$, where M_B^0 is the mass of the B system in its ground state, a different energy can be introduced[22]:

$$\mathcal{E} \equiv E_B - E_B^0 \tag{1.8}$$

which can in some situations be more convenient to use than the missing energy, since it will be equal to zero when the residual nucleus is in the ground state. This energy can be used instead of the missing energy. The two are related by:

$$\begin{aligned} E_m &= E_s + \mathcal{E} + \left(T_{rec}^0 - T_{rec}\right) \\ &\cong E_s + \left[1 - \frac{\vec{p}_B^2}{2M_B^0 M_B}\right]^{-1} \mathcal{E}, \ \text{for}\, \vec{p}_B^2 \ll 2M_B^0 M_B \end{aligned} \tag{1.9}$$

---

[22] First introduced in Day, McCarthy,Donnelly and Sick, *Ann. Rev. Nucl. Part. Sci..* **40**, 357 (1990)

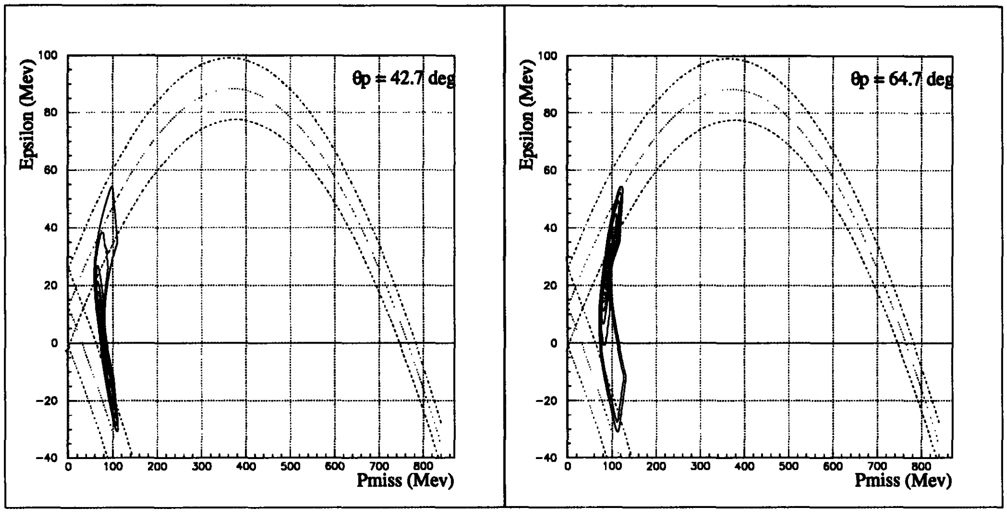

Figure 1.5 $\mathcal{E}$(Epsilon) versus P_m (Pmiss) Phase Space plot. The contour lines represent the region covered by the spectrometers. The dotted lines represent the three theoretically accessible areas for three fixed settings of {q,ω}, representing the minimum, typical and maximum region for the kinematics of this experiment. The region for $\mathcal{E}$<0 is not physical.

where $T^0_{rec} = E^0_B - M^0_B$ is the recoil kinetic energy of the B system in it's ground state, and $E_s \equiv M_N + M^0_B - M_A$ is the separation energy, the smallest amount of energy needed to separate a particle N from nucleus A to produce nucleus B.

The kinematic reaction can now be completely described by a set of four scalar variables (for in-plane non-polarized scattering.) There are several choices that can be made for this set: $\{Q^2, Q_\mu P^\mu_A, P_{N\mu} P^\mu_A, Q_\mu P^\mu_N\}$ or $\{q, \omega, E_N, \theta_{pq}\}$ or $\{q, \omega, \mathcal{E}, P_m\}$, $\{q, \omega, E_m, P_m\}$, and so on. There are various transformations that would take you from one set to another, but you need to be careful not to over-specify the kinematics. Thus one can plot against P_m where one could just as well have used θ_p, but one must be careful when specifying both.

It is interesting to see what the phase space in the $\mathcal{E}$(epsilon) versus P_m plot looks like, and what region is theoretically available. This is plotted in figure 1.5, where the contour lines indicate the region covered by the spectrometers in this experiment. The dotted lines indicate the theoretically accessible region for the minimum, typical and maximum combination of q and ω that were covered by the finite acceptance of the spectrometers. Note that the angle for θ_p that is indicated on the plots refers to the angle setting of the proton spectrometer, while the actual value of θ_p for the proton varies with

P_m. The geometry of the contour lines is different when the proton arm is moved to the other side of the q-vector because of the finite acceptance of the spectrometers.

1.3.2 Born Approximation

For light or medium nuclei at high q^2 it is reasonable to simplify the scattering process by assuming the one-photon approximation, or Born approximation. A diagram of this process is depicted in figure 1.6. This approximation allows one to write the scattering cross-section in terms of the well understood electron tensor, and the nuclear current, which contains all the information of interest. This can then be expressed as a linear combination of a set of structure functions which contain the information on the nuclear structure. The details of this derivation can be found in several standard references, among which are 23, 24, 25 and 26.

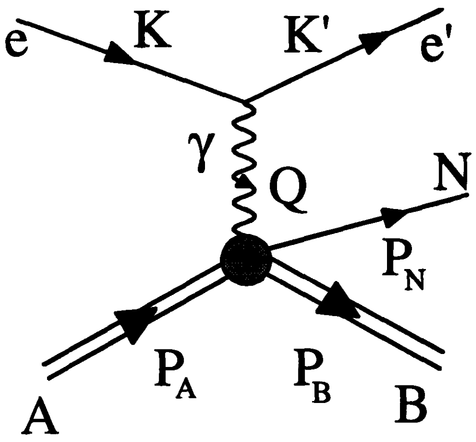

Figure 1.6 Feynman picture for the A(e,e'N)B reaction in Born Approximation

The Born approximation allows for the factorization of the transition matrix element. Following the Feynman rules for this interaction one finds a propagator for the virtual photon that takes the form: $D_F(Q)_{\mu\nu} = -g_{\mu\nu} / Q^2$. On the electron side the electromagnetic current can be written as[27]:

$$j_e(K';K)_\mu = -e\left(\frac{m_e^2}{E_b E_f}\right)^{1/2} \bar{u}_e(K')\gamma_\mu u_e(K) \tag{1.10}$$

---

[23] T. W. Donnelly and J. D. Walecka, *Annual Review of Nuclear Science,* **25**, 329 (1975)

[24] S. Frullani and J. Mougey, "Single Particle Properties of Nuclei Through (e,e'p) Reactions," in *Advances in Nuclear Physics*, Vol 14, edited by J. W. Negele and E. Vogt, Plenum Press, New York (1984)

[25] A. S. Raskin and T. W. Donnelly, *Annals of Physics*, **191**, 78-142 (1989)

[26] S. Boffi, C. Giusti and F. D. Pacati, *Phys. Rep.* **226**, (1993)

[27] Notice that the normalizations used here are those of T. W. Donnelly and S. Boffi who follow the conventions of Bjorken and Drell, with $\bar{u}_e\gamma^0 u_e = 1$, while Frullani and Mougey use $\bar{u}_e\gamma^0 u_e = 2k_o$.

where u_e and $\overline{u}_e$ are the incoming and outgoing Dirac spinors, with four momenta K and K' and the spin labels are suppressed. On the hadron side one can use $J^\mu(P_f,P_B;P_i)_{fi}$ to represent the nuclear electromagnetic transition current. Using these two currents the invariant matrix element can now be written as:

$$\mathcal{M}_{fi} = \frac{ie}{Q^2}\left(\frac{E_b E_f}{m_e^2}\right)^{1/2} j_e(K';K)_\mu J^\mu(P_N,P_B;P_A) \tag{1.11}$$

Following Bjorken and Drell, the scattering cross-section in the laboratory frame then takes the form:

$$\begin{aligned} d\sigma &= \int \frac{d^3\vec{p}_N}{(2\pi)^3}\frac{d^3\vec{p}_B}{(2\pi)^3}\frac{d^3\vec{k}'}{(2\pi)^3}\frac{M_N}{E_N}\frac{M_B}{E_B}\frac{m_e}{E_f}\frac{m_e}{E_b}\frac{M_A}{E_A}\overline{\sum_{if}\left|\mathcal{M}_{fi}\right|}^2 \\ &\times\frac{(2\pi)^4\delta^4(K+P_A-K'-P_B-P_N)}{\left|J_{inc}\right|V} \end{aligned} \tag{1.12}$$

where the summation is an appropriate average over all initial states and a sum over all final states. The term $\left|J_{inc}\right|V$ is the incident flux times the reaction volume, which reduces to $\left|v_e\right| = k / E_b$. Since the nucleus is at rest in the laboratory frame $M_A = E_A$, and since the recoiling nucleus is not detected an integration is performed over $\vec{p}_B$. This results in:

$$\begin{aligned} d\sigma &= \frac{1}{(2\pi)^5}\frac{m_e^2}{kE_f}\frac{M_N M_B}{E_N E_B}\overline{\sum_{if}\left|\mathcal{M}_{fi}\right|^2}k'^2\,dk'\,p_N^2 dp_N d\Omega_e d\Omega_N \\ &\times\delta\left(E_b+M_A-E_f-E_N-E_B\right) \end{aligned} \tag{1.13}$$

This gives the form of the 6-fold differential cross-section. The delta function enforces energy conservation, and can be rewritten as $\delta(E_m+M_A-M_N-M_B)$[28]. For discrete states equation 1.13 can be integrated over the missing energy, by transforming the differential with the use of a Jacobian[29] (see table 1.1 later in this section). This is equivalent to integrating over the momentum of the outgoing proton, after a

---

[28] M_B in this equation is the mass of the residual nucleus, which for excited states includes the excitation energy.

[29] Sylvester, *Camb. & Dubl. Math Journal*, (1852)

transformation of the variables in the delta function. The transformation introduces the term:

$$\begin{aligned}\mathscr{J}_{[dP_N \to dE_m]} &= \left|\frac{\partial P_N}{\partial E_m}\right| \\ &= \left[\frac{\partial}{\partial P_N}\left(E_b + M_A - E_f - E_B - E_N\right)\right]^{-1} \\ &= \left(\frac{E_B E_N}{M_A P_N}\right)\mathrm{f}_{rec}^{-1}\end{aligned} \qquad \textbf{(1.14)}$$

with

$$\mathrm{f}_{rec} = \left|1 + \frac{\omega p_N - E_N q \cos\left(\theta_{pq}\right)}{M_A p_N}\right| \qquad \textbf{(1.15)}$$

Note that this term is different from the recoil factor that is used for single arm scattering. It is also worth noting that Frullani and Mougey do not take the E_B/M_A factor out of the recoil function, which means that their kinematic constant differs by a factor M_A/E_B. The 5-fold differential cross-section is then given by:

$$\frac{d\sigma^5}{dE_f d\Omega_e d\Omega_p} = \frac{m_e^2 M_N M_B}{(2\pi)^5 M_A}\frac{k' \, p_N}{k}\mathrm{f}_{rec}^{-1}\overline{\sum_{if}}\left|\mathscr{M}_{fi}\right|^2 \qquad \textbf{(1.16)}$$

The invariant matrix element $\mathscr{M}_{fi}$ can be written in terms of a lepton tensor,

$$\eta_e(K';K)_{\mu\nu} \equiv \overline{\sum_{if}}\left[\bar{u}_e(K')\gamma_\mu u_e(K)\right]^*\left[\bar{u}_e(K')\gamma_\nu u_e(K)\right] \qquad \textbf{(1.17)}$$

and a hadron tensor, $W^{\mu\nu}(Q)_{fi} \equiv \overline{\sum_{if}} J^{\mu *}(Q)_{fi} J^{\nu}(Q)_{fi}$, which results in:

$$\overline{\sum_{if}}\left|\mathscr{M}_{fi}\right|^2 = \frac{(4\pi\alpha)^2}{Q^4}\eta_e(K';K)_{\mu\nu} W^{\mu\nu}(Q)_{fi} \qquad \textbf{(1.18)}$$

The electron tensor can be simplified by making use of some of its properties, namely current conservation, $Q_\mu J^\mu = 0$, and symmetry properties. The trace of equation 1.17 can then be evaluated in the extreme relativistic limit (ERL, $m_e=0$)[30]:

$$4m_e^2\eta_e(K';K)_{fi}^{ERL} = 2\left(K_\mu K'_\nu + K'_\mu K_\nu\right) + Q^2 g_{\mu\nu} - 2ih\varepsilon_{\mu\nu\alpha\beta}K^\alpha K'^\beta \tag{1.19}$$

The contraction of the lepton tensor and hadron tensor can now be rewritten in a more convenient form:

$$4m_e^2\eta_e(K';K)_{\mu\nu} W^{\mu\nu}(Q)_{fi} = v_0 \sum_K v_K R_{K\,fi} \tag{1.20}$$

which defines the form of the nuclear response functions, $R_{K\,fi}$, which contain all the information about the nuclear structure and nuclear dynamics. The label K takes on the values L, T, TT, and LT (the terms that require polarization are left out). There are four structure functions, which corresponds to the four independent scalar quantities that are available from the kinematics (see section 1.3.1). The label L refers to the longitudinal, and T refers to the transverse, component of the virtual photon polarization. If the scattering is not constrained to be in-plane and unpolarized, a two more independent scalar quantities are available: ϕ_p, the out-of-plane angle, and h the helicity of the beam. Now additional response functions can be extracted: T' and LT'. The common factor $v_0 \equiv \left(E_b + E_f\right)^2 - q^2 = 4E_b E_f \cos^2\left(\tfrac{1}{2}\theta_e\right)$ is taken out of the v_k functions for simplification later. The cross-section can then be written as:

$$\frac{d\sigma^5}{dE_f d\Omega_e d\Omega_p} = \frac{1}{(2\pi)^3} C_{kin}\sigma_{Mott}\, \mathrm{f}_{rec}^{-1} \left\{ \begin{array}{l} v_L R_{L\,fi} + v_T R_{T\,fi} + v_{TT} R_{TT\,fi} + v_{LT} R_{LT\,fi} \\ + h\left(v_{T'} R_{T'} + v_{LT'} R_{LT'}\right) \end{array} \right\} \tag{1.21}$$

where f_{rec} is the recoil function defined by equation 1.15, and σ_{Mott} is the Mott cross-section defined by:

$$\sigma_{Mott} \equiv \frac{\alpha^2}{Q^4}\frac{E_f}{E_b} v_0 = \left(\frac{\alpha \cos\theta_e/2}{2E_b \sin^2\theta_e/2}\right)^2 \tag{1.22}$$

The factor C_{kin} is a kinematic constant, and for this formalism equates to:

---

[30] T. W Donnelly and A. S. Raskin, *Ann. Phys.*, **169** (1986),247

$$C_{kin} = \frac{M_B M_N p_N}{M_A} \tag{1.23}$$

However in other works, namely the work of Boffi[26,32] (programs based on his work such as **PV5FF** and **DWEEPy**), a different formalism with a different constant and a different recoil function is used. This constant takes on the form:

$$C_{\mathrm{Boffi}} = (2\pi)^3 p_N E_N \left[\frac{E_B}{M_A}\right] = (2\pi)^3 \left(\frac{E_B E_N}{M_B M_N}\right) C_{kin} \tag{1.24}$$

where the term in square brackets is absorbed in the recoil function for the Boffi formalism. The ratio of the two constants for our kinematics is $C_{\mathrm{Boffi}}/C_{kin}$ = $(E_B E_N/M_B M_N)(2\pi)^3 \approx E_N/M_N(2\pi)^3 = 1.09(2\pi)^2$. The difference between the two formalisms is embedded in the conventions used for normalizing the nuclear current[31]. It is also important to note that different differential cross-sections are related by Jacobian transformations. Thus a cross-section with a different differential will have a different kinematic constant. Table **1.1** list a number of frequently used differential cross-sections with the appropriate Jacobian transformation and kinematic constant times recoil function. The differential cross-sections are given as six-fold differentials. Notice that a five fold differential cross-section can only be obtained by an integration over the delta function, $\delta(E_b + M_A - E_f - E_B - E_N) = \delta(E_m + M_A - M_B - M_N)$, which can only be done readily with the $d^6\sigma/d\omega dE_m d\Omega_e d\Omega_p$ differential (see equations 1.13 - 1.16). The Jacobians that are given in this table present the transformation relative to equation 1.21. The kinematic constants are for the formalism presented in this chapter.

---

[31] The $(2\pi)^3$ can be traced back to the normalization used by T. De Forest. The remainder of the term could alternatively be caused by neglecting the energy of the recoil system when integrating equation 1.13.

The form factors and the electron kinematic factors R_k and v_k are given in table 1.2. The coordinate system is one where the z-axis lies along $\vec{q}$ and the y-axis is perpendicular to the scattering plane. The current is expressed in spherical coordinates using:

$$
\begin{aligned}
\vec{J}(\vec{q}) &= \sum_{m=0,\pm1} J(\vec{q};m)\vec{e}^{\,*}(q;1,m) \\
\vec{e}(q;1,0) &= u_z \\
\vec{e}(q;1,\pm1) &= \mp {}^{1}\!/\!_{\sqrt{2}}\left(u_x \pm i u_y\right)
\end{aligned}
\qquad \textbf{(1.25)}
$$

And $J(\vec{q};0)$ was eliminated in favor of $\rho(\vec{q}) \equiv J_0(\vec{q})$ by using the current conservation equation,

$$
Q^0 J_0(\vec{q}) - \vec{q}\cdot\vec{J}(\vec{q}) = \omega\rho(\vec{q}) - qJ(\vec{q};0) = 0 \qquad \textbf{(1.26)}
$$

Table 1.1 Kinematic constants for different differential cross-sections.

Differential	**Jacobian, $\mathcal{J}$**	$C_{kin}\,\mathrm{f}_{rec}^{-1} =$
$\dfrac{d^6\sigma}{dE_f dE_m d\Omega_e d\Omega_p}$	1	$\dfrac{M_B M_N p_N}{M_A}\mathrm{f}_{\mathrm{rec}}^{-1}$
$\dfrac{d^6\sigma}{dE_f dp_N d\Omega_e d\Omega_p}$	$\left\lvert\dfrac{\partial E_m}{\partial p_N}\right\rvert = \left(\dfrac{M_A P_N}{E_B E_N}\right)\mathrm{f}_{\mathrm{rec}}$	$\left(\dfrac{M_B M_N}{E_B E_N}\right)p_N^2$
$\dfrac{d^6\sigma}{dE_f d\Omega_e d^3\vec{p}_N}$	$\left\lvert\dfrac{\partial E_m}{p_N^2\partial E_N}\right\rvert = \dfrac{1}{p_N^2}\left(\dfrac{M_A P_N}{E_B E_N}\right)\mathrm{f}_{\mathrm{rec}}$	$\left(\dfrac{M_B M_N}{E_B E_N}\right)$
$\dfrac{d^6\sigma}{dE_f dE_p d\Omega_e d\Omega_p}$	$\left\lvert\dfrac{\partial E_m}{\partial E_N}\right\rvert = \left(\dfrac{E_N}{p_N}\right)\left(\dfrac{M_A P_N}{E_B E_N}\right)\mathrm{f}_{\mathrm{rec}}$	$\left(\dfrac{M_B M_N}{E_B E_N}\right)p_N E_N$

To convert the kinematic constants of the last column to the Boffi formalism, the constants should be multiplied by the factor $(E_B E_N / M_B M_N)(2\pi)^3$. The differential dE_f can be exchange with dk' or $d\omega$ in the limit of $m_e = 0$.

Table 1.2 Definition of the form factors and electron kinematic factors.

$v_L = \left(\frac{Q^2}{q^2}\right)^2$	$R_{L\,fi} \equiv \left\|\rho(\vec{q})_{fi}\right\|^2$
$v_T = -\frac{1}{2}\left(\frac{Q^2}{q^2}\right) + \tan^2\frac{\theta_e}{2}$	$R_{T\,fi} \equiv \left\|J(\vec{q};+1)_{fi}\right\|^2 + \left\|J(\vec{q};-1)_{fi}\right\|^2$
$v_{TT} = \frac{1}{2}\left(\frac{Q^2}{q^2}\right)$	$R_{TT\,fi} \equiv 2\,\mathrm{Re}\left\{J^*(\vec{q};+1)_{fi}\,J(\vec{q};-1)_{fi}\right\}$
$v_{LT} = \frac{1}{\sqrt{2}}\left(\frac{Q^2}{q^2}\right)\sqrt{-\left(\frac{Q^2}{q^2}\right) + \tan^2\frac{\theta_e}{2}}$	$R_{LT\,fi} \equiv -2\,\mathrm{Re}\left\{\rho^*(\vec{q})_{fi}\left(J(\vec{q};+1)_{fi} - J(\vec{q};-1)_{fi}\right)\right\}$
$v_{T'} = \tan\left(\frac{\theta_e}{2}\right)\sqrt{-\left(\frac{Q^2}{q^2}\right) + \tan^2\left(\frac{\theta_e}{2}\right)}$	$R_{T'\,fi} \equiv \left\|J(\vec{q};+1)_{fi}\right\|^2 - \left\|J(\vec{q};-1)_{fi}\right\|^2$
$v_{LT'} = \frac{1}{\sqrt{2}}\left(\frac{Q^2}{q^2}\right)\tan\left(\frac{\theta_e}{2}\right)$	$R_{LT'\,fi} \equiv -2\,\mathrm{Re}\left\{\rho^*(\vec{q})_{fi}\left(J(\vec{q};+1)_{fi} + J(\vec{q};-1)_{fi}\right)\right\}$

It is sometimes useful to write the equation for the cross-section in a form where the dependence on the out-of-plane angle φ_p is explicit. There are two forms that appear frequently:

$$\frac{d^5\sigma}{dE_f\,d\Omega_e\,d\Omega_p} = \frac{1}{(2\pi)^3}C_{kin}\sigma_{mott}\,\mathrm{f}_{rec}^{-1}\left\{\begin{array}{l} v_L W_L + v_R W_R + \\ v_{TT} W_{TT}\cos(2\phi_p) + \\ v_{LT} W_{LT}\cos(\phi_p) + \\ h\left(v_{T'} W_{T'} + v_{LT'} W_{LT'}\sin(\phi_p)\right) \end{array}\right\} \tag{1.27}$$

and[32]

---

[32] S. Boffi, C. Giusti and F. D. Pacati, *Nucl. Phys.* **A435**, 697

$$\frac{d^6\sigma}{d\vec{k}'\,d\vec{p}_N} = \frac{e^4}{8\pi^2}\frac{1}{Q^4kk'}\left\{\begin{array}{l} \rho_{00}f_{00} + \rho_{11}f_{11} + \\ \rho_{1-1}f_{1-1}\cos(2\phi_p) + \\ \rho_{01}f_{01}\cos(\phi_p) + \\ h\left(\rho_{11'}f_{11}' + \rho_{01'}f_{01}'\sin(\phi_p)\right) \end{array}\right\} \tag{1.28}$$

which is written as a six fold differential cross-section in the Boffi convention. The relationship between the various R, W and f structure functions and between the ρ and v kinematic functions are given in table 1.3.

Table 1.3 Relationships between various form factors and kinematic functions.

R_L	W_L	f_{00}	v_L	$\beta^{-1}\rho_{00}$	$\left(\frac{Q^2}{q^2}\right)^2$
R_T	W_T	f_{11}	v_T	$\beta^{-1}\rho_{11}$	$-\frac{Q^2}{2q^2}\varepsilon^{-1}$
R_{TT}	$W_{TT}\cos(2\phi_p)$	$f_{1-1}\cos(2\phi_p)$	v_{TT}	$\beta^{-1}\rho_{1-1}$	$\frac{1}{2}\left(\frac{Q^2}{q^2}\right)$
R_{LT}	$W_{LT}\cos(\phi_p)$	$-f_{01}\cos(\phi_p)$	v_{LT}	$-\beta^{-1}\rho_{01}$	$-\frac{1}{2}\left(\frac{-Q^2}{q^2}\right)^{3/2}\sqrt{\varepsilon^{-1}+1}$
$R_{T'}$	$W_{T'}$	f_{11}'	$v_{T'}$	$\beta^{-1}\rho_{1-1}$	$-\frac{Q^2}{2q^2}\frac{\sqrt{1-\varepsilon^2}}{\varepsilon}$
$R_{LT'}$	$W_{LT'}\sin(\phi_p)$	$-f_{01}'\sin(\phi_p)$	$v_{LT'}$	$\beta^{-1}\rho_{1-1}$	$-\frac{1}{2}\left(\frac{-Q^2}{q^2}\right)^{3/2}\sqrt{\varepsilon^{-1}-1}$
$\beta = 2E_bE_f\cos^2(\frac{1}{2}\theta_e) = \frac{1}{2}v_0$			$\varepsilon^{-1} \equiv 1-(2q^2/Q^2)\tan^2(\frac{1}{2}\theta_e)$		

1.3.3 Plane Wave Impulse Approximation

For the Plane Wave Impulse Approximation (PWIA) the following assumptions are made:

1. A single virtual photon is absorbed by a single proton in the nucleus, and the full momentum and energy transfer is absorbed by this proton.

2. This proton exits the nucleus without further interactions. Thus the outgoing proton is a plane wave.

3. This proton, not a spectator proton, is detected in the experiment, so that exchange terms can be neglected.

A diagram of this situation is sketched in figure 1.7 on the left hand side.

The initial momentum of the struck proton is now simply given by

$$\vec{p}_i = \vec{p}_N - \vec{q} = -\vec{p}_B. \tag{1.29}$$

which is equivalent to the definition of the missing momentum in equation 1.6. Using these assumptions the final state can now be factorized as a product of the final state of the outgoing proton and the final state of the recoiling nucleus. The hadronic tensor can then be written as[33]

$$W^{\mu\nu} = (2\pi)^3 \sum_{mm'} \mathscr{W}^{\mu\nu}_{mm'}(\vec{p}_i;\vec{q}) n_{mm'}(\vec{p}_i,\Omega^*) \tag{1.30}$$

where the quantity $\mathscr{W}^{\mu\nu}$ represents the part of the total hadronic tensor that depends on the γNN vertex and n which represents the probability of finding a nucleon with momentum p_i in the nucleus. The spectral function can now be introduced:

$$S(\vec{p}_i,\mathscr{E}) = n(\vec{p})\delta\left(\mathscr{E} - \left[M_A + \omega - E_N - E_B^0\right]\right) \tag{1.31}$$

which represents the probability of finding a proton with momentum $\vec{p}_i$ and energy $\mathscr{E}$ in the initial nucleus. Now combining equation 1.16 with equation 1.18 and 1.30 the 5-fold cross-section can be written as:

$$\begin{aligned} \frac{d^5\sigma}{dE_f d\Omega_e d\Omega_p} = {} & \frac{m_e^2 M_N M_B}{M_A} \frac{k' p_N}{k} \mathrm{f}_{rec}^{-1} \frac{2\alpha^2}{Q^4} \eta_e(K';K)_{\mu\nu} \mathscr{W}^{\mu\nu}(\vec{p}_i;\vec{q}) \\ & \times S(\vec{p}_i,\mathscr{E}) \end{aligned} \tag{1.32}$$

Next the off-shell electron nucleus cross-section is defined, which follows a prescription first developed by De Forest[34]:

---

[33] J. A. Caballero, T. W. Donnelly and G. I. Poulis, *Nucl. Phys.* **A555**, 709 (1993),
The factor $(2\pi)^3$ in this equation is inserted to make the following equations consistent with the formalism of T. De Forest.

[34] T. De Forest, *Nucl. Phys.*, **A392** (1983) 232

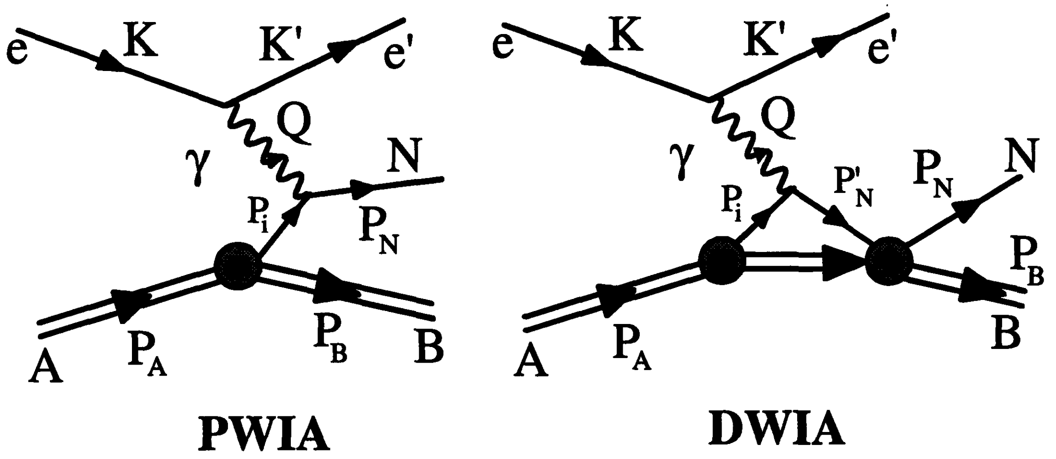

Figure 1.7 Diagram of Plane Wave Impulse Approximation and Distorted Wave Impulse Approximation

$$\sigma^{eN}_{CC1} = \frac{2\alpha^2}{Q^4}\left(\frac{k'}{k}\right)\eta_{\mu\nu}\mathcal{W}^{\mu\nu}(\vec{p};\vec{q}) \tag{1.33}$$

A more detailed treatment of the "CC1" half-off-shell cross-section can be found in Appendix B. A final expression for the 5-fold differential factorized cross-section is then given by:

$$\frac{d^5\sigma}{dE_f d\Omega_e d\Omega_p} = C_{kin}\, f^{-1}_{rec}\, \sigma^{eN} S(\vec{p}_i, E_m) \tag{1.34}$$

where the recoil function is given by equation 1.14 and the kinematic constant is the same as in equation 1.23 or 1.24 depending on the formalism used. This expression is appropriate for scattering from a shell in the nucleus where the binding energy is well defined. However, for scattering from the continuum it is appropriate to use a 6-fold cross-section, since the binding energy is not well defined and thus there is one additional degree of freedom. In this case the 6-fold cross-section can be expressed as:

$$\frac{d^6\sigma}{dE_f dE_m d\Omega_e d\Omega_p} = C_{kin}\, f^{-1}_{rec}\, \sigma^{eN} S(\vec{p}_i, E_m)\delta(E_m - M_A + M_N + M_B) \tag{1.35}$$

1.3.4 Distorted Wave Impulse Approximation

In the Distorted Wave Impulse Approximation the assumptions for the PWIA are made but now a final state interaction between the nucleus and the outgoing proton is allowed. This situation is depicted in the right hand side diagram of figure 1.7. This section will follow the discussion of S. Frullani and J. Mougey[35]. In order to still allow for the factorization of the cross-section a few additional assumptions about the reaction process need to be adopted:

1. The final state interaction does not depend on spin and does not change the internal nuclear quantum numbers.
2. Only a small range of initial nucleon momenta contribute to a specific final momentum, thus the final nucleon momentum is shifted only a small interval away from the PWIA value.
3. The PWIA spectral function (transition matrix element) is diagonal.

The cross-section can then be written in a form very similar to equation 1.34 but then with a distorted spectral function:

$$\frac{d\sigma^5}{dE_f d\Omega_e d\Omega_p} = C_{kin}\, \mathrm{f}_{rec}^{-1} \sigma_{cc1}^{eN} S^D(\vec{p}_m, \vec{p}_N, E_m) \tag{1.36}$$

The distorted spectral function can be related back to the undistorted spectral function by means of a distortion function $\chi(\vec{p}_N', \vec{p}_N)$:

$$S^D(\vec{p}_m, \vec{p}_N, E_m) = \int d\vec{p}_i \left|\chi(\vec{p}'_N, \vec{p}_N)\right|^2 S(\vec{p}_i, E_m) \tag{1.37}$$

where $\vec{p}_i = \vec{p}'_N - \vec{q}$. The function $\chi(\vec{p}'_N, \vec{p}_N)$ must be fairly sharply peaked to satisfy condition 2.

---

[35] S. Frullani and J. Mougey, "Single Particle Properties of Nuclei Through (e,e'p) Reactions," in *Advances in Nuclear Physics*, Vol 14, edited by J. W. Negele and E. Vogt, Plenum Press, New York (1984)

The details of the final state interactions are usually handled by an optical model with a complex potential. This potential can be derived from extensive analysis of (p,p') data on the nucleus of interest, and is frequently cast in the form of a Woods-Saxon potential with a real and complex part and a spin-orbit term. The complex part of the potential simulates the loss of strength to other channels. The real part of the potential shifts the average measured momentum:

$$\vec{p}\,'_f \approx \left(1 - \frac{E_N}{p_N^2}\left\langle \tilde{V} \right\rangle\right)\vec{p}_f \tag{1.38}$$

where $\left\langle \tilde{V} \right\rangle$ is the average value of the real part of the optical potential over the interaction region.

In the most general case however, the factorization of the cross-section is destroyed by the final state interactions. It is then still possible to write an *effective spectral function*, which is useful for analysis of data:

$$S^{eff}\left(\vec{p}_m, \vec{p}_f, E_m\right) = \left[C_{kin}\, f_{rec}^{-1}\, \sigma^{eN}\right]^{-1} \frac{d^6\sigma}{dE_f dE_m d\Omega_{e'} d\Omega_p}. \tag{1.39}$$

Only this effective spectral function can be determined from the experimental cross-section.

The validity of the factorization of the cross-section was examined by Boffi[36] on ^{12}C(e,e'p) at a momentum transfer around 480 MeV/C. This was done by comparing a full unfactorized calculation of the cross-section with a standard DWIA calculation. He used a Woods-Saxon optical potential, and varied the depth of the real and imaginary part to verify the sensitivity of the results to the distortion. He found that the two calculations did not differ for parallel kinematics, while a discrepancy of up to 10% was found for perpendicular kinematics, depending on the well depth. Since in this experiment the kinematics are mostly perpendicular, this will strongly affect the reliability of factorized DWIA calculations.

---

[36] S. Boffi, C. Giusti and F. D. Pacati, *Nucl. Phys.*, **A319**, 461 (1979)

Chapter 2 The Experimental Setup

This experiment was performed at the Bates Linear Accelerator Center, in Middleton Massachusetts, during the spring of 1991. It made use of the Energy Loss Spectrometer System (ELSSY) in the North Experimental Hall (see figure 2.1) for the detection of the outgoing electrons, and the Out Of Plane Spectrometer (OOPS) for the detection of the outgoing protons. This experiment was part of the first set of experiments with OOPS and it was also the first time that a coincidence experiment was performed in the North Hall with two magnetic spectrometers. The North Hall and the ELSSY spectrometer were originally designed for single arm experiments, and posed geometric and design constraints to our setup. The size of the North Hall limited the possible positions of the OOPS spectrometer, which meant we could not run with an opening angle θ_{pq}, the angle between the direction of q and the outgoing proton, larger than 11°. Because ELSSY is a dispersion matched spectrometer, while OOPS is not designed for dispersion matching, the beam had to be tuned in "squashed dispersed" mode, where the beam dispersion is over a smaller beam spot, which compromised the resolution of ELSSY.

This chapter will describe the experimental setup that was used for this experiment, including the accelerator, the OOPS and ELSSY spectrometers, and the data acquisition electronics, computers and software.

2.1 Overview of the Experiment

The kinematics were on the quasielastic peak, with a momentum transfer q of 404 MeV/c and an energy transfer ω of 112 MeV. The data were acquired at two proton angles, θ_p= 42.9° and 64.7°. For each angle setting, four different momentum settings for the proton spectrometer were used, to ensure that the deep missing energy region of the data were included. This way both the p-shell and the s-shell of carbon were accounted for. The experimental parameters are summarized in table 2.1

Table 2.1 Summary of Experimental Parameters.

	Median Values	**Min Values**	**Max Values**
Beam Energy	576 MeV		
Momentum Transfer (q)	403.6 MeV/c	396.1 MeV/c	411.7 MeV/c
Energy Transfer (ω)	111.9 MeV	101.3 MeV	122.5 MeV/c
θ_q	53.12°		
θ_{pq} for $\theta_p = 42.9°$	10.15°	7.79°	12.50°
θ_{pq} for $\theta_p = 64.7°$	11.65°	9.30°	14.01°
Electron Spectrometer:	**ELSSY**		
Angle, θ_e	44°	43.25°	44.75°
Central Momentum*	470 MeV/c	453.6 MeV/c	474.7 MeV/c
Momentum Acceptance		-3.5%	+1%
Horizontal Acceptance	26.18 mr	-0.75°	0.75°
Vertical Acceptance	126.3 mr	-3.62°	3.63°
Solid Angle	3.31 msr		
OOPS Spectrometer:	**OOPS**		
Angle, θ_p (φ_p= 0)	42.9°	42.2°	43.6°
θ_p (φ_p= π)	64.7°	64.0°	65.4°
Central Momenta: 1	440 MeV/c	369 MeV/c	484 MeV/c
2	405 MeV/c	364.5 MeV/c	445.5 MeV/c
3	373 MeV/c	335.7 MeV/c	410.3 MeV/c
4	343 MeV/c	308,7 MeV/c	377.3 MeV/c
Momentum Acceptance	+/- 10%		
Horizontal Acceptance	24.0 mr	-0.69°	0.69°
Vertical Acceptance	50.0 mr	-1.43°	1.43°
Solid Angle	1.20 msr		
Target Material	^{12}C		
Target Thickness	208.9 mg/cm^2	Target Angle	-10° and 0°

* Due to the misalignment of the scintillators, the central momentum was not the central value of the acceptance for ELSSY (see also section 2.4)

Note that the Min and Max values reflect the acceptances of the spectrometer and not the uncertainty in these values.

2.2 The BATES Linear Accelerator Center

An overview of the Bates Linear Accelerator Center is given in figure 2.1. The accelerator was designed to produce a pulsed beam with a duty factor around 1% and a maximum energy of about 1 GeV[1]. It is currently being upgraded to be able to produce a continuous beam (near 100% duty factor) with internal target capabilities, through the use of a stretcher ring.

The accelerator section starts with a 400 keV injector which produces pulses with a duration of approximately 15 μsec at a repetition rate of 450 to 600 Hz. In this experiment the instantaneous peak current was between 0.1 mA and 0.4 mA, which means that the average current was between 1 μA and 4 μA at a 1% duty factor. The injector is followed by a series of accelerator cavities that boost the energy to a maximum of around 500 MeV. In order to get up to higher energies the beam is "recirculated" by being rerouted to the start of the accelerator and then accelerated for a second time, to the maximum energy around 1 GeV. This experiment used an energy of 576 MeV[2] with a recirculated beam. After the accelerator section, the beam is transported by a number of magnets to either the North Hall (S-line) , the 14° area (also used as a beam dump) or one of the beam lines in the South Hall which includes the new ring.

This experiment was performed in the North Hall, and so it used the F-line and S-line beam transports. The F-line starts right after the accelerator section, after some dipole magnets that can steer the beam to the South Hall. This line contains two 7° bending magnets, FB1 and FB2, with a set of energy defining slits in between them. These slits can be used to determine the momentum spread of the beam which in this experiment was nominally $\Delta P/P = \pm 0.15\%$. At high beam currents the slits can not be set too narrow because they would become too radioactive. In this experiment the beam current was also limited to obtain a better signal to noise ratio, and to prevent overheating of the CD_2 target.

---

[1] Unfortunately this energy was never reached, the maximum energy produced to date is 913 MeV, but is usually lower.

[2] The measured energy during this experiment was 576 MeV see section 3.4.1, the "nominal" beam energy as given by the accelerator operators was about 580 MeV.

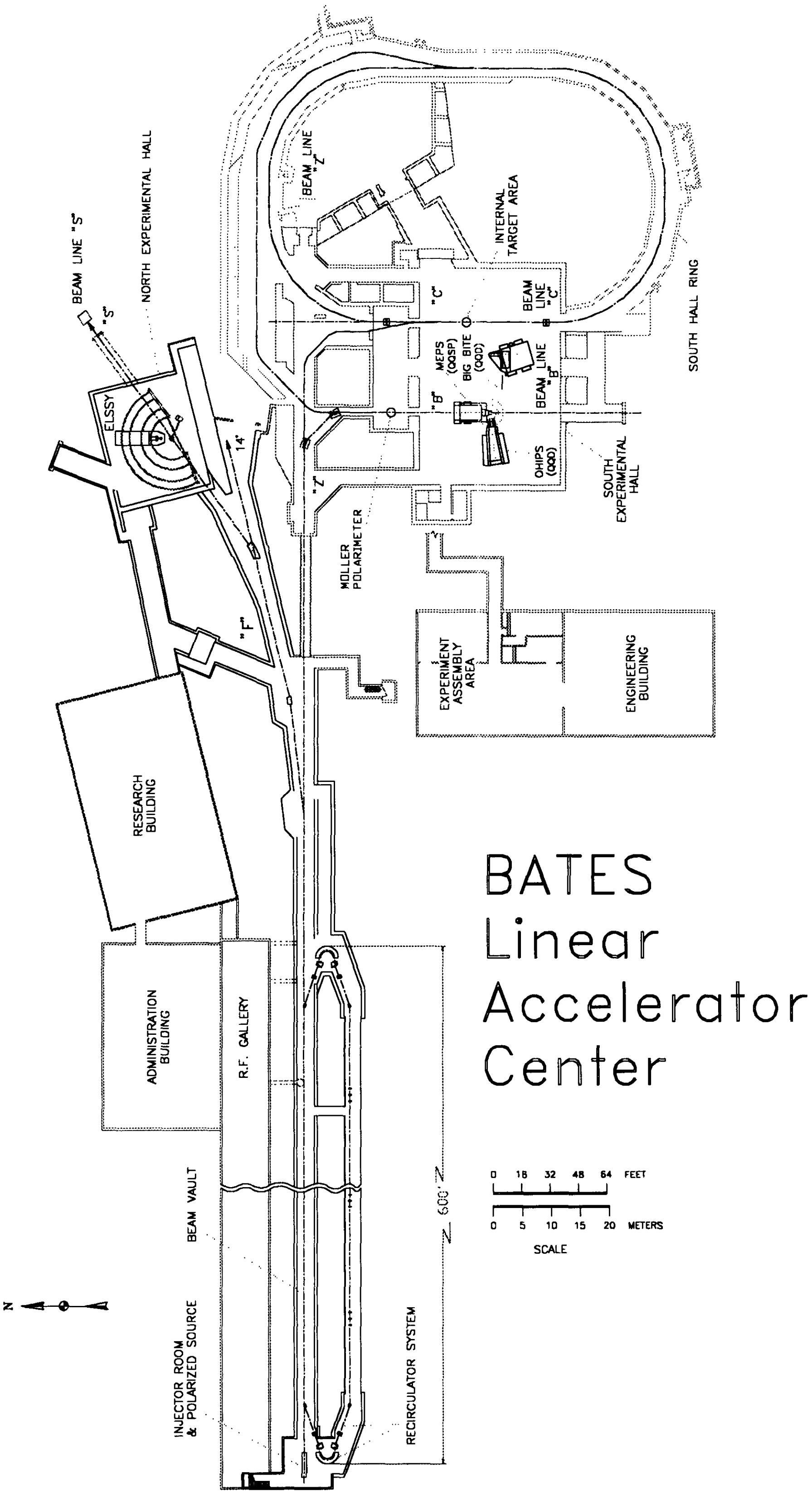

Figure 2.1 The Bates Linear Accelerator, including the newly constructed stretcher ring.

The beam then continues to the S-line which has a 22.5° bending magnet, SB3, which causes it to disperse. The beam is then rotated by a set of quadrupole magnets so that the dispersion is in the vertical plane and can be matched to the dispersion of the ELSSY spectrometer. All care is taken that the beam is centered on the quadrupoles so that they do not steer the beam, but only adjust the dispertion rotation and the beam size. This allowed the dispersed beam to be reduced from its usual vertical size of 2 cm down to a smaller spot of 6 mm, for improved resolution with the OOPS spectrometer. This is a tradeoff between optimizing for ELSSY resolution and OOPS resolution. For optimal resolution in ELSSY a fully dispersed beam is needed, but for OOPS a non-dispersed beam would be best. The horizontal size of the beam spot is usually about 1 mm.

The position, angle and size of the beam can be monitored by several BeO flip targets that are removed during data taking. A set of strip-line monitors were used during data taking to determine the beam location and angle. Additionally the beam halo[3] was monitored by an old photo-tube that was taped to the beam line. This proved to be a very useful check of the beam quality, something to which we were sensitive because of the minimal shielding of the OOPS spectrometer.

The instantaneous current and integrated total charge are monitored by two toroidal transformers, ST4 and ST5, which feed a set of BIC integrators. The integrators are read out by a scaler module and the results are entered into the data stream. These toroids are positioned about 5 meters upstream of the scattering chamber and are spaced about 1 meter apart. They were calibrated at the National Bureau of Standards in February 1991, just before this experiment, by comparing their reading to that of a Faraday cup. They were found to be accurate to 0.2% for ST4 and 0.1% for ST5. During our experiment a discrepancy between the reading of ST4 and ST5 of up to 3-4% was found, which was attributed to beam halo. The reading of ST4, which is further upstream and thus less sensitive to halo, was used for the charge computation. The discrepancy was taken into account in the error analysis by increasing the uncertainty in the beam current to 0.3%.

---

[3] Beam halo is a wide spray of unfocused electrons that surround the well defined and properly focused beam.

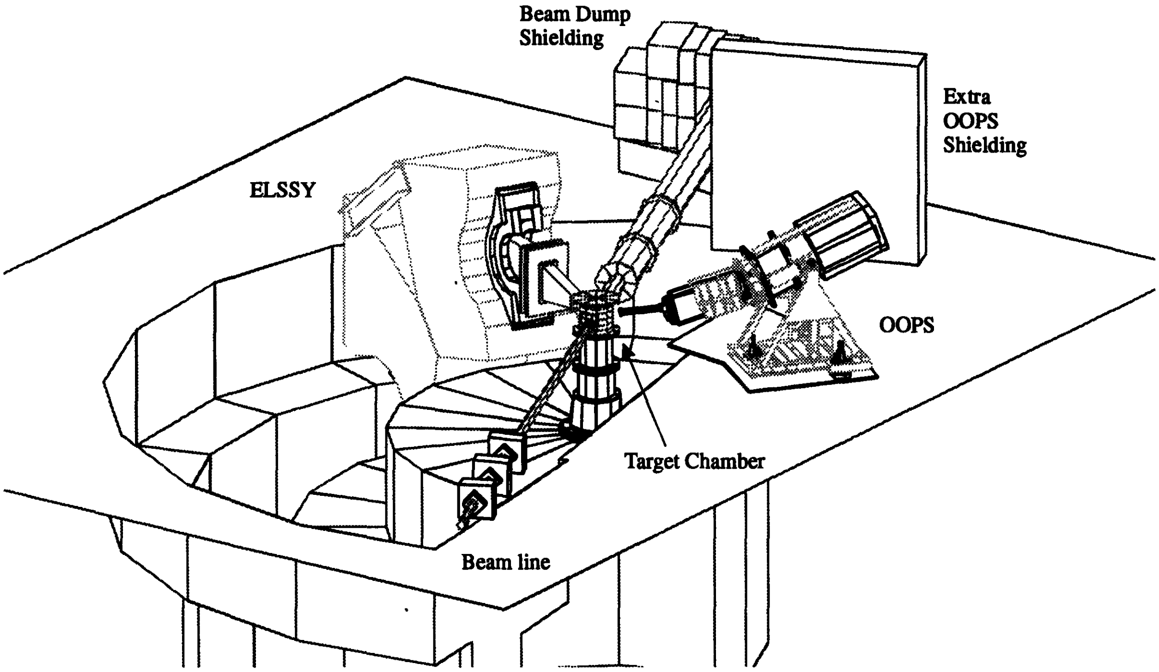

Figure 2.2 Layout of experimental apparatus in the North Hall

2.3 Experimental Layout

The layout of the experimental apparatus in the North Hall is shown in figure 2.2. The beam pipe and three quadrupoles are in the foreground, where the beam enters the experimental hall. The beam then enters the target chamber where it interacts with the target and part of it will scatter. The rest continues out to the beam dump, which is well shielded to avoid back scattered radiation from causing background noise in the detectors. However this did not provide enough shielding for OOPS, and additional shielding had to be added, in the form of large concrete blocks, between the beam dump pipe and the OOPS detector.

The target chamber contained the targets that were used for this experiment. The main target was a simple, thin square piece of ^{12}C with an areal thickness of 208.9 mg/cm^2. The target is inserted into a ladder which holds several targets and can be moved up and down and also rotated. The ladder also contained a ^{12}C target of 69.07 mg/cm^2, a LiF target, a BeO target and two spinner targets one with CH_2 and one with CD_2. These targets were used during the calibrations and for the measurements on Deuterium that were performed contiguously with this experiment.

The ELSSY spectrometer is positioned on the left hand side of the beam, when viewing down the beam line, and bends 90° down into a large pit in the floor. This spectrometer was directly coupled to the target chamber with the aid of a sliding seal, which allows the spectrometer to be positioned at all the needed angles. This direct coupling has the advantage that the scattered electrons do not undergo multiple scattering in the scattering chamber window and spectrometer entrance window, on their way to the spectrometer, which degrades the resolution. ELSSY can be moved with the use of a set of electric motors, and its position can then be read off from an accurate scale on the floor. This procedure was relatively easy.

The OOPS was positioned on the right hand side of the beam on a steel plate which was put on the floor and provided a smooth, flat surface for moving OOPS. The OOPS is moved with the aid of the crane and a set of pulleys. This positioning procedure was rather difficult. The final position was then measured with theodolites with respect to fixed markers in the experimental hall. The OOPS was not coupled directly to the scattering chamber but viewed the target through a set of very thin Kapton windows.

The information from the detector packages in the spectrometers was fed to electronic modules in the experimental hall (nicknamed "downstairs") and then transported over long coaxial cables to the counting bay ("upstairs"). In the counting bay this information was processed further by more electronic modules, and finally sent to a computer which wrote it to tape. The experimenters monitored the progress of the experiment from the counting bay.

2.4 The ELSSY Spectrometer

The Energy Loss Spectrometer System, ELSSY, (see figure 2.3) was used for the detection of the scattered electrons. ELSSY is a large, high resolution spectrometer system that was previously used for single arm scattering experiments. It is designed to be capable of *dispersion matching*[4]. In this mode of operation, the dispersion of the beam is matched to the dispersion of the spectrometer, which greatly improves the resolution of the energy loss of the electron due to the scattering process in single arm experiments. This spectrometer has achieved a maximum resolution of $\Delta P/P = 4 \cdot 10^{-5}$.

---

[4] W. Bertozzi *et. al.*, Nuclear Instruments and Methods **162**, 211 (1979) and **141**, 457 (1977).

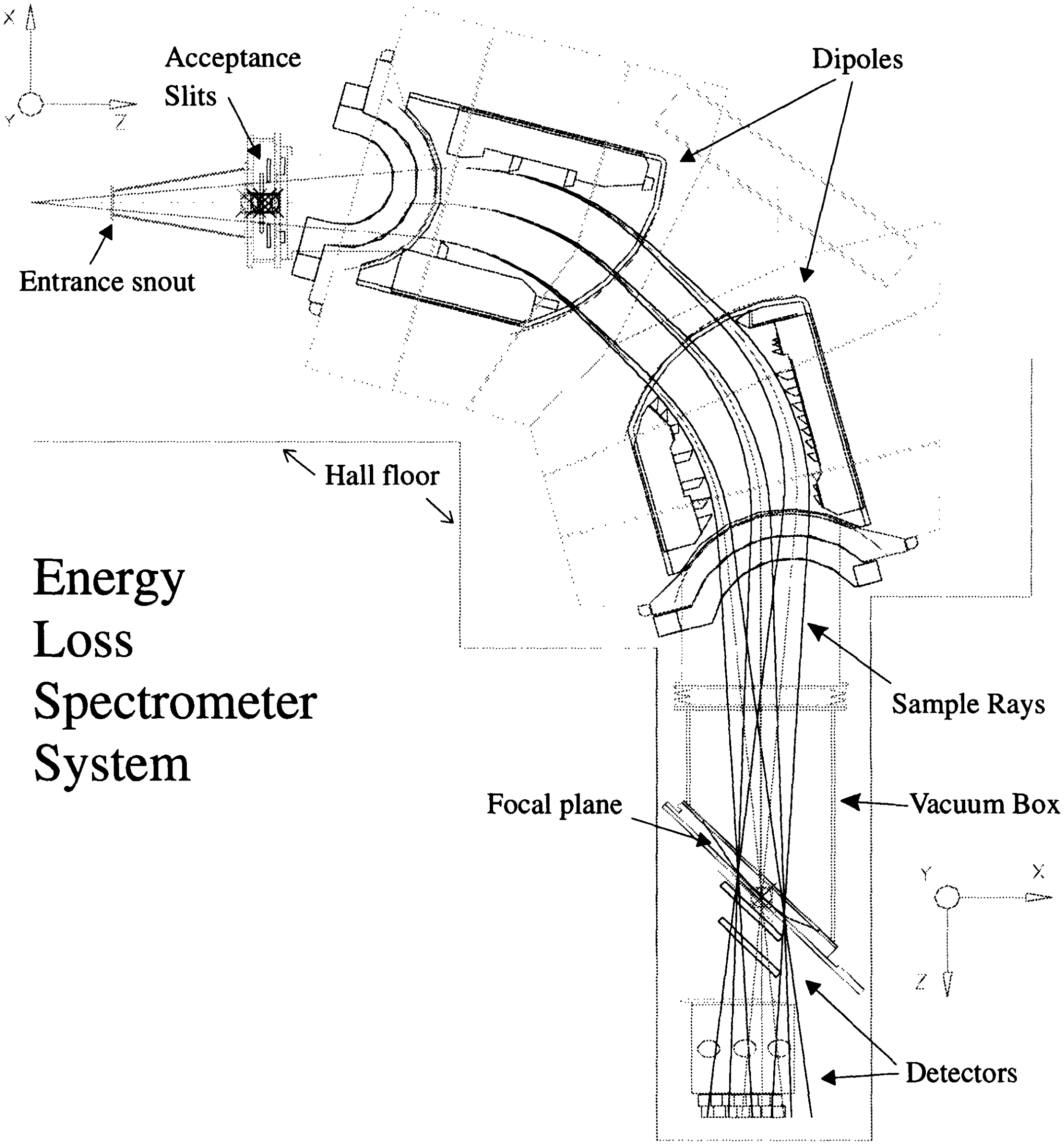

Figure 2.3 The Energy Loss Spectrometer System with three sets of particle rays indicated.

At the entrance of the spectrometer is a pair of solid angle defining slits that can be moved in and out by a set of electric stepping motors to vary the acceptance. The horizontal and vertical slits are positioned at 76.375" and 78.75" from the target respectively. This means that at the nominal setting of 2 inches horizontal and 10 inches vertical, the acceptance of the spectrometer is 26.18 mr for the scattering angle and 126.3 mr for the out-of-plane angle. This translates into a solid angle of 3.31 msr. The momentum acceptance is normally about 6 % but in this experiment it was only 4.5 % because the detector package was miss-aligned with the center of the spectrometer. As a result of this misalignment 1/4 of the nominal acceptance on the high momentum side (larger x) had a poor detection efficiency and was not used. This is reflected in the figures and in table 2.1.

2.4.1 Definition of the Coordinate System.

The coordinate system used in this thesis follows the convention of the program Transport[5]. The coordinate system is right handed, with Z pointing in the direction of the particles motion and X pointing outwards in the bend plane of the dipole. This means that the coordinate system rotates along with the particle's trajectory. The Y coordinate is now defined by using a right handed coordinate system. See figure 2.3 and figure 2.4 for graphical presentations. Since ELSSY bends down, X at the target points up, and since it is on the left hand side of the beam line, ϕ is positive for smaller scattering angles and Y points towards the beam dump. For OOPS, which bends up and is positioned on the right hand side of the beam line, X at the target points down, and ϕ is again positive for smaller scattering angles with Y pointing towards the beam dump. A fifth coordinate, $\delta = P/P_{central} \cdot 100\%$, determines the momentum of the particle relative to the momentum of the central ray of the spectrometer.

In order to determine the out of plane scattering angle accurately, a special calibration of all matrix elements was performed[6], some of which had never been measured before, with a sieve slit. The transfer matrix can be written as a polynomial expansion. The target variables can be expressed in terms of the focal plane variables or, for the inverse matrix, the focal plane variables can be expressed in terms of the target variables. Note that they are occasionally mixed up, as in the case for δ.

The basic notation used is:

$$\begin{aligned}\theta_{target} = &\left\langle \theta_{target} \middle| \theta_{focal} \right\rangle \theta_{focal} + \left\langle \theta_{target} \middle| \theta_{focal}\, x_{focal} \right\rangle \theta_{focal}\, x_{focal} + \\ &\left\langle \theta_{target} \middle| \theta_{focal}\, x^2_{focal} \right\rangle \theta_{focal}\, x^2_{focal} + \dots\end{aligned} \tag{2.1}$$

where each matrix element is denoted by a < I >. The subscripts "target" and "focal" are frequently abbreviated to "t" and "f", and where they are not ambiguous, are omitted.

---

[5] K. L. Brown *et. al.*, **Transport**, SLAC (unpublished)

[6] M. Holtrop *et. al.*, Internal Report B/IR 92-04, Bates Linear Accelerator Center (unpublished).

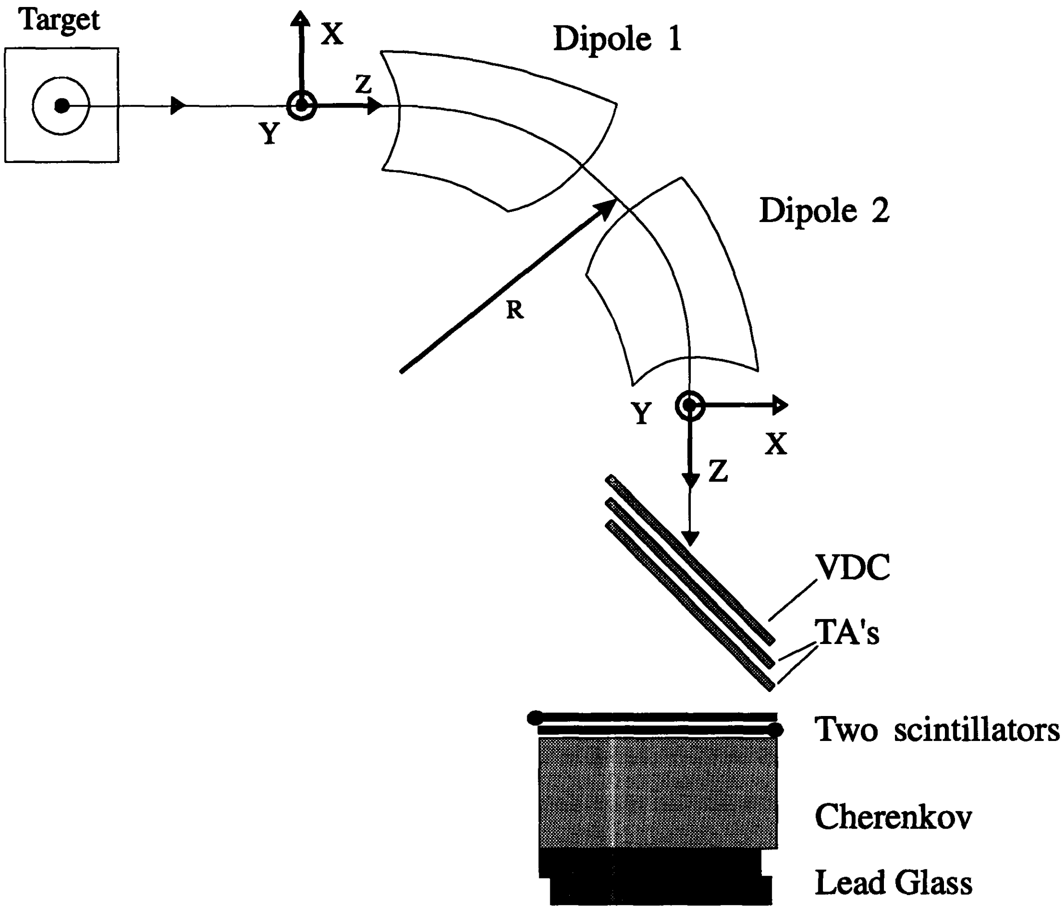

Figure 2.4 Schematical layout of ELSSY, with the coordinate convention indicated for the central ray.

2.4.2 The ELSSY Focal Plane and Optics

ELSSY is constructed from two dipole magnets causing a 90° bend with a 2.23 meter bending radius for the central ray. The dipoles have specially shaped pole faces to provide focusing, which eliminated the need for focusing quadrupoles. In normal operation each dipole is powered by a separate power supply, but during this experiment one of the power supplies was needed for OOPS, so the dipoles were powered in series by a single power supply. The magnetic field in the magnets is measured using an NMR probe, and it was found that the difference of field strength between the two dipoles was slight, about 5 parts in 10^4. The single power supply did however limit our ability to cycle the magnets.

ELSSY has point to point focusing in the radial plane (x-plane), which allows for dispersion matching, and parallel to point focusing in the transverse plane (y-plane), which gives a good determination of the scattering angle. This means that the first order matrix elements $\langle\theta_t|x_f\rangle$ and $\langle y_t|y_f\rangle$ vanish. Theoretically it should be possible to calculate four of the five properties (x,θ,y,ϕ,δ) of the particle at the target from the four quantities (x,θ,y,ϕ) measured at the focal plane. In practice the values measured for ϕ_f are almost identical to zero for this spectrometer (that is, the width of ϕ_f is equal to that expected from multiple scattering in the spectrometer windows). Thus, one can really only calculate three properties at the target. The design is such that these are (θ,ϕ,δ).

If a general matrix element is written as $\langle t \mid x_f^i\, \theta_f^j\, y_f^k\, \phi_f^l \rangle$, where t is one of $(\theta_t,\phi_t,\delta_t)$, then midplane symmetry of the spectrometer poses a theoretical constraint on the matrix elements allowing only even values of $k+l$ for dispersive coefficients (δ_t,θ_t) and odd values for the non-dispersive coefficients (ϕ_t). In practice this is only true for a perfectly symmetric spectrometer with perfectly centered detectors that are perfectly straight. Since this is not necessarily the case[7] none of the matrix elements that violate midplane symmetry were left out of the analysis. The results of this measurement are reproduced in Appendix A.

It was found that the angular resolution of ELSSY was 0.5 mr and 8 mr for the scattering angle and the out-of-plane angle respectively. The resolution of the out-of-plane angle can be greatly improved with the installation of a second VDC. A summary of the ELSSY optical properties is given in table 2.2.

---

[7] We found that the VDC sagged somewhat under gravity.

Table 2.2 Summary of ELSSY optical properties.

Radius of Central Ray	2.23 meters
Deflection Angle	90°
Distance from Target to Focal Plane	11.1 meters
Weight	225 tons
Maximum Momentum	0.90 GeV/c^2
Dispersive Plane Focusing	point → point
Transverse Plane Focusing	$\parallel \rightarrow$ point
Momentum Dispersion $<x\|\delta>$	6.6 cm/%
Momentum Acceptance actual* (nominal)	4.5 % (6 %)
Momentum Resolution, $\Delta P/P$ actual* (best)	0.2 % (0.01 %)
Distance of Horizontal Slit to Target	76.375"
Horizontal Angular Acceptance (slit at 2")	26.18 mr
Horizontal Angular Resolution	0.5 mr
Distance of Vertical Slit to Target (slit at 12")	78.75"
Vertical Angular Acceptance	126.3 mr
Vertical Angular Resolution	8 mr
Solid Angle	3.31 msr

* Actual values for this experiment.

2.4.3 The ELSSY Focal Plane Instrumentation

A diagram of the ELSSY detector package is given in figure 2.5. During this experiment it consisted of one vertical drift chamber (VDC), two sets of transverse arrays (TAs, called HDC1 and HDC2 in figure 2.5), two scintillators, a gas filled Cherenkov counter and one row of lead-glass-block shower counters. It is possible to equip ELSSY with two VDC's, which improves the angular resolution for the out of plane angle, but the second VDC was not available for this experiment.

The VDC provides information on the position and angle of the detected particle in the dispersive plane, while the TAs determine the position and angle in the transverse plane. The details of these detectors are discussed in the next two sections. The scintillators, Cherenkov counter and lead-glass blocks determine the event trigger and timing, and also provide particle identification.

ELSSY has two 1/2 inch thick NE-110 plastic scintillators, which are placed on top of the Cherenkov counter. They each have an active area of about 23 by 74 cm, and are coupled to a photo-multiplier tube (PMT) by means of a cylindrical light pipe. The PMT gives a strongly amplified pulse when its photocathode is hit by the light from the

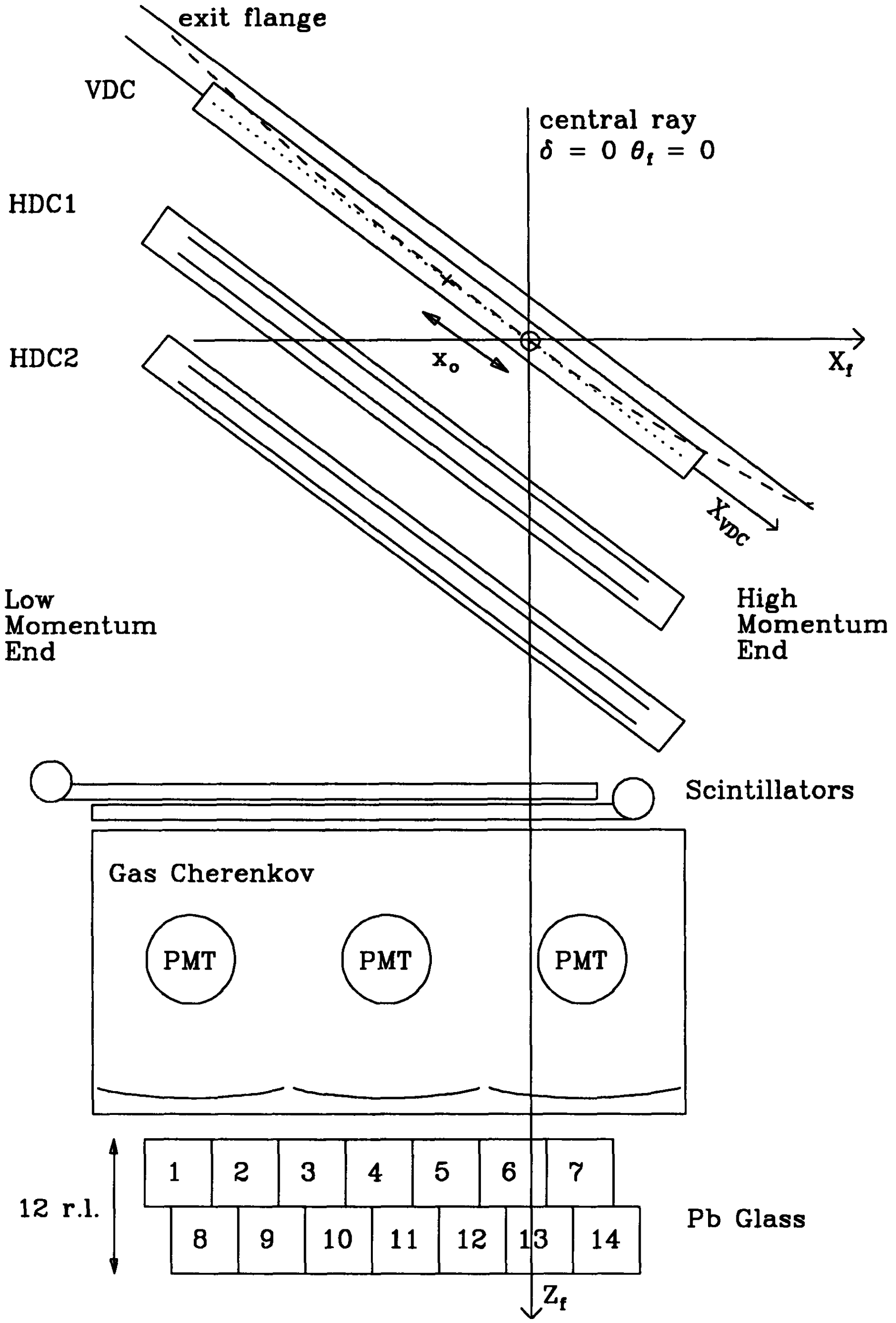

Figure 2.5 ELSSY focal plane instrumentation. During this experiment only one row of lead-glass blocks was available.

scintillator. The height of this pulse gives information about the energy of the particle, while the time of the pulse is used to provide a reference to the VDC and TAs and to the coincidence circuit. The PMTs are placed facing opposite sides of the central ray so that by taking the mean time of the incoming pulses a trigger start-time could be calculated that was independent of the position of the particle track in the scintillators.

The Cherenkov counter allowed one to distinguish various particles from each other. The gas Cherenkov counter consists of a large box filled with isobutane gas at atmospheric pressure and has three mirrors and PMTs to collect and amplify the Cherenkov light. Cherenkov light occurs when a charged particle passes through a medium with a velocity that exceeds the propagation velocity of light in that medium (c/n where n is the index of refraction.) Particles with the same momentum but different masses have a different velocity, thus they can be distinguished if one produces light and the other does not. The index of refraction of isobutane is about $n = 1.00127$, so the momentum threshold for producing light for electrons ($m_e = 0.511$ MeV/c^2) is 10 MeV/c. For pions ($m_p = 139.5$ MeV/c^2) this threshold is 2.7 GeV/c and for muons ($m_\mu = 105.6$ MeV/c^2) it is 2.1 GeV/c. Thus the electrons can be clearly separated from other particles in the trigger.

The lead-glass array was not important for this experiment. It is used for experiments with very low count rates to veto the cosmic-ray background. More information on the lead-glass can be found in reference 8.

2.4.4 The ELSSY VDC

The Vertical Drift Chamber[9] (VDC) measures the X_f position and the θ_f angle of the particle track. The VDC is positioned just below the vacuum window in ELSSY, in the center of the focal plane and is tilted at a 45° angle (see figure 2.3.) This means that if the higher order effects are ignored, X_f corresponds to the momentum of the particle, and θ_f corresponds to the out-of-plane angle at the target. The VDC has a resolution of approximately 120 μm (at 2σ) in the X direction and 17 mr for θ_f.

---

[8] Bill Schmitt, *Ph. D. thesis*, MIT, unpublished (1993).

[9] W. Bertozzi *et. al.* Nuclear Instruments and Methods, **141**, 457 (1977)

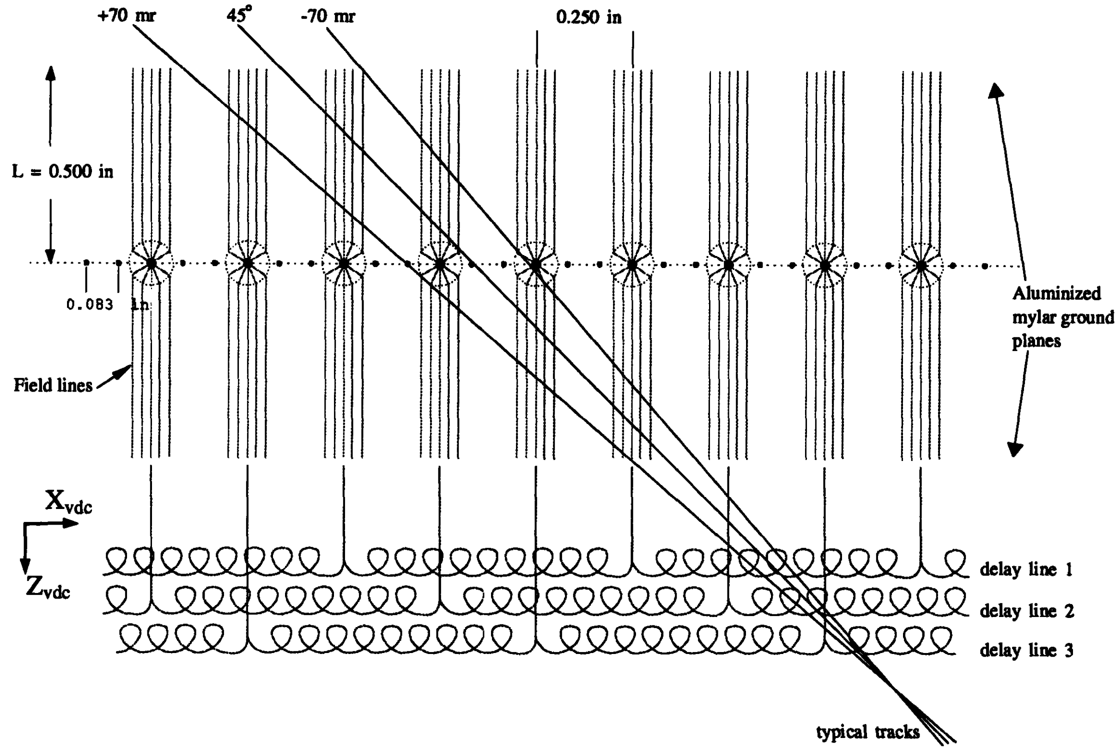

Figure 2.6 Schematic cross section of the VDC, with field lines shown for the signal wires. The particle tracks drawn are 45° ± 70 mr, which corresponds to the central ray and the full acceptance of ELSSY. A schematic indication of the delay lines is also indicated. The dotted lines coming from the wires represent the field lines.

The ELSSY Vertical Drift Chamber (VDC) consists of 99 gold-plated signal wires, 20 μm in diameter, separated by 6.35 mm (0.25 inch), that run in the Y_f direction. Between each of the signal wires are two ground wires, 50 μm in diameter, 2.11 mm (0.083 inch) apart. The wires are in a plane between two aluminized mylar planes and at a distance of 1.27 cm (0.5 inch) from each (see figure 2.6). The mylar planes are maintained at a potential of -9.1 kV with respect to the wires, which are at ground potential. The volume between them is filled with a 50/50 mixture (by volume) of argon and isobutane gases.

The VDC derives its name from the vertical drift. The drift cells in the VDC are narrow vertical regions that are formed by the field lines between the signal wires and the mylar planes. Each drift cell is separated by two ground wires to shape the field lines. When a charged particle crosses the VDC at an angle around 45° it will ionize the gas and cause an electron-ion track that will cross 3 to 5 adjacent drift cells. Because of the high potential difference the free electrons will drift towards the signal wire at a terminal velocity of 50 μm/ns. When the electrons get very close to the signal wire, an avalanche occurs in which more atoms of the gas are ionized, which greatly multiplies the number of free electrons. This creates a small pulse on the wire which is passed on to an amplifier/discriminator card, one for each signal wire. This card amplifies and then discriminates the pulse and passes it on to the delay line, where it travels to both ends of the VDC to two time-to-digital converters (TDCs) at the end of the delay line. The time of arrival of these pulses is recorded and analyzed. The difference in the timing of the signals can be decoded to give the wire number of the wire that was hit. The sum of the two timing signals, when compared to the timing of the trigger, measures the amount of time it took for the electrons to drift to the wire, which can be converted to the distance of the wire. This will be discussed in more detail in chapter 3.

Each delay line consists of 32, 1-foot long coaxial cables, which cause a 1.7 ns delay of the signal. There are only three delay lines, so every third signal wire is bussed together on a delay line, 33 signal wires to a delay line. This means that when 4 or more signal wires are hit, one of the signals is lost since two signals travel on the same delay line, and the TDC can record only one of them[10]. A wiring diagram for the VDC and the TAs is given in figure 2.7.

2.4.5 The ELSSY Transverse Arrays

There are two sets of transverse arrays (TAs) in ELSSY, each TA consists of two horizontal drift chambers. The TAs are located below the VDC approximately 12 cm and 36 cm below the focal plane and are also tilted at 45° degrees. The TAs measure Y_f and ϕ_f, where Y_f maps to the scattering angle of the particle. As stated earlier ϕ_f is consistent with zero for all real events, but measuring ϕ_f is still useful rejecting background events.

---

[10] Often VDC chambers have 4 or more delay lines, and sometimes even a TDC per delay line. This increases the accuracy of the VDC and the maximum count rate.

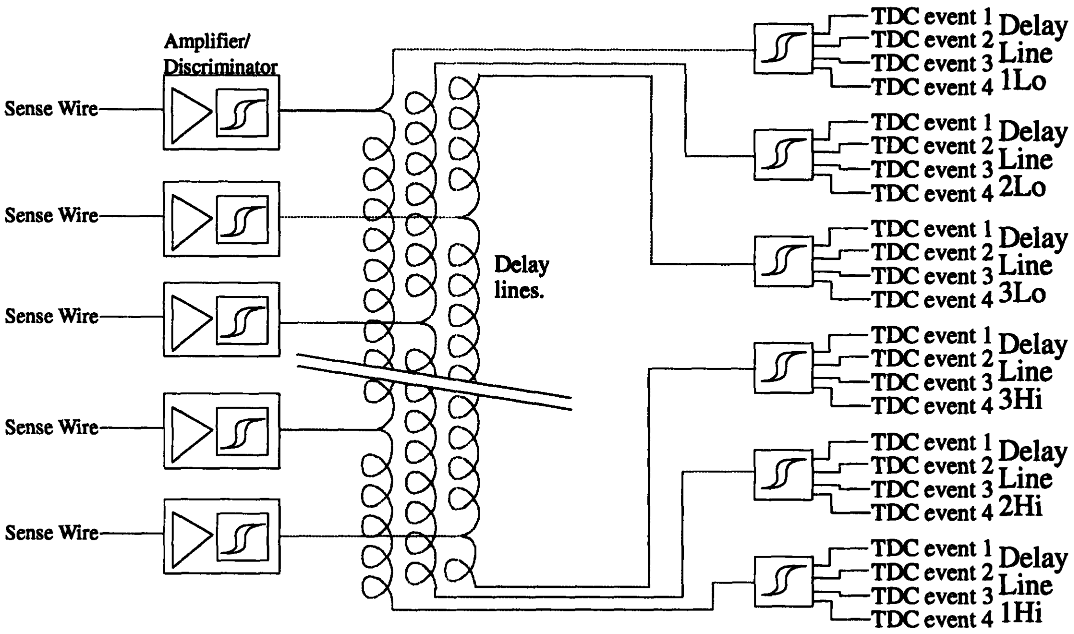

Figure 2.7 Logic diagram for the VDC electronics. The signal from each sense wire is amplified and discriminated and then sent to the delay line. Each end of the delay line is connected to a long cable that carries the signal to the counting bay. There a set of discriminators recondition the signals and distribute them to four TDCs per delay line, one for each event in a beam burst. The labels "Hi" and "Lo" refer to the high and low momentum sides of the VDC respectively.

Each TA contains eight gold-plated signal wires, 20 μm in diameter, that run in the X direction, and are separated by guard wires (see figure 2.8.) The wire separation between signal wires is 30.5 mm (1.2 inch.) On each side, at a distance of 3.175 mm (1/8 inch) of a row of signal wires, runs a row of field shaping wires (berylium-copper wires), with a diameter of 50 μm and a wire separation of 2.54 mm (0.1 inch.) The vertical distance between the two rows of signal wires is 19.05 mm (3/4 inch.) The chambers are separated by a 50.8 μm (2 mil) thick aluminized mylar plane, and they are isolated from the outside by a double wall of 50.8 μm (2 mil) thick aluminized mylar. The two planes are offset by half a wire spacing in the Y direction, and the two TA-sets are offset by 1/4 wire spacing with respect to each other.

The signal wires are held at a potential of +1.56 kV and the guard wires are held at -2.1 kV. The field shaping wires range in potential from -2.1 kV, for the wire nearest to a guard wire, to 0 V for the wire nearest to a signal wire, in equal steps. This assures a uniform field strength throughout the drift cell. The TAs use the same gas mixture as the VDC, a mixture of 50/50 argon and isobutane. Each signal wire is connected to a single

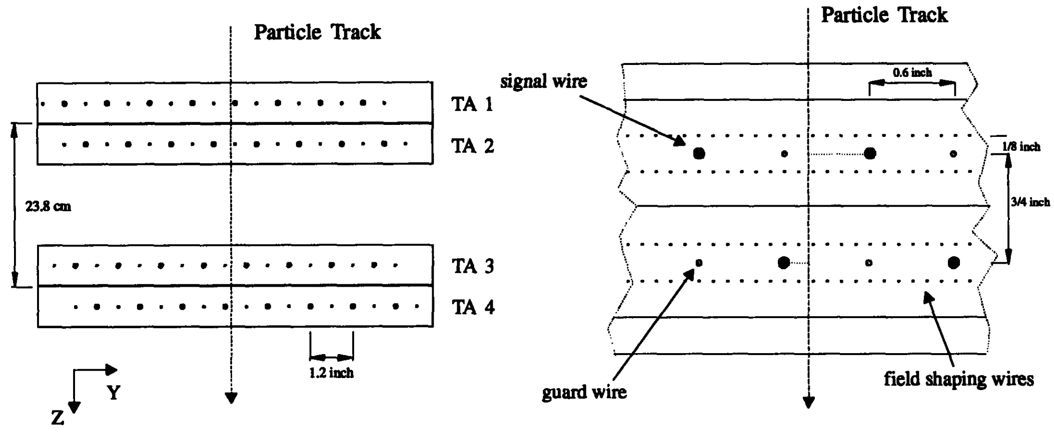

Figure 2.8 Schematic cross section of the TAs. The thicker wires represent the sense wires while the thinner wires represent the guard wires. The left hand picture shows the relative alignment of the wires.

delay line per plane, and each delay line, after amplification and discrimination, is connected to two TDCs.

When a particle traverses a TA chamber it leaves an ion track similar to that in the VDC. However, in these chambers the field lines run horizontally, and thus only one wire will receive a signal. This would not be enough information to decode the position, since there is an ambiguity about which side of the wire the track passed. This ambiguity is solved by having a chamber pair, where the second chamber is offset by half a wire spacing. The second pair of chambers is needed to accurately decode the angle. The distance of the track to the wire is decoded from the timing of the signals on the delay line, in a similar way to the case of the VDC.

During this run cycle, the TAs had a problem with being very noisy. This caused them to be fairly unreliable, and not very efficient. Fortunately it is possible to still decode all the needed information from only three planes. For the method of decoding the chamber information see the next chapter.

2.4.6 The ELSSY Trigger and Electronics

Before an event of a particle hitting the detectors is recorded by the data acquisition hardware it needs to be determined whether this event is to be recorded. This is done by the trigger electronics, which is part of the setup for each spectrometer. In the case of ELSSY all the electronic modules that make up the trigger were located in the experimental bay area, where they are easily accessible during the experiment. This has the disadvantage that all the signals have to be transported over long cables, which degrades the signal shapes. All the information that is needed to form a trigger is sent "upstairs" over fast coaxial cable, while all the other signals (VDC and TA information and analog signals) are sent up over normal coaxial cable. This allows the trigger electronics to make a decision before the information that needs to be recorded arrives at the ADC and TDC modules. Note that all the detector pulses are also sent to scaler modules.

The electronics for the ELSSY detectors allow for the recording of up to four events per beam burst. This mode, dubbed "multiple event per beam burst mode", is not useful for coincidence experiments with OOPS, since the OOPS electronics do not have this capability. This mode was used during the single-arm beam-energy calibration runs and sieve-slit runs. Since recording the data to tape takes a fairly long time the pulses that needed to be recorded were fanned out to four different ADC or TDC modules. A special coincidence fanout circuit (not indicated in the diagram) provides the gate for these modules so that only one of them records the pulses for each event in the beam burst. At the end of the beam burst all the modules are read out and recorded to tape.

The logic diagram of the electronics is given in figure 2.9. The signal from the scintillators was discriminated using a constant-fraction discriminator (CFD) to provide accurate timing information. The timing of these signals was recorded with TDCs to allow for software corrections. The analog signals were sent to ADCs to allow for particle identification in software. From the signals of the three PMTs in the Cherenkov counter an analog sum was formed. This improves the response of the Cherenkov counter, since the light of a particle could be distributed over more than one PMT. The individual PMTs and the analog sum were also read out with ADCs to allow for the verification of the signals. Similarly, the signals from the lead-glass blocks were summed and then discriminated. The trigger was formed from the mean timed *AND* of the two scintillator pulses which is then combined (*AND*) with the *OR* of the Cherenkov and the lead-glass blocks. For a low count rate experiment the *AND* of the Cherenkov and the lead-glass blocks would be used, but during this experiment not all the blocks were present so an *OR* of the signals was used. This was mainly a way to check the Cherenkov efficiency. Care was taken that the timing of the trigger was determined by the pulse from the

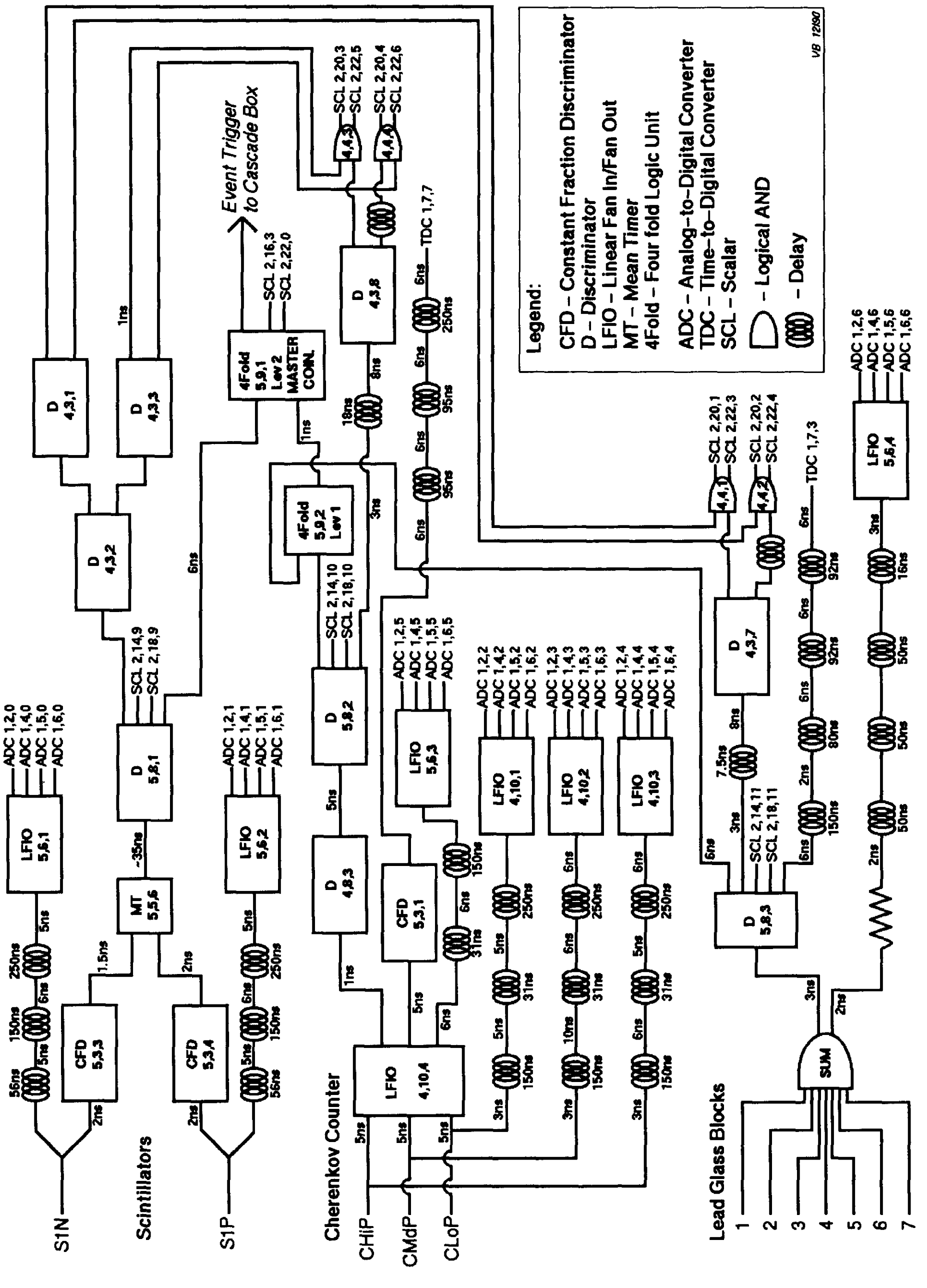

Figure 2.9 Logic diagram of the ELSSY trigger electronics.

scintillators. This is important because this signal provides the start signal for all the ELSSY TDCs, and the timing for the coincidence time-of -flight.

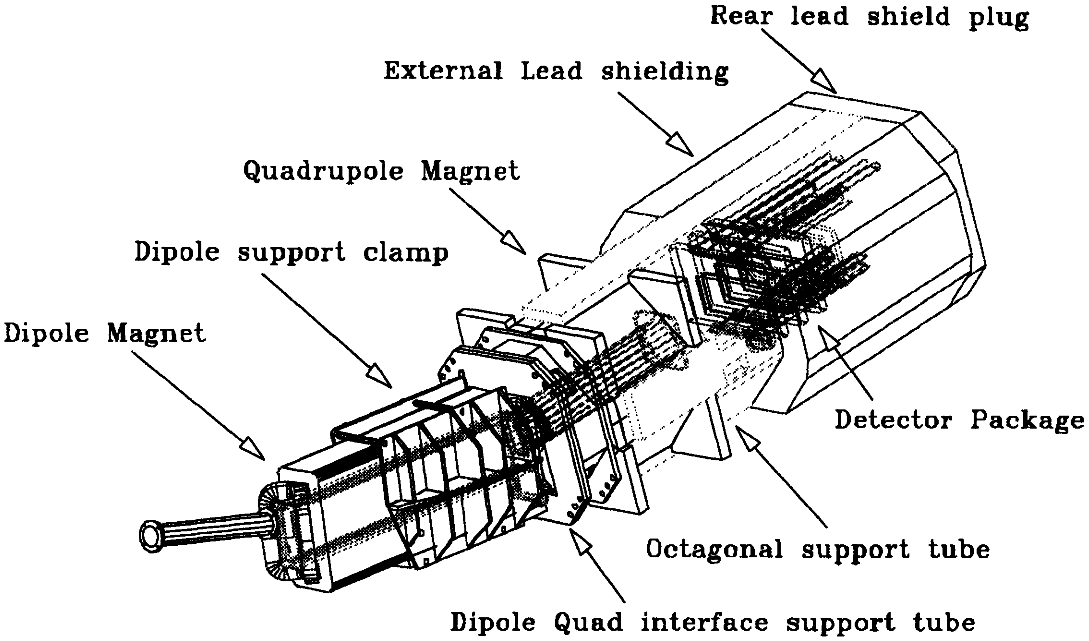

Figure 2.10 Exterior view of the OOPS, showing the position of the magnets, shielding, vacuum boxes and the detectors.

2.5 The OOPS Spectrometer

The "Out of Plane Spectrometer" (OOPS) was used for detecting protons. The OOPS is a compact 16 ton spectrometer that was designed to have the capability of being moved out of the scattering plane. This experiment is one of the first experiments performed with the OOPS after a six month period of testing and calibrations. The OOPS module that was used for this experiment is a prototype[11,12] for a cluster of four OOPS spectrometers that are currently under construction and are to be installed in the South Hall.

The OOPS magnetic elements consist of a dipole magnet followed by a quadrupole magnet. These magnetic elements were not specially designed for this spectrometer. The dipole came from Fermi National Laboratory and the quadrupole came from Brookhaven National Laboratory. They do not form as nice a focal plane as the ELSSY spectrometer does. This means that the focal plane does not coincide with the detectors, since it is tilted at approximately 12°. Instead, the information from the detectors has to be projected to the focal plane by a calculation in order to extract the

---

[11] J. B. Mandeville *et. al.*, Nuc. Inst. & Methods **A344** (1994) 571
[12] S. M. Dolfini *et. al.*, Nuc. Inst. & Methods **A344** (1994) 583

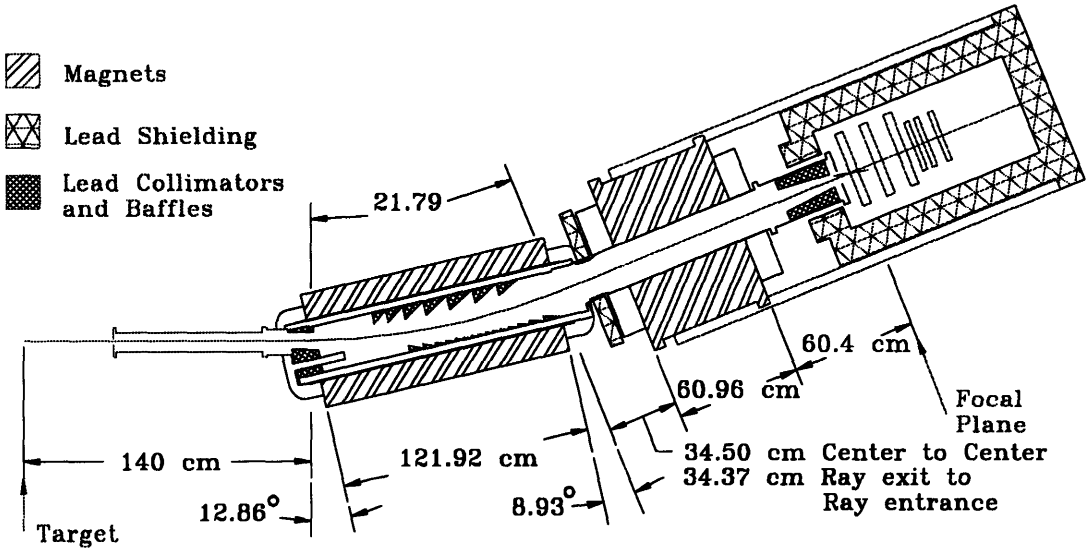

Figure 2.11 Cross-sectional diagram of the OOPS, with rays traced from the target. The label "focal plane" indicates the start of the focal plane.

momentum and angle information for the particle track. The maximum central momentum for OOPS is 832 MeV/c, and the maximum momentum bite is ± 20 %. However the efficiency of the focal plane drops significantly beyond ± 10 %, so only this region was used.

Due to the relatively small bend, 21.7°, the OOPS has a small dispersion of 0.22 cm/% and a modest momentum resolution of 10^{-2}. The solid angle is 1.2 msr (±12 mr horizontal by ±25 mr vertical.) The angular resolution is high, around 1.2 mr, for both angles as was measured by a sieve slit run. Figure 2.10 shows a drawing of the outside of the spectrometer, with some of the internal elements, such as the vacuum system and the detectors.

The shielding for the detectors is made of a 2.0 inch thick octagonal steel tube with 6.0 inches thick lead slabs attached on the outside. The back wall is made of a 6.0 inch thick lead end-cap with a 4.5 inch octagonal lead plug that slides into the detector house. The end cap can be removed with a crane. It has two slots for the detector cables. This shielding was found to be minimal, and an extra concrete shielding block was required to be placed between the OOPS and the beam dump. It is expected that, in the friendlier environment of a continuous beam, this will no longer pose a problem. Figure 2.11 shows a cross section of the OOPS with the central particle ray indicated.

Table 2.3 Summary of OOPS optical properties.

Radius of Central Ray	3.47 meters
Deflection Angle	21.7°
Distance from Target to Focal Plane	4.6 meters
Weight	16 tons
Maximum Momentum	0.83 GeV/c^2
Dispersive Plane Focusing	point → point
Transverse Plane Focusing	no focus
Momentum Dispersion $<x\|\delta>$	0.22 cm/%
Momentum Acceptance used (max)	20 % (40 %)
Momentum Resolution, $\Delta P/P$ (best)	1 % (0.5%)
Horizontal Angular Acceptance	24 mr
Horizontal Angular Resolution	1.2 mr
Vertical Angular Acceptance	50 mr
Vertical Angular Resolution	1.3 mr
Solid Angle	1.20 msr

More detail on the construction and measured properties of the OOPS can be found in references 11,12,13 and14. Table 2.3 summarizes the properties of the OOPS spectrometer.

2.5.1 The OOPS Focal Plane Instrumentation

The OOPS detector package consists of three scintillators and three horizontal drift-chambers (HDCs) that were build following a design from LAMPF[15]. Each of the three horizontal drift chambers (HDCs) in the detector package consists of two planes, x and y, that measure the position in the x and y direction respectively. The detector package of the OOPS consisted of three such chambers even though only two HDCs are needed to also get the angle information. The third chamber greatly increases the over all detection efficiency of the detector package, and allowed for the continuous monitoring of the efficiency and resolution of the wire chambers. The HDCs are spaced 12.7 cm apart.

---

[13] S. M. Dolfini *et. al.*, Internal report, University of Illinois at Urbana-Champaign (unpublished)

[14] J. B. Mandeville *et. al.*, Internal report, University of Illinois at Urbana-Champaign (unpublished)

[15] L. G. Atencio, J. F. Amann, R. L. Boudrie and C. L. Morris, Nuclear Instruments an Methods **187**, 381 (1981)

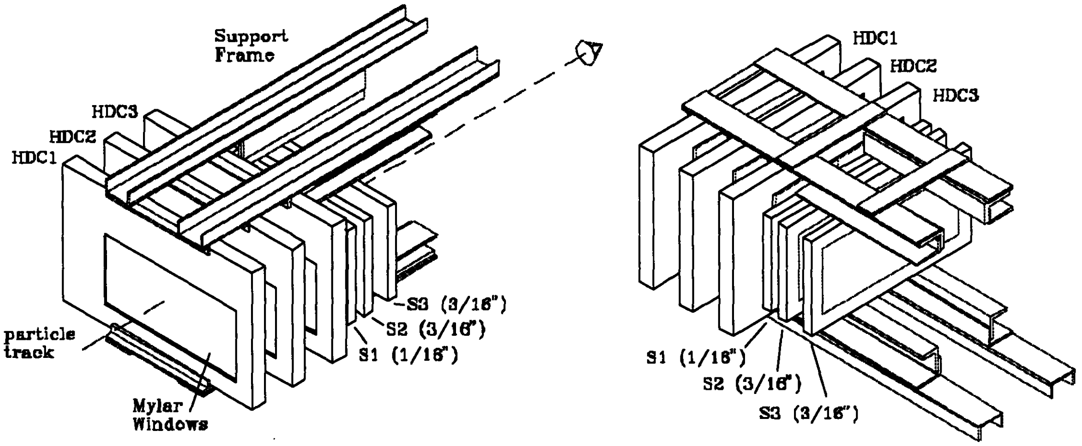

Figure 2.12 Schematic drawing of the OOPS detector package from two angles, the front and rear on the left and right hand side respectively. The light pipes and PMTs that connect to the scintillators are not shown.

The focal plane instrumentation for the OOPS had to be unusually small to fit in the small space provided by the OOPS shielding can. These tight space limitations affected the design of the package, most noticeably in the light pipes used for the scintillators. The entire package was mounted on an aluminum frame and could slide as a unit in and out of the OOPS detector house on a set of rails. It was verified that this procedure could be accomplished while accurately reproducing the alignment of the detectors with respect to the spectrometer. A schematic drawing of the detector package is given in figure 2.12.

2.5.2 The OOPS Horizontal Drift Chambers

The horizontal drift chambers (HDCs) were constructed and tested at MIT. The chambers are small, with an active area that is 17 cm in the X-direction and 32 cm in the Y-direction. They are constructed of eight 4.8 mm thick machined aluminum plates that are stacked on top of each other and create a volume that is sealed from the outside using O-rings. The chambers use five 6.35 μm (0.25 mil) aluminized mylar sheets to provide the isolation between the chamber and the outside. They are also used as ground planes on each side of the wire planes.

There are 21 signal wires in the x plane and 38 signal wires in the y plane at a spacing of 8 mm. These are 20 μm thick wires, and are at a distance of 4 mm from the ground planes. Each signal wire is connected to a common delay line, one for each plane, that is internal to the chamber. The signal wires are held at a potential of about 2500 to 2600 volts, and are connected to a high voltage box which provides a positive potential and also isolates the amplifiers from this high potential by means of a capacitor. Between the signal wires are 76 μm thick sense wires. These are held at ground potential, and are bussed together on two lines which feed the "odd/even" (O/E) amplifiers. The odd/even amplifiers are read out by a special gated ADC. The entire chamber is filled with a gas mixture of 65 % argon, 35 % isobutane and about 0.5 % alcohol. The alcohol is added to the gas mixture by bubbling the gas through a bottle filled with alcohol which is refrigerated at 2 °C. The alcohol is added to the mixture to help prevent buildup of unwanted residues on the wires. A schematic drawing of the chamber is presented in figure 2.13.

The internal functioning of the HDCs is slightly different from that of the TAs that are found in ELSSY. When a particle crosses the chamber it leaves an electron-ion track. The electrons travel to the signal wire, and when they are very close to this wire they accelerate and free even more electrons by colliding with other gas molecules. This process resembles an avalanche of electrons impinging on the wire. In the HDCs, the shortest path to a signal wire is almost horizontal (in the plane of the wires), hence the name horizontal drift chamber. When these electrons hit the signal wire they produce a small negative electric pulse. Unlike the case of the TAs or the VDC, this pulse first travels down the delay line, and then to a high gain amplifier. Because the wires are kept at a high potential they need to be isolated from the rest of the electronics by a capacitor between the delay line and the amplifier, which is inside the high voltage distribution box. Next, the signal is discriminated in a constant fraction discriminator, and sent to a TDC. The sense wires are thicker than the signal wires and are alternately connected to a bus. When an avalanche occurs near a signal wire, there is a small induced positive charge on the sense wire that is closest to the ion track. The charge on the sense wire that is on the opposite side of the signal wire is smaller. These signals are sent to a high gain comparator amplifier (O/E amplifier), that makes an O-E and an O+E signal. The resulting O-E signal is a negative or positive pulse, depending on the side of the wire were the track occurred. This signal was used to resolve the left-right ambiguity by adding a negative offset and reading the pulse out with an ADC.

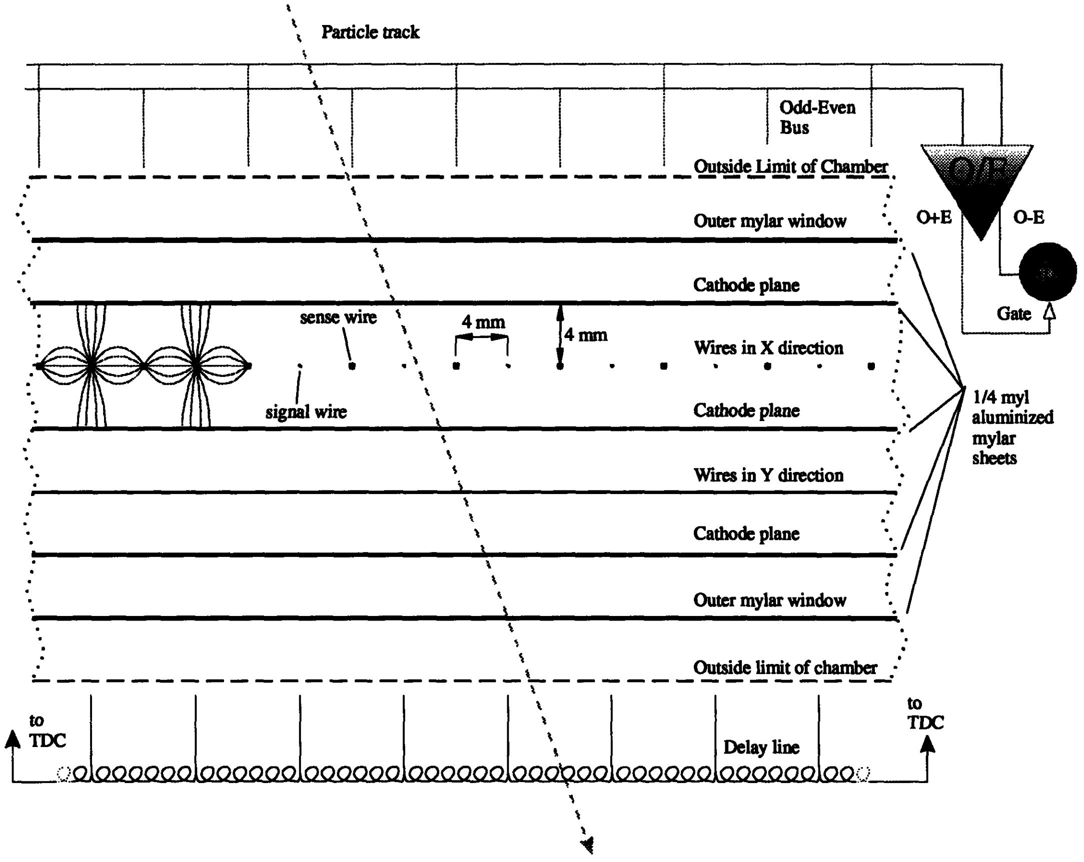

Figure 2.13 Schematic drawing of the HDC, showing the different layers. The field lines are sketched as illustration.

The treatment of the odd/even signals requires much care. They are very sensitive to the operating voltage and the gas mixture in the chamber. This was the first time that the LAMPF design was used at sea level. The difference in atmospheric pressure meant that the operating parameters (gas mixture and chamber voltage) needed to be adjusted. It was found that the best result was achieved when the O+E signal was used to gate each individual ADC (one per chamber plane), rather than using a common gate. The difference between the two methods is illustrated in figure 2.14. Although the actual separation of the left and right peaks in the spectrum is clear in both cases, the individually gates spectrum is much easier to work with. Another problem was a long chamber dead time, which caused a poor efficiency at high rates. It was found that when two particles passed through the chamber in a short interval, their O-E signals would be summed together, resulting in something meaningless. Also the O+E signal could not recover in time to provide a new gate for the next event. These problems were

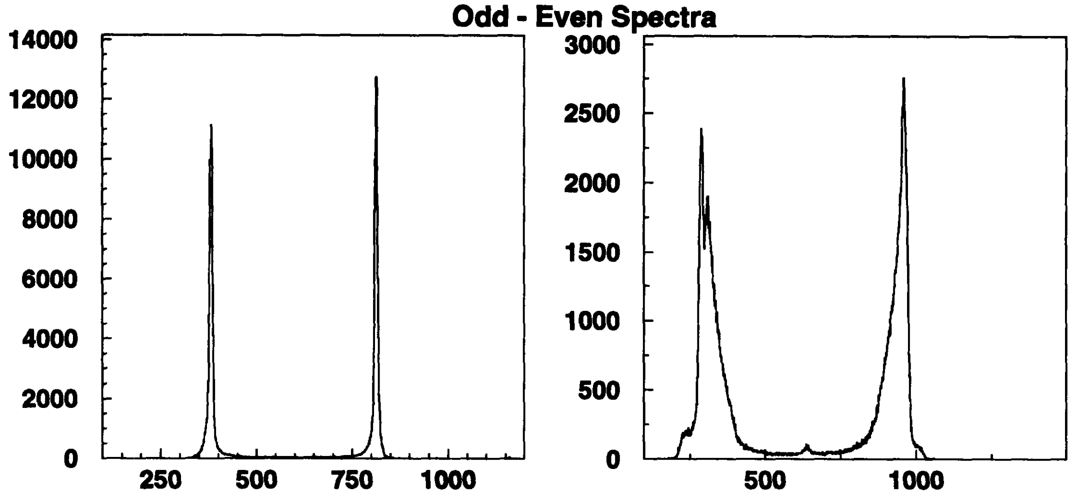

ADC gated on O+E

ADC not gated

Figure 2.14 Two odd-even spectra, with different methods for gating the ADC. The "gated ADC" refers to an individually gated ADC, while the "not gated" refers to a common gated ADC.

solved after this experiment by redesigning the Odd/Even amplifiers to have a faster response time. The O/E inefficiency was reduced to better than 1-2 % at a rate of 1 khz.

The performance and resolution[16] of these chambers was studied extensively. This was done with data from one of the early test runs with 250 MeV electrons; and with a test setup using a ^{90}Sr source. The intrinsic resolution of the chambers, when the multiple scattering is unfolded, was found to be 175±9 μm. When the chambers and the software are properly optimized this results in a trajectory reconstruction resolution of 216±7 μm (including multiple scattering). This translates into an angular resolution of 0.9 mr over the 25.4 cm of moment-arm due to the separation distance of the chambers. Thus the OOPS resolution for target reconstruction was limited by multiple scattering in the spectrometer and target and not by the internal resolution of the chambers.

2.5.3 The OOPS Scintillators

The OOPS detector package has three plastic scintillators that are mounted behind the HDCs. The first scintillator (S1) has a thickness of 1.59 mm (1/16 inch) and each of the next two (S2 and S3) scintillators have a thickness of 4.76 mm (3/16 inch.)

---

[16] David A. Toback, B. S. Thesis (unpublished)

Each scintillator is coupled to two photo multiplier tubes via light pipes that are made up of approximately 90 optical fibers for S1 and 270 optical fibers for S2 and S3. The fibers are 2 mm thick, multi-layered and cladded with a protective layer. Care was taken that all the fibers were the same length so that there is no degradation of the timing of the light pulse. The fibers are clamped in an aluminum frame on one side that matches the frame that holds the scintillators, and on the other side in a round collar that matches the diameter of the phototube. Both ends were carefully polished, and the optical connection was made with optical cement. This construction formed a fairly flexible light pipe that could be bent in the tight radius needed to fit the package in the OOPS shielding can.

The light from the scintillator transfers through the light pipe to a photomultiplier tube (PMT), which converts and amplifies the light signal to an electrical pulse. The voltage on the PMTs was optimized to ensure that all proton events produced a large enough pulse to trigger the constant fraction discriminator (CFD) that was fed by the PMT. The signal from the 1/16 inch scintillator, S1, was amplified by a 10x fixed gain amplifier before it was discriminated. The light is collected from both sides of the scintillator to improve the vetoing of random pulses by taking the logic AND of both sides. There were not enough meantime modules to allow for the meantime signal to be computed in hardware. Instead the signal from each PMT was sent to a TDC. This allows for a software correction of the time differences caused by the different distances that the light has to travel through the scintillator when particles hit it at different locations (see section 3.2.6.a.) To simplify this correction, the start of the OOPS trigger was always determined by a single PMT, in this case the PMT from S2 labeled S2L. A schematic drawing of one of the scintillators is given in figure 2.15.

The thickness of the scintillators was chosen to optimize the particle identification of protons, pions and deuterons. The best particle identification is achieved when the pulse height values for the left and right side are combined by a geometric mean ($\sqrt{Ph_L + Ph_R}$) and then plotted in a two dimensional histogram, see figure 2.16. From this plot it is clear that a very good particle identification was achieved.

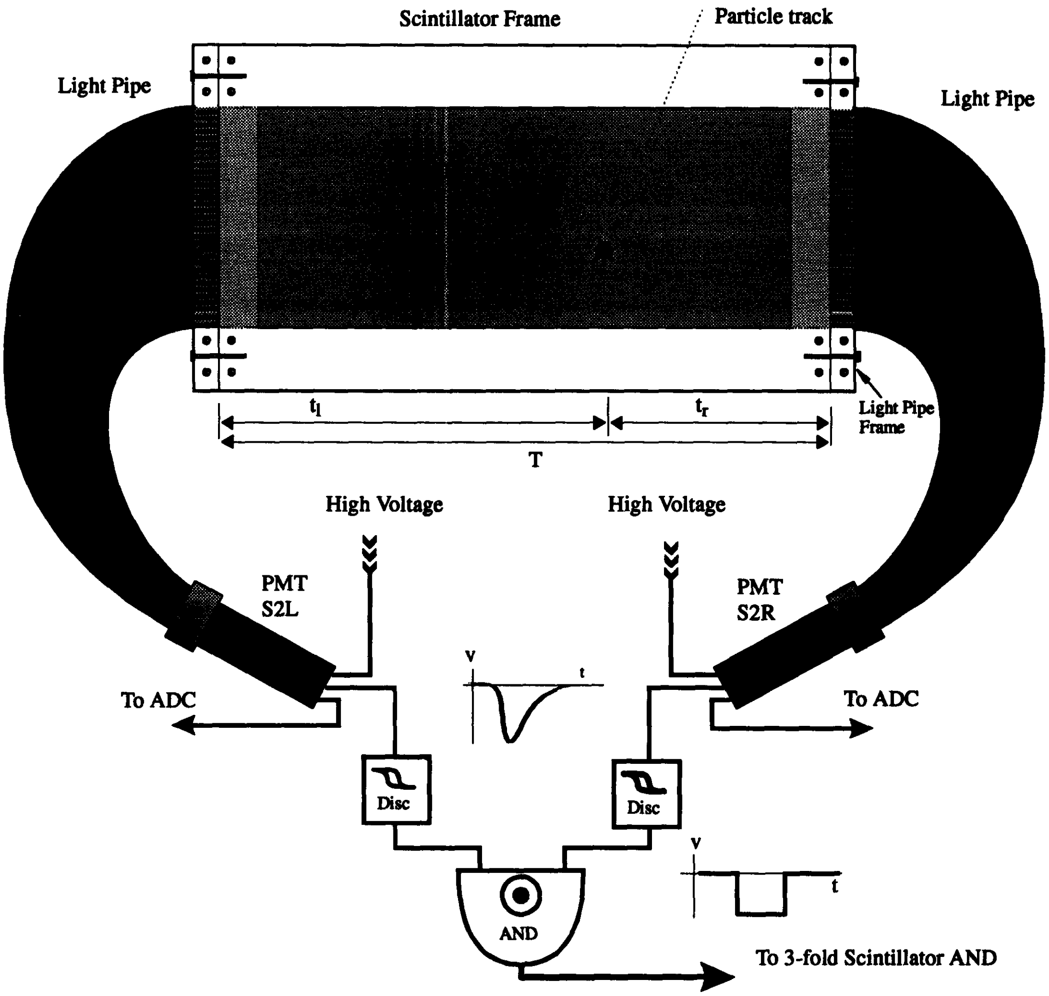

Figure 2.15 Schematic drawing of one of the scintillators, with the electronics setup indicated.

2.5.4 The OOPS Trigger and Electronics

The trigger for the OOPS was determined from the combined signal of all three scintillators. The analog signals from a scintillator were sent to a pair of constant fraction discriminators (CFDs) and then the signal from each side was combined with a logic AND. The resulting three AND signals were then combined in a logic unit to form a three fold AND. A schematic of the OOPS electronics is drawn in figure 2.17.

This setup had some problems with the trigger dead-time that was caused by a less than perfect width (too large) for the logic pulses from the CFDs and the AND units. This allowed a larger than necessary window in which a random particle or random firing of the PMT could inhibit proper functioning of the circuit. The other problem was that the

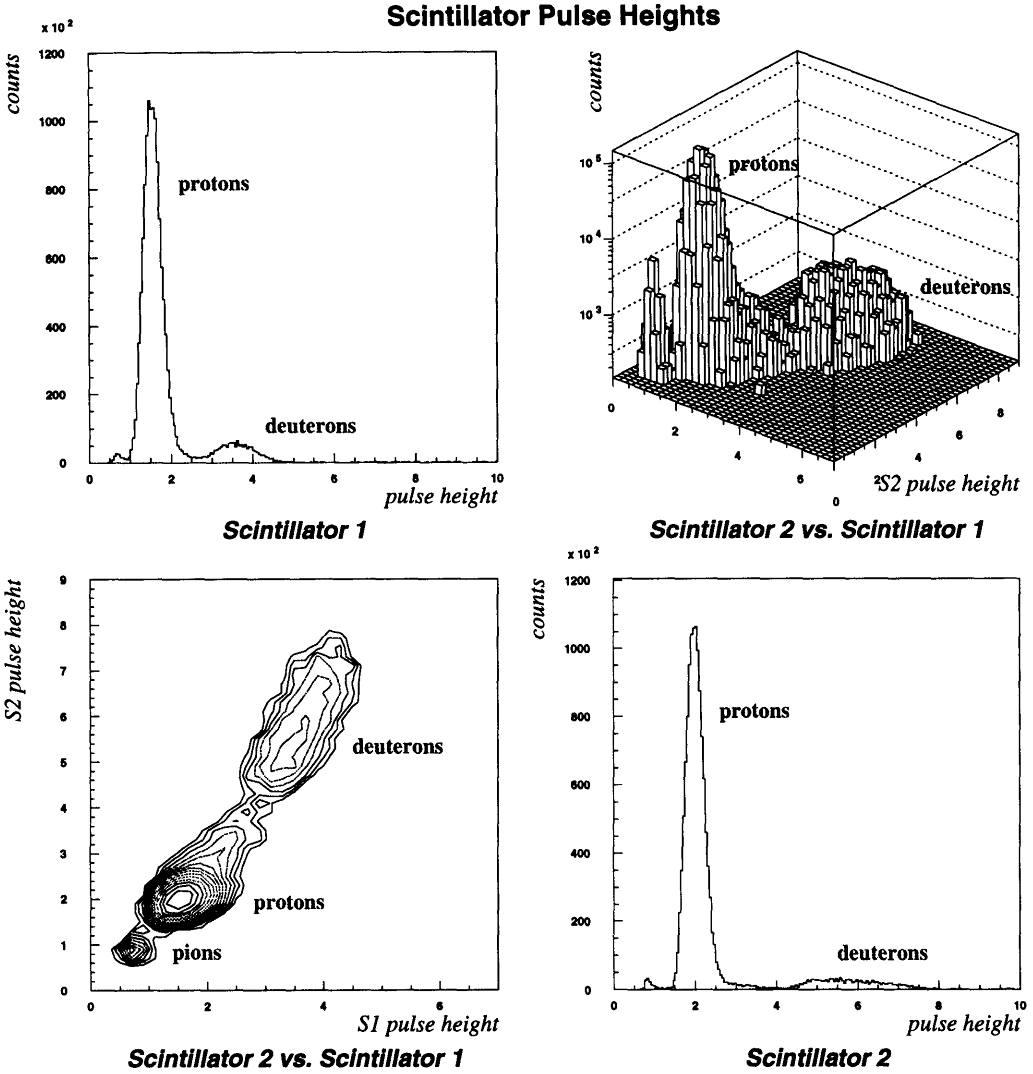

Figure 2.16 A histogram of the pulse height in S1 versus the pulse height in S2. Notice that the z axis on the two dimensional plots is logarithmic.

signals to the TDCs were delayed too much, which again allowed a random pulse to arrive earlier and preempt the real signal.

These two problems were studied extensively and a computer code named Electronics Monte Carlo[17] (ElMoCa) was written to verify the assumptions. This program models the behavior of various electronic components and accurately reproduced the results that were seen from the experiment. Figure 2.18 shows some histograms comparing the experimental TDC spectra with those from the simulation.

---

[17] This code was written by M. Holtrop; a code with a very different implementation was also written by J. Mandeville, who confirmed these findings.

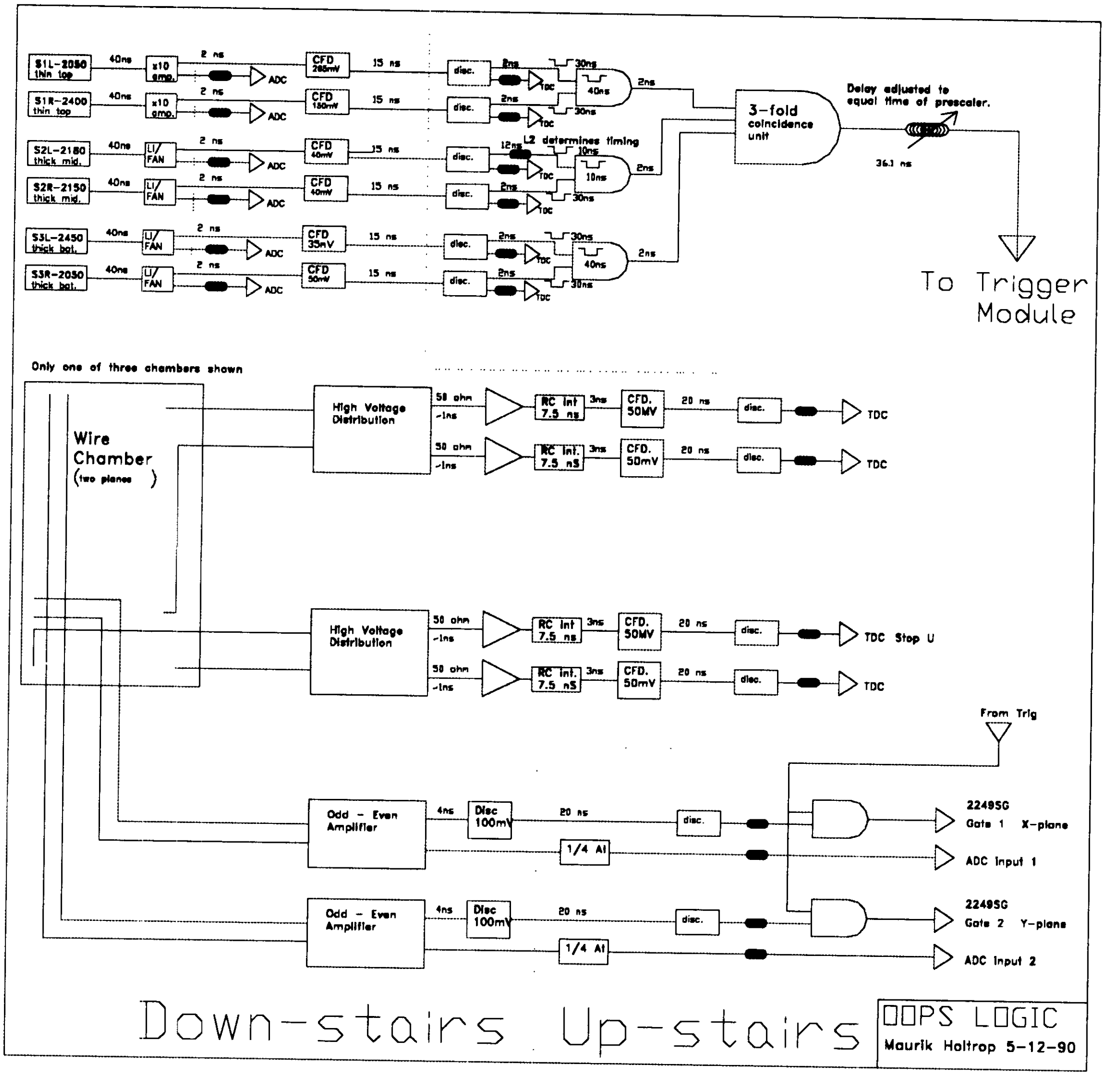

Figure 2.17 Schematic of the OOPS electronics. The scintillator voltages indicated are those recorded at the end of the runs; they varied somewhat over the run cycle. The dotted line running through the diagram indicates the separation between the down-stairs and up-stairs electronics.

We concluded that the problem was well understood and made corrections in the software (see section 3.2.6.a) and to the dead time (5-8%) to correct the problem. More detail of these corrections can be found in chapter 3 and chapter 4.

2.6 Coincidence Trigger Electronics.

The coincidence trigger electronics circuit processes the trigger signals from the two spectrometers and determines whether to trigger the CAMAC controller to read the TDCs and ADCs. The CAMAC is read by the Micro-programmable Branch Driver (MBD).

From the MBD the data is passed to the VMS computer in buffers of several events. The data acquisition system is triggered for each coincidence event and also for a pre-set fraction of the single arm events by means of two pre-scalers. The pre-scalers are dividing units that pass on a single signal for every n-th incoming signal. The single arm events were recorded to be able to check the efficiencies and proper functioning of the detector packages with a higher statistical accuracy than would be possible with only coincidence events.

A schematic flow chart of the data acquisition chain is presented in figure 2.19. The two input signals shown at the top of the figure come from the trigger circuits of each of the spectrometers. These signals arrived sufficiently before the ADC and TDC signals, to make the coincidence decision. It is then decided whether the event is a pre-scale event or whether it is a coincidence event. An event is considered a coincidence event if the trigger signals arrived within a time window of 100 ns from each other. Next, an AND makes sure that the timing of the starts of the TDCs and the gates of the ADCs do not fluctuate depending on how the decision was made (this is called "re-timing".) Finally, this signal arrives at the trigger module, which sends a signal to the MBD to read out the CAMAC crates and process the information. The type of signal "OOPS pre-scale", "ELSSY pre-scale" or "coincidence" was recorded by a scaler module that was read out at each event. Also the relative timing of the OOPS trigger to the ELSSY trigger was recorded with a TDC. This allows for cuts on the coincidence time of flight, which makes it possible to separate the real coincidences from the accidental ones (see chapter 3).

All the scalers, except for the trigger identifying scaler, were read out as a separately triggered event that was produced by an interval circuit every few seconds. This was done to make sure that the computer does not spend too much time reading scalers, thus causing unnecessary computer dead time. The scaler modules were cleared after each reading, and on-going sums were provided by the computer.

The circuit diagram for the coincidence electronics is given in figure 2.20. Some important features of this circuit are:

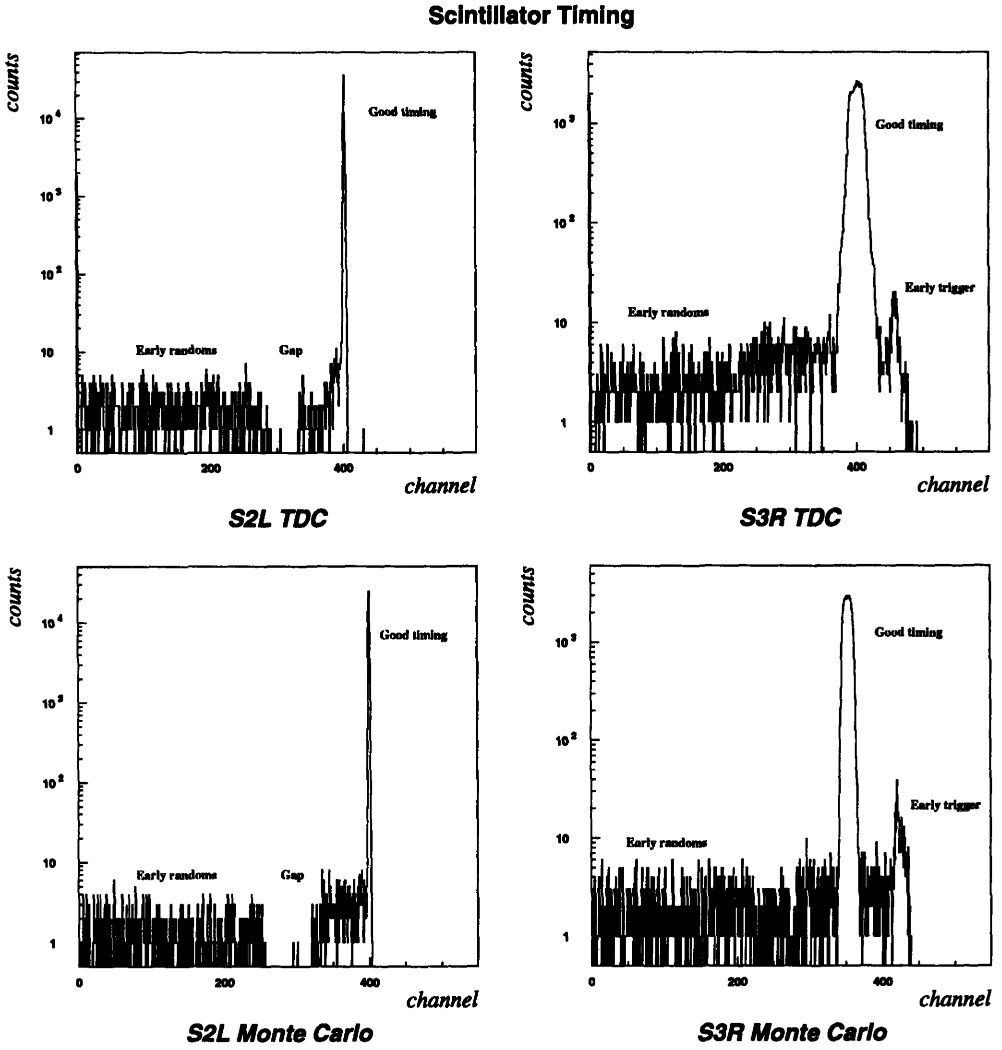

Figure 2.18 Some histograms comparing the scintillator TDC stops with the Monte Carlo. The top two histograms are data from run 1031, the bottom two are from the Monte Carlo simulation with similar rates. The area labeled "early randoms" is caused by random events in the PMT that occur shortly before a real event that causes a trigger. The area labeled "gap" is caused by the shift in timing when the early randoms on S2L come early enough to cause another PMT to determine the timing. This corresponds to an early trigger, as shown in the histogram for S3R in the peak "early trigger".

- There is a limit of one event per beam burst, to allow for enough time to read out all the electronics before the next event. If more than one event arrived in a beam burst, the other events were vetoed, and counted so that a correction could be made.

- Computer dead time is accounted for by counting the number of triggers that arrive while the computer was busy taking an event. During such a period, all triggers were

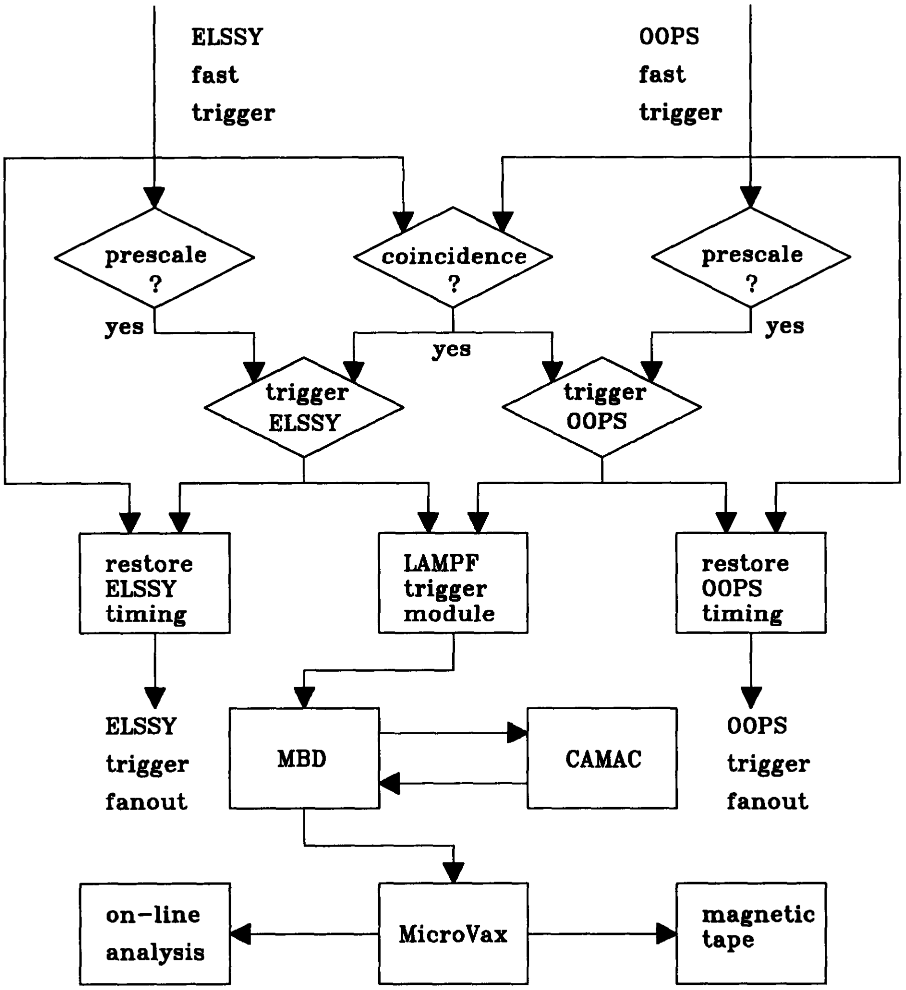

Figure 2.19 A flow chart of the coincidence trigger circuit.

vetoed and counted. This ensured the knowledge of an actual number for the computer dead time.

- A "pile-up" circuit vetoed all events that arrived within 300 ns of each other. This is done to make sure that the wire chamber information is not confused. Pile-up events were also counted.

2.7 Data Acquisition System

The data acquisition system consisted of several parts. The chain starts with the CAMAC crate, which contains the ADCs, TDCs and scaler modules. It also contains a

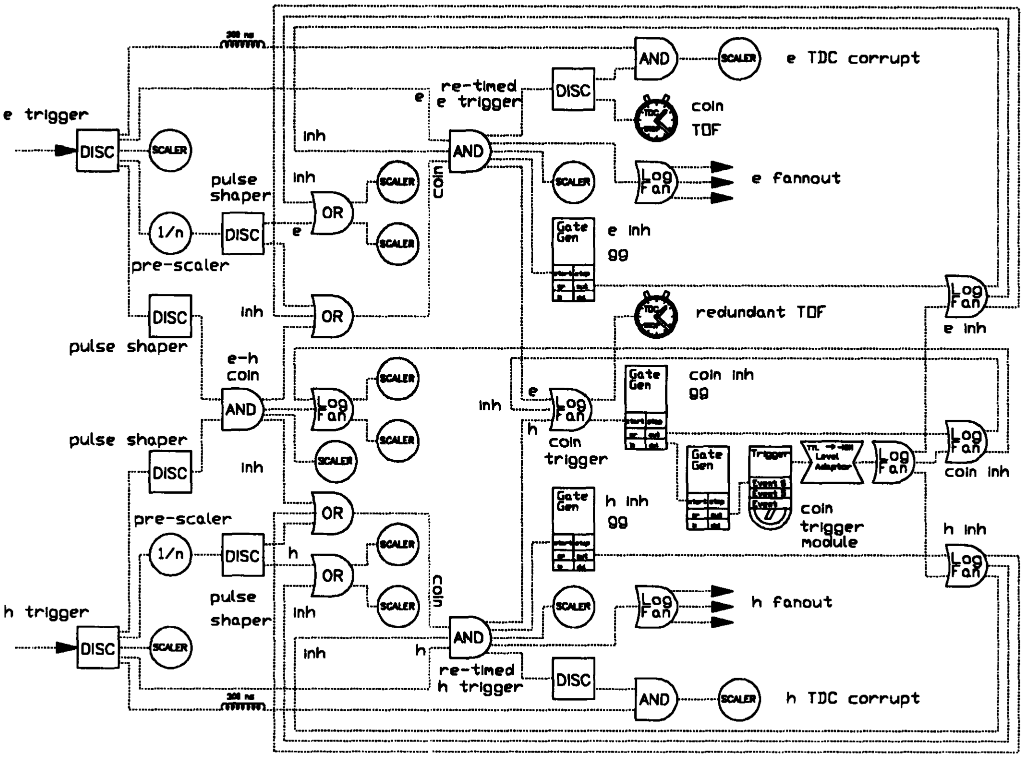

Figure 2.20 A diagram of the coincidence circuit.

LAMPF trigger module and a crate controller, which controls the crate and the interface between the crate and the Micro-programmable Branch Driver (MBD.) The MBD buffers the data from the crate and passes them on to a MicroVax II when the buffers are full. The MicroVax stores the raw data on tape, and if it has enough time, processes the data for histograms.

The LAMPF trigger module orchestrates the interaction between the MBD, the trigger circuits and the CAMAC crate. It contains 31 levels of event triggers with decreasing priority. Events 4 through 11 can be triggered externally with a logic pulse. Event 5 was used for reading the scalers and event 8 for reading data. Separate events were used for clearing and flushing data, which were triggered by software. The trigger module also provides a computer-busy output to inhibit incoming data when the computer is too busy to handle them. This ensures that when the computer becomes available again, the data in the ADCs and TDCs belong to the next event, not accumulated noise from previous events.

The crate controller is a unit that reads out the CAMAC modules and passes the information on to the MBD. Each CAMAC crate needs to have a crate controller to function. The various crate controllers are all linked in series, each having its own address. The crate controller reads the specific modules as specified by the commands from the MBD and passes this information back to the MBD. It also clears, sets or resets modules according to MBD instructions.

The Micro-programmable Branch Driver (MBD) is a small computer unit with a few buffers and a primitive programming language called QAL-code. The MBD is rather slow, and proved to be the bottle-neck in our data acquisition setup. The MBD receives triggers from the trigger unit, or commands from the MicroVax, and executes small pieces of QAL-code. A QAL-code subroutine[18] must be written for each of the events, and it must contain all the detailed instructions, such as "read and clear ADC number 3 in crate 2" for each action that needs to be taken. The MBD buffers the data that it receives from the CAMAC crate, and when a buffer is filled passes the data on to the MicroVax.

The MicroVax was controlled by a software package from the Los Alamos Meson Physics Facility (LAMPF) called the Q Data Acquisition System (Q-system), which runs on top of the VMS operating system. The Q-system controls the interactions between the MBD and the tape drive, and provides the experimenter with an experiment-control subsystem and an interactive histogramming and test package. The experimenters have to provide their own analyzing software[18], which does all the experiment-specific calculations, and on-line/off-line analysis of the data. The analyzer consists of a set of subroutines that are integrated closely with the rest of the Q-system. It reads the raw data from the buffers, decodes the information from the wire chambers and processes this information to make histrograms that the experimenters can use to verify the experimental process and view physical observables. The details of this analysis can be found in chapter 3.

---

[18] The QAL code and analyzer were written by M. Holtrop

Chapter 3 Data Analysis Methods and Software

In modern scattering experiments the bulk of the data analysis is done after the experiment is finished by analyzing the data that were written to computer tapes. This *off-line* analysis is much more detailed than the analysis that is performed during data taking. A considerable amount of time was spent on improving the analysis methods and many of the details of the calculations, and on accurate calibrations of the instruments. This meant that a lot of new software had to be developed to perform these tasks. The next three chapters will work out the details of the off-line analysis as follows:

- Chapter 3 deals with the analysis methods and the software that was developed for this experiment.
- Chapter 4 deals with the calibrations that were necessary for this experiment, including spectrometer optics, focal plane efficiency and beam energy calibration.
- Chapter 5 will deal with the details of the analysis of the ^{12}C(e,e'p) data, the corrections that were applied to these data and the results.

Note that the division between software and calibrations is somewhat arbitrary and can not be maintained accurately. It is intended to simplify the presentation of this analysis.

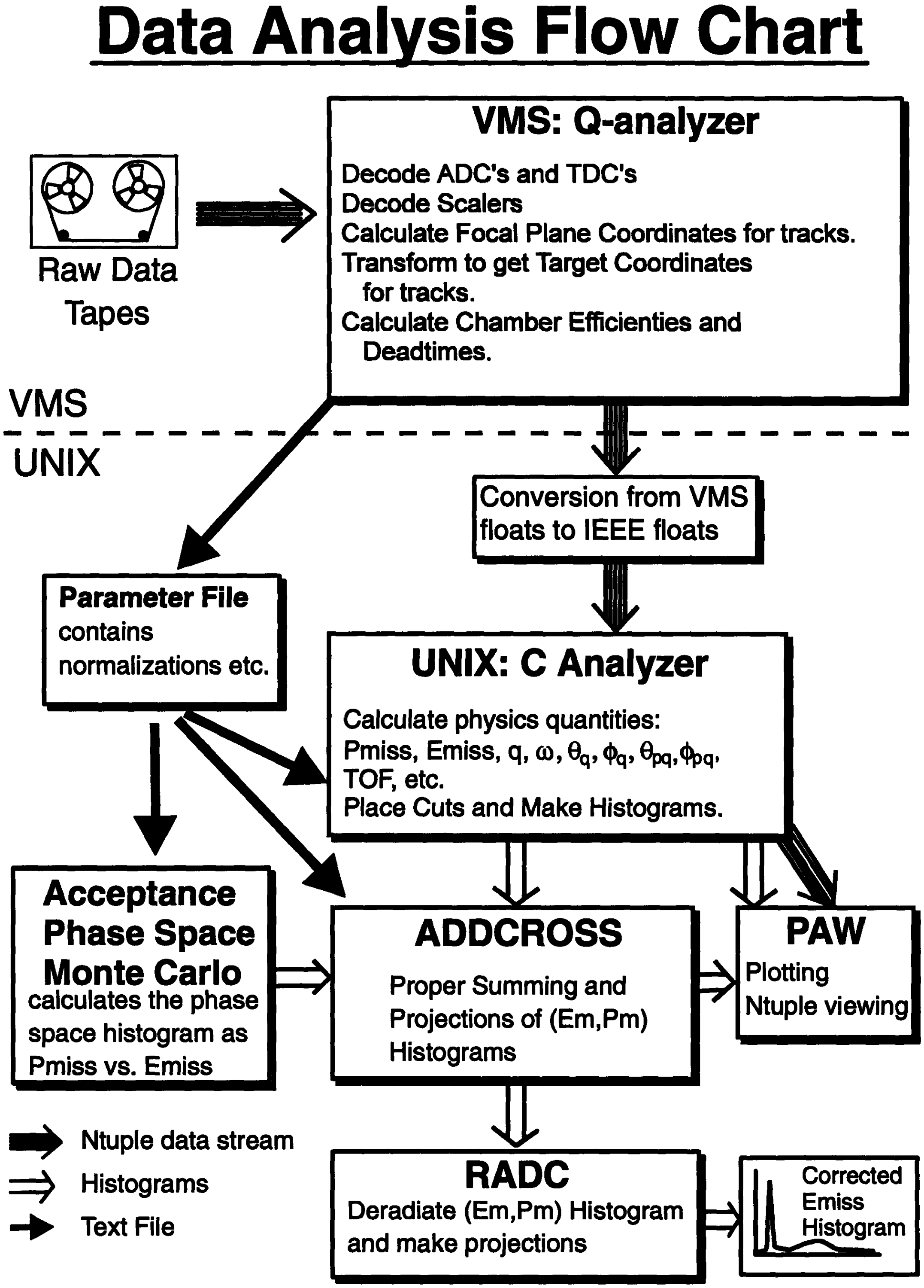

Figure 3.1 Flow chart of the data analysis. The programs above the dashed line only run on VMS, the programs below this line were written for UNIX but are easily ported to other systems. Arrows indicate the flow of information. Note that each program also accepts an input file with general parameters, which is not indicated on the graph.

3.1 Overview

In this analysis the results are calculated as two-dimensional histograms in missing momentum versus missing energy. These two-dimensional histograms can be projected onto the missing energy or the missing momentum axis to get a one-dimensional representation of the data. This method is an improvement over previous one dimensional methods of analysis because it makes it clearer how the data are distributed in (E_m,P_m) and allows for the radiative corrections to be done in the two dimensional plane, which is more accurate. This two dimensional approach also allows for a clear way to check the experimental overlap in (E_m,P_m) between the two settings of the proton spectrometer angles, which enhances the accuracy of the R_{LT} extraction.

A flow chart of the core set of programs for the analysis, and the links between them, is presented in figure 3.1. The analysis was split between two different types of computer systems. The first stage of the analysis was done on VMS since the Q data acquisition software works only on this computer system, and an analyzer was already working under VMS which was used during the experiment. The later stages of the analysis were done on UNIX workstations since this became advantageous when several fast UNIX systems with large hard disks were introduced to our computing environment. Using these systems also allows one to overcome some of the limitations of the Q-system, such as allowing only integer increments of the histograms, and the absence of proper error bar handling. All the programs that were developed for the second part of the analysis were written in an operating system independent way, so that they could be used on any system. The division point between the VMS and the UNIX part of the analysis is fairly arbitrary. There is no reason why the entire analysis could not be performed on either VMS or UNIX.

The data analysis starts with extracting the data from the data tapes and storing them on the hard disk. This is done with the aid of a small utility called ***qtaputil,*** that runs on the VMS systems, and conveniently copies the tapes run by run, skipping over bad blocks and other tape problems. Once the data is on disk it can be analyzed by the Q-system analyzer, called the ***Q Analyzer***. This analyzer decodes the raw TDC and ADC information, and calculates the coordinates of the actual particle tracks in the spectrometer. It also keeps track of the wire chamber efficiencies and computer dead times. The data are then written to a binary file that contains the coordinates of the particle tracks in the spectrometer, and any other useful quantities for the next step of the analysis. All the other information such as chamber efficiencies is written to a separate text file. The details of this program are presented in section 3.2.

Next, the binary files are copied from the VMS computers to the UNIX workstations. In order for the files to be useful on UNIX, the floating point byte order has to be swapped from VMS specific to IEEE floating point numbers (the international standard). This is done with a small converter routine that also compresses the data files. At this point it is possible to reduce the size of the data files even further by selecting only the coincidence events, which reduces the total size of the ^{12}C(e,e'p) data to slightly more than 100 Mbytes.

At this point the data are further analyzed by an analyzer program written for UNIX in the C programming language, which is referred to here as the ***C Analyzer***. In this program, all the physics quantities such as missing energy and momentum are calculated and written to *hbook* files for plotting with PAW[1]. PAW also allows for fast temporary analysis and viewing of data through its *n-tuple* interface. The final output of this step is a set of histograms. The details of this stage of the analysis are presented in section 3.3.

The program ***Addcross*** now combines the histograms for each of the runs using proper weighting for each run, and divides out the spectrometer phase-space that was calculated by the ***Acceptance*** Monte Carlo program. After this division the experimental cross-section histograms are available for plotting. These cross-section histograms have not yet been corrected for radiative processes. Finally, these histograms are passed to the program ***RADC*** which de-radiates the spectrum and produces the fully corrected two-dimensional histograms. These histograms are then projected onto the missing energy and missing momentum axes for physics insight.

3.2 The Q Analyzer

As mentioned earlier, the Q analyzer was used during data acquisition to monitor the progress of the experiment. The Q-system is set up in such a way that one can use the same analyzer for the off-line analysis (replay mode), so it was a natural choice to

---

[1] PAW (Physics Analysis Workstation) is part of the CERN libraries, and maintained and distributed by CERN

use this existing analyzer as the first stage of the analysis. This analyzer comes in the form of a set of user supplied subroutines that link into the larger framework of the Q data acquisition system. The Q-system provides the following services:

- A set of input/output routines to retrieve data from tape or disk. During data acquisition they will also retrieve data from the MBD buffers and write them to tape or disk.
- A histogramming package that allows the user to view two- and three-dimensional representations of raw or calculated variables. It allows the user to set up these histograms interactively, and display them even while the analysis is still in progress. Its shortcomings, among others, are that it will only increment histograms by integer values and the axes are also only integer increments of the variable plotted. Also it can only display error bars as the square root of the contents of a bin, instead of storing the uncertainty as an number calculated by the user.
- A test package that allows the user to set a condition on any raw or calculated variable, and to combine these tests through logical operations. These tests can be specified on a histogram as the condition under which the histogram is to be updated. Also the test package provides a summary of the number of events that passed each test, which was used to calculate chamber efficiencies and dead times.
- A parameter subsystem that allows the user to set specially declared variables in the analyzer, and thus control some of the variables needed in the calculations. A short coming of the parameter subsystem was the cumbersome way in which the user had to manually set the parameters for each run if experimental conditions had changed from the previous run. This was overcome by a utility called ***runInfo***, that is executed at the beginning of a run (in replay mode), and looks up in a text file which parameters need to be changed for that run.
- A scaler subsystem that counts up all the results from the scaler modules, and allows the user to display the final summed results. These results are passed on to programs that calculate the deadtimes and efficiencies.

All the actual calculations that need to be performed are supplied by the user as a set of subroutines that are referred to here as the **Q analyzer**. These subroutines performed the following tasks:

- Correct the TDC values for variations in the slope and offset. The correction is based on a separate calibration of the TDCs.
- Apply timing corrections to the scintillators TDC values, to get a position independent "event start signal." See section 3.2.6.a.
- Decode the position and angle of the tracks in the wire chambers from the corrected TDC values. See sections 3.2.2 and 3.2.7.
- Calculate the target coordinates from the coordinates of the track at the focal plane. See sections 3.2.5 and 3.2.8.
- Calculate the relative corrected Time-Of-Flight[2] (TOF) for each event, to distinguish between real and random coincidence events. See section 3.3.2

The following sections present some details of the tasks performed by the Q analyzer. Some sections will include a few calculations that were actually done in the C analyzer, but are presented here for the sake of clarity.

3.2.1 Input data to the Q analyzer.

Most of the format complexity of the Q-system data tapes is handled transparently by the input/output routines. The data are organized on the tape in records. Each record contains a header that stores the time and the date when it was created during data acquisition, a sequence number, the run number and some other information such as tape format, length of the data array and the record type (which can be *data, comment, error record, beginning of tape, end of tape, beginning of run, end of run*). It also contains the type of event for the record, which corresponds to the trigger event type. Next follows the actual data. During this experiment, there were two event types that contained data. Event 8 contained the readout values of the TDCs and ADCs, and event 5 contained readout values of the scaler modules.

---

[2] The relative Time Of Flight is the difference between the start event in the electron spectrometer and the start event in the proton spectrometer.

The data structure of event 8 is presented in table 3.1. All words in the record are 2 byte integers. The first words are flags that are read out from the trigger identifying scaler module, see section 2.6. These flags determine which spectrometer was triggered, and whether the information in it was valid. They also make the distinction between single arm events and coincidence events.

Table 3.1 Data Structure for Event 8

Word Index	**Description**
	Flag Words
1	Coincidence Flag Word
2	OOPS Pre-scale Flag Word
3	ELSSY Pre-scale Flag Word
4	OOPS Pileup Flag
5	ELSSY Pileup Flag
	OOPS Data Words
6	LAM Flag
7-12	Scintillator ADCs
13-18	HDC O-E ADCs (individual gating)
19-24	Scintillator TDCs
25-36	HDC Delay Line TDCs
37-42	HDC O-E ADCs (common gate)
43	Time Of Flight TDC (OOPS-ELSSY)
44	Beam Halo Monitor
45	Not Used (spare)
46,47	Beam Position Monitor X and Y
48-50	Not Used (spare)
	ELSSY Data Words
51	LAM Flag
52-57	VDC Delay Line TDCs
58-65	TA Delay Line TDCs
66,67	Scintillator ADCs
68	Cerenkov Sum ADC
69	Lead Glass Sum ADC
70,71	Scintillator TDC
72-74	Cherenkov ADCs

3.2.2 Decoding the ELSSY VDC.

Although the ELSSY spectrometer has been used for many years we found that there were still many ambiguities in the proper treatment of the VDC (Vertical Drift Chamber) and TA (Transverse Array) information. It was found that especially the angle measured by the VDC (θ_f) is extremely sensitive to the method of analysis. This section will present this analysis in some detail since some previous implementations were not fully consistent.

It is important to realize that the matrix elements, which are found through a sieve slit experiment, are directly coupled to the method that was used to analyze those data. It is possible to find matrix elements that give the correct target coordinates based on incorrectly calculated focal plane coordinates, and as long as this is done consistently every thing will work fine. For matrix elements that were derived from a theoretical model of the spectrometer, it is essential that the actual position and angles of the particle track are computed. This means that the detector information has to be interpreted correctly. Such matrix elements can be found with the aid of ray tracing programs, such as Transport or Raytrace.

The ELSSY Vertical Drift Chamber is oriented at 45° with respect to the central ray of the spectrometer, and contains 3 delay lines that bus every third wire together. The details of the construction of the VDC are presented in section 2.4.4. To find the location at which the particle track crosses the VDC (x_f) and the angle of this track (θ_f), two pieces of information must be decoded from the six TDC values (two TDCs per delay line, three delay lines) :

1. The position of the wire that fired, (i.e. the wire number of the active drift cell.)
2. The distance of the track from this wire, which is found from the *drift time.*

By measuring these two quantities for each of the three wires that fired, the particle trajectory through the VDC can be reconstructed and (X_f,θ_f) for the event determined. There are many different schemes for doing this, and a detailed analysis of them can be found in the BATES internal report, "Understanding the ELSSY VDC" by D. Jordan et al.[4] It was discovered that there can be quite a large difference in the decoded θ_f for the different methods. For correct target coordinates of the particle track it is important that the same method for the VDC analysis is used, as was used for the determination of the matrix elements. The next few sections will present the details.

3.2.2.a Getting the wire numbers.

When a particle traverses a drift cell it ionizes the chamber gas. The free electrons drift along the field lines towards the sense wires at a constant drift velocity of $50\,\mu m/ns$. When they get near the wire they will accelerate because of the high field in this region. Due to collisions they knock out more electrons in the gas, which results in an amplification of the signal which is often called an avalanche. The time it takes for the electrons to reach the sense wire is proportional to the distance of the particle track to this sense wire. When the electrons reach the sense wire they cause a small electrical pulse. This is amplified and discriminated, and then travels to both ends of the delay line. If there are N wires on the delay line, n is the wire that fired, and each delay line element has a delay time of τ (here we have $N = 33$ and $\tau = 1.7$ ns) the total time it takes the pulse to reach each end of the delay line is:

$$T_{left} = t_{drift} + n \cdot \tau + T_{left}^{other} \tag{3.1}$$

and,

$$T_{right} = t_{drift} + (N - n) \cdot \tau + T_{right}^{other} \tag{3.2}$$

T^{other} is the amount of time the signal travels through all the other cabling before it is read out. For the VDC, "right" refers to the high momentum side (positive X) and "left" refers to the low momentum side. For the TAs, "right" refers to the smaller scattering angle side (positive Y). The inconsistencies between the TDC slopes due to small differences in the TDC module hardware are corrected by multiplying each TDC value by a factor and adding an offset. Each TDC is calibrated separately before the experiment.

The wire number is found by subtracting equation 3.2 from 3.1:

$$n = \frac{1}{2\tau} \cdot \left(T_{left} - T_{right}\right) + \tfrac{1}{2} N - \frac{1}{2\tau} \cdot \left(T_{left}^{other} - T_{right}^{other}\right) \tag{3.3}$$

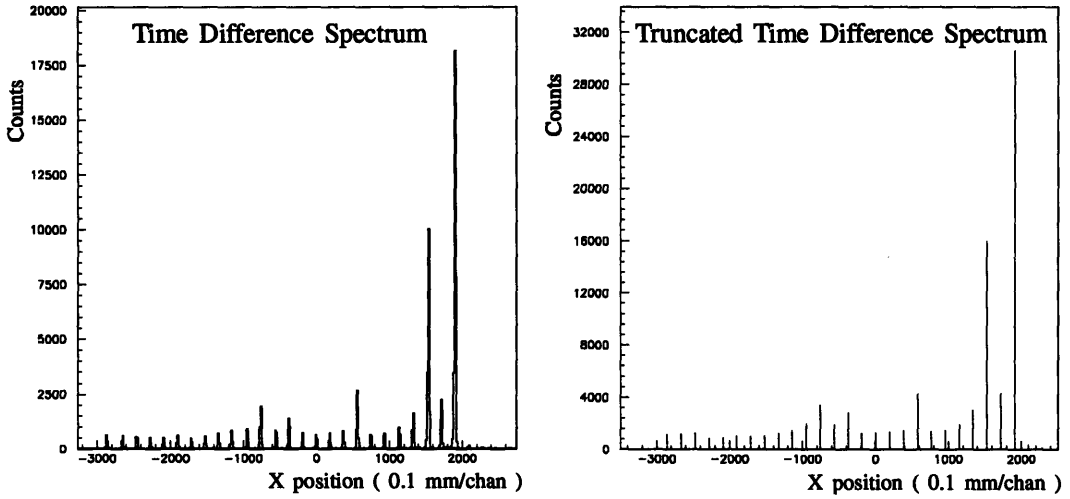

Figure 3.2 Time Difference Spectrum for the VDC. The left hand histogram is a correctly adjusted time difference spectrum. This time difference is equivalent to the position of the wire in the wire chamber. The right hand histogram is the corresponding truncated histogram. Note that the 16th wire is set at zero. The data for these histograms came from one of the carbon runs, which contained several peaks.

In practice there are non-linearities and dispersive effects in the delay line that need to be corrected. This is done by adding a second order term (and sometimes a third order term) to equation 3.3. Defining $T_{diff} = T_{left} - T_{right}$, the wire number n can be written as:

$$n(T_{diff}) = a_0 + a_1 \cdot T_{diff} + a_2 \cdot T_{diff}^2, \tag{3.4}$$

The constant a_1 is adjusted so that the peaks in the $n(T_{diff})$ distribution are separated by 3 wire spacings. This is more convenient than determining the exact value of $1/(2\tau)$. The constant a_2 is adjusted so that the peaks are evenly spaced, which corrects for dispersive effects in the delay line, and a_0 is adjusted so that the 16th wire of the delay line is at zero. For the TAs this would be the 4th wire. This last adjustment corrects for any difference in the length of cable between the path for the left TDC signal and the right TDC signal (a_0 absorbed the $N/2-(T_{left}^{other} - T_{right}^{other})/2\tau$ term). Making these adjustments is simplified by a program called ***calibrate***, which determines the three constants directly from a histogram.

The corrected time difference spectrum can now be converted to a wire number by "truncating" the quantity n. This is done by dividing the wire number by the wire spacing, and taking the nearest integer ("nint"). When this number is again multiplied by the wire spacing, the resulting quantity corresponds to a position of the wire in the chamber. An offset is added that corresponds to the physical position of the 16th wire of this delay line to the center of the chamber. In formula form this is given by:

$$X_{trunc} = \mathrm{nint}\left(\frac{n}{spacing}\right) \cdot spacing + offset \qquad (3.5)$$

This quantity is then histogrammed (see figure 3.2). X_{trunc} represents the physical location of the wire that fired with respect to the central ray. Table 3.2 presents the offsets that were used for this experiment.

Table 3.2 Offsets for the VDC

Item	*X Offset*
Delay line 1	0.635 cm
Delay line 2	0 cm
Delay line 3	-0.635 cm
Overall offset	-9.0 cm

3.2.2.b Converting drift time to distance.

Next the drift time is found for each delayline by adding equation 3.1 to 3.2, which gives:

$$t_{drift} = \frac{T_{left} + T_{right}}{2} + \Delta t_{corr} + C_d \qquad (3.6)$$

The Δt_{corr} term is a correction that takes into account that the VDC is at 45° with respect to the scintillators. The VDC is about 60 cm long, so the high momentum side is about 40 cm lower than the low momentum side. For an electron traveling at c this is a 1.3 ns difference in both T_{left} and T_{right}. The correction is calculated using the truncated position (X_{trunc}), which is available before the actual position is calculated. This correction, which is added into equation 3.6, is:

$$\Delta t_{corr} = \frac{-X_{trunc} \cdot \sin(45^o)}{c} \qquad (3.7)$$

where c is the speed of light.

The drift time is converted to a drift distance using a lookup table. Figure 3.3 shows the histogrammed result for one of the delaylines. The constant C_d of equation 3.6 is adjusted for each delayline to shift the drift time histograms so that the rising edge starts at the same channel (note that this is a little tricky, because the rising edge is more than one channel wide). This allows the same drift table to convert all three drift times to

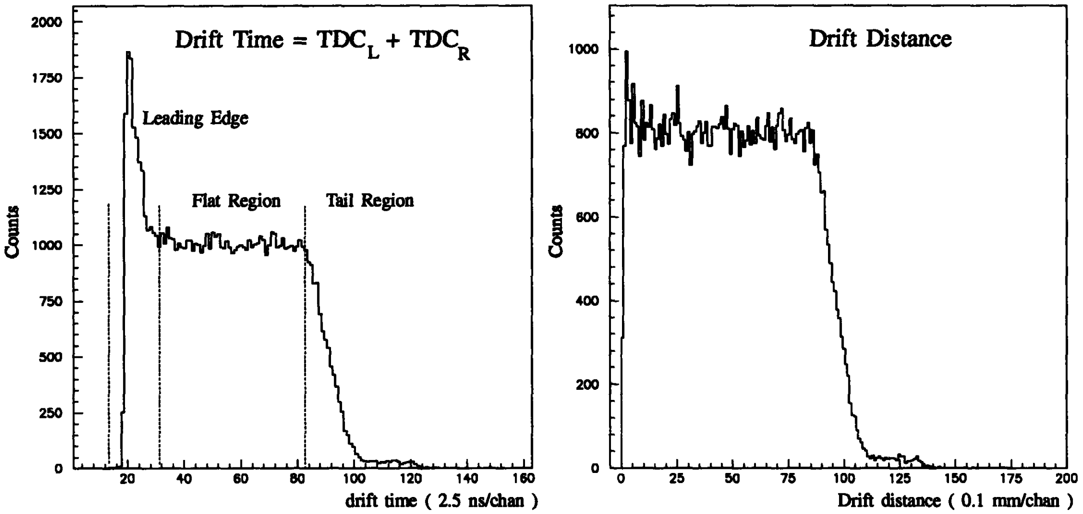

Figure 3.3 Drift Time and Drift Distance for a VDC delayline. On the drift distance histogram the three different regions are indicated. The drift velocity of the *flat region* is constant at 50 μ/ns, the drift velocity in the *leading edge region* is corrected for non linear effects.

drift distances. The histogram was created by illuminating the chamber (and each drift cell) uniformly. If the electric field lines were parallel everywhere in the cell, the drift velocity would be a constant of $50\,\mu/ns$. This is true for the *flat region* of the histogram. At the *leading edge* this value has to be adjusted for geometric effects in the *non-linear region*, which cause a higher apparent drift velocity, see figure 3.4. This is taken into account in an empirical manner by assigning a local drift velocity which is calculated from:

$$v_i = 50\,{}^{\mu}\!/_{ns}\cdot\frac{H_i}{H_{flat}} \tag{3.8}$$

where H_i is the number of counts ("height") for bin i and H_{flat} is the average height of the flat region of a drift time histogram that was created by uniformly illuminating the VDC (see figure 3.3). This was done by taking data on the quasielastic region of carbon. In this manner a table is created with one entry for each bin of the *drift time* histogram. The *drift distance* is then calculated by looking up the appropriate value in the table.

3.2.2.c Calculation of X_f and θ_f.

At this point it is known which wires fired, and what the distance of the track to these wires (the drift distance) is, which determines the X (position along the VDC) and Z (position perpendicular to the VDC) coordinate of three points on the particle track (see

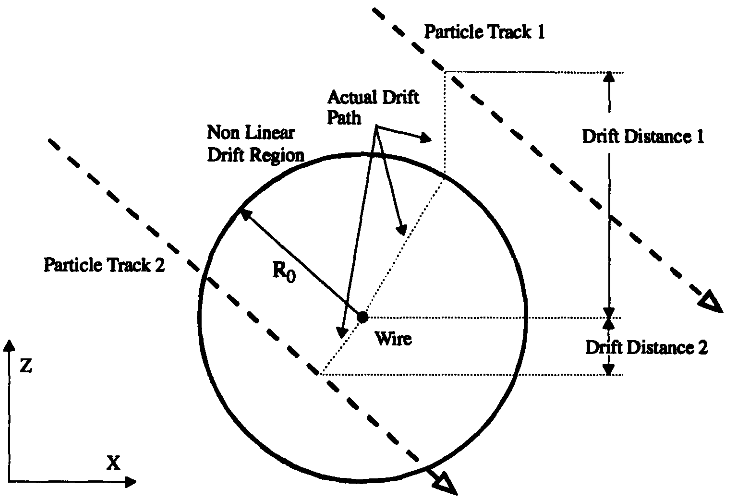

Figure 3.4 Schematical drawing of two VDC drift tracks. Track 1 falls outside of the non-linear drift region, and consequently contributes to the flat part of the drift time histogram. Track 2 falls inside this region, which causes the leading edge region, see figure 3.3.

also figure 2.6). From this information the intersection point and angle of the track can be calculated. One possibility is to perform a least chi-square (χ^2) fit on the three points. However, this does not give very satisfactory results, because the VDC has only three delay lines, while the track can go through up to five drift cells. This causes an unequal weighting of events on the delay lines, favoring shorter drift times, which in turn makes it difficult to calculate the Z distances exactly. The fit method depends heavily on the accuracy of X and Z.

A much better method was used in the original paper on the VDC[3]. This method was modified slightly to improve the angular accuracy. The prescription of this method is as follows:

- Find the drift distances from the drift times using the lookup table. These are approximately the Z positions of the known points on the particle track.
- Sort the pair $\{X_{trunc}\ , Z\ \}$ of each delay line in ascending order in X. These will be referred to as $X_w(i)$ and Z_i.
- Then find the largest drift distance as $Z_> = \max(\ Z_1,\ Z_3\ )$. Note that the Z values are always positive in this analysis.

---

[3] W. Bertozzi *et al.*, Nuclear Instruments and Methods **162**, 211 (1979)

- Now the intercept of the track is given by:

$$X_{fine} = X_w(2) + \frac{Z_1 - Z_3}{(Z_> - Z_2)} \cdot U \tag{3.1}$$

where U is the spacing between two adjacent wires. This gives the position along the VDC accurately. (Note that it makes use of the fact that $Z_>$ is always on the same side of the wire plane as Z_2, and is thus not sensitive to the distortions caused by the non-linear drift region.)

- The slope of the track can be found in two ways. The slope, m, is found from:

$$m = \frac{Z_> - Z_2}{U} \tag{3.9}$$

This gives the correct slope, but it has a lower resolution than if the two outer wires were used. This second method gives:

$$m = \frac{Z_1 + Z_3}{2U} \tag{3.10}$$

The angle θ_f is found from the slope with:

$$\theta_f = 45° - \arctan(|m|) \tag{3.11}$$

which takes the angle of the VDC with respect to the central ray into account.

This last method does not give the correct slope. The error for this slope is caused by the drift path, which is not perfectly vertical, due to the horizontal drift in the non-linear region, see figure 3.5. From the figure it can be seen that two tracks with identical drift distances, D, can have a different Z intercept. (Alternatively, one can take the view point that the X position is shifted.) This effect is angle dependent, and affects only the slope given by equation 3.10, since Z_1 and Z_3 are on

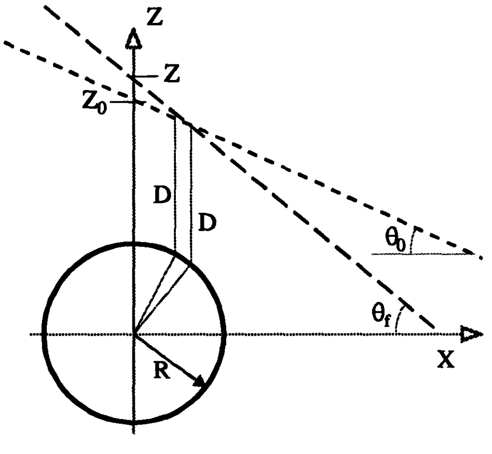

Figure 3.5 Diagram showing the angle correction to the drift distance. The two particle tracks have an identical drift distance D but a different Z intercept because of the difference in slope.

opposite sides of the wire plane. Equation 3.9 is not affected by it, since $Z_{>}$ and Z_2 always fall on the same side, causing the same shift. It is possible to express the shift in Z as a function of the angle θ, relative to a reference track defined by Z_0 and θ_0. By solving the equation for θ, it can be shown that the intersection angle is given by[4]:

$$\cos\theta_f = \frac{-\psi\zeta + \sqrt{1+\psi^2-\zeta^2}}{1+\psi^2} \tag{3.12}$$

where

$$\psi = \frac{Z_1 + Z_3 - 2R\sec\theta_0}{2U} \tag{3.13}$$

and

$$\zeta = \frac{R}{U} \tag{3.14}$$

The quantities R and θ_0 represent the radius of the nonlinear drift region and the central angle (central with respect to the VDC); they are determined experimentally to be $R = 0.1\ mm$ and $\theta_0 = 46°$. The Z's are the uncorrected drift distances.

Since the correct X and θ are now available, the corrected drift distances can be found from:

$$Z_i^{corr} = z_i + R\left(\sec\theta_f - \sec\theta_0\right) \tag{3.15}$$

for z_i larger than $R\sec\theta_0$ (in the linear region), or for z_i smaller than $R\sec\theta_0$ (in the non-linear region):

$$Z_i^{corr} = z_i \cdot \left(\frac{\cos\theta_0}{\cos\theta_f}\right) \tag{3.16}$$

---

[4] D. Jordan, M. Holtrop, B. Schmitt, *Understanding the ELSSY VDC*, BATES INTERNAL REPORT B/IR 92-03.

If these drift distances are used in equation 3.10 the correct θ_f is found, which is equal to the angle given by equation 3.12.

There are some events that can not be properly decoded, and thus have to be eliminated from the analysis. These events are counted, and the final histograms are corrected by a factor that reflects the VDC decoding efficiency (see section 4.2.2). The eliminated event types were:

1. Events with hit patterns of $(+++)$ or $(---)$, which would correspond to the track falling completely above, or below the wires that fired. Normal events are of $(++-)$ or $(+--)$ type, where a +(−) stands for a cell where the track was above (below) the wire. This effect was investigated and it was found that it mostly occurs at the edges of the chamber. The simple remedy was to reject events where the last wire fired, which resulted in only a small decrease in the momentum bite, affecting about 1.3% of the events.
2. Events where the 3 hits did not decode to be consecutive wires. This is most likely caused by multiple events on a delay line, and these events were eliminated. About 1.6% of the events were lost this way.
3. Events where the drift ratio

$$B = \frac{Z_1 + Z_3}{Z_> - Z_2} \tag{3.17}$$

is more than 3 sigma away from the value 2, which occurred for approximately 2.4% of the events. From geometry this ratio is expected to always be equal to two. If it is not, the VDC information is assumed to be not accurate enough to decode the track properly. A crude estimate for the X_f intercept can still be used by using the position of the middle wire. Events of this type were eliminated from the final spectra. Figure 3.6 shows two final spectra for high resolution runs.

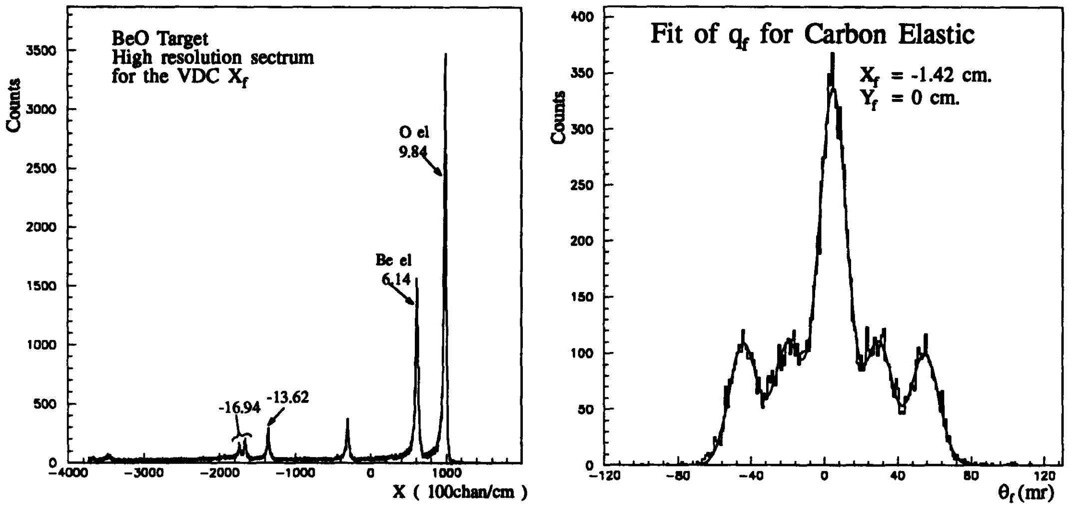

Figure 3.6 Two final histograms from the VDC. On the left hand side is a histogram of X for a high resolution run on BeO and on the right hand side is a histogram of θ for a sieve slit run with a curve fit to the peaks.

3.2.2.d Angle correction.

The θ_f measured by the VDC depends on X_f. This dependency caused irregular bumps in the spectrum of θ_f versus X_f. These irregularities are probably caused by some inconsistency in the construction of the VDC, causing a less than perfectly uniform spacing across the VDC, or the readout electronics are not perfectly uniform causing variations in the timing of the discriminated signals. This effect was corrected by constructing a lookup table. The details for this are VDC specific, and can be found in reference 4.

3.2.3 Decoding the ELSSY Transverse Arrays.

The process of decoding the information from the Transverse Arrays (TAs) is somewhat different from that of the VDC, and comes closer to the method that was used to decode the HDCs. The TAs consist of 4 separate wire-chamber planes, each with its own delay line. The details of the construction are presented in section 2.4.5.

Similar to the VDC, the position and angle of the particle track are found by first decoding the wire number and drift distance for each plane. This information is extracted from the two TDC values. The wire that fired is identified by taking the time difference, and the drift time is extracted from the time sum.

Table 3.3 Offsets for the ELSSY TAs

TA plane	Z position	Y offset
TA 1	11.7 cm	-1.524 cm
TA 2	13.6 cm	0.0 cm
TA 3	35.5 cm	-0.762 cm
TA 4	37.4 cm	0.762 cm
Overall Offset		-1.6482 cm

The response of a TDC depends on an offset, which is the time difference between a start and a stop signal that produces a zero output, and a slope, which determines the number of channels per nano-second. When the two TDCs on a delay line have a different response, the time difference will have a dependence on the drift time. This causes a broadening of the peaks in the time difference spectrum, making wire identification more difficult. This effect is much larger in the TAs than in the VDC, because the drift distance, and thus the drift time, is much larger. It is thus important to correct for the variations of the TDC response, which was done by calibrating the TDCs with a test setup.

Each wire plane in a Transfer Array is offset by half a wire spacing with respect to the other plane in that TA, and the two sets of planes are offset by one quarter wire spacing with respect to each other. The offsets that were used are presented in table 3.3. To use these offsets, the fourth wire must be located at the center of the spectrum. This is done by adjusting the zeroth order term in the delay line correction polynomial (see the case for the VDC in section 3.2.2.a.)

The drift time is converted to a drift distance with the use of a drift time to distance conversion table, which is generated using the program ***DRT***[5]. In this method the table is constructed purely empirically. This is done by uniformly illuminating the chambers, and collecting data in a drift time histogram. The table can now be constructed by inverting the drift time histogram, with the assumption that the resulting drift distance histogram is perfectly flat, and has a maximum drift distance of 15.24 mm, which is half the wire spacing for the signal wires. These assumptions only hold when certain cuts are applied to the data, which assure that they are free of random and

---

[5] Los Alamos Meson Physics Facility, MP10 group. DRT is part of the Q system.

corrupted events (see below). Figure 3.7 shows a typical TDC difference spectrum, the associated truncated wire position spectrum, and drift time and distance spectra.

Unlike the HDCs, the TAs have no built-in system to determine whether a particle passes on the left or right hand side of a wire. This information can only be found by using the other planes. Unfortunately there were many events where one of the TA planes either failed to fire properly, or had a wire mis-identification. This is most likely caused by the high noise and the poor quality of the signal from the delay line amplifiers (there was some *ringing* on the delay lines.)

To make sure that the data from the TAs were valid, the following cuts were made:

1. Both planes of the TA fired.
2. The two wires that fired in the two planes of a TA were adjacent.
3. The drift distances of the two wires add up to approximately 1/2 a wire spacing.

The first cut is needed because the information of one single TA plane can not be disentangled due to the "left-right ambiguity". The second and third cuts are important to reject accidental events in one of the two planes, which can be caused by multiple particles crossing the TA or by noise on the delay lines or in the delay line electronics.

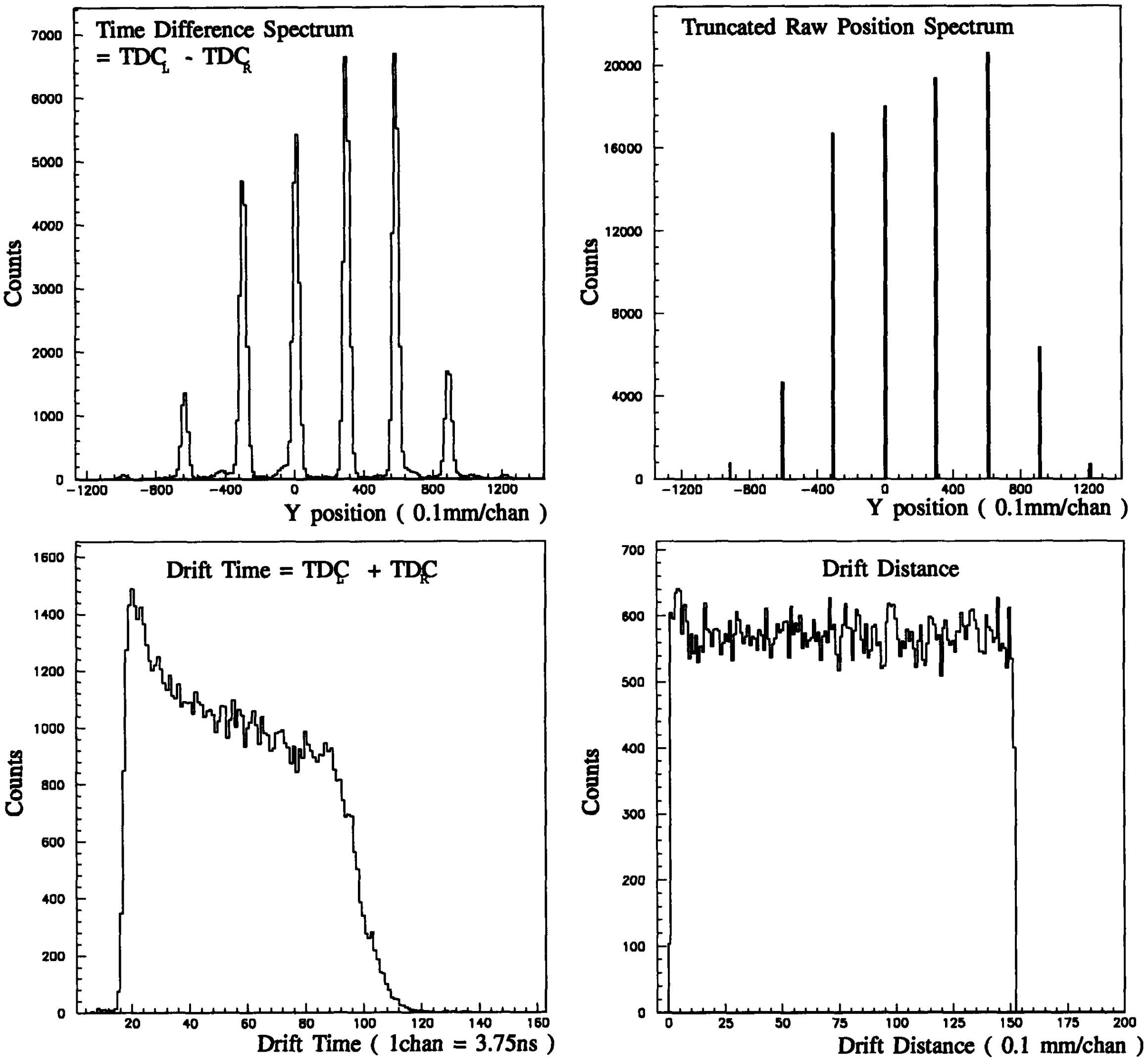

Figure 3.7 Typical spectra for the ELSSY TA. The top left hand histogram is a TDC time difference histogram with the polynomial corrections applied. The top right hand histogram is the same data after the truncation, clearly showing the location of the wires for the events. The bottom left histogram is a TDC time sum histogram (drift time.) The bottom histogram on the right hand side is the same data after the drift time to distance conversion.

The analysis of the TAs is much simplified by the assumption that all particles cross the detector almost perpendicular to the plane. This is true for all real events, since the matrix elements $\langle\theta_t|\phi_f\rangle$ and $\langle\phi_t|\phi_f\rangle$ are identically zero. This was checked by fitting a line for all possible left-right assignments, and then selecting the line with the best fit. This best fit method gave similar results but was less reliable and used more computer time. Using the simplification the complications and ambiguities involved with fitting for all possible left-right assignments are avoided, and a left-right decision can be assigned based on the information from only two adjacent planes.

The position spectra for the TAs are constructed by combining the drift distances with the wire number information. When looking at a wire, if the wire in the other plane of the set is to the left, the drift distance is subtracted. If it is to the right, the drift distance is added. The same is done for all 4 planes, resulting in 4 position spectra.

Next a straight line is fitted to the 4 positions. (If only one TA had valid data, then the two positions are averaged to get y_f, and ϕ_f is chosen to be zero). y_f is found from eq. 3.18:

$$y_f = \frac{\sum_i Z_i^2 \cdot \sum_i Y_i - \sum_i Z_i \cdot \sum_i (Y_i \cdot Z_i)}{4 \cdot \sum_i (Z_i^2) - \left(\sum_i Z_i \right)^2} \tag{3.18}$$

and ϕ_f from eq. 3.19:

$$\phi_f = \frac{4 \cdot \sum_i (Y_i \cdot Z_i) - \sum_i Z_i \cdot \sum_i Y_i}{4 \cdot \sum_i (Z_i^2) - \left(\sum_i Z_i \right)^2} \tag{3.19}$$

where the Ys are the positions in the TA planes, and the Zs are the location of the TA plane relative to the focal plane (Z is the same as in transport coordinates).

To determine the position and angle accurately, a correction is made for the slope of the TAs with respect to the Z-vector of the particle track (see figure 2.4 for the coordinate definitions). This correction depends on θ_f (which determines the angle of the track), which was found from the VDC information. The easiest method for making this correction is to correct the z-position of each plane. The z-correction is then:

$$Z_i^{corrected} = \frac{Z_i \cos(\theta_f)}{\cos(45° + \theta_f)} \tag{3.20}$$

Using these corrected Zs in equation 3.18 and 3.19 the correct y_f and ϕ_f are found.

3.2.4 The ELSSY Trigger and Particle Identification.

The ELSSY trigger consists of the logical ***and*** of the two scintillators combined with the logical ***or*** of the Cherenkov and the lead-glass blocks (see section 2.4.3 for details.) The two scintillator TDC signals are combined with a mean-timer module in hardware. This corrects for the fluctuation in the trigger time that is caused by the difference in the path length of the light when the particle hits the scintillator at opposite ends (see section 3.2.6.a for a description on how this correction is made in OOPS.) There was no need to apply any additional timing corrections.

The *geometric mean* (the square root of the product) of the two ADC signals from the scintillators was calculated in software. This quantity gives a measure of the total amount of energy that the particle deposited in the scintillators and can be used to identify various particle types. The output from the three Cerenkov ADCs was summed and compared with the Cerenkov hardware sum signal. The two signals were found to be very similar and the latter was used for particle identification.

3.2.4.a Pion rejection by the Cherenkov.

The Cerenkov signal can be used to separate the π^- events from the e^- events (see section 2.4.3). Since the trigger was the logical ***or*** of the lead glass blocks and the Cerenkov, some pions can enter the data stream because they produce a trigger in the lead glass blocks. The pions would show up as a zero peak on a histogram of the Cerenkov signal (see figure 3.8). For this data only a very small number of counts can be seen which could have been caused by pions. This is expected because β for the pions is small, and thus the signal in the lead glass blocks is expected to be small. This is also expected from purely kinematical reasoning, which shows that the phase space for the reaction:

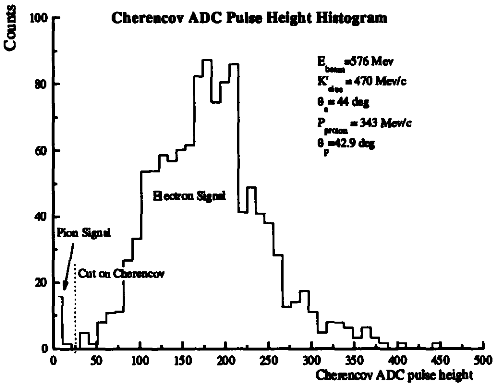

Figure 3.8 Histogram of the Cherenkov signal with the pion peak and the placement of the cut indicated.

$$e^- + {}^{12}C \rightarrow e^- + \pi^- + p^+ + {}^{11}C \qquad \textbf{(3.21)}$$

is extremely small. (For this reaction the outgoing pion is detected instead of the outgoing electron.) This means that the constraints on the reaction are that the outgoing pion has a momentum larger than *454 MeV/c* (the minimum momentum detected by ELSSY) and that the outgoing proton has a momentum of *309 MeV/c* the minimum detected proton momentum in this experiment. The energy balancing equation for this reaction gives:

$$E_{beam} - k_e' = T_\pi + M_\pi + T_p + M_p + T_{recoil} - \left(M_{^{12}C} - M_{^{11}C}\right) \tag{3.22}$$

where $E_{beam} = 576MeV$, $M_\pi = 140MeV/c^2$, $M_p = 938\,MeV/c^2$, $M_{^{12}C} - M_{^{11}C} = 921\,MeV/c^2$, and from the constraints, $T_\pi \geq 335MeV$ and $T_p \geq 50MeV$. This means that there is only *34 MeV* available to be shared between the outgoing electron and the recoiling nucleus in the worst case. The phase space for this is very small, which helps to explain that less than 20 events were seen that could possibly be a pion event. These events are eliminated by a cut on the Cerenkov ADC in the C analyzer.

3.2.5 ELSSY Particle Tracking.

Once the coordinates of the particle track at the focal plane are known, the track can be traced back to the target coordinates. The is done with the matrix elements that were found with a sieve slit run (see section 2.4.1 and appendix A.) The calculation is a simple multiplication of the focal plane coordinates with the relevant matrix elements.

The target coordinates that are calculated in this manner are not always within the physical boundaries, and so cuts were placed on the target variables θ_f and ϕ_f to ensure that the target coordinates are physical. The events that were cut in this manner were valid data that had either undergone multiple scattering in one of the windows or were not decoded properly in one of the detectors. About 3% of the events were rejected in this manner. This loss was corrected with an efficiency factor (see section 4.2.2).

3.2.6 The OOPS Scintillators and Particle Identification.

The OOPS spectrometer is equipped with a set of three plastic scintillators (for details on the construction of the scintillators see section 2.5.3.) The scintillators provide the trigger for the spectrometer, and also provide a means for particle identification.

The scintillator ADC signal can provide information on the particle that is detected, because the energy loss (dE/dx) in the scintillator, which is given by the Bethe-Bloch formula[6], depends on the velocity of the particle as $1/\beta^2$. Since the different particles that reach the focal plane of the spectrometer have the same momentum but different masses, their velocities are different and they will create a different pulse height in a scintillator. This is illustrated in figure 2.16 of the previous chapter.

To get the best measure of the energy loss in the scintillators, the *geometric mean* of the two ADC values for each scintillator is used. These values are histogrammed in pairs on contour histograms, and a cut is placed on the proton region on each of these histograms (see figure 3.9). The histograms on the left hand side, for single arm proton data, show that three types of particles are detected: pions (π^+), protons and deuterons. The histograms on the right hand side were cut only on the condition for true coincidence (with the accedentals subtracted), and show that there are only protons in the coincidence data. The proton cut was still applied for the analysis of the coincidence data analysis, because it improves the signal to noise ratio of the Time-Of-Flight.

The separation of the protons from the other particles by means of this cut on the scintillators is very good. However, it is not the only means by which the pions and deuterons are eliminated. From an energy argument similar to that of section 3.2.4.a it can be seen that the coincidence data should not contain any pions, since $\omega \leq 120 MeV$ is not sufficient to produce them. The deuterons are eliminated by the cut on the Time-Of-Flight (TOF), since the deuterons are sufficiently slower than the protons. The histogram of figure 3.10 shows that the peaks in the scintillator data, which correspond to pions and deuterons, are absent for coincidence events. Note that for this histogram the cut on the scintillators was turned off.

---

[6] see Leo, *Techniques for Nuclear and Particle Physics Experiments*, Springer-Verlag (1987) or *Particle Physics Booklet*, Particle Data Group, Phys Rev **D50**, 1173

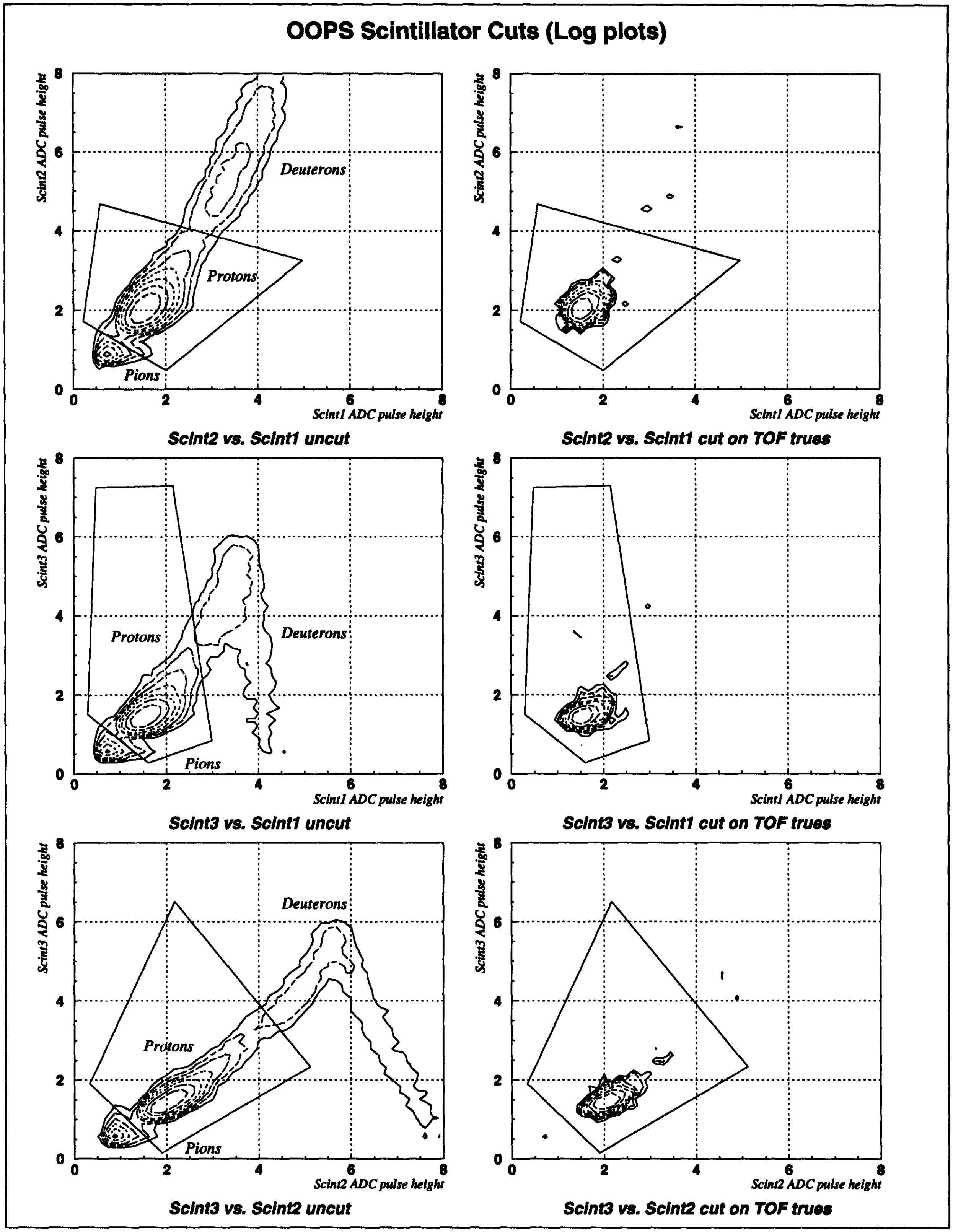

OOPS Scintillator Cuts (Log plots)

Scint2 vs. Scint1 uncut

Scint2 vs. Scint1 cut on TOF trues

Scint3 vs. Scint1 uncut

Scint3 vs. Scint1 cut on TOF trues

Scint3 vs. Scint2 uncut

Scint3 vs. Scint2 cut on TOF trues

Figure 3.9 Contour histograms for the OOPS scintillators, with the proton particle identification cuts drawn. The z-axis is logarithmic. The three plots on the left hand side are single arm proton data, the three plots on the right hand side are coincidence data cut on the trues peak of the TOF signal with accidentals subtracted. As expected, the coincidence data contain only protons. (The points outside the proton peak are single counts and reflect the uncertainty in trues - accidentals subtraction.)

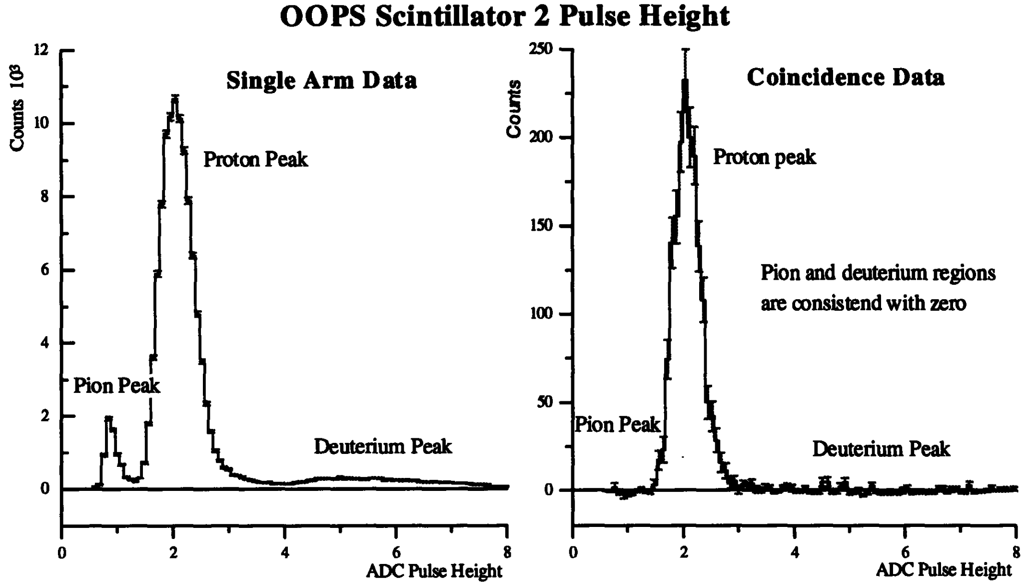

Figure 3.10 Histogram of the second OOPS scintillator, showing the absence of pions and deuterons in the coincidence data. The coincidence data were cut on only the time of flight peak, with accidentals subtracted, and not on any particle identification cuts.

3.2.6.a Scintillator Timing corrections.

The timing for the OOPS trigger was determined by one of the photomultiplier tubes (PMT) on the second scintillator (see section 2.5.4.) Since there were no mean-time modules on the OOPS scintillators, the timing of the trigger depended on the distance the light had to travel to reach this PMT. This trigger signal formed the start for all the OOPS TDC modules, and thus all the OOPS TDC values fluctuated with the location of the particle track in the second scintillator. The only exception to this is the TDC of the PMT that determined the timing of the trigger, denoted with OS2L (for the OOPS Scintillator 2 on the left hand side,) which formed a narrow spike on the histogram, since the same signal determined both the start and the stop for the TDC, see figure 3.11.

This fluctuation is corrected by taking a mean-time in software. The mean-time is simply the sum of the two TDC values divided by two, with an offset added to center the peak at zero:

$$Meantime_i = \left(TDC_i^L + TDC_i^R\right)/2 + OFFSET_i \tag{3.23}$$

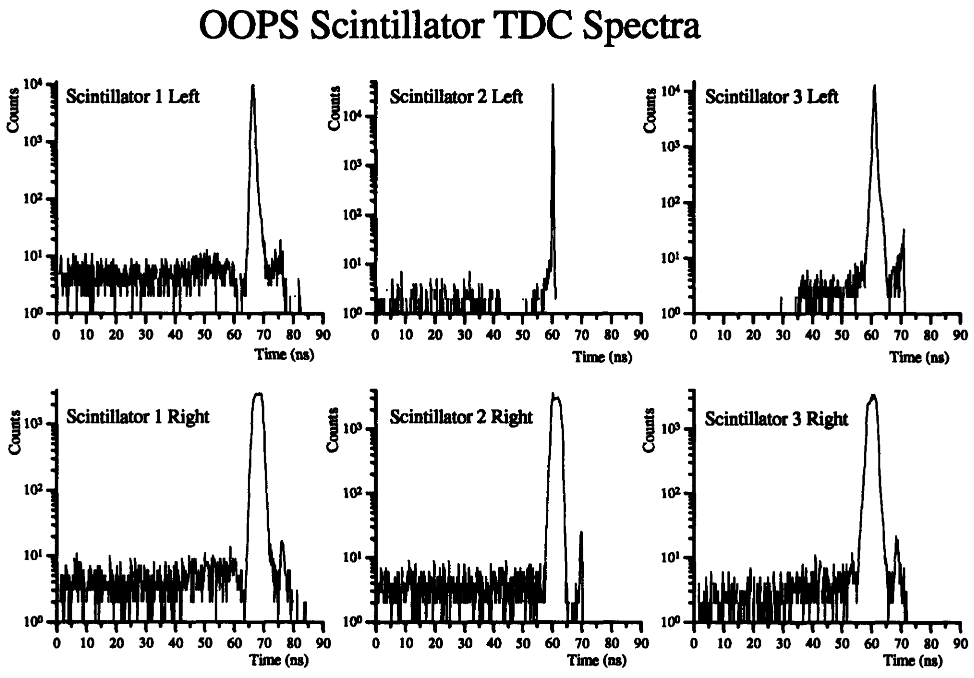

Figure 3.11 OOPS Scintillators TDC Spectra, "Left" refers to small Y and "Right" refers to large Y. Notice that *Scintillator 2 Left* was a self stop, hence the narrow spike. The events before and after the peak are caused by various randoms in the PMT. The events before the peak are caused by an earlier random on the same PMT, causing the TDC to stop on the random rather than the actual particle. The events after the peak are caused by such an early random on *Scintillator 2 Left* causing the start signal to come early. When this occurs it is possible that an other PMT determines the timing.

where the index runs over the 3 scintillators. The histograms for this quantity are plotted in figure 3.12.

It still needs to be determined which of these mean-time values makes an accurate correction to the TDCs. For most events the timing for each TDC falls in the peak of the TDC spectra, and each of the mean-time corrections of equation 3.23 will work equally well. However, for those events that had a random signal (a signal that is not caused by the particle that caused the trigger) interfere on one of the TDCs, a meantime correction must be chosen from a scintillator that did not have such a random on it. The easiest way to do this is to plot the difference of the meantime values. This difference should peak at zero for the ideal case in which all scintillators fired properly. A cut on this difference determined whether the meantime value was valid for those two scintillators. Figure 3.13 shows the histograms of this meantime difference.

Once the correct meantime value is picked, the correction to the TDC is given by the equation:

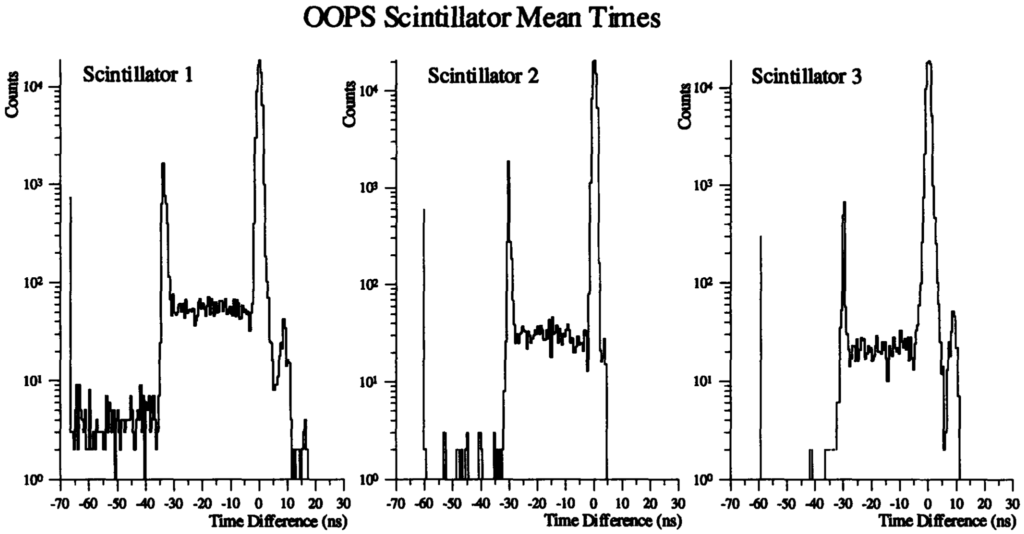

Figure 3.12 OOPS Scintillator Meantimes, the complicated structure of these plots comes from the details of the TDC spectra presented in figure 3.11.

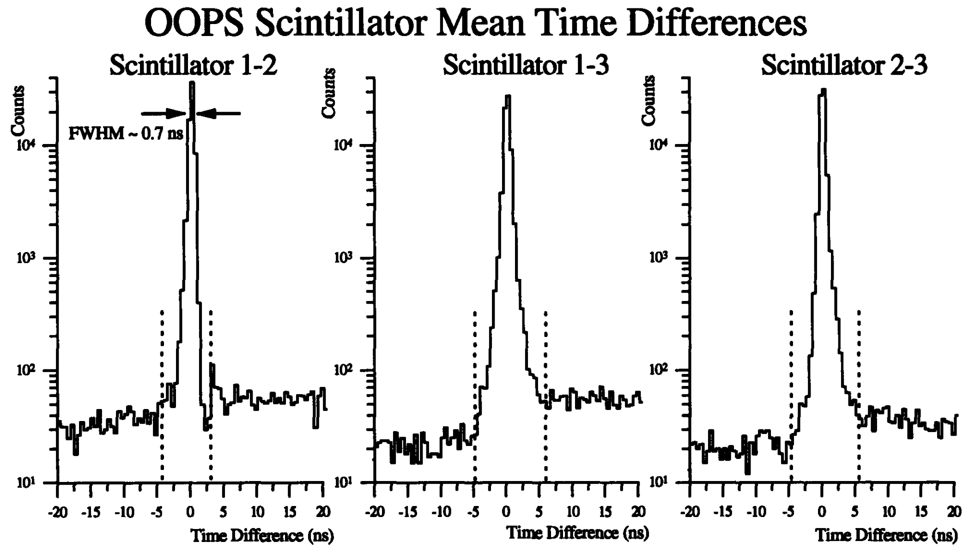

Figure 3.13 OOPS Scintillator Meantime Differences. The values plotted are the difference of the meantime values (see figure 3.12.) Also indicated on each plot is the cut that determined whether the meantimes involved were useful.

$$TDC_i^{corr} = TDC_i^{uncorr} + Meantime \tag{3.24}$$

These corrected TDC values can then be used to calculate the drift times for the wire chambers. The meantime correction is also applied to the Time Of Flight histogram.

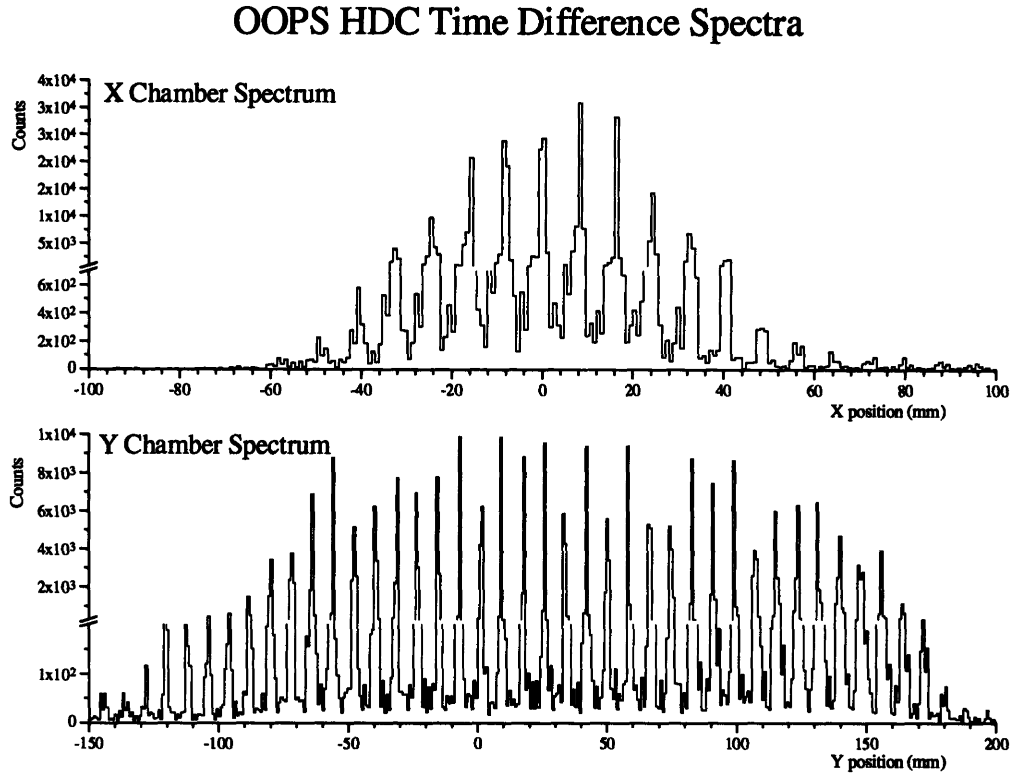

Figure 3.14 OOPS HDCs TDC Difference Spectra. Note the axis break which accentuates the channels with a small number of counts. Data with poor signal discrimination or random events can fill up the regions between the peaks. The ability to distinguish between peaks was greatly influenced by the chamber operating voltage and gas mixture.

3.2.7 The OOPS HDCs.

The OOPS detector package contains three Horizontal Drift Chambers (HDCs) to determine the location and angle of the particle track in the focal plane of the spectrometer. The details of the construction of the HDCs can be found in section 2.5.2. The analysis of the information from the HDC is only slightly different from that of a Transverse Array. The main differences are that the drift cells are smaller and that a special setup allows the determination whether the particle passed on the left or the right side of the wire.

The wire number is extracted from the TDC values in the same manner as described in section 3.2.2.a, by taking the difference of the left and right side (see figure 3.14.) For the OOPS HDCs this does not give as clear a spectrum as for the TAs because the delay line segments have a smaller time difference between two neighboring wires. The ability to distinguish wires was greatly influenced by the chamber

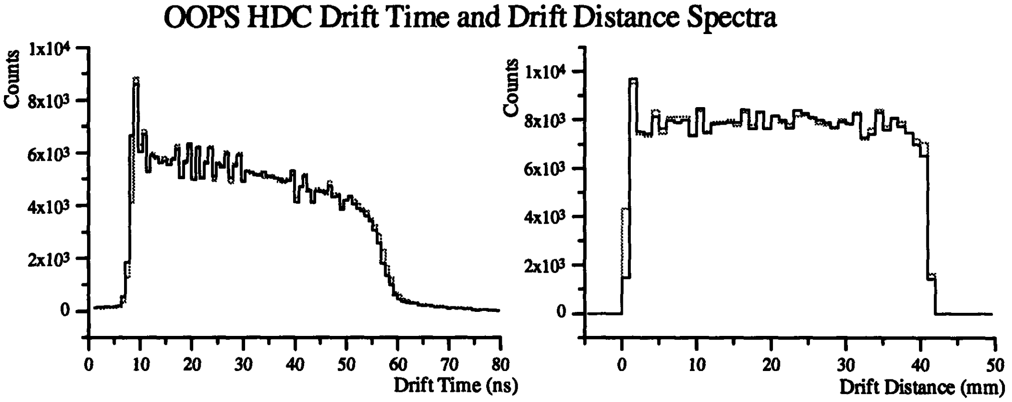

Figure 3.15 OOPS HDC Drift Time and Distance Spectra. Two sets of data are plotted on each plot, showing how closely different planes matched up, allowing the same table to be used for all six wire chamber planes.

operating voltage and the gas mixture. It was also improved by fine tuning the discriminators.

The drift time was calculated by taking the sum of the two TDC values, corrected with the meantime. The drift time is then converted to a drift distance with the ***DRT*** program, using a maximum drift distance of 4.064 mm, half the wire spacing of the signal wires. The drift time histograms are lined up so that the same lookup table can be used for all three chambers (six planes.) Two of these histograms are presented in figure 3.15.

3.2.7.a Left-Right decisions for the HDC.

One of the special features of the OOPS HDCs is the ability to distinguish whether the particle passed on the right- or on the left-hand side of the wire. This greatly simplifies the calculation of the position and angle in the chambers, and makes this calculation more reliable. The details of the electronics which are involved in this can be found in section 2.5.2. In this experiment, each Odd-Even signal was read with two different types of ADCs: common gated ADCs and individually gated ADCs. The individually gated ADCs gave better results, and they were used in the data analysis.

A spectrum of one of the Odd-Even signals is presented in figure 3.16. It was found that the "zero peak" on the spectrum represents an inefficiency of the Odd-Even amplifiers that is caused by the slow response time of the amplifier to a second particle hitting the delay line. It resulted in the absence of the Odd+Even signal and a zero reading in the ADC. Events like that were the largest cause of chamber inefficiency (up to 3.5% inefficient for a single plane).

The position spectrum for each chamber plane is constructed by adding or subtracting the drift distance to the position of the wire that fired. The decision whether to add or subtract the drift distance is made using the gate on the Odd-Even spectrum. When the wire number of the wire that fired is odd (even), and the gate on the Odd-Even spectrum indicated that it was on the odd (even) side of the wire, the two are added, otherwise they are subtracted. The assignment of odd and even is rather difficult to establish directly from the hardware, since it requires very accurate knowledge of exactly which wire is which. The correct assignment is more easily accomplished experimentally, by examining the histograms of the resulting chamber positions, and plotting these positions against each other on two dimensional histograms[7]. The result can be checked in a histogram of the difference between the position in the chamber and the expected position in the chamber calculated from the other two chambers, see figure 3.17. In this histogram an erroneous left-right decisions will show up in side peaks. When the assignment of odd and even is incorrect, two large peaks appear in this histogram, instead of one central one.

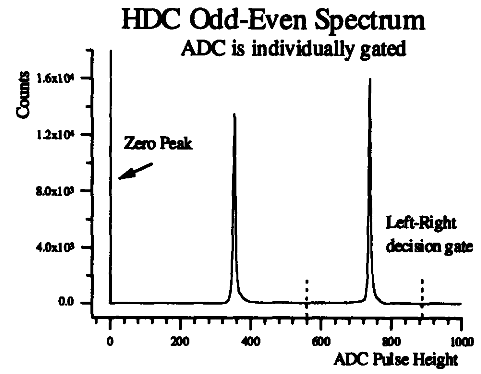

Figure 3.16 Odd-Even signal from an individually gated ADC. The gate position for the left-right decision is indicated.

3.2.7.b Calculation of the coordinates.

Once the position of the particle track is known for each of the three chambers, the location and angle of this track is calculated by making a straight line fit to the three positions in the spectrometer. For this to work properly, however, the chambers need to be perfectly aligned, both in the x and y directions and with respect to the rotation around the central-ray axis. This is clearly not possible in hardware, so the alignment is done in

---

[7] See David A. Toback, B. S. Thesis (unpublished)

Table 3.4 Offsets for the OOPS HDCs.

Chamber	X-Offset	Y-offset	Z-offset	Rotation
1	0.186 cm	-2.717 cm	0 cm	0.49°
2	0.405 cm	-2.450 cm	12.7 cm	0.64°
3	0.242 cm	-2.809 cm	25.4 cm	0.49°

These are the offsets used for this experiment; they are presented as an example only. Note that these offsets changed every time the detector package was taken out and parts replaced. The Z-offsets represent the actual distance between the chambers, and were measured with a ruler. All the other offsets and the rotations were found experimentally with a sieve slit run.

software by adding experimentally determined offsets to the positions of the chamber, and rotating the center chamber x and y coordinates.

The offsets are found by plotting the distance of the fitted track to the positions found in the chambers. This "difference plot" should be a Gaussian peak which is centered at zero, and with a width that is directly related to the chamber resolution and the multiple scattering in the chambers (see figure 3.17.) This histogram can also be used to make a cut on the resolution, attaining a better resolution in exchange for a lower efficiency. If the peak is not at zero, the chambers are not in a straight line, and if the peak position depends on the position in the chamber, there is a rotation of one of the chambers with respect to the other two. This information was used to find the correct offsets and rotations of the chambers. These corrections are relative. The absolute position of the detector package can only be accurately determined by taking data with a sieve slit, and centering the center hole. The offsets that were used are given in table 3.4.

To increase the efficiency of the overall detection of particles by the detector package, for events where only two of the planes in X or Y had valid information were also allowed. When only two planes are valid, the position and angle can be calculated from a straight line through the two points. This gives a slightly lower resolution, and the resolution cut that was possible with the three point fit is no longer possible.

3.2.8 OOPS Particle Tracking

The calculation of the target coordinates from the coordinates at the detector package is similar to the method used for ELSSY. One of the differences is that for OOPS the focal plane does not coincide with any of the detector planes. Rather it is at a 12.7° angle with respect to the central ray. This results in some of the second and third

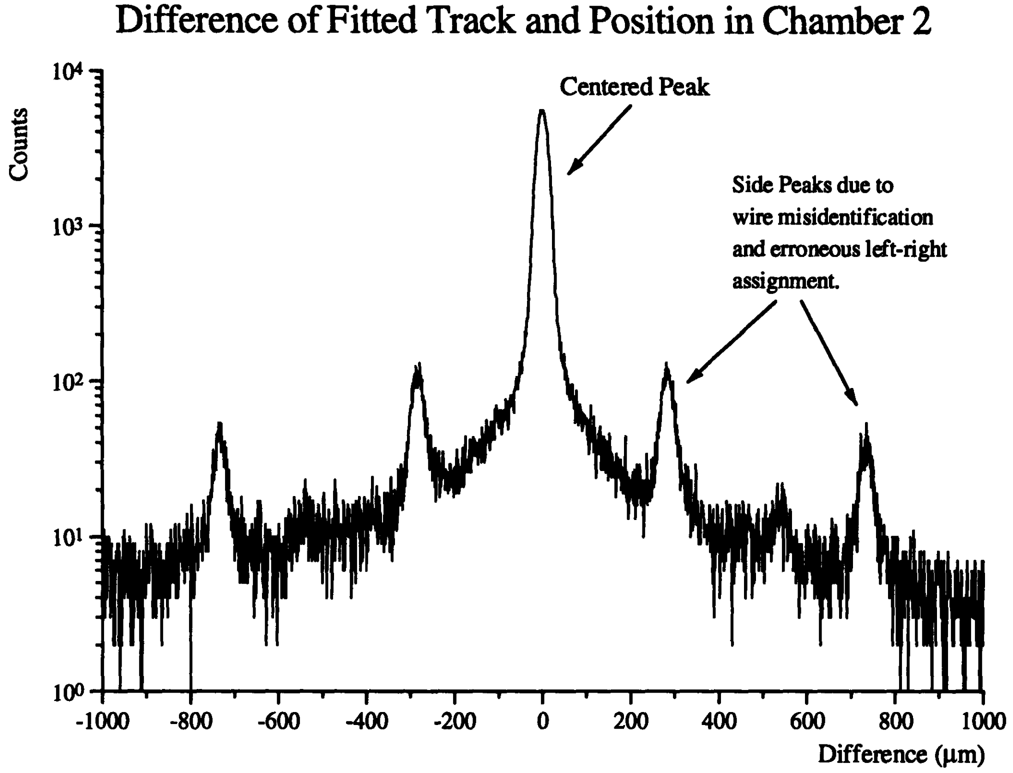

Figure 3.17 Histogram of a Difference Plot. Note that the y-scale is logarithmic. The central peak is centered to obtain correct chamber alignment in software. The width of this peak reflects the intrinsic resolution of the chambers and multiple scattering in the chambers. The tails on the central peak can be explained from multiple scattering in one of the chambers. The side peaks are caused by an error in the left-right assignment, or a wire mis-identification.

order matrix elements being important in the reconstruction of the target coordinates of the particle track, and it means that accurate matrix elements are needed for reasonable reconstruction of the target coordinates.

The matrix elements were determined by a set of a sieve-slit experiments[8]. An angular resolution of 1 mr, and a momentum resolution of better than 0.5 % was achieved. A histogram of a sieve-slit image is presented in figure 3.18.

---

[8] J. B. Mandeville *et al.*, Internal Report, University of Illinois at Urbana-Champaign (unpublished)

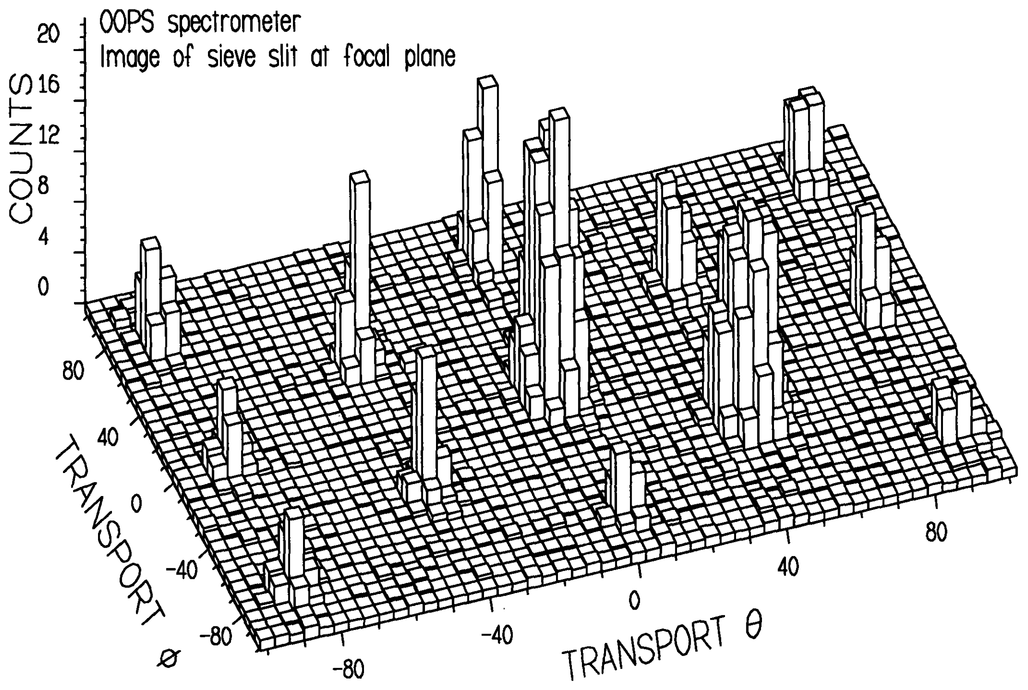

Figure 3.18 Image of a Sieve Slit at the OOPS Focal Plane. This data is for a 26 mg/cm^2 ^{12}C elastic peak.

3.3 The C Analyzer

The second stage of the analysis was done in the *UNIX* environment with an analyzer that was written in the C programming language and which interfaces with the Physics Analysis Workstation (*PAW*) program from *CERN*. The main reasons for doing this were the increased CPU power of the workstations, more available disk space, and the advantages of C and *PAW*, which overcome some of the limitations of FORTRAN77[9] and Q.

The C analyzer calculates all the physics quantities, such as the missing energy and the missing momentum, and calculates the data for the *reals* and *accidentals* histograms. It also takes some of the detector inefficiencies into account and folds the spectrometer acceptance profiles in with the data. The output of the C analyzer is a set of histograms, and if requested, an n-tuple file, that can be read into *PAW* for further processing and viewing.

---

[9] FORTRAN '90 overcomes many of the limitations of FORTRAN77, but it was not available yet.

Table 3.5 Input File Format for the C analyzer.

Number	Data Item	Description
1	Event Number	A sequential counter of events.
2	Data Flag	A flag of 20 bits containing test output
3-5	OS1S,OS2S,OS3S	Mean of OOPS Scintillator ADCs
6-11	OS1TL,......OS3TR	Timing from the OOPS Scintillator TDCs
12	meantime	Meantime value used in timing correction (OOPS)
13-16	X,θ,Y,φ	OOPS focal plane coordinates.
17-18	DiffX2, DiffY2	Wire chamber difference in chamber 2 (OOPS)
19	OOPS Delta	Momentum in OOPS in % of central value
20-22	θ,φ,Y	OOPS target coordinates
23	P OOPS	OOPS momentum
24-25	TOF	Time Of Flight TDC values
26-28	ES1,ES2,ESsum	ELSSY Scintillator ADC values and mean.
29-30	ES1T,ES2T	ELSSY Scintillator TDCs
31-32	CerSum	ELSSY Cherencov ADC sums
33	PBGSum	ELSSY LeadGlass sum
34-37	X, θ,Y, φ	ELSSY Focal Plane Coordinates
38	ELSSY Delta	Momentum in ELSSY in % of central value
39-40	θ,φ	ELSSY Target Coordinates
41	P ELSSY	ELSSY Momentum
42-43	DELTA abb., full	ELSSY full and abberatively corrected DELTA
44-45	BMP X,Y	X and Y Beam Position Monitors

3.3.1 Input file format.

The C-analyzer reads compressed and standard data files from disk in a binary format. As mentioned earlier, the VMS floating point values had to be converted to IEEE format before they could be used. This was done with a simple converter program. The input file consists of a header that contains the run number, the number of variables in the data set, and labels for these variables. Then follow the data records, which are read into the data arrays in binary mode. The contents of the input file is presented in table 3.5. The special variable, the *Data Flag,* is an integer number that has data bits set if certain tests were true in the Q analyzer. This allows information about the event, such as whether the event was coincidence or single arm, to be passed in a compact way.

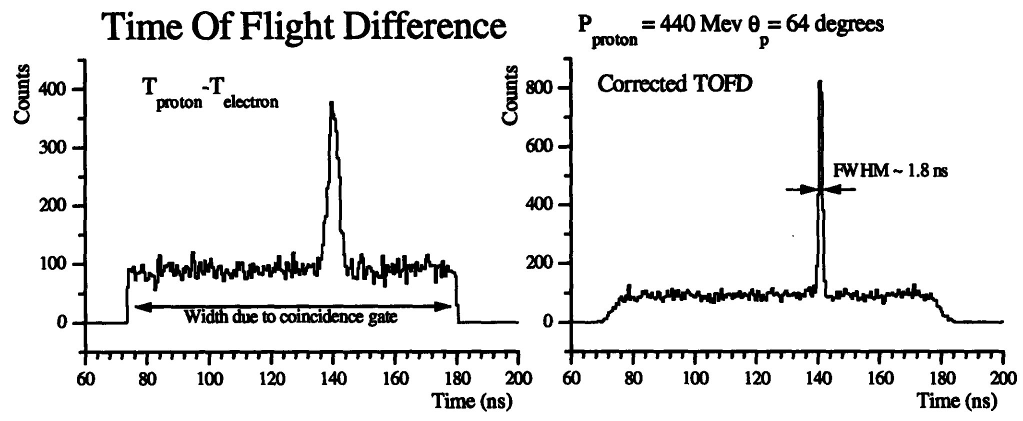

Figure 3.19 Time Of Flight Difference histogram for best signal to noise ratio.

3.3.2 Time Of Flight.

The Time Of Flight Difference (TOFD[10]) is the difference in time that the particle took to travel from the target to the focal plane of one spectrometer, relative to the time it took the other particle to travel from the target to the focal plane of the other spectrometer. The TOFD was measured by starting a TDC with the trigger of the proton spectrometer and stopping the TDC with the trigger of the electron spectrometer, but this might as well have been done the other way around.

The TOFD allows for the distinction between a coincidence trigger that comes from an actual coincidence event and a trigger that comes from a background event that in fact is caused by two simultaneous single arm events. Coincidence events come from the same instance at the target, thus a peak reflecting this narrow timing window is expected in the histogram of TOFD. For double singles events the timing is not correlated, and so a continuous flat background is expected, which extends for the duration of the coincidence timing gate of the AND circuit (see section 2.6.) The ratio of the TOFD peak to the background depends on the singles rates in the spectrometers, and thus on the beam current, and target thickness (luminosity). When this ratio is too small, it is difficult to distinguish the real coincidence events from the background, and the instantaneous (peak) beam current must be lowered or a thinner target must be used.

---

[10] This same quantity is frequently referred to as TOF, or time-of-flight, although strictly speaking it is a time difference.

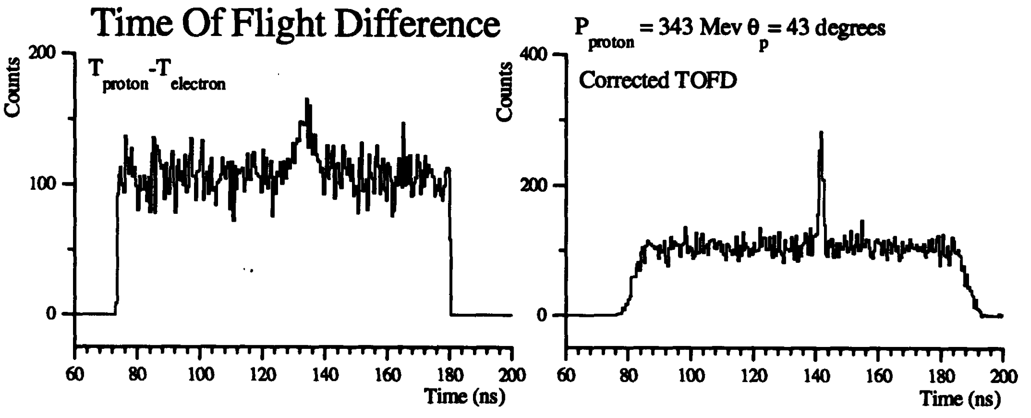

Figure 3.20 Time Of Flight Difference for the least favorable signal to noise ratio.

The TOFD spectrum can be improved by several corrections which narrow the peak, and thus improve the peak to background ratio. The corrections that were applied to create the *corrected TOFD* were:

- Correct for the difference in flight time for protons with different momenta.
- Correct for the differences in the length of the flight paths.
- Correct for timing variations in the OOPS scintillators.

Figure 3.19 and figure 3.20 show the TOFD and Corrected TOFD for the runs with the best and the worst peak to background ratio respectively.

3.3.3 Efficiency Corrections.

The C analyzer takes the wire chamber efficiency corrections, spectrometer acceptance profiles and computer dead-time corrections into account on an event by event basis. This was done to avoid the confusion in trying to unfold the spectrometer profiles from the final spectra, which becomes complicated for two dimensional histograms. The final cross section histograms are two dimensional, plotting cross section versus missing momentum and missing energy.

The spectrometer acceptance profiles were extracted from white spectra runs (see chapter 4), and the other efficiency corrections were passed on from the Q analyzer test package. They are folded in by weighting each event with the efficiency for that event, and keeping track of the errors for each bin in the histogram separately as the square of the weight. When all the events have been counted, the square root of the sum of the squared weights is taken. Using this method the output histograms are weighted properly and are normalized.

3.4 The Acceptance program

The acceptance program calculates the acceptance volume (phase space) for the experimental settings of the spectrometers. This is needed to calculate the cross section from the raw counts spectra. The form of the acceptance volume can be derived by starting with the equation for the cross section. From equation 1.35:

$$d^6\sigma = C_{kin}\sigma^{eN}S(\vec{p}_m, E_m)dE_f dE_m d\Omega_e d\Omega_p \tag{3.25}$$

In the experimental case, however, the data are acquired in a two dimensional array (two dimensional histogram) $N(E_m, P_m)$ with a finite bin size. This means that the best result that can be obtained is calculating the average cross section for all elements $dE_f dE_m d\Omega_e d\Omega_p$ that contribute to the bin $\mathscr{B}$. N is given by:

$$\begin{aligned} N(E_m, P_m)_{\mathscr{B}} &= \int_{\mathscr{B}} \left(\frac{d^6\sigma}{dE_f dE_m d\Omega_e d\Omega_p} \right) \varepsilon_A dE_f dE_m d\Omega_e d\Omega_p \\ &= \left\langle \frac{d^6\sigma}{dE_f dE_m d\Omega_e d\Omega_p} \right\rangle_{\mathscr{B}} \int_{\mathscr{B}} \varepsilon_A dE_f dE_m d\Omega_e d\Omega_p \end{aligned} \tag{3.26}$$

where ε_A is the six dimensional detector efficiency function for measuring bin $\mathscr{B}$, and the integration is over the acceptance of the spectrometers. The experimental cross section is found from:

$$\left\langle \frac{d^6\sigma}{dE_f dE_m d\Omega_e d\Omega_p} \right\rangle_{\mathscr{B}} = \frac{N(E_m, P_m)}{V(E_m, P_m)} \tag{3.27}$$

where the acceptance volume is defined by:

$$V(E_m, P_m)_{\mathrm{B}} = \int_{\mathscr{B}} \varepsilon_A dE_f dE_m d\Omega_e d\Omega_p \tag{3.28}$$

This cross section approaches the theoretical cross section only if the latter does not vary appreciably over the volume $V(E_m, P_m)$ of bin $\mathscr{B}$.

The calculation of this volume is rather complicated due to the nature of the integration region, which is defined by the spectrometer properties. Thus it requires a Monte Carlo approach. This is be done by sampling the appropriate random distribution for each of the six variables and then testing whether this sample satisfies all the acceptance requirements. It is much more efficient, however, to calculate a slightly different volume:

$$V'(E_m, P_m) = \int_{\mathscr{B}} \varepsilon_A dE_f dT_p d\Omega_e d\Omega_p . \tag{3.29}$$

This has the advantage that the limits of the integration are well defined so that no samples need to be rejected, and the shape of the distributions is flat. However, if this volume is used instead of the one defined by equation 3.28, the cross section is differential in $dE_f dT_p d\Omega_e d\Omega_p$ instead of differential in $dE_f dE_m d\Omega_e d\Omega_p$. The conversion from one to the other is done with a Jacobian[11]. Starting with the definition of a Jacobian, and using the definition for the missing energy (equation 1.7), this takes the form:

$$\begin{aligned} J &= \left|\frac{\partial E_m}{\partial T_p}\right| = \left|\frac{\partial E_m}{\partial p_p}\left[\frac{\partial T_p}{\partial p_p}\right]^{-1}\right| = \\ &= \left|-1 + \frac{E_p}{E_{rec}}\left(\frac{\vec{p}_p \cdot \vec{P}_m}{p_p^2}\right)\right| \\ &= \left|-1 - \left(\frac{T_p + M_p}{T_{rec} + M_{rec}}\right)\left(1 - \frac{q}{p_p}\cos(\theta_{pq})\right)\right| \end{aligned} \tag{3.30}$$

This Jacobian is close to 1 for the kinematics of this experiment. Similarly the cross section differential in $dP_m dE_m d\Omega_e d\Omega_p$ can be calculated by using the Jacobian:

$$J' = \begin{vmatrix} \frac{\partial E_m}{\partial E_f} & \frac{\partial P_m}{\partial E_f} \\ \frac{\partial E_m}{\partial T_p} & \frac{\partial P_m}{\partial T_p} \end{vmatrix} = \left|\frac{p_p}{E_p}\frac{\vec{k}' \cdot \vec{P}_m}{k' P_m} - \frac{\vec{p}_p \cdot \vec{P}_m}{p_p P_m}\right| \tag{3.31}$$

---

[11] Sylvester, *Camb. & Dubl. Math Journal*, (1852)

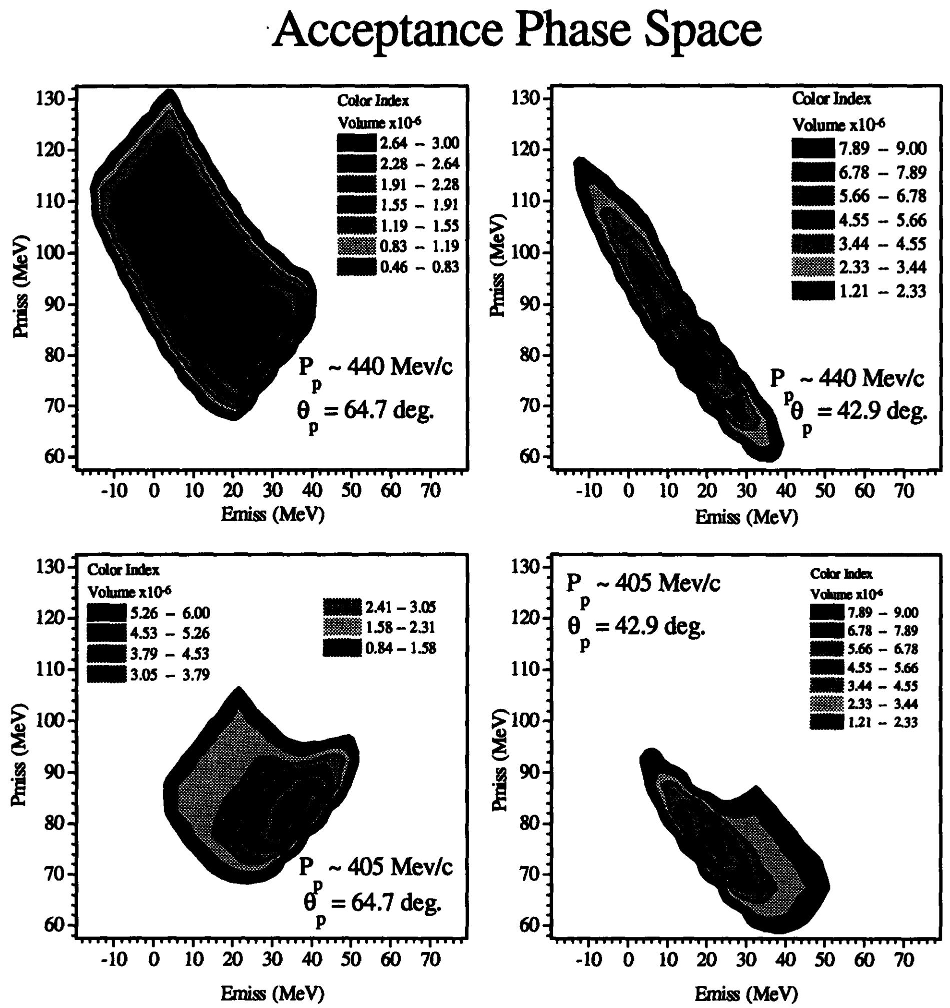

Figure 3.21 Phase Space Histograms calculated by the Acceptance program. Each histogram represents a specific run with specific settings of the spectrometers. The labels P_p and θ_p are the central momentum and angle of the proton spectrometer, the settings for the electron spectrometer were constant at $E_{beam}=576\,MeV$, $P_e \sim 470\,MeV$ and $\theta_e = 44°$.

This Jacobian varies between 8 and 14 for the kinematics of this experiment. These Jacobians are calculated at the same time as the volume for each bin $\mathcal{B}$. Alternatively they can be evaluated separately and stored in a two dimensional (E_m, P_m) histogram.

The actual calculation of the volume V' is performed by taking N_{itt} random samples of E_f, θ_e, φ_e, T_p, θ_p and φ_p. From these variables the missing energy and the missing momentum are calculated, and these quantities are used to make a histogram of the number of events that fall within a bin (Em, Pm). This counts histogram is then normalized with a factor:

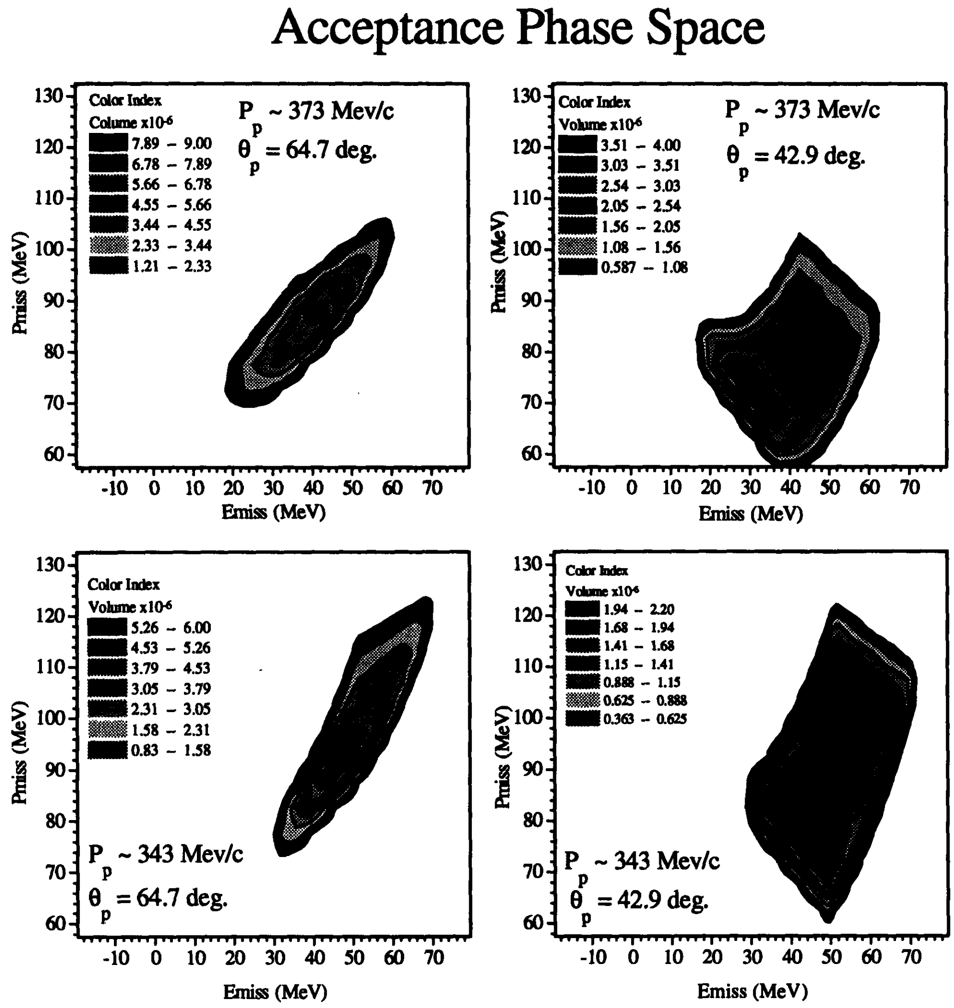

Figure 3.22 Phase Space Histograms calculated by the Acceptance program. Each histogram represents a specific run with specific settings of the spectrometers. The labels P_p and θ_p are the central momentum and angle of the proton spectrometer, the settings for the electron spectrometer were constant at $E_{beam}=576\,MeV$, $P_e \sim 470\,MeV$ and $\theta_e = 44°$.

$$n = \frac{\Delta k' \, \Delta\Omega_e \Delta T_p \Delta\Omega_p}{N_{itt} \Delta E_m \Delta P_m} \tag{3.32}$$

where $\Delta k'$, $\Delta\Omega_e$, ΔT_p and $\Delta\Omega_p$ are the acceptances in momenta (energies) and solid angles for the electron and the proton spectrometers. The resulting histogram contains the acceptance volume. The factor $\Delta E_m \Delta P_m$ is the area of a bin so that this result is independent of the binning of the histogram.

For this data, eight different acceptance histograms were needed for the eight different settings, four momentum settings at two angles. The histograms for the phase space calculation of the individual runs are presented in figures 3.21 and 3.22.

3.5 The Addcross program

Once all the individual runs are analyzed and the data is sorted in histograms, these histograms can be added to obtain the final results. For this the program ***Addcross***[12] was written, which will also make projections onto the missing momentum and missing energy axes.

First the background of accidental coincidence events is subtracted from the data. This process is illustrated in figure 3.23. In the C analyzer, the *Real* events are identified by a gate on the timing peak in the corrected Time Of Flight Difference spectrum. This gate has a width W_R. Similarly, two regions on this spectrum are identified for *accidental* events, with widths W_{A1} and W_{A2}. During the analysis all the events from the *Reals* region are collected into one set of histograms, and all the events from the *accidentals* region are collected into another set of histograms.

The events that go into the *accidentals* histograms are scaled on an event by event basis by the ratio of the two regions:

$$Weight_A = \frac{W_R}{(W_{A1} + W_{A2})} \tag{3.33}$$

These two sets of histograms are passed from the analyzer to the ***Addcross*** program, where the *accidentals* histograms are subtracted from the *reals* histograms to obtain the *trues* histograms.

---

[12] Written by M. W. Holtrop.

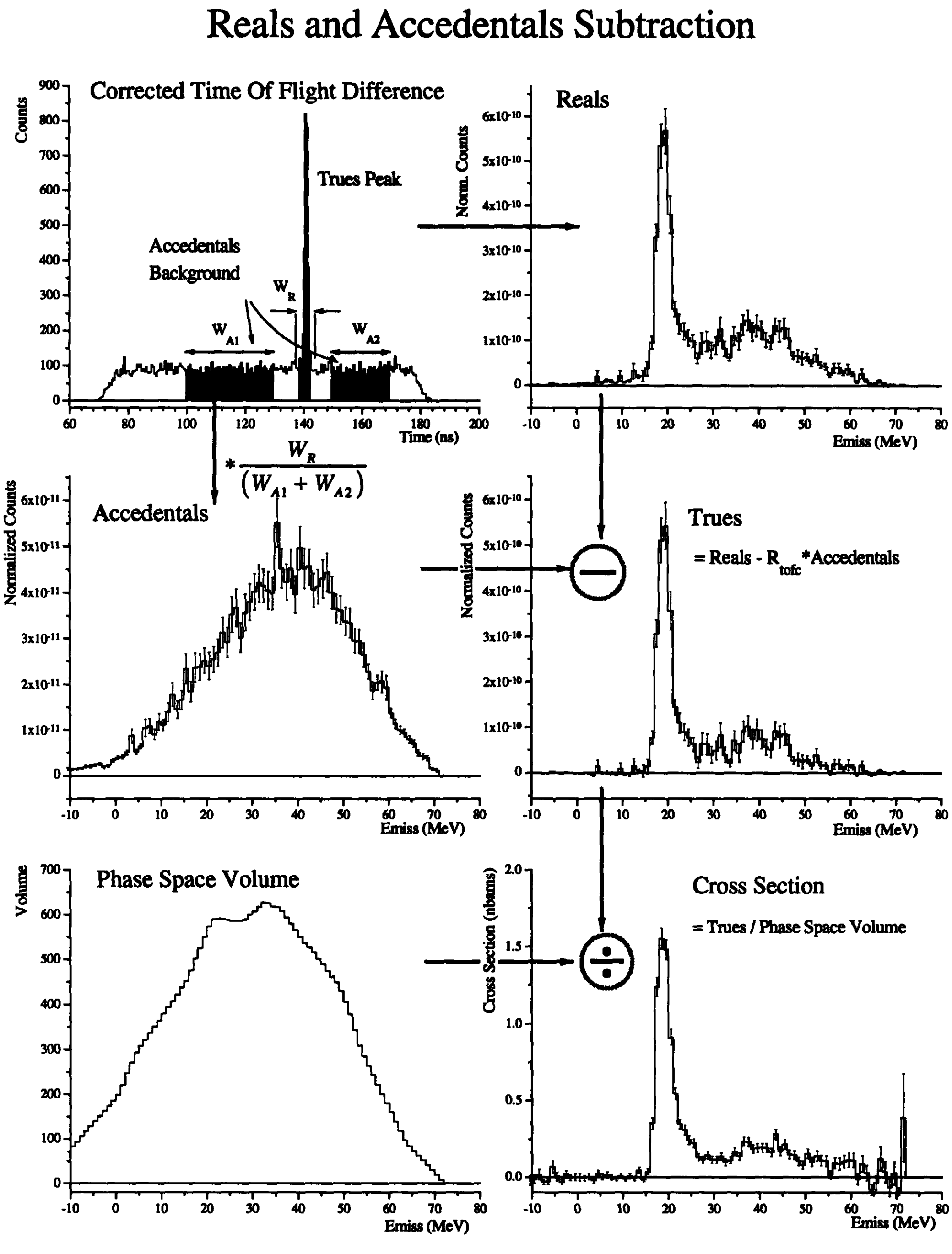

Figure 3.23 Histograms representing the step taken in the program Addcross. The top left hand histogram is the corrected Time Of Flight Difference. The events that fall in the shaded regions of the TOFD are sorted into histograms labeled *reals* and *accidentals*. The events in the *accidentals* histograms are scaled by the ratio of the widths of the regions in the TOF histogram. The *accidentals* are then subtracted from the *reals* leaving the *Trues*. The *trues* histograms are then turned into cross section histograms by dividing out the phase space volume. Note that in the actual analysis all this was done on two dimensional (*Em,Pm*) histograms rather than one dimensional (*Em*) histograms as shown here.

The *trues* histograms are added together and divided by the appropriate acceptance volume. This is done twice, producing final cross section histograms for the 42.9° data and for the 64.7° data. The method for adding the various runs comes from equation 3.27. Writing out all the indexes and including the normalization factors explicitly:

$$\left\langle \frac{d^6\sigma}{dE_f dE_m d\Omega_e d\Omega_p} \right\rangle_{\mathscr{B}} (E_m, P_m) = \frac{\sum_r n_r N_r(E_m, P_m)}{\sum_r v_r V_r(E_m, P_m)}$$
$$v_r = \frac{C_r}{e} \frac{N_A t_r}{A \cos(\theta^r_{tar})} \left(\Delta_{bin} E_m \Delta_{bin} P_m\right) \tag{3.34}$$

where the variables have the following meaning:

N_r	Counts from the Trues histogram for run r.
n_r	Normalizations for run r, not already included in N_r.
V_r	Phase space acceptance volume, for the $dE_f dE_m d\Omega_e d\Omega_p$ differential.
C_r	Total charge deposited on the target for run r in Coulombs.
e	electric charge of the electron: $1.602\text{x}10^{-19}$ C.
N_A	Avogadro's number: $6.673\text{x}10^{23}$ mol^{-1}.
t_r	Target thickness: 208.9 mg cm^{-2}.
A	Target atomic weight. For Carbon this is 12.
θ^r_{tar}	Target angle: angle between the normal of the target and the beam line, -10° for the 64.7° data and 0° for the 42.9° data.
$\left(\Delta_{bin} E_m \Delta_{bin} P_m\right)$	2-dimensional bin size for one bin. (This is the corresponding factor to the 2-dimensional bin size in equation 3.32; the factors effectively cancel each other.)

This produces the cross section in a two dimensional histogram, $\sigma(Em,Pm)$, which can be projected onto the missing energy or missing momentum axis. It is possible to project the entire histogram, or just a section of it. This allows the projection of only certain regions (e.g. the p-shell or s-shell), and makes a perfect overlap between the acceptance areas for the 64.7° and the 42.9° data possible.

For data with very high statistics and where there are no bins with low counts or small acceptance, the projections can be calculated as a weighted average over one dimension. The weighting factor in this case would be the square of the uncertainty. For instance, a projection onto the missing energy axis is calculated with:

$$\begin{aligned}\sigma(E_m) &= \frac{\sum\limits_{P_m} \frac{\sigma(E_m,P_m)}{\Delta_\sigma^2(E_m,P_m)}}{\sum\limits_{P_m} 1/\Delta_\sigma^2(E_m,P_m)} \\ \Delta_\sigma(E_m) &= \sqrt{\sum_{P_m} 1/\Delta_\sigma^2(E_m,P_m)}\end{aligned} \tag{3.35}$$

where the summations are over the relevant bins in missing momentum; $\sigma(E_m, P_m)$ and $\sigma(E_m)$ are the two dimensional cross-section histogram and it's projection, and the Δ's are the uncertainty values.

However, this common method breaks down when some of the bins have low counts or zero counts, in which case Gaussian statistics are no longer valid. The best solution in this case is to go back to equation 3.34 and project the summed counts ($\mathscr{N}$) and summed volume ($\mathscr{V}$) histograms separately, and then calculate the projected cross section histogram by dividing the two:

$$\begin{aligned}\mathscr{N}(E_m,P_m) &= \sum_r n_r N_r(E_m,P_m), \quad \Delta_{\mathscr{N}}^2(E_m,P_m) = \sum_r n_r^2 \Delta_{N_r}^2(E_m,P_m) \\ \mathscr{V}(E_m,P_m) &= \sum_r v_r V_r(E_m,P_m), \quad \Delta_{\mathscr{V}}^2(E_m,P_m) = \sum_r v_r^2 \Delta_{V_r}^2(E_m,P_m) \\ \sigma(E_m) &= \frac{\sum\limits_{P_m} \mathscr{N}(E_m,P_m)}{\sum\limits_{P_m} \mathscr{V}(E_m,P_m)}, \quad \Delta_\sigma^2(E_m) = \frac{1}{\left(\sum\limits_{pm}\mathscr{V}\right)^2}\left[\sum_{P_m}\Delta_{\mathscr{N}}^2 + \left(\frac{\sum\limits_{pm}\mathscr{N}}{\sum\limits_{pm}\mathscr{V}}\right)^2 \sum_{P_m}\Delta_{\mathscr{V}}^2\right]\end{aligned} \tag{3.36}$$

where the summation in the first two lines is over runs, r, and the summation in the last line is over P_m. This means that for projections it is convenient to save the summed volume, which allows the summed counts to be calculated from the cross section.

3.6 Radiative Corrections: The RADC program.

In the next step of the analysis the cross section is corrected for the radiative processes that occur in the interaction. Although this is a physical process and not an artifact of the experiment, most theoretical calculations do not take these effects into account, because they depend on experimental parameters such as the target thickness. Thus, to compare directly to a theoretical calculation it is important to unfold the radiative processes from the data. This unfolding was done with the RADC program, which was written at NIKHEF by E. Quint[13] and modified for use at MIT.

3.6.1 Theory of Radiative Processes

There are three processes that are considered for radiative corrections:

1. Internal bremsstrahlung (Schwinger correction), where the incoming or outgoing electron interacts with the Coulomb field of the nucleus involved in the (e,e'p) reaction, via the exchange of a virtual photon other than the one involved in the reaction itself.
2. External bremsstrahlung, in which the electron interacts with the Coulomb field of a nucleus other than the nucleus involved in the (e,e'p) reaction.
3. Landau straggling, in which the electron or the proton loses energy due to the ionization of the target atoms.

The largest correction is due to the internal bremsstrahlung, which was first described by Schwinger[14] and was improved upon by Mo and Tsai[15]. The diagrams for these processes are depicted in figure 3.24. The diagrams labeled A and B correspond to the emission of a real photon before and after the interaction respectively. If the energy of the emitted photon, k_γ, is greater than the cutoff energy, ($k_\gamma > \Delta E_m$, *hard photon* emission), this process causes a radiative tail. The strength is thus shifted, and has to be counted back into the peak. If the emitted energy is smaller than the cutoff

---

[13] E. Quint, "Limitations of the Mean-Field Description of Nuclei in the Pb-Region, Observed with the (e,e'p) Reaction", Ph.D. Thesis (1988), unpublished.

[14] J. Schwinger, Phys. Rev. **76**, 760 (1949)

[15] L. W. Mo and Y. S. Tsai, Reviews of Modern Physics **122**, 1898 (1961)

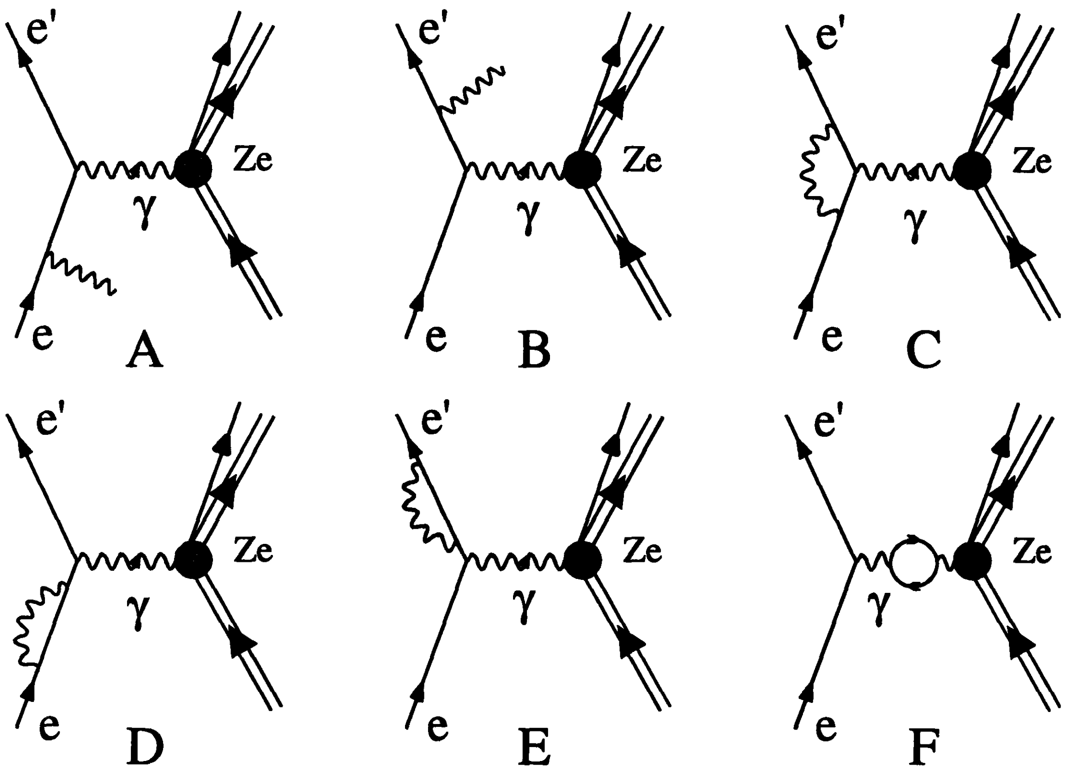

Figure 3.24 The first order Feynman diagrams for internal bremsstrahlung. Diagram A and B correspond to real photon emission, diagram C corresponds to the vertex correction, diagrams D and E correspond to the renormalization of the electron mass, and diagram F corresponds to vacuum polarization of the exchanged photon.

energy, ($k_\gamma < \Delta E_m$, *soft photon* emission) no correction is necessary since the strength is merely shifted within the peak.

Diagram C depicts the emission of a virtual photon by the incoming electron, which is then reabsorbed by the outgoing electron. This vertex correction causes a shift in the transferred 4-momentum and thus a change in the cross section. Diagrams D and E correspond to the emission and re-absorption of a virtual photon, which results in a renormalization of the electron mass, and diagram F results in a corresponding renormalization of the virtual photon due to vacuum polarization.

The RADC program uses the Schwinger correction as it was proposed by Penner[16], who based his formalism on Mo and Tsai[17]. But it uses the suggestions by

---

[16] S. Penner, Nuclear Structure Physics, Proceedings of the 18th Scottish Univ. Summer School in Physics, page 284 (1977)

[17] L. W. Mo and Y. S. Tsai, Reviews of Modern Physics, 41, 208 (1969)

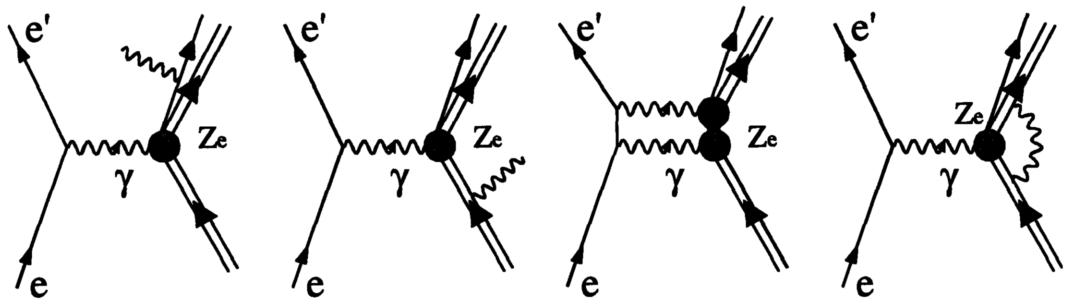

Figure 3.25 The omitted first order Feynman diagrams for internal bremstrahlung.

Schwinger[18] to replace $(1-\delta_{real}) \rightarrow e^{-\delta_{real}}$, and include a recoil term. The correction factor then takes the form:

$$C_{Schw} = \frac{e^{\delta_{real}}}{(1-\delta_{virtual})} \tag{3.37}$$

where the δ are given by:

$$\begin{aligned} \delta_{real} &= \frac{\alpha}{\pi}\ln\left(\frac{E_b E_f b}{\eta^2 \Delta E_m^2}\right)\left\{\ln\left(\frac{-Q^2}{m_e^2}\right)-1\right\} \\ \delta_{virtual} &= -\frac{2\alpha}{\pi}\left\{\frac{13}{12}\left[\left(\frac{-Q^2}{m_e^2}\right)-1\right]-\frac{17}{36}-\frac{\pi^2}{12}+\frac{1}{2}L_2\left(\cos^2(\tfrac{1}{2}\theta_e)\right)-\frac{1}{4}\ln^2\left(\frac{E_b}{E_f}\right)\right\} \end{aligned} \tag{3.38}$$

In these equation L_2 is the Spence function defined by:

$$L_2(x) = -\int_0^x \frac{\ln(1-y)}{y}dy \tag{3.39}$$

and b and η are given by[19]:

$$\begin{aligned} b &= 1+\frac{2\omega}{M_A}\sin^2(\tfrac{1}{2}\theta_e) \\ \eta &= 1+\frac{2E_b}{M_A}\sin^2(\tfrac{1}{2}\theta_e) \end{aligned} \tag{3.40}$$

---

[18] J. Schwinger, Phys. Rev. **75**, 898 (1949)

[19] Note that there seems to be a misprint in S. Penner (1977), who defines: $b = 1+\omega/(2M_A)\sin^2(\tfrac{1}{2}\theta_e)$

This formalism was tested at NBS[16] with ^{12}C data, and it was found to be accurate to within their statistical uncertainty of 0.1%, over the range $0.1 \le q \le 1.0\ \mathrm{fm}^{-1}$. However, it was noted recently by D. Wasson[20] that for coincidence experiments these results break down since one can no longer integrate over the final states of the scattered proton. Also the diagrams shown in figure 3.25 for bremsstrahlung of the protons were not included in the analysis. The size of these effects is expected to be small for the modest momentum transfer in this experiment.

The formalism for the external bremsstrahlung correction, given by Friedrich[21], is based on an approximation of the probability for the particle to radiate one real photon. This probability can be integrated analytically to give an approximate one photon correction factor:

$$\begin{aligned} C_{brem}^{approx}(\Delta E) &= 1 - \int_0^{E_i-\Delta E} \frac{t}{X_0\left(E_i - E_f\right)}\left[1 - \eta\frac{E_f}{E_i} + \frac{E_f^2}{E_i^2}\right] \mathrm{d}E_f \\ &= 1 - \delta^{rad} \end{aligned} \tag{3.41}$$

where after the integration:

$$\delta^{rad} = \frac{t}{X_0}\left[-\left(\tfrac{1}{2} - \eta\right) + (2-\eta)\ln\left(\frac{E_i}{\Delta E}\right) + (2-\eta)\frac{\Delta E}{E_i} - \frac{1}{2}\frac{\Delta E^2}{E_i^2}\right] \tag{3.42}$$

Now in a similar argument as was made for the Schwinger correction the substitution $\left(1-\delta_{real}\right) \to e^{-\delta_{real}}$ is made to give the proper limiting behavior as $\Delta E \to 0$. Replacing also $2-\eta$ with the function ζ [22], the correction factor becomes:

$$C_{Brem} = \exp\left\{\frac{t}{X_0}\left[-\left(\zeta - \tfrac{1}{2}\right) + \zeta\ln\left(\varepsilon/\Delta E_m\right) + \zeta\frac{\Delta E_m}{\varepsilon} - \tfrac{1}{2}\left(\frac{\Delta E_m}{\varepsilon}\right)^2\right]\right\} \tag{3.43}$$

---

[20] N. Makins, "Measurement of the Nuclear Dependence and Momentum Transfer Dependence of the Quasielastic (e,e'p) Scattering at Large Momentum Transfer", Ph.D. Thesis 1994, unpublished, and D. Wasson private communications.

[21] J. Friedrich, Nuclear Instruments and Methods, **129**, 505 (1975)

[22] Y. S. Tsai, Rev. Mod. Phys. **46** (1974) 815

where ε is the electron energy: the beam energy, E_b, if radiating before the interaction and the final electron energy, E_f, after the reaction. The function ζ and the radiation length X_0, are given by:

$$\begin{aligned} \zeta &= \tfrac{1}{9}\left[12+(Z+1)/(l_1 Z+l_2)\right] \\ X_0 &= 716.405(A/Z)/\left[Z(l_1-f(Z))+l_2\right]\mathrm{g/cm^2} \\ f(Z) &= (Z\alpha)^2\left\{1.202+(Z\alpha)^2\left[-1.0369+1.008(Z\alpha)^2/\left((Z\alpha)^2+1\right)\right]\right\} \end{aligned} \tag{3.44}$$

Table 3.6 Parameters used for the radiation length calculation.

Z	l_1	l_2
1	5.31	6.114
2	4.79	5.621
3	4.74	5.805
4	4.71	5.924
≥5	5.216-ln(Z)/3	7.085-2ln(Z)/3

The function $f(Z)$ is the Coulomb correction for the one photon exchange approximation[23] and l_1 and l_2 are tabulated functions of Z, see table 3.6[22]. This correction is only applied for the electrons, since it is about six orders of magnitude smaller for protons, and can thus be ignored.

The Landau correction, or straggling correction needs to be applied for both the electrons and the knocked out proton. It describes the loss of energy due to inelastic collisions with the atomic electrons of the target. The formalism used in this program is an approximation of nine Gaussians[24]:

$$\begin{aligned} C_{Land} &= \sum_{i=1}^{9} f_i \Big/ \sum_{i=1}^{9} f_i \,\mathrm{prob}(x), \\ \mathrm{prob}(x) &= 1-1\Big/\left\{2\left[1+\sum_{i=1}^{4}\delta_i x^i\right]^4\right\}, \\ x &= \sqrt{2}\left[\Delta E_m/\xi-\Lambda-c_i\right]/d_i, \\ d_i &= \sqrt{g_i^2+2\cdot 10^{-5} Z^{3/4}\lambda/\xi^2} \\ \xi &= 0.1536(Z/A)\, t/\beta^2\,\mathrm{MeV}, \\ \Lambda &= \ln\left(\xi\beta^2/(1-\beta^2)\right)-1.8\ln(Z)-\beta^2-5.1004 \end{aligned} \tag{3.45}$$

---

[23] H. A. Bethe and W. Heitler, Proc. Roy. Soc. **A146** (1934) 83

[24] D. J. S. Findlay and A. R. Dusautoy, Nucl. Instr. and Meth. **174**, 531 (1980)

Table 3.7 Parameters for the Landau distribution.

i	g_i	f_i	c_i	δ_i
1	0.737	0.0271	-1.48	0.196854
2	0.947	0.0798	-0.738	0.115194
3	1.23	0.1085	0.170	0.000344
4	1.68	0.1087	1.33	0.019527
5	2.40	0.0862	2.95	
6	3.68	0.0604	5.39	
7	6.18	0.0396	9.40	
8	12.3	0.0258	16.8	
9	39.7	0.0238	30.8	

The mean energy loss of a charged particle in an absorber, λ, for a proton or electron is

$$\begin{aligned} \lambda_{proton} &= 2\xi \ln\left(\beta^2 \Big/ \left(1-\beta^2\right) - 0.9\ln(Z) - \beta^2 + 11.06469 \right) \\ \lambda_{electron} &= \xi\left[19.26 + \ln\left(t \big/ \rho \right) \right] \end{aligned} \tag{3.46}$$

where ρ is the target density in g/cm^3. Table **3.7** gives the values for the constants f_i,c_i,g_i and δ_i.

The correction to the peak is given by:

$$N_o = C(\Delta E_m) N_{exp}(\Delta E_m) \tag{3.47}$$

where N_0 is the corrected strength, N_{exp} is the experimental integrated strength, and ΔE_m is the *cutoff energy*, the difference between the upper limit of the integration region and the center of the peak. The exact choice of the integration region, and thus the value of ΔE_m, is somewhat arbitrary[25]. It determines where the region of the peak ends and the radiative tail begins, and thus directly influences the magnitude of the correction, but it also influences the precision of the correction, since small terms proportional to $\Delta E_m / E_{beam}$ are neglected in the derivation of C. A commonly used choice for ΔE_m is the experimental missing energy resolution, which is what was used in this analysis. The correction factor C is given by:

---

[25] L. C. Maximon, Reviews of Modern Physics, 41,193 (1969)

$$C = C_{Schw} C_{Brem} C_{Land} \tag{3.48}$$

where the three factors represent the Schwinger correction, the bremsstrahlung correction and the Landau correction respectively.

3.6.2 The Radiative Unfolding Procedure

The radiative corrections detailed in the previous section can be used to calculate the tails for a theoretical calculation, which can then be subtracted from the data, or it can be used to correct experimental data by unfolding these tails directly. The latter method is preferred since it is less model dependent. Unfortunately it is not possible to unfold the radiative from of the data perfectly. This would require knowledge of the cross section at all momentum and energy transfers that could cause strength to shift into the acceptance of the experiment. This is clearly not feasible. Instead, the unfolding program extends the data into the unmeasured regions by extrapolation, or by fitting a theoretical model to the data and then using this model to calculate the extension. The RADC program extends the data in the missing momentum dimension by fitting a polynomial or logarithmic curve to the data. The details for this are presented at the end of this section.

Another difficulty in unfolding procedures is that the correction is usually applied to some final spectrum of one or two variables (here E_m and P_m) and uses the central value for all the other relevant variables. This causes small inaccuracies in the unfolding procedure since many possible combinations of the $\mathbf{e}'$ and $\mathbf{p}$ vectors can contribute to the same (E_m, P_m) bin. The RADC program allows for several options for the reconstruction of $\mathbf{e}'$ and $\mathbf{p}$. For this data the option was usedin which all the angles were fixed at the central value, and the electron and proton momenta were varied. Other options allow one to force parallel kinematics or perpendicular kinematics. A better but more computationally intensive method would be to use Monte Carlo methods to average over the acceptances.

The unfolding of the (E_m, P_m) spectrum starts with the row of P_m bins for the value of E_m corresponding to the proton separation energy. Since there can be no data below this energy, no strength can be shifted into this row due to radiation from lower E_m

values. The contents of each bin in this row is treated as a peak[26], which must be corrected for radiative processes and which causes a radiative tail that must be subtracted from the next successive bins. Thus, the original contents of the bin, N_{exp}, is multiplied by the correction factors C from equation 3.48 using a cutoff energy of one half bin width:

$$\begin{aligned} N_0(E_m,P_m) &= N_{exp}(E_m,P_m)\cdot C_0(\vec{\mathrm{e}})\cdot C_0(\vec{\mathrm{e}}')\cdot C_0(\vec{\mathrm{p}}) \\ &= N_{exp}(E_m,P_m)\cdot C_{Schw}(\vec{\mathrm{e}})\cdot C_{Schw}(\vec{\mathrm{e}}')\cdot C_{Brem}(\vec{\mathrm{e}})\cdot C_{Brem}(\vec{\mathrm{e}}') \\ &\cdot C_{Land}(\vec{\mathrm{e}})\cdot C_{Land}(\vec{\mathrm{e}}')\cdot C_{Land}(\vec{\mathrm{p}}) \end{aligned} \tag{3.49}$$

where it is made explicit that the correction is calculated for each of the three particles: $\vec{e}$ for the incoming electrons, $\vec{e}'$ for the outgoing electrons, and $\vec{p}$ for the outgoing protons. The C factors are found from equations 3.37, 3.43 and 3.45. It is assumed in this treatment that the incoming electron and the final electron contribute equally to the Schwinger correction, thus $C_{Schw}(\vec{\mathrm{e}}) = C_{Schw}(\vec{\mathrm{e}}') = \sqrt{C_{Schw}}$, which is accurate to better than 0.5%.

Next the tails are subtracted for this bin. The tail can be calculated as the derivative with respect to E_m of the reciprocal of the correction function:

$$T(E_m,P_m) = N_0(E_m,P_m)\cdot\frac{\partial}{\partial\Delta E_m}\left(1\big/C_o(\Delta E_m)\right) \tag{3.50}$$

(It should be noted that the virtual part of the Schwinger correction, which takes into account the vacuum polarization and vertex correction, is independent of the cutoff energy, ΔE_m, and thus does not contribute to the tail.)

Since discrete bins are used, the tail must be integrated over the bin width to get the amount that must be subtracted from each bin in the tail. Also it needs to be to taken into account that there are actually three tails, one due to the radiation of the incoming electron, one due to the radiation of the outgoing electron, and one due to the Landau straggling of the proton. These three tails each have a different direction on the (E_m, P_m) histogram, as can be seen most clearly for data on hydrogen, for which the cross-section is a very narrow peak at $E_m=P_m=0$ (see figure 3.26). The amount that should be

---

[26] This was first suggested by H. Crannell, Nucl. Inst. and Meth. **71**, 208 (1969)

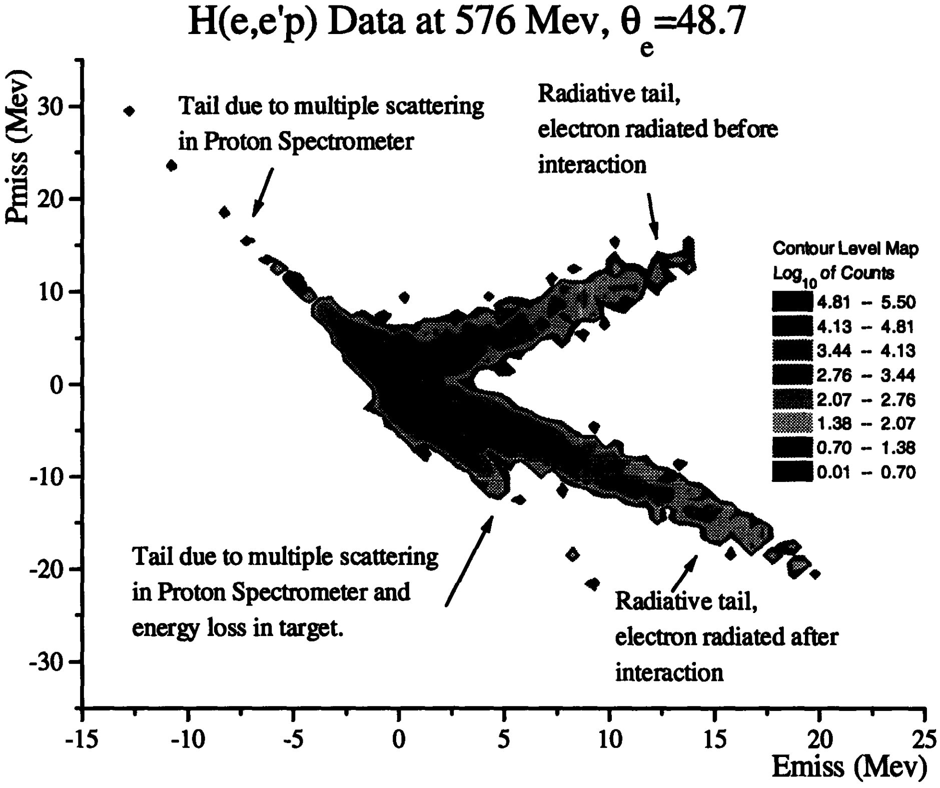

Figure 3.26 Radiative tails for the hydrogen peak. The width and shape of the central region is determined by the resolution of the spectrometers and multiple scattering. Negative missing momentum corresponds to $\mathbf{P}_m$ anti with $\mathbf{q}$.

subtracted from a bin *i,j* (the *i*-th bin in the E_m direction from the bin (E_m, P_m) $i,j = 0,0$ that caused the tail) is given by:

$$\Delta N^{\vec{\mathbf{e}}}_{i,j} = N_o(E_m,P_m)\left[\frac{1}{C_i(\vec{\mathbf{e}})} - \frac{1}{C_{i-1}(\vec{\mathbf{e}})}\right]\cdot\left\{2+\frac{1}{C_0(\vec{\mathbf{e}}')}+\frac{1}{C_0(\vec{\mathbf{p}})}+\frac{2}{C_0(\vec{\mathbf{e}}')C_0(\vec{\mathbf{p}})}\right\}\Big/6 \quad \textbf{(3.51)}$$

for the tail caused by radiation of the incoming electron $(\vec{\mathbf{e}})$,

$$\Delta N^{\vec{\mathbf{e}}'}_{i,j} = N_o(E_m,P_m)\left[\frac{1}{C_i(\vec{\mathbf{e}}')} - \frac{1}{C_{i-1}(\vec{\mathbf{e}}')}\right]\cdot\left\{2+\frac{1}{C_0(\vec{\mathbf{e}})}+\frac{1}{C_0(\vec{\mathbf{p}})}+\frac{2}{C_0(\vec{\mathbf{e}})C_0(\vec{\mathbf{p}})}\right\}\Big/6 \quad \textbf{(3.52)}$$

for the tail caused by radiation of the outgoing electron $(\vec{\mathbf{e}}')$, and

$$\Delta N^{\vec{\mathbf{p}}}_{i,j} = N_o(E_m,P_m)\left[\frac{1}{C_i(\vec{\mathbf{p}})} - \frac{1}{C_{i-1}(\vec{\mathbf{p}})}\right]\cdot\left\{2+\frac{1}{C_0(\vec{\mathbf{e}})}+\frac{1}{C_0(\vec{\mathbf{e}}')}+\frac{2}{C_0(\vec{\mathbf{e}})C_0(\vec{\mathbf{e}}')}\right\}\Big/6 \quad \textbf{(3.53)}$$

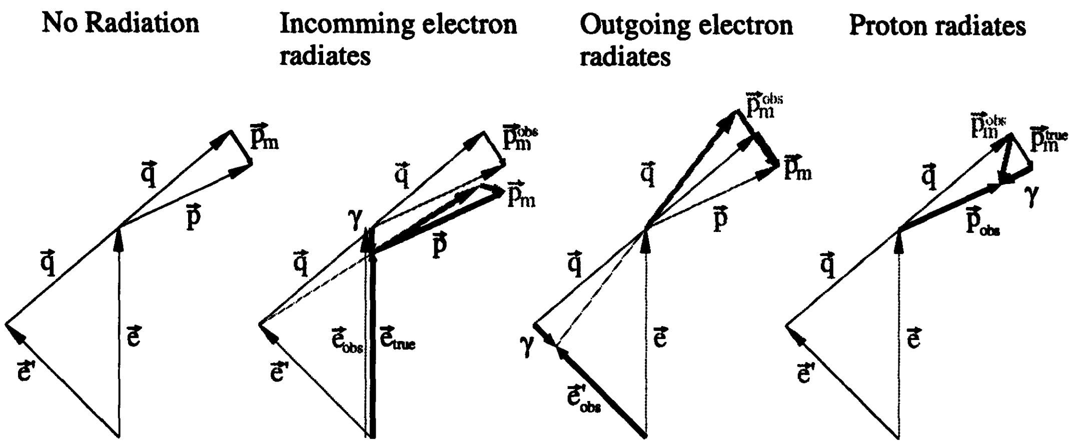
No Radiation

Incomming electron radiates

Outgoing electron radiates

Proton radiates

Figure 3.27 Reconstruction of the missing momentum vector when one of the particles radiates. The vectors are drawn approximately to scale for a $E_{beam} = 576$ MeV, $\theta_e = 44°$ and $\theta_p = 64.7°$. Notice that when the incoming electron radiates the analysis is done as if no radiation occurred, even though the physics is modified. When the outgoing electron radiates, the analysis is done with a modified e', while at the interaction point e' was not modified. In both cases the q vector moved to a larger angle due to the radiation and P_m is shifted to a smaller value. On the other side of q, $\theta_p = 42.9°$, P_m would be shifted to a larger value. These diagrams depend strongly on the details of the kinematics.

for the tail caused by the Landau straggling of the proton $(\vec{p})$.

The correction factors C_i are evaluated with ΔE_m equal to i-$1/2$ times the E_m bin size. Note that the property of the C_i factors is such that $C_0 > C_1 > C_2 > \ldots > 1$, with $C_\infty \rightarrow 1$, and thus the ΔN terms are larger than zero and must be subtracted from the bins. Conservation of counts can be demonstrated by summing the results of equations 3.51, 3.52 and 3.53 for $i=1$ to infinity. Replacing N_0 with $N_{exp}C_0(e)C_0(e')C_0(p)$, this is shown by:

$$\begin{aligned}
\sum_{i=1}^{\infty} \Delta N^{\vec{e}}_{i,j} + \Delta N^{\vec{e}'}_{i,j} + \Delta N^{\vec{p}}_{i,j} &= \tfrac{1}{6} N_{exp} \left\{ \begin{matrix} \left[C_o(\vec{e}) - 1\right]\left(2C_0(\vec{e}')C_0(\vec{p}) + C_0(\vec{e}') + C_0(\vec{p}) + 2\right) + \\ \left[C_o(\vec{e}') - 1\right]\left(2C_0(\vec{e})C_0(\vec{p}) + C_0(\vec{p}) + C_0(\vec{e}) + 2\right) + \\ \left[C_o(\vec{p}) - 1\right]\left(2C_0(\vec{e})C_0(\vec{e}') + C_0(\vec{e}) + C_0(\vec{e}') + 2\right) \end{matrix} \right\} \\
&= N_{exp}\left[C_o(\vec{e})C_o(\vec{e}')C_o(\vec{p}) - 1\right] \\
&= N_0 - N_{exp}
\end{aligned} \tag{3.54}$$

The direction of the tails is found by reconstructing the missing momentum vector after the radiation occurs on one of the particles. Consider one of the particles losing an amount of energy γ due to radiation. Using the peaking approximation, the assumption can be made that the radiation was in the forward direction, and thus the vector corresponding to the momentum of the particle is shortened by γ (this must be corrected for the proton mass by a factor E_p/p.) The conceptual difficulty that now arises is that the data were analyzed as if no radiation has occurred. If the incoming electron radiated, the beam energy at the point of interaction was actually lower than the beam energy used in the analysis. Thus an error is made in the analysis, which skews the q vector further backward than the actual q vector. On the other hand the momenta at the interaction point are not modified if the outgoing electron radiated, but it is analyzed as if the outgoing electron momentum is lower than the actual momentum (at the interaction.) As a result, the q vector is again analyzed as if it was further backward. Figure 3.27 shows that the tails go in the three directions given by:

$$\begin{aligned} E^{obs}_{m,1,2,3} &= E_m + \gamma \\ \vec{p}^{\,obs}_{m1} &= \vec{p}_m + \gamma\, \vec{\mathbf{e}}/e \\ \vec{p}^{\,obs}_{m2} &= \vec{p}_m + \gamma\, \vec{\mathbf{e}}'/e' \\ \vec{p}^{\,obs}_{m3} &= \vec{p}_m + \gamma(\vec{\mathbf{p}}/p)(E_p/p) \end{aligned} \qquad (3.55)$$

With these equations the tails can be subtracted from the (E_m, P_m) histogram. The amount that is subtracted from bin $\left(E^{obs}_m, \left|\vec{P}^{obs}_{m1}\right|\right)$ is given by equation 3.51, the amount for bin $\left(E^{obs}_m, \left|\vec{P}^{obs}_{m2}\right|\right)$ is given by equation 3.52, and the amount for bin $\left(E^{obs}_m, \left|\vec{P}^{obs}_{m3}\right|\right)$ is given by equation 3.53.

Figure 3.28 shows how strength from outside of the acceptance region can radiate into the acceptance. Note that in this non-parallel case the vectors are quite different than in the parallel case of figure 3.26. To account for these tails in the subtraction procedure the data have to be extended beyond the borders of the acceptance. This is done by fitting a polynomial to the data bins in the row of P_m bins. First several rows of P_m bins are averaged in the E_m direction over the full width at half maximum of the ground state peak. This ensures that there are sufficient data in the row, and that it is sufficiently smoothed out. Next a polynomial of an order less than three is fitted to the data, or if desired to the logarithm of the data. This fit is then used to extend the data beyond the acceptance so that the radiative tails can be calculated.

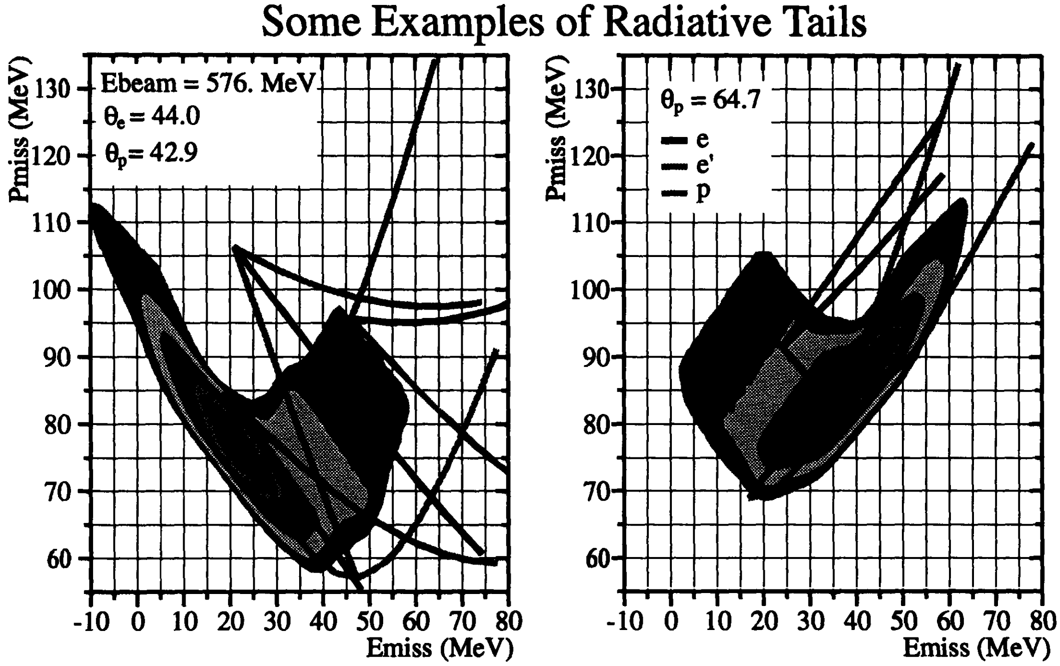

Figure 3.28 Diagram showing the directions for the tails of several bins. Due to the different kinematics the tails look very different for the 64.7° data then for the 42.9° data. The three tails that emanate from the bins correspond to radiation of the incoming electron (e), radiation of the outgoing electron (e') and energy loss of the proton (p).

Figure 3.29 shows an example of data where this extrapolation is performed. This method for extrapolating is very sensitive to the quality of the data, and the number of bins in *Pm* that are available to perform a good fit. This caused some difficulty in the radiative unfolding procedure because the acceptance in this experiment is fairly narrow. A better method would be to fit a theoretical shape from a DWIA calculation to the data with a single parameter (strength) and use that to extend the data. Unfortunately the program RADC is currently not capable of doing this.

After the radiative corrections are applied, the two dimensional histogram is projected onto the missing energy and missing momentum axis by the procedure described in section 3.2 and equation 3.20. The counts histogram ($\mathcal{N}$) is recovered by multiplying the two dimensional cross section histogram with the acceptance volume histogram ($\mathcal{V}$). This results in a counts histogram that is corrected for radiative processes. This histogram is then projected onto the missing energy (momentum) axis, and divided by the projected acceptance volume, which results in a properly normalized missing energy (momentum) histogram.

Figure 3.30 presents a missing energy histogram of the 64.7° data before and after the radiative correction is applied. The correction is largest for the p-shell peak, a

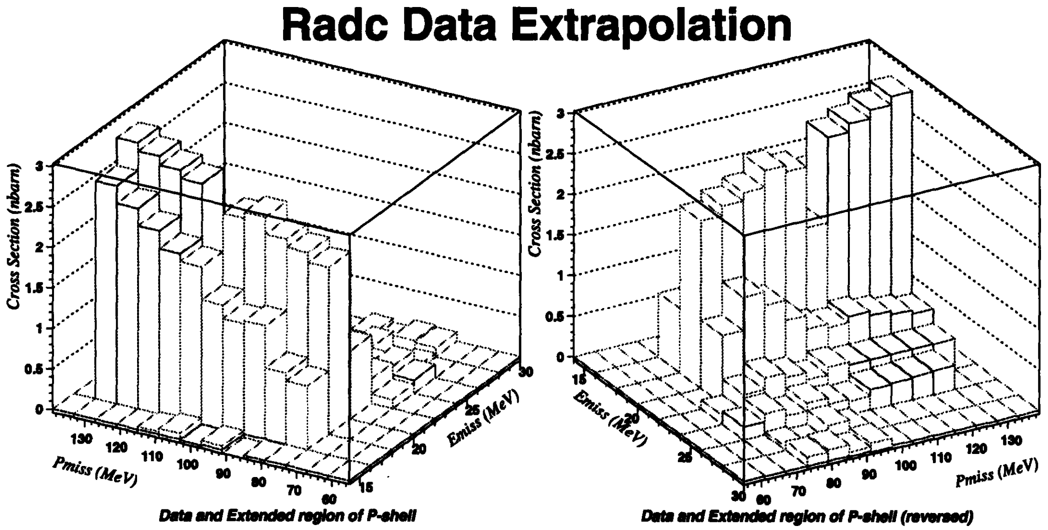

Data and Extended region of P-shell

Data and Extended region of P-shell (reversed)

Figure 3.29 An illustration of data extrapolation beyond the acceptance region. The darker lines indicate the extended bins.

factor of about 1.28. The tail caused by radiation from the p-shell compensates for the radiative correction to the s-shell. These two effects almost cancel so that radiative processes do not make a significant contribution to the s-shell or the deep missing energy region (E_m > 50 MeV). The total correction factors are listed in table 3.8. In this table the column labeled "before" ("after") contains the corrections factors for the tail that is caused by radiative processes that occur before (after) the interaction. The first four rows contain the correction factors for the p-shell peak, at E_m= 18.5 MeV. The last rows contain the factors for the end of the data set, at E_m= 70 MeV. These last numbers indicate the amount of tail that is expected to fall outside the data set for not-corrected data. Note that this amount of tail is correctly taken into account when the data are corrected for the radiative processes.

Table 3.8 Total correction factors for radiative processes.

	64.7°			42.9°		
p-shell correction	Total	Before	After	Total	Before	After
internal Bremsstrahlung	1.2222	1.1198	1.1149	1.2222	1.1198	1.1149
external Bremsstrahlung	1.0291	1.0135	1.0154	1.0291	1.0135	1.0154
Landau: electron	1.0000	1.0000	1.0000	1.0000	1.0000	1.0000
Landau: proton	1.0173		1.0173	1.0027		1.0027
correction at Em = 70 MeV.						
internal Bremsstrahlung	1.0329	1.0339	1.0311	1.0329	1.0339	1.0311
external Bremsstrahlung	1.0083	1.0040	1.0043	1.0083	1.0040	1.0043
Landau: electron	1.0000	1.0000	1.0000	1.0000	1.0000	1.0000
Landau: proton	1.0000		1.0000	1.0000		1.0000

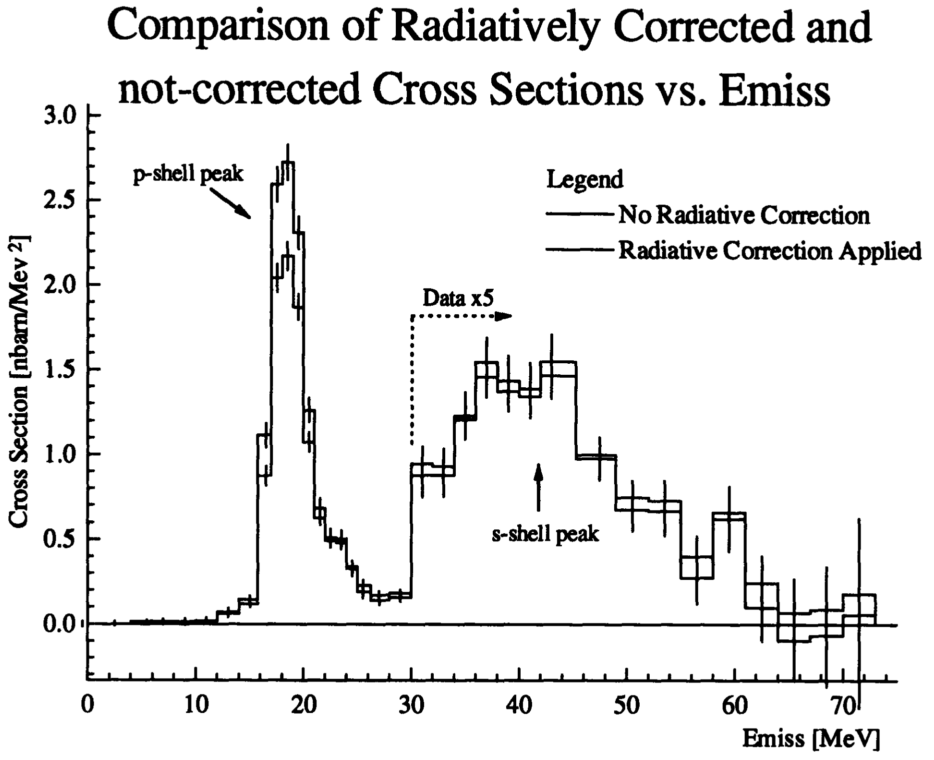

Figure 3.30 Histogram of the data before and after the radiative unfolding procedure. This procedure was applied to the 2-dimensional (*Em,Pm*) histogram, which was then projected onto the missing energy axis. The radiative correction is largest for the p-shell peak. The tails are relatively small and do not make a significant contribution to the deep missing energy region (*Em* > 50 MeV). This histogram is from the 64.7° data.

Chapter 4 Calibrations and Normalizations

The calibrations and normalizations of the experimental apparatus are an important part of every experiment. Since the extraction of R_{LT} is very sensitive to small differences between two measurements, the calibrations for this experiment had to be performed to a high degree of accuracy to rule out any systematic errors. This chapter will detail the calibrations and their results.

Section 4.1 presents corrections that were applied to the data to account for the electronics dead times. Section 4.2 discusses the details of the calibration of ELSSY and section 4.3 discusses those for OOPS. The details of the optics of the spectrometers is delegated to appendix A. Section 4.4 presents the method and results of the beam energy calibration.

4.1 Computer and Electronics Deadtimes.

The deadtime correction accounts for events that were not recorded because the electronics have not yet fully processed some other event. These events could have been legitimate counts, and so the data has to be corrected for the fraction of events that were rejected, by multiplying the data with a deadtime correction. This is done on an event by event basis in the C analyzer.

The deadtime correction is implemented mostly in hardware with scalers that count trigger pulses (see chapter 2 for details.) There are four sources for deadtime:

1. The "one event per beam burst" circuit makes sure that all events after the first event in a beam-burst are inhibited. It takes several microseconds to process an event, during which time no other events can be accepted by the system. This processing time is longer than the length of a beam burst, thus data acquisition is limited to one event per beam burst. About 1% of the events were rejected in this manner.

2. A separate circuit inhibits the trigger when the computer is busy processing an event or writing to tape. This "computer busy" signal is generated by the trigger module. It is accounted for by the same scalers that account for the "one event per beam burst" limitation. Dead-times due to the computer being busy are estimated at less than 1%.
3. For ELSSY (or OOPS) single arm events another circuit that can inhibit an event from being recorded is the pre-scaler, which lets only a fraction of the incoming single arm triggers through.
4. A "pile-up" scaler counts how many trigger signals were generated in the spectrometer in a short time interval around the trigger that was accepted by the trigger module. This scaler is read out for every event, and a test in the test package checks whether its value is 1. The "pile-up" test makes sure that a second trigger cannot corrupt the information in the wire chambers from the first trigger.

The first three dead-times are taken into account through pair of scalers. One scaler counts the total number of events that caused a legitimate trigger in the spectrometer, and an other scaler module counts the number of these triggers that are actually passed to the trigger event module. There were three such circuits, one for the ELSSY pre-scale trigger, one for the OOPS pre-scale trigger and one for the coincidence trigger. Since these circuits include the ELSSY and OOPS single arm pre-scalers, the single arm deadtimes for these spectrometers includes the prescale factor. The resulting deadtime correction is then simply the fraction of the counts in the two scalers:

$$C_{dead\_time} = \frac{N_{tot}}{N_{acc}} \qquad \Delta C_{dead\_time} = \frac{\sqrt{N_{tot}N_{acc} + N_{tot}^2}}{N_{acc}\sqrt{N_{acc}}} \tag{4.1}$$

where N_{tot} is the total number of triggers in the spectrometer and N_{acc} is the number of triggers that was accepted by the trigger module. The spectrometer "live-time" is defined as the inverse of the dead time correction: $L_t = 1/C_{dead\_time}$, while the "dead-time" is usually taken as $1 - L_t$. A typical value for the ELSSY live-time in a coincidence run was 99.22%, with the ELSSY pre-scaler set to 1 event out of every 20. For OOPS the same run gave a live-time of 99.24%, with the pre-scaler set to 1 out of 30, and the coincidence live-time was 94.9%.

A separate count is taken of the "pile-up" events. This is done in the test package of the Q-analyzer, where it is checked how many counts there were in the scaler that counts pile-up triggers. Another test checks to make sure that there was a proper "Look At Me" (LAM) signal generated for each spectrometer. The LAM signal indicated that all the TDCs and ADCs converted properly, and was absent very rarely, about 1 in $1{*}10^5$ events. To account for this the test package counts the number of events that had a "good LAM signal", N_{lam} , a "LAM Time-out", N_{to} , and "no pile-up", N_{nopu}. Since $N_{lam} + N_{to} = N_{tot}$, the "pile up" correction is given by:

$$C_{pile\_up} = \frac{(N_{lam} + N_{to})^2}{N_{lam} N_{nopu}}, \quad \Delta C_{pile\_up} = C_{pile\_up}\sqrt{\frac{N_{lam} + N_{nopu}}{N_{lam} N_{nopu}}} \tag{4.2}$$

and the corresponding live-time is the reciprocal of this. Typical pile-up live-times were 98.1% for ELSSY and 97.3% for OOPS.

During these experiments all the events that were accepted by the trigger module were also written to tape. Thus during replay there was no additional computer deadtime. This was verified for each run by comparing the number of events that were analyzed with the number in the scaler module that counted triggers. The ratio of these two numbers is the "analyzing fraction", which is 100% for the off-line analysis, but smaller during data taking.

4.2 ELSSY Calibrations.

The calibration of the ELSSY spectrometer includes determinations of the optical properties and the focal plane efficiency. The positioning accuracy of ELSSY is very high, and was not independently verified for this experiment. It made use of a theodolite that verifies the position of the spectrometer with respect to a fixed scale on the floor. For the analysis of the systematic error an estimated positioning uncertainty of 0.05° for the scattering angle was used.

The beam energy was determined with the ELSSY spectrometer, which linked this calibration to the one for the focal plane of ELSSY. This meant that the ELSSY momentum had to be calibrated before an accurate beam energy was available. These two calibrations could be treated in an iterative manner, but it was found that a single iteration provided sufficiently accurate results.

4.2.1 ELSSY Momentum calibration.

Since the VDC in ELSSY lies approximately along the focal plane, there is a direct relationship between the location of a particle in the X direction of the VDC and the momentum of the particle relative to the central ray. The relative momentum of the particle is usually called delta (δ), which is defined as[1]:

$$\delta = \frac{(P - P_0)}{P_0} \tag{4.3}$$

where P is the momentum of the particle and P_0 is the central momentum of the spectrometer. The central momentum is the product of the magnet constant, R, and the magnetic field, B, i.e. $P_0 = RB$. The central ray, corresponding to a particle with momentum P_0, crosses the focal plane at X_0. The relative momentum of a particle can be expressed as a polynomial of the measured location X_f in the VDC:

$$\delta(X_f) = C_0 + C_1(X_f - X_0) + \tfrac{1}{2}C_2(X_f - X_0)^2 \tag{4.4}$$

where $\delta = 0$ corresponds to $X_f = X_0, P = P_0$, and so $C_0 = 0$. The energy or momentum of the particle can be expressed in terms of δ as:

$$E_f = P_f = RB(1+\delta) = RB\left(1 + C_1(X - X_0) + \tfrac{1}{2}C_2(X - X_0)^2\right) \tag{4.5}$$

where the electron mass is ignored.

In principle this defines the central ray as the physical center of the spectrometer. From the experimental view point however the magnet constant and the exact center of the spectrometer are not precisely known. So in practice a value for X_0 or R is chosen and the other values are determined experimentally. For this experiment the

---

[1] Often delta is used as a percentage instead of a fraction.

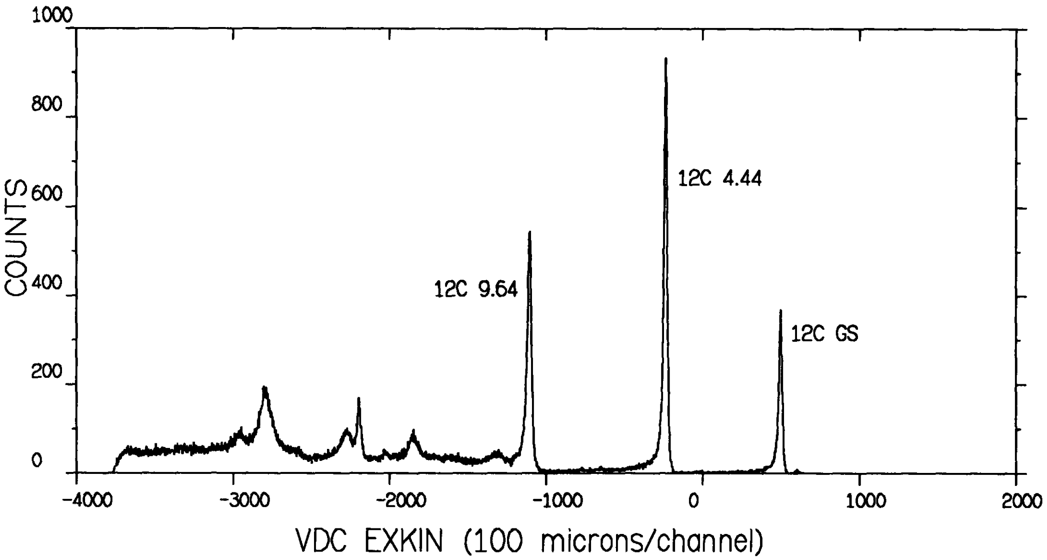

Figure 4.1 Focal plane calibration spectrum for ^{12}C.

value for R was chosen to be $66.85\ MeV/kGauss$, which corresponds to the standard value used in many other experiments[2].

There are two methods for determining the constants C_1, and C_2. In the first method the magnetic field is held at a constant value, and the excited states of several different target nuclei are used as reference points for a fit of the constants[3]. This method is advantageous for the beam energy calibration where the momentum of the spectrometer needs to remain fixed (see section 4.4). Notice that this method cannot determine the constant X_0, since that would require knowledge of the beam energy.

Figure 4.1 and figure 4.2 show the spectra of a carbon and a beryllium-oxide target with the energy levels of the excited states of the nuclei indicated. These spectra were improved by applying a correction for the kinematic broadening of the peaks. This broadening is caused by the variation in the recoil term due to the range of scattering angles accepted by the spectrometer. This kinematic correction can be calculated from a first order expansion in θ of the energy of the scattered electron. The energy of the

---

[2] We actually chose a value for X_0, then found the magnet constant corresponding to this choice and used this information to convert all the constants and X_0, to values corresponding to the standard value of R.

[3] This method is described in much greater detail in D. Jordan, *Ph.D. Thesis, MIT* (1994).

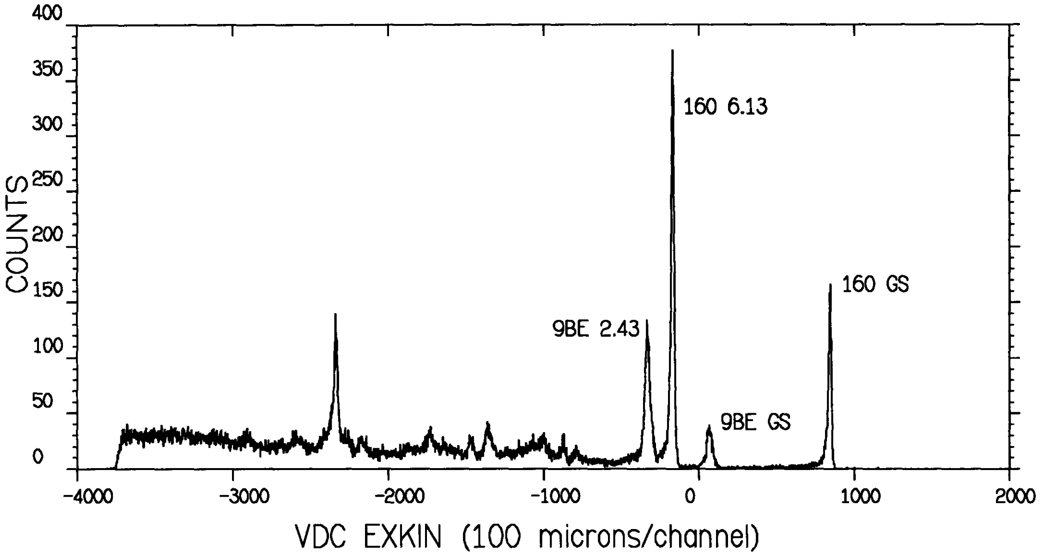

Figure 4.2 Focal plane calibration spectrum for ^{9}Be^{16}O.

scattered electron, E_f, for single arm elastic scattering from a state with excitation energy E_{exc} is given by:

$$\begin{aligned} E_f &= F_{rec}^{-1}\left(E_{beam} - E_{exc} - \frac{E_{exc}^2}{2M_{tar}}\right) \\ F_{rec} &= 1+\frac{2E_{beam}}{M_{tar}}\sin^2\left(\theta_{e0}/2\right) \end{aligned} \tag{4.6}$$

where E_{beam} is the beam energy, M_{tar} is the target mass and θ_{e0} is the central electron scattering angle. The kinematic correction is then given by:

$$\Delta E_f^{kin} = \frac{\partial E_f}{\partial \theta_e}\cdot(\Delta\theta_e) = \frac{-E_f^2\sin(\theta_{e0})}{M_{tar}}\cdot(\Delta\theta_e) \tag{4.7}$$

where $\Delta\theta_e$ is the measured scattering angle relative to θ_{e0}. This correction is then converted to a correction for X with equation 4.4 using a value for the C_1 constant that is derived from the design values[4]:

$$\Delta X^{kin} = \frac{\Delta E_f^{kin}}{E_0 C_1^{design}} = \frac{-E_f^2\sin(\theta_{e0})}{M_{tar}E_0 C_1^{design}}\Delta\theta \tag{4.8}$$

---

[4] Note that C_1 is equivalent to the matrix element $\langle\delta|X\rangle$.

where E_f is the measured energy of a particle and $E_0 \equiv P_0$ is the central value for the spectrometer.

The expected momentum for the peaks cannot be calculated until the beam energy is known. Only the energy difference between two states of the same nucleus can be calculated. The energy difference between two states of two different nuclei depends on the beam energy and the scattering angle through the recoil term, and thus is also not known.

The energy difference of two peaks can be written as:

$$\begin{aligned}\Delta E_f &= E_f(X_1) - E_f(X_2) \\ &= C_1(X_1 - X_2) + \tfrac{1}{2}C_2(X_1 - X_2)(X_1 + X_2) \\ &\Rightarrow \\ \frac{\Delta E}{\Delta X} &= C_1 + C_2 X_{ave}\end{aligned} \tag{4.9}$$

where X_{ave} is the average location in the VDC and ΔX is the distance between the two peaks. The energy for each peak in the spectrum is calculated using equation 4.6, with E_{exc} given by the Table of Isotopes, and an estimated initial value for the beam energy, E_{beam}, which only affects the recoil correction terms. The peak positions were determined using the program ALLFIT[5], which fits an asymmetric hyper-Gaussian line shape with radiative tails to the data. The pairs of peaks that are used have to be selected carefully to ensure that their position can be determined accurately. Frequently an excited state cannot be used because another state is too close and the fit cannot determine a reliable peak position. By plotting three or more pairs of $\Delta E_f / \Delta X$ versus X_{ave} the constants C_0 and C_1 can be found from a linear fit. A quadratic fit did not improve the results.

In the second method for obtaining a focal plane calibration the elastic peak of ^{16}O is moved across the focal plane by changing the magnetic field of the spectrometer several times in 1% steps. Here the assumption is made that the changes in the field cause a linear change in the central momentum. The position of each of the peaks in the resulting histograms for the kinematically corrected position in the VDC can be fit with ALLFIT. Each of the peaks can also be assigned an energy, computed from

---

[5] J. Kelly, *Ph.D. Thesis, MIT*, unpublished (1981).

equation 4.6, and the pairs (E,X) can then be used to obtain a fit for the constants in equation 4.5. If the beam energy is not known exactly this method will give an incorrect answer for the constant X_0, resulting in a shift of the computed momentum. However, once the accurate beam energy is known the result is easily converted to give the accurate momentum. The constants that were found using this method were used for the data analysis. The results are presented in table 4.1.

Table 4.1 Momentum Calibration Constants.

R	66.85 MeV/kGauss
X_0	-3.605 cm
C_1	0.105 %/cm
C_2	$1.4 \cdot 10^{-4}$ %/cm^2

This method can also be used to obtain higher order corrections to the focal plane calibration, which are also called abberative corrections. This is done with the ray-writing technique described in appendix A. The rays that are written to disk correspond to a gate that is set around the elastic peak for each of the runs. The fit that is then performed minimizes the equation:

$$\langle\delta|1\rangle+\langle\delta|X_f\rangle X_{f,ray}+\langle\delta|X_f^2\rangle X_{f,ray}^2+\langle\delta|X_f\theta_f\rangle X_{f,ray}\theta_{f,ray}\cdots-\delta_{peak} \qquad \textbf{(4.10)}$$

where the <δl...> term represent matrix elements, with $\langle\delta|x_f\rangle = c_1$ and $\langle\delta|x_f^2\rangle = \frac{1}{2}c_2$ for the case where $X_0=0$. For this experiment the aberrative corrections gave no significant improvement in resolution and were not used.

4.2.2 ELSSY Detector Normalizations.

During the analysis of the data a number of events are rejected because the information from the VDC or TAs could not be properly decoded. Some of these events could have been legitimate counts, and these would need to be counted back into the final histograms (see chapter 3 for details on the analysis). This is done by a normalization correction, which is a factor by which the data is multiplied in the C analyzer.

The determination of the normalization correction is more complicated than the deadtime correction. Some of the rejected events may have been stray particles that were not related to the target and should not be corrected, while some of them may have been good events that were corrupted by noise in the detector. There are two approaches to this problem. In the first approach the ratio of good events to stray events is determined, and then for all later analysis this same ratio is assumed. [3] The ratio can be determined from a single arm X_f spectrum with a clear elastic peak and a "super elastic" region. This region in the focal plane cannot have any counts other than stray particles because it corresponds to energies that are higher than those that correspond to the elastic peak of the heaviest nucleus in the target. If there are any good events in the set of events that were cut, then they would exhibit the same features as the rest of the data, with an elastic peak and a super elastic region. The ratio of good events to stray events in the set of rejected events can then be determined from a histogram of X_f for the rejected particles. The stray particles should not have any correlation in X_f, and thus it is expected that they are evenly distributed. The total number of stray events, N_{stray}, in the spectrum is then given by:

$$N_{stray} = N_{super\_elastic}\left(\frac{\Delta X_{tot}}{\Delta X_{super\_elastic}}\right) \quad \textbf{(4.11)}$$

where $N_{super\ elastic}$ is the number of particles in the super-elastic region, ΔX_{tot} is the total size of the X_f spectrum and $\Delta X_{super\ elastic}$ is the size of the super elastic region. The correction factor to the data for run *i* would then be given by:

$$C_t^r = \left.\left(\frac{N_{tot}}{N_{tot} - N^t_{reject} R^t}\right)\right|_r \quad \textbf{(4.12)}$$

where N_{tot} is the total number of triggers for run r, and N_{reject} is the subset of those events that failed the test. The factor $R^t = \left(N^t_{rejected} - N^t_{stray}\right) / N^t_{rejected}$ is derived from the reference data for each software cut t, and is assumed to be the same for every run. All the cuts have to be designed in such a way that they are independent so that the C factors can be multiplied together to give an overall normalization.

This method has several problems associated with it. The largest problem is that the assumption that the ratio R stays constant for all other runs breaks down when the quality of the beam changes causing more stray events due to large halo effects. Also it does not take into account that some of the events in the super-elastic region could be have been target related events, and thus constitute good particles as far as the analysis of the efficiency is concerned. One such class of particles are those that underwent multiple scattering and so end up in the super-elastic region.

The second method attempts to define a condition under which it is highly unlikely that an event was caused by a stray particle, eliminating the need for a correction to the normalization. The detector efficiency is then evaluated for each cut separately for this class of events. The total efficiency of the detector is then the product of the separate efficiencies for each cut. It is thus important to make sure that the cuts are independent and that the "good particle" condition is sufficiently stringent.

The best condition for a good particle is one that requires an event to pass all tests, other than the test that is being looked at. This is not always practical since some tests are not computed until much later in the analysis, but it is approximated reasonably by the requirement that all delay lines in all chambers fired, and the event caused a clean trigger. In practical terms this means that when the efficiency of a delay line is being tested, the condition for a good event requires that all the other delay lines fired properly, and also all other detectors in the spectrometer fired properly. This method assumes that for good particles the failure rate of one component in the detector is independent of the failure rate of all the other components. Thus for good particles, delay line 1 is not more likely to fail if delay line 2 also failed. The efficiency factor for a component is then simply given by:

$$C_x = \frac{N_{pass}}{N_{pass} + N_{fail}}, \quad \Delta C_x = \frac{\sqrt{N_{pass} N_{fail}}}{\left(N_{pass} + N_{fail}\right)^{3/2}} \tag{4.13}$$

where N_{pass} is the number of events that passed the test and N_{fail} is the number of events that failed the test. The efficiency correction of a detector part is then simply $\varepsilon_x = 1/C_x$

The actual tests that were performed for this analysis are listed in table 4.2, with the resulting efficiency for a typical run in the last column. The wires in the Vertical Drift Chamber were very efficient, presumably because of the high operating voltage. For the efficiency analysis it did not make any difference whether the TDCs where checked for time-outs individually or in pairs. The VDC analysis was slightly less efficient. The analysis could fail on one of four tests, "+++ hit pattern", "failed wire spacing", "bad drift ratio" and "drift denominator >0", for details see chapter 3. The test "+++ hit pattern" would only occur on the last wire in the chamber. Thus it cannot be taken into account

Table 4.2 Tests for the analysis of the ELSSY detector efficiency

Test	Condition	N_x in formula	Formula	Result
VDC Delay Lines	Good Trigger + Good TA information.	$N_{5+/6}$ = 5 or more TDCs fired OK $N_{6/6}$ = all 6 TDCs fired OK.	$C_{vdc\_delay} = N_{(6/6)} / N_{(5+/6)}$	100%
VDC Analysis	Good Trigger + Good Delay Lines + Good TA inf.	N_{vdc+ta} = All VDC Delays + TAs N_{+++} = Bad event +++ hit pattern N_{other} = Bad event, other failure	$C_{vdc\_anal} = 1 - \left(N_{other} / (N_{vdc+ta} - N_{+++}) \right)$	94.9%
VDC Total	-	-	$C_{vdc\_tot} = C_{vdc\_delay} \cdot C_{vdc\_anal}$	94.9%
TA Delay Lines: Delay line n=1,2,3,4	Good Trigger + Good VDC information.	N_{vdc} = VDC analysis good. N_{dl_n} = TA delay line n good + VDC analysis good.	$C_{ta\_delay\_n} = N_{dl\_n} / N_{vdc}$	TA 1: 96.7% TA 2: 94.9% TA 3: 96.9% TA 4: 96.7%
TA Delay Line Pairs	Good Trigger + Good VDC.	$C_{TA\_plane1} = C_{TA\_dl1} C_{TA\_dl2}$ $C_{TA\_plane2} = C_{TA\_dl3} C_{TA\_dl4}$	$C_{TA\_4/4} = C_{TA\_plane1} C_{TA\_plane2}$ $C_{TA\_2/4} = 1 - (1 - C_{TA\_plane1}) \cdot (1 - C_{TA\_plane2})$	Pl 1: 91.8% Pl 2: 93.7% T 4/4:86.1% T 2/4:99.8%
TA Analysis Plane p=1,2	Good Trigger + Good VDC + Good TA Delay lines	$N_{vdc+dls}$ = Good VDC and TA delays N_{not_adj} = Wires are not adjacent. N_{drbad} = Bad drift sum.	$C^{p}_{TA\_anal} = 1 - \frac{N_{not\_adj} + N_{drbad}}{N_{vdc+dls}}$	Pl 1: 93.9% Pl 2: 93.6%
TA Analysis Total.	2 out of 4 planes are good	-	$C^{tot}_{1/2} = 1 - (1 - C^{[1]}_{ta\_anal} C_{ta\_dl\_1} C_{ta\_dl\_2}) \cdot (1 - C^{[2]}_{ta\_anal} C_{ta\_dl\_3} C_{ta\_dl\_4})$	98.1%
TA Analysis Total.	All 4 planes are good	-	$C^{tot}_{2/2} = C^{[1]}_{ta\_anal} C^{[2]}_{ta\_anal} \cdot \prod_{i=1}^{4} C_{ta\_dl\_i}$	75.7%
Event Inside Bounds	All VDC + All $TA_{1/2}$ good	N_{inside} = Inside boundaries. $N_{outside}$ = Outside boundaries	$C_{bounds} = \frac{N_{inside} + N_{outside}}{N_{inside}}$	96.9%
ELSSY Tot	-	-	$C_{tot} = C_{vdc\_tot} \cdot C^{tot}_{1/2} \cdot C_{bounds}$	90.2%

with an efficiency correction, but has to be accounted for in the size of the momentum acceptance. The other tests in the VDC analysis are mutually exclusive, and should thus be lumped together in one. This is done in N_{other} which is the sum of the three tests.

The Transverse Arrays were not as efficient as the VDC. For these chambers the TDCs would frequently fail in pairs on time-out, indicating that there was no signal on the wire, or the signal was corrupted. With an oscilloscope it was verified that this was caused by occasional bursts of high frequency noise on all delay lines. As a result the failing of the TA delay lines are no longer independent and thus they cannot be included in the condition for a "good particle" when the TA delay lines themselves are being tested. The efficiency of the wires was checked by testing for time-outs in the TDCs of a delay line under the condition that the VDC had all three delay lines fire, and there was a good trigger. Since one of the two planes in the TAs provides sufficient information to analyze the particle track, the condition that all four TA chambers decode correctly is overly stringent. When the condition is eased to one out of two chambers decode correctly, the overall efficiency increases from 75.7% to 98.1% for a typical run. The data was analyzed requiring only one plane, to increase the efficiency of the spectrometer.

As a final test of the detector analysis a "bounds" test verifies that the calculated particle track for an event is within the physical limits of the spectrometer. Particles that do not fall within these limits are thrown out. The most likely causes for such events are multiple scattering and bad information in the TDC that was not caught by an earlier test. The condition for this test is that none of the previous tests failed, since otherwise a track could not be calculated. For a typical run about 3% of the events failed the bounds test. The overall efficiency of the ELSSY detector package, as derived from the combination of all these tests, varied between 89.8% and 94%.

4.2.3 ELSSY Focal Plane Efficiency.

The measurement of the ELSSY focal plane efficiency was broken up into two parts. First the relative focal plane efficiency was determined by collecting data for the carbon quasielastic peak at several settings of the central momentum. Next the shape of the carbon quasielastic peak was deconvoluted from the spectrum to form the focal plane efficiency curve. Finally the overall efficiency of ELSSY was measured by comparing H(e,e') data with a well known parametrization.

The relative focal plane efficiency calibration produces the spectrometer acceptance profile that is used in the C analyzer to correct for differences in the spectrometer acceptance as a function of X_f. This profile is a one dimensional approximation of the three dimensional acceptance of the spectrometer. In the ideal case the three dimensional acceptance volume would be calculated in the ***Acceptance*** Monte Carlo, and then compared with experiment. This volume could then be divided out of the data event by event, instead of dividing out the acceptance profile. Alternatively it could be divided out of the final histograms by the ***Addcross*** program together with the acceptance volume. However the theoretical model of the spectrometer that is needed for such a calculation was not available, and constructing one was outside the scope of this experiment. Also such a calculation could not easily account for local variations in the trigger efficiency of the detector package. Therefore a one dimensional profile was used instead.

If there existed a target that produced a perfectly flat spectrum, then this target could be used to measure the spectrometer profile in a single run. Since such a target does not exist, the carbon quasielastic peak was used. This means that the intrinsic shape of the quasielastic peak has to be deconvoluted from the data to separate out the spectrometer profile. The profiles of ELSSY and OOPS were measured in parallel by acquiring carbon data on the quasielastic peak in a series of runs, with overlapping momentum regions for the spectrometers for each run. The quasielastic region is chosen because it has a sufficiently smooth cross section. The experimental parameters for these runs are summarized in table 4.3. The resulting histograms of delta were deconvoluted by the program ***RELEFF***[6]. This program takes the results from all the runs and then fits a polynomial curve to the experimental cross section. This curve is then used to adjust the efficiency of each bin. With the resulting new spectra this process is repeated until the χ^2 of the fit between two successive iterations changes by less than a preset limit, usually 0.001.

The relative efficiency profile and the cross section for ELSSY are presented in figure 4.3. This profile was smoothed by rebinning the curve by a factor of 10, to remove most of the fluctuations due to poor statistics. The remaining profile is fairly flat between

Table 4.3 Experimental Parameters for the Relative Focal-plane Efficiency Runs.

	Run	ELSSY	OOPS
Incident Energy		577 MeV	
Target		^{12}C 69 mg/cm^2	
angle:		48.73°	53.93°
Central Mom. 1:	1032	485.5 MeV/c	422.8 MeV/c
Central Mom. 2	1031	490.3 MeV/c	431.2 MeV/c
Central Mom. 3	1029,1030	495.0 MeV/c	449.3 MeV/c
Central Mom. 4	1028	502.7 MeV/c	458.2 MeV/c

---

[6] Steve Penn, *Ph.D. Thesis, MIT,* unpublished (1993),
Paul Ulmer, *Ph.D. Thesis, MIT,* unpublished (1987)

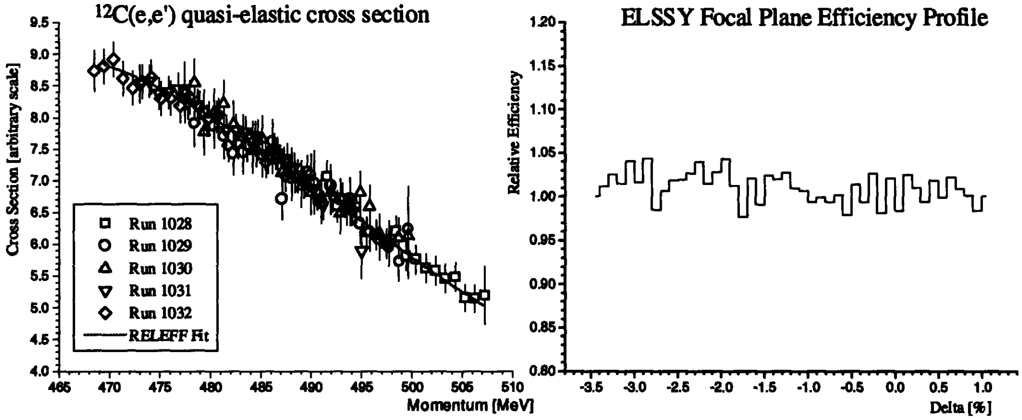

Figure 4.3 ELSSY relative efficiency profile, and the $^{12}C(e,e')$ quasielastic cross section from the program RELEFF.

-3.5% and 1%, with some fluctuations at the ±3% level. These fluctuations could be caused by local variations in efficiency or still be statistical in nature. They did not affect the results of the coincidence data significantly since these data average over a sufficient number of bins to remove local variations in efficiency. The efficiency for momenta higher than 1% dropped off quickly due to the misalignment of the scintillators (see chapter 2). This region was not used for the coincidence data, and no efficiency profile was generated for it. The profile was normalized to 1, which was taken into account in the overall normalization procedure for ELSSY.

The final step in normalizing the ELSSY spectrometer involves an overall efficiency test, or "trigger" efficiency calibration. Since it was not possible to calibrate the detection efficiency of the scintillators and the Cherenkov counter directly, the overall spectrometer efficiency was normalized to a well known cross section. This has the disadvantage that it couples this measurement with a previous measurement. On the other hand it has the advantage that this normalization includes all aspects of the spectrometer, such as multiple scattering, inefficiencies in the wire chambers that are not yet accounted for, and the detection efficiency in the scintillators and Cherenkov counter.

The ELSSY trigger efficiency was normalized to the $^{1}H(e,e')$ cross section, at a momentum transfer, q, around 444 MeV/c and an energy transfer of 100 MeV. The beam energy for these normalization runs was 577 MeV, and three scattering angles were used: 48.26°, 48.73° and 49.26°. The target was a 52.6 mg/cm^2 spinner target and the peak beam current was 1 mA. These runs were also used for the OOPS H(e,e'p) normalization. The data were corrected for the computer dead-times and all the known detector efficiencies and then plotted as a kinematically corrected spectrum versus δ. Figure 4.4 shows such a histogram. There was a small amount of carbon contamination in the spectrum that manifested itself as a smoothly varying background. This background was parametrized by a fit to the super-elastic region of the hydrogen peak. This spectrum was then fit with ALLFIT, which subtracted the background, and corrected for radiative processes.

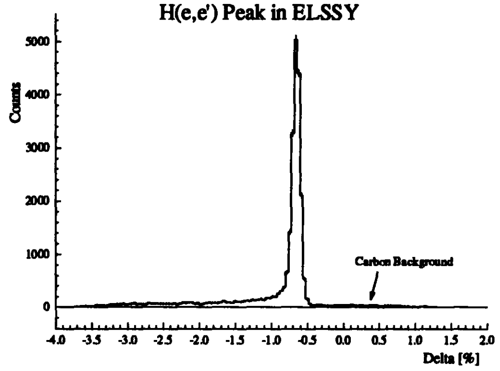

Figure 4.4 Kinematically corrected ELSSY delta histogram.

The resulting cross sections were compared to the H(e,e') cross section derived from the Mainz fit to the proton form factors[7]. The details of the Mainz parametrization are delegated to Appendix B. The cross section of a proton is found from the form factors by:

$$\frac{d\sigma}{d\Omega_e} = F_{rec}^{-1}\sigma_{Mott}|F|^2 \tag{4.14}$$

where σ_{Mott} is the Mott cross section given by equation 1.22, and F_{rec} is the recoil function given by:

$$F_{rec} = 1 + \frac{2E_b}{M_p}\sin^2\left(\theta/2\right) \tag{4.15}$$

The form factor F is derived from the electric and magnetic form factors G_E and G_M by:

$$F = \frac{G_E^2 + \tau G_M^2}{1+\tau} + 2\tau G_M^2 \tan^2\left(\theta_e/2\right) \tag{4.16}$$

with $\tau = q_\mu^2/4M_p^2$.

---

[7] C. G. Simon et. al., *Nucl. Phys.* **A333** (1980) 381.

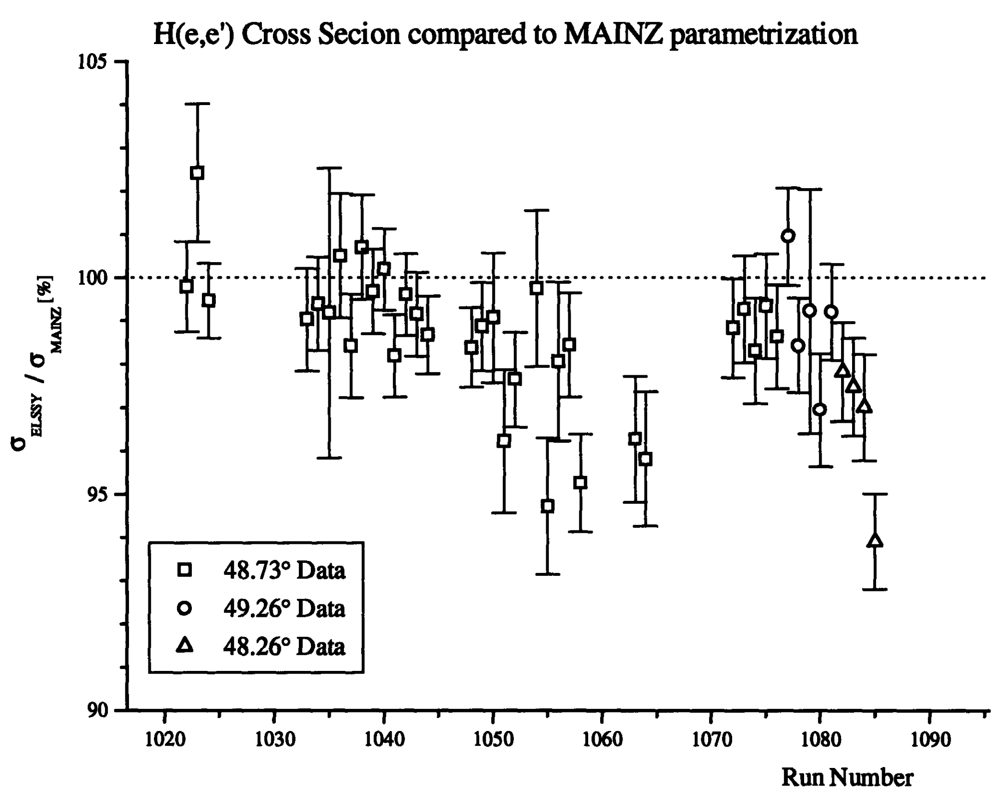

Figure 4.5 Ratio of the H(e,e') Cross Section measured by ELSSY to the MAINZ prediction.

The results of the comparison are plotted in figure 4.5 as a ratio with respect to the run number. Since the runs were approximately of equal length, the x-axis is directly related to the amount of charge on the target. The graph shows several dips in the experimental cross section, one after run 1055, one after run 1081, and a smaller one after run 1042. The decrease in the cross section in these regions is attributed to the loss of hydrogen in the target due to "target burn", caused by the beam. After each of these dips there were several runs with a different target. When the CH_2 target was put back in the beam it would be at a slightly different height, causing a different area of the target to be exposed to the beam, and the cross section was then restored to its original strength. The ELSSY normalization from these experiments would be 98.0±0.2% if all runs are included, and 98.4±0.2% if the target depleted runs are left out. This latter number was used to correct the coincidence data.

This same calibration was repeated at a beam energy of 292 MeV and a scattering angle of 117°. This resulted in a normalization of 99.1±0.3%, which is consistent with the previous results. There was also an abundance of $^{12}C(e,e')$ data which could possibly verify this calibration. However, the existing parametrizations of the carbon cross-section vary by 5 to 6% relative to each other, and are therefore not useful for this purpose.

4.3 OOPS Calibrations.

The calibration of the OOPS spectrometer follows very similar lines to the calibration of the ELSSY spectrometer. It includes a measurement of the optical properties and a momentum calibration. The overall detector normalization was treated differently since it could make use of the H(e,e'p) reaction.

The OOPS spectrometer was difficult to position since it did not have an elaborate support mechanism and so none of the six spatial coordinates were constrained. It was placed using the North Hall crane, and fine alignment was done with a set of pulleys and the adjustable feet on the support platform. The goal was to be able to position OOPS with an accuracy of 1 mm and 1 mr in all coordinates. The final placement of OOPS was then checked using theodolites and a precision level. The distance from the target was established using the radial distance of the edge of the target chamber to the front of the dipole. The pointing angle ("yawl") and scattering angle of OOPS were determined by positioning the ELSSY spectrometer at the complementary angle and optically aligning two markers on top of the OOPS dipole. The "pitch" and "roll" were established with a precision level. For this analysis an uncertainty in scattering angle of 0.1° was used. This is slightly larger than the 1 mr positioning accuracy, since it also includes an estimated error due to the uncertainty in the recontruction of the target coordinates. The matrix elements needed for this reconstruction were derived from data at a different OOPS angle.

4.3.1 OOPS Momentum calibration.

The OOPS wire chambers do not lie along the focal plane, which is tilted at approximately 12° with respect to the central ray. This means that the higher order matrix elements become more important for the computation of δ. These matrix elements were established up to third order as part of the OOPS optics study which is described in more detail in appendix A. The maximum resolution that was achieved with these matrix elements was 0.5%. The results are presented in table 4.4. There was no improvement in going up to fourth order.

Table 4.4 OOPS Delta Matrix Elements.

1	0.18
x	4.65
θ	0.0049
$x\theta$	0.0217
y^2	0.0021
$x\theta^2$	$0.82 \cdot 10^{-4}$
θy^2	$-0.54 \cdot 10^{-4}$

During the experiments the central momentum of the OOPS spectrometer was computed from the design values of the magnets. For the data analysis the central momentum of OOPS was adjusted to put the hydrogen peak at 0 MeV in the missing energy spectrum. During the analysis of the coincidence data on carbon it was found that the p-shell peak would shift in energy by as much as 3 MeV. It could not be established whether these shifts were caused by fluctuations in the beam energy, the position of the beam on target (which couples with the momentum measured by ELSSY) or by instabilities in the OOPS power supply. One run had to be eliminated from the data because this shift was larger than the resolution of the missing energy peak.

4.3.2 OOPS Detector Normalizations.

The efficiency of the OOPS detector package was determined in a similar manner as the efficiency of the ELSSY detectors. There were four items that contributed to the efficiency correction:

- Dead-time in the scintillators due to the electronics.
- The efficiency of the delay lines.
- The efficiency of the odd/even amplifier circuit.
- The efficiency of the wire chamber analysis.

The scintillator dead-time correction could not be derived from the number of events that passed or failed a set of tests, because the scintillators were part of the trigger. Since there were three scintillators in the detector package it would have been possible to accumulate data with a "2 out of 3" trigger, where only two scintillators are required for an event to be recorded. This would have allowed for an analysis in which the efficiency of the scintillators was tested by counting how often a scintillator failed to fire while all other scintillators and the wire chambers fired properly. The data that are accumulated in such a manner have the disadvantage that the timing of the spectrometer trigger signal will now jump from the second scintillator to one of the other

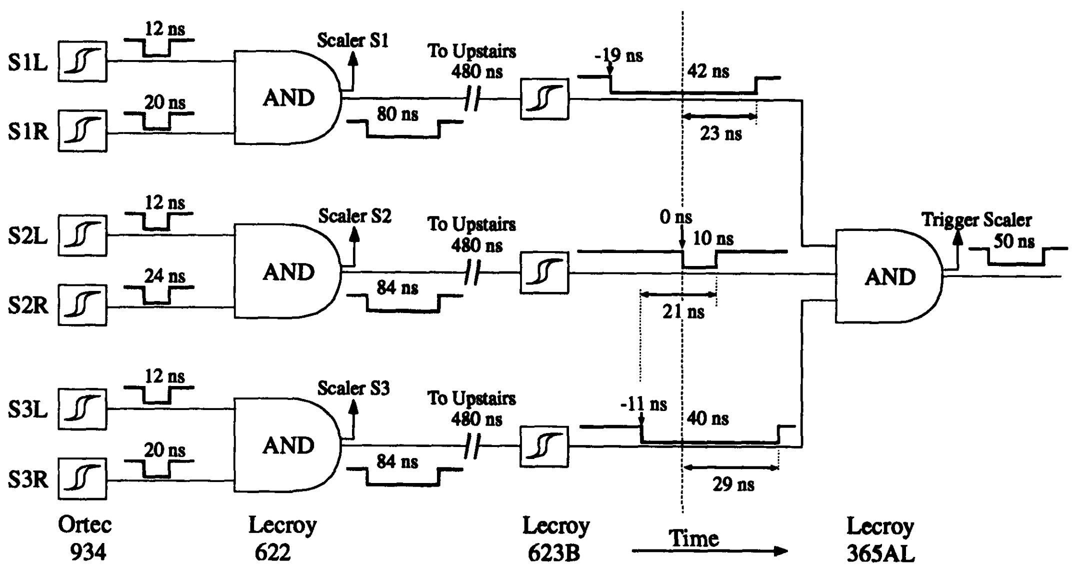

Figure 4.6 Section of the OOPS trigger circuit responsible for the electronics dead-times. The widths of the output pulses are indicated for each module, and the relative timing for those modules that are critical.

scintillators, depending on whether the second scintillator fired or not. This timing fluctuation could be corrected in software, as is described in section 3.2.6.a, but adds a significant complication to the analysis. Alternatively the events that caused less than three scintillators to fire could be rejected from further analysis. This approach was not followed for these experiments because it significantly increased the OOPS trigger rate, and would have increased the computer and electronics dead-times. Unfortunately not enough calibration experiments were performed to accurately measure the scintillator inefficiency as a function of trigger rate.

For this experiment the trigger efficiency was calculated directly from the trigger rates for each of the scintillators. To understand the behavior of the electronics, the circuit was modeled with a Monte Carlo program, as described in section 2.5.4. This study concluded that the rate dependent trigger efficiency was caused by accidental triggers of the scintillators, presumably due to stray particles.

Figure 4.6 shows the section of the electronics that was responsible for the inefficiency, with some of the widths and relative timings of the signals indicated on the graph. All the efficiency problems for this circuit occur at the Lecroy 623B discriminators, which reconditioned the pulses from the "down stairs" electronics. The output of all the modules are "updating", which means that a second pulse that arrives before the output has reset to logical 0, will extend the length of the output pulse, rather than pulse a second time. The result is that a random trigger of one of the scintillators, that comes less than 84 ns (80 ns for S1) before the actual 3-fold trigger, will cause a single long pulse on the output of the AND. When this pulse is discriminated again by the upstairs electronics, the width of the pulse is reset to a much shorter length. The net effect of this is that this pulse is shifted to an earlier time. If the pulse is shifted enough it will no longer result in a coincidence and the trigger is lost. In a similar manner the trigger will be lost (and not counted) if two 3-fold triggers are separated by less than 80 ns. The timing windows for each of these situations are presented in table 4.5.

Table 4.5 Timing windows for random triggers that preempt the real trigger.

Scintillator	**Low, t_1**	**High, t_2**
S1	-80 ns	-23 ns
S2	-84 ns	-21 ns
S3	-84 ns	-29 ns
6-fold coin.	-80 ns	0 ns

The distribution of the random triggers follow Poisson statistics, so that the time distribution of events is described by the Poisson distribution:

$$P(n,t,\tau)=\frac{1}{n!}\left(t/\tau\right)^{n}e^{-t/\tau} \qquad \textbf{(4.17)}$$

which gives the probability of observing n events in time interval t when the average pulse separation is τ, which is the inverse of the rate. Thus the probability of an event being pre-empted is given by the likelihood that an accidental pulse arrives between times t_1 and t_2, which is equal to:

$$P(n=1,t_1<t<t_2,\tau)=\frac{t_2}{\tau}e^{-|t_2/\tau|}-\frac{t_1}{\tau}e^{-|t_1/\tau|} \qquad \textbf{(4.18)}$$

Where the timing window is $[t1,t2]$, and the assumption is made that $t/\tau \ll 1$ so that only one accidental needs to be accounted for. The efficiency of the circuit is then just $1\text{-}P$, which can be calculated from pulse the rates on the AND circuit. The overall efficiency is then just the product of each of the efficiencies. For a typical run about 3% of the events were lost.

The OOPS wire chamber efficiencies are determined by a set of tests in the test package of the Q analyzer in a similar manner as the efficiencies for the ELSSY detector. The condition for a "good particle" in OOPS was that all three scintillators had a good signal indicating the particle was a proton, all six delay lines fired, and there was a good LAM signal and no pile-up. The test requiring all odd/even amplifiers to produce an Odd+Even signal, is left out of the "good particle" test, because the response time of the odd/even amplifiers is too slow. This test would effectively eliminate all closely spaced events, which are a significant source of the inefficiency of the detector.

The tests that were used for the OOPS detector efficiency analysis are summarized in table 4.6, with the results for a typical run indicated in the last column. The individual delay lines were fairly efficient, failing less than 1% of the time, but the Odd/Even decision did not perform as well. This was caused by the slow response time of the Odd/Even amplifiers, as noted in section 2.5.2. The "analysis" test checks whether the drift time could be decoded properly. A random pulse on a delay line that arrives at the TDC just before the real trigger can cause this TDC to stop counting early. This can result in a drift time that cannot be converted to a drift distance. These events would fail on the analysis for that delay line, which occurred for about 2.4% of the events. This number is directly linked with the amount of noise on the delay lines. This noise can be caused by stray particles hitting the detector.

The overall efficiency of the OOPS detector package is only 58.8% when all three chambers are required. Fortunately this improves when only two out of the three chambers are required. In this case the efficiency is restored to an acceptable 78.8%. The OOPS detector efficiency would have been greatly improved with better shielding, better optimized trigger electronics and the redesigned Odd/Even amplifiers.

Table 4.6 Tests for the analysis of the OOPS efficiency.

Test	Condition	N_x in formula	Formula	Result
Scintillators	-	$C_\chi = \frac{t_{2,\chi}}{\tau_\chi} e^{-\lvert t_{2,\chi}/\tau_\chi \rvert} - \frac{t_{1,\chi}}{\tau_\chi} e^{-\lvert t_{1,\chi}/\tau_\chi \rvert}$	$C_{sc} = C_{s1} \cdot C_{s2} \cdot C_{s3} \cdot C_{6fold}$	94.8%
Delay Line /	Good Trigger + Proton	N_6= All 6 delay lines OK. N_i = Delay line i failed, all other delay lines OK.	$C_i^{dl} = N_6 \big/ (N_6 + N_i)$	~99.4%
Odd/Even *i*	Good Trigger + Proton + All delay lines	N_{lr6} = All 6 O+E's OK. N_{lr_i} = O+E i failed, all other O+E's OK.	$C_i^{lr} = N_{lr6} \big/ (N_{lr6} + N_{lr\_i})$	~97.3%
Analysis *i*	Good Trigger + Proton + All delay lines + All LR's	N_{an6}= All 6 planes OK. N_{an_i}= Plane i failed analysis. (bad drift time)	$C_i^{an} = N_{an6} \big/ (N_{an6} + N_{an\_i}$	~97.6%
Plane *i* Combined	-	-	$C_i = C_i^{dl} \cdot C_i^{lr} \cdot C_i^{an}$	~94.4%
Chamber Total 3/3	-	-	$C_{3/3}^{cham} = C_1^x \cdot C_2^x \cdot C_3^x \cdot C_1^y \cdot C_2^y \cdot C_3^y$	70.9%
Chamber Total 2./3	-	$C_{2/3}^{x,y} = C_1^{x,y} \cdot C_2^{x,y} + C_1^{x,y} \cdot C_3^{x,y} + C_2^{x,y} \cdot C_3^{x,y} - 2C_1^{x,y} \cdot C_2^{x,y} \cdot C_3^{x,y}$	$C_{2/3}^{cham} = C_{2/3}^x \cdot C_{2/3}^y$	98.2%
Event Inside Bounds 3/3	X,Y 3/3 + Good Trigger + Protons	N_{inside}= Inside boundaries $N_{outside}$= Outside boundaries	$C_{3/3}^{bounds} = \frac{N_{inside} + N_{outside}}{N_{inside}}$	87.4%
Event Inside Bounds 2/3	X,Y 2/3 + Good Trigger + Protons	N_{inside}= Inside boundaries $N_{outside}$= Outside boundaries	$C_{2/3}^{bounds} = \frac{N_{inside} + N_{outside}}{N_{inside}}$	84.4%
Detector Total 3/3	-	-	$C_{3/3}^{tot} = C_{3/3}^{cham} \cdot C_{3/3}^{bounds} \cdot C_{sc}$	58.8%
Detector Total 2/3	-	-	$C_{2/3}^{tot} = C_{2/3}^{cham} \cdot C_{2/3}^{bounds} \cdot C_{sc}$	78.8%

4.3.3 OOPS Focal Plane Efficiency.

The OOPS focal plane efficiency profile was determined in a similar manner as the profile for ELSSY, except that the C(e,p) cross section was used instead of the C(e,e') cross section. The resulting profile and the quasi-elastic cross section are plotted in figure 4.7. The OOPS profile is fairly flat between -6% and 6% and begins to drop off towards ±10%. The efficiency for the bins beyond ±10%, all the way out to ±20%, drops off dramatically. This region was not useful for analysis of the coincidence data, and no profile was generated for it. The profile for OOPS was smoothed using a third order spline fit. This smoothed out some of the local oscillations in the profile due to poor statistics, but only marginally improved the data analysis. The OOPS profile curve is normalized to 1 between -10% and +10%. As a result the central region from -1% to

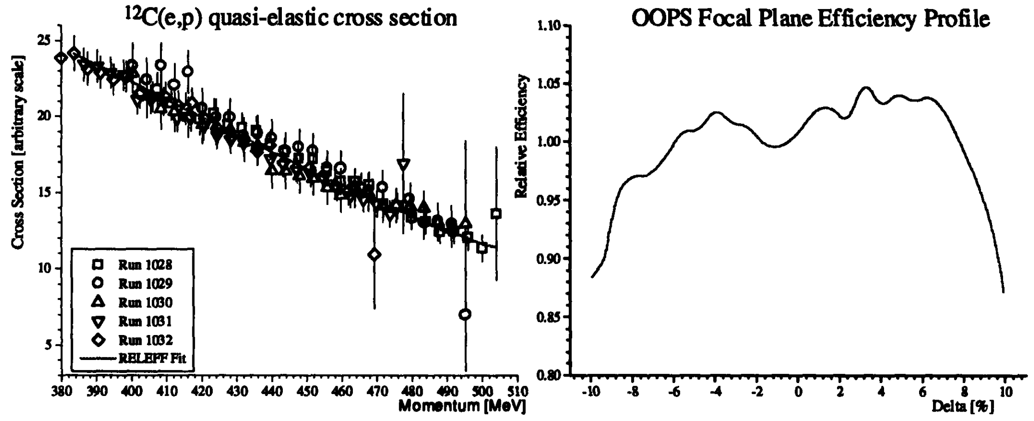

Figure 4.7 OOPS relative efficiency profile, and the ^{12}C(e,p) quasielastic cross section from the program RELEFF.

+1% is slightly higher, averaging at 1.01. This is taken into account when the overall OOPS normalization is computed.

The overall OOPS normalization was determined from a series of H(e,e'p) runs. Because the H(e,e'p) reaction is over determined, the direction of the recoiling proton can be computed from the electron kinematics. This allows for a direct normalization of the proton spectrometer, since the experiment can be set up in such a manner that for each electron in the electron spectrometer, a corresponding proton is expected in the proton spectrometer. The normalization of the proton spectrometer is then given by:

$$C_{prot} = \frac{N_{coin}}{N_{elec}} \tag{4.19}$$

where N_{elec} is the number of events in the electron spectrometer for a single arm spectrum of X_f, and N_{coin} is the number of coincidence events in that same spectrum. The wire chamber efficiencies for the proton spectrometer do not need to be accounted for, since the proton spectrometer is only used to tag the coincidence events. The only efficiencies that are important are the efficiencies of the electron spectrometer and the trigger efficiency of the proton spectrometer. This includes the efficiency of the trigger electronics of the proton spectrometer and the coincidence module, so that these are also calibrated.

For a thin, pure hydrogen target, a similar reaction could be used to calibrate the electron spectrometer. The situation is somewhat complicated by the use of a CH_2 target of finite thickness, because of multiple scattering in the target. Also the carbon in the CH_2 target will cause a carbon background in the electron single arm spectrum, making it more difficult to accurately count the events that belong in the hydrogen peak. This background is absent from the coincidence spectrum because the kinematics are very unfavorable for C(e,e'p). This problem can be rectified by a background subtraction, but this would mean that carbon data have to be accumulated for a similar amount of time as the CH_2 data.[8] The other possibility is to estimate the background strength from the super elastic region. This latter procedure was used in this analysis, since insufficient carbon background data were available, and the background was small enough that this would not add significantly to the uncertainty of the measurement.

For most experiments the number of events that scatter into the acceptance due to multiple scattering in the target is comparable to the number of events that scatter out of the acceptance. This is valid to about 0.1% and thus no corrections are necessary. For the H(e,e'p) reaction however the situation is slightly different since the tight beam of tagged protons can only scatter out of the acceptance, no events can scatter in. This effect shows up clearly in the data of a number of runs where the overlap between the proton bundle and the acceptance of OOPS was varied by varying the ELSSY slit settings. Figure 4.8 illustrates how the ELSSY acceptance maps onto the OOPS acceptance for several slit settings.

The data for several such runs were analyzed and compared with a multiple scattering calculation by a Monte Carlo program. This program simulated the experimental situation by sampling the Mainz H(e,e') distribution to generate events in which the electron falls within the ELSSY acceptance. The proton trajectory was then calculated from the kinematics and passed to a program called REVMOC[9]. This program traces a particles through a spectrometer, modeled as a series of magnetic elements interspersed by solids and gasses. It accounts for all multiple scattering and nuclear absorption processes in these materials. The input to REVMOC was a model of the OOPS spectrometer derived from the design parameters of the magnets, and the properties of the target and all windows in the target chamber, spectrometer and detector package.

---

[8] Background subtractions are only useful if the background that is being subtracted has similar statistics and characteristics as the background in the original. Thus an equal amount of time has to be spend taking data with a target of the same thickness.

[9] C. Kost and P. Reeve, Technical Report No. TRI-DN-82-28, TRIUMF (unpub.)

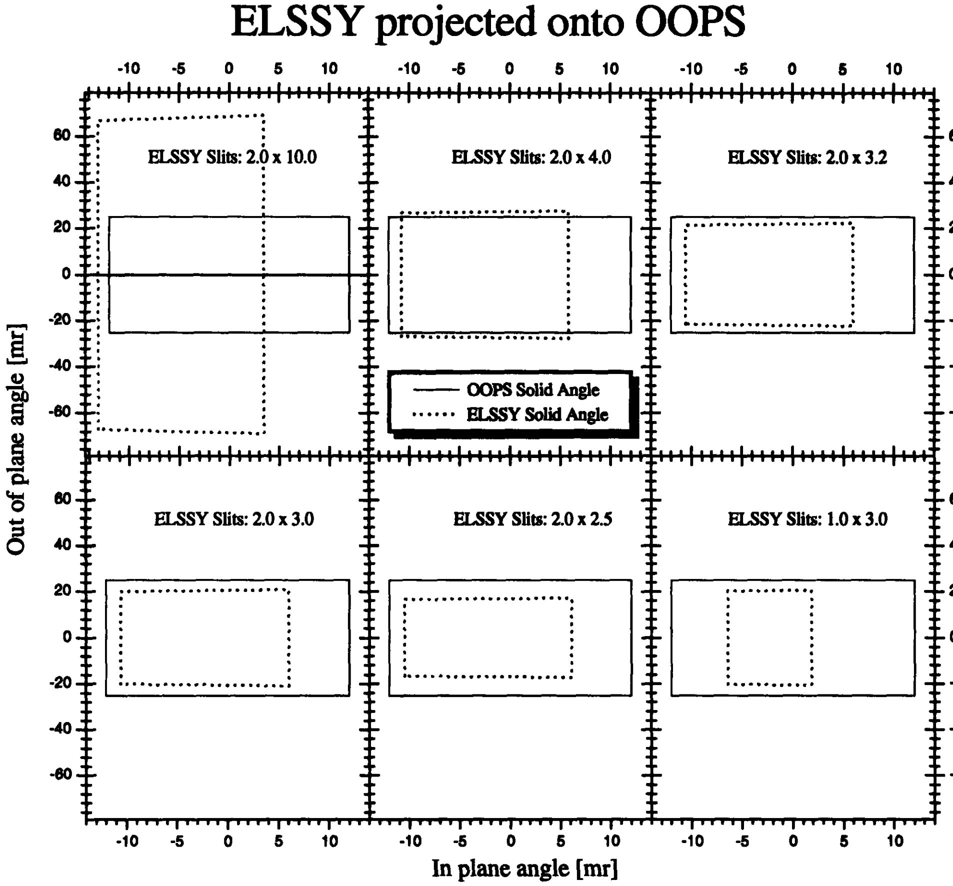

Figure 4.8 Overlap of the OOPS acceptance and the ELSSY acceptance for the H(e,e'p) reaction. The beam energy for these runs was 577 MeV, somewhat lower than expected, which caused the in plane misalignment between OOPS and ELSSY. The OOPS scattering angle was 53.9° and the ELSSY scattering angle was 48.7°.

The calculation was performed for the same slit settings as in the experiment to facilitate a direct comparison. The results of this calculation are presented in figure 4.9, with the y-axis representing the relative efficiency of the OOPS spectrometer as defined by equation 4.19. The calculation does not give a 100% efficiency even for those runs where the acceptance of ELSSY falls completely inside the OOPS acceptance. This is caused by protons scattering out of the OOPS acceptance, due to the multiple scattering in the target, which causes a loss of about 1%. For less restricted kinematics this would be offset by a nearly equal amount of scattering into the acceptance, thus this loss does not represent an inefficiency of OOPS.

The experiments were performed at a beam energy of 576 MeV, and a proton scattering angle of 53.93°. The electron scattering angles were 48.26°, 48.73°, and

49.26°. Three angles were used to allow for a study of the alignment of the OOPS spectrometer, and to ensure a complete coverage of the OOPS acceptance. The data were analyzed with corrections for computer live-times, pile-up, the efficiency of the ELSSY detector package, and the electronics dead-time of the OOPS scintillators. Taking all these effects into account there is still a discrepancy of about 3.7% ± 1% in the OOPS efficiency for the smallest slit setting. This discrepancy cannot be attributed to any of the known efficiencies of the detector package or the electronics. Therefore it represents the combination of all efficiencies that are not yet taken into account in the analysis, such as the efficiency of the scintillator material and the light pipes. The data were corrected by 1/96.3% = 1.038 ± 0.01 to take this into account.

4.4 Beam Energy Calibration.

The beam energy is an important parameter for most experiments. It determines the kinematics (ω, q, θ_q), and enters directly into cross section calculations through the Mott cross section and the kinematic constants. An accurate beam energy calibration is essential to keep systematic errors to a minimum.

The beam energy is determined by the accelerator and the magnet settings in the switch yard. The energy spread of the beam is determined by the slits between the FB1 and FB2 bending magnets. In principle it should be possible to accurately determine the beam energy from the magnetic fields in these magnets, but hysteresis of the magnets and alignment shifts over time make such an approach inaccurate. So instead the accelerator is tuned to a nominal energy, and the accurate energy has to be determined experimentally. For this set of experiments the beam energy was determined using the differential recoil technique.[10] This technique uses the difference in the recoil term for two nuclei with different masses to extract the beam energy. The final electron energy for elastic electron scattering from a nucleus is given by (see also equation 4.6):

---

[10] More detail can be found in: D. Jordan, *Ph.D. Thesis, MIT*, unpublished (1994), and V. Bushan, *S.M. Thesis, MIT* (1992).

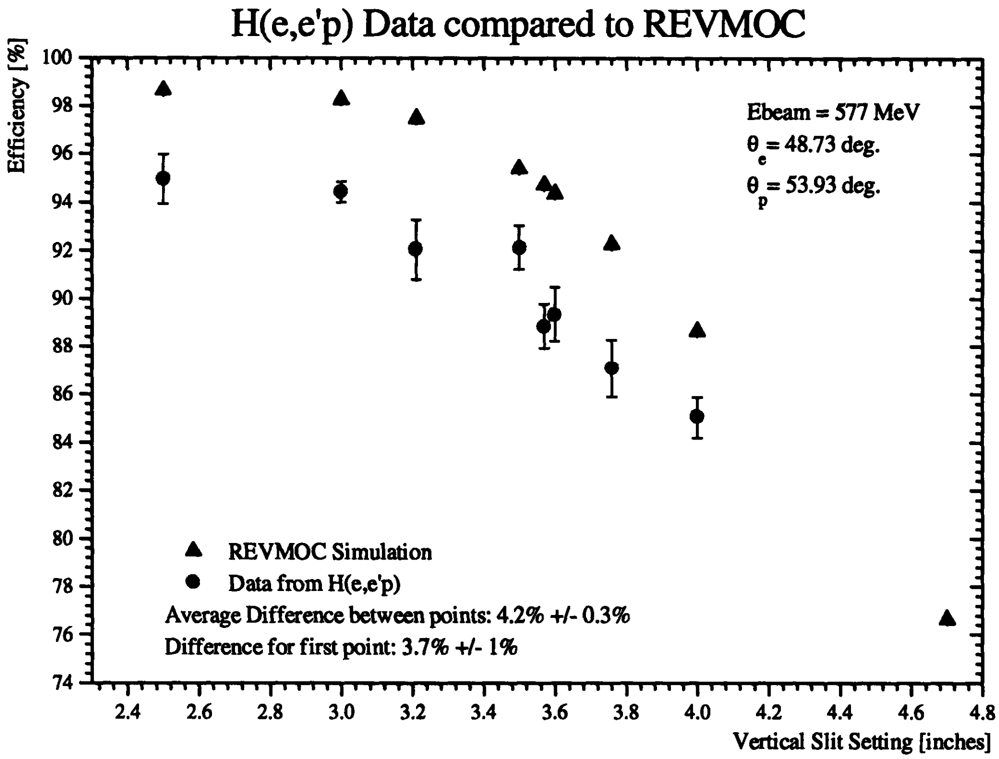

Figure 4.9 Comparison of the H(e,e'p) data to a Monte Carlo simulation as a function of the ELSSY slit settings.

$$E_f = F_{rec}^{-1}\left(E_0 - \tfrac{1}{2}E_{loss} - E_{exc} - \frac{E_{exc}^2}{2M_{tar}}\right) - \tfrac{1}{2}E_{loss}$$

$$F_{rec} = 1 + \frac{2(E_0 - \tfrac{1}{2}E_{loss})}{M_{tar}}\sin^2\left(\theta_e/2\right) \qquad (4.20)$$

where E_f is the final electron energy, E_o is the beam energy, E_{exc} is the energy level of an excited state, M_{tar} is the mass of the nucleus and θ_e is the electron scattering angle. The term E_{loss} is the average energy loss in the target due to multiple scattering. The assumption is made that the electron will, on average, interact at the center of the target, and thus lose 1/2 E_{loss} before the interaction, and 1/2 E_{loss} after the interaction. This is a good approximation for transmission mode scattering. For a 36 mg/cm^2 BeO target, E_{loss} is on the order of 40keV.

The beam energy is found from the measured difference in E_f for two different nuclei in the same target, by solving the equation:

$$\begin{aligned}\Delta E_f &= E_{f1} - E_{f2} \\ &= F_{rec,1}^{-1}\left(E_0 - E_{exc1} - \frac{E_{exc1}^2}{2M_{tar1}}\right) - F_{rec,2}^{-1}\left(E_0 - E_{exc2} - \frac{E_{exc2}^2}{2M_{tar2}}\right)\end{aligned} \tag{4.21}$$

for E_0, the beam energy. Here the energy loss in the target approximately cancels, to the order of $\left(F_{rec1}^{-1} - F_{rec2}^{-1}\right)E_{loss}/2$, because the same target contains both nuclei. The solution is a quadratic equation with one valid root, which is given by:

$$\begin{aligned}E_0 &= \left(-B+\sqrt{B^2-4AC}\right)/2A \\ A &= 2\sin^2(\tfrac{1}{2}\theta_e)\left[2\sin^2(\tfrac{1}{2}\theta_e)\frac{\Delta E_f}{M_{t1}M_{t2}} + \left(\frac{1}{M_{t1}} - \frac{1}{M_{t2}}\right)\right] \\ B &= 2\sin^2(\tfrac{1}{2}\theta_e)\left[\Delta E_f\left(\frac{1}{M_{t1}} + \frac{1}{M_{t2}}\right) + \left(\frac{E_{exc1}}{M_{t2}} - \frac{E_{exc2}}{M_{t1}} - \frac{E_{exc1}^2 + E_{exc2}^2}{2M_{t1}M_{t2}}\right)\right] \\ C &= \Delta E_f + E_{exc1} + \frac{E_{exc1}^2}{2M_{t1}} - E_{exc2} - \frac{E_{exc2}^2}{2M_{t2}}\end{aligned} \tag{4.22}$$

This method works reliably if the following subtleties are taken into account:

- The two nuclear states that are used come from the same target, and the molecules in the target are uniformly mixed. A sandwich target, such as a Carbon-Lithium-Fluoride does not work.
- The nuclear states that are used are well separated, and are not contaminated by other small peaks.
- The scattering angle that is used is the weighted mean of the actual scattering angle distribution. This can be approximated with a Monte Carlo calculation that takes the distribution of events weighted by the Mott cross section. The mean scattering angle differed from the central angle by about 0.02° at a central angle of 43.7°.
- An accurate calibration of the focal plane is needed to measure ΔE_f accurately. This calibration should be independent of the beam energy calibration.

For this study the beam energy was determined using a BeO target with a central scattering angle of 43.7° for ELSSY. The locations of the peaks for the ground states of beryllium and oxygen were found from a fit with ALLFIT. The resolution of the peaks in a kinematically corrected spectrum was on the order of $2\cdot10^{-4}$. The accuracy with which the peak locations could be determined was on the order of 10^{-5}, which was sufficient to achieve a precision in the final beam energy on the order of $5 \cdot 10^{-4}$, or 576.0 ± 0.3 MeV. However, the systematic uncertainty of this measurement is dominated by the uncertainty in the scattering angle. The positioning accuracy of ELSSY was approximately 0.05°, but the uncertainty of the horizontal beam position, which was about 1 mm, adds an additional uncertainty in the scattering angle of about 0.03°. The resulting uncertainty in the scattering angle is 0.06°, which contributes an uncertainty of 0.8 MeV to the final answer. The final result of the beam energy measurement is therefore 576.0 ± 0.3 ± 0.8 MeV.

Chapter 5 C(e,e'p) Data Analysis and Results

This chapter describes the results of the ^{12}C(e,e'p) experiment and the extraction of R_{LT}. Section 5.1 contains some specific details of the ^{12}C(e,e'p) data analysis that have not yet been given in previous chapters. Next the results will be presented and discussed in section 5.2, and a comparison to theoretical predictions will be made in section 5.3. Finally the conclusions are presented in section 5.4.

5.1 Data analysis.

The experimental data were taken in two sets of runs, and analyzed with the method that is described in chapter 3. The first set, with OOPS at 64.7°, contained 8 runs, and the second set, with OOPS at 42.9°, contained 13 runs. Of this last set, one run was rejected because the p-shell peak was shifted by 10 MeV to lower missing energy. No explanation could be found for this shift other than an unrecorded experimental error, such as an incorrect magnet setting. A second run was rejected because it contained too few counts to verify its integrity; the statistics were too small to observe any features in the histograms. Table 5.1 lists the runs that were used. The corrected time-of-flight counts in the table were adjusted for the efficiencies of both spectrometers, listed in the last column, and the background counts were subtracted. Notice that these carbon runs were interspersed with some of the deuterium runs, so that the run numbers are not always consecutive.

5.1.1 Phase Space overlap.

In order to extract R_{LT}, the data for ϕ_{pq}=0 and ϕ_{pq}= π has to overlap perfectly in (E_m, P_m). This ensures that each two dimensional bin in the final (E_m, P_m) histogram of the 42.9° data (ϕ_{pq}=0) has a corresponding bin in the histogram of the 64.7° data (ϕ_{pq}= π). The overlap is imposed by creating a mask that contains the value 1 in all bins that overlap, and 0 in all bins that don't. Each of the final histograms is then multiplied with

Table 5.1 Summary of C(e,e'p) data runs.

run #	OOPS Central mom.	Total Charge. (Coulombs)	corrected TOF (reals)*(efficiencies)	Total Efficiency Correction
OOPS Angle = 64.7°				
1312	440	0.0417	2731.	1.63
1314	404.99	0.00172	145.	1.68
1315	404.99	0.0172	1289.	1.65
1316	404.99	0.0326	2512.	1.56
1317	373	0.00203	97.	1.56
1318	373	0.0344	1593.	1.60
1319	343.27	0.0219	670.	1.62
1320	343.27	0.0168	482.	1.64
Total		0.168	9524.	
OOPS Angle = 42.9°				
1329	440	0.0410	1687.	1.65
1332	404.99	0.00811	379	1.70
1333	404.99	0.0244	1225.	1.71
1334	404.99	0.00158	76.	1.76
1335	404.99	0.0135	602.	1.69
1338	373	0.00919	303.	1.65
1339	373	0.00949	371.	1.62
1340	373	0.00309	106.	1.63
1341	373	0.00404	127.	1.63
1342	373	0.0106	371.	1.61
1343	343.26	0.0369	754.	1.65
Total		0.162	5999.	

this mask before the R_{LT} histogram is computed. The masking histogram is created by the following steps:

- Two two-dimensional phase-space histograms are created by the ***Acceptance*** program and ***Addcross***, see section 3.5. Each histogram contains the summed acceptance volume by which the summed counts histograms are divided to obtain a cross-section.
- These two phase-space histograms are divided by themselves, using a threshold. This creates two histograms, each with the value 1 in the bins where the acceptance volume is larger than the threshold, and 0 in all other bins. The best results were

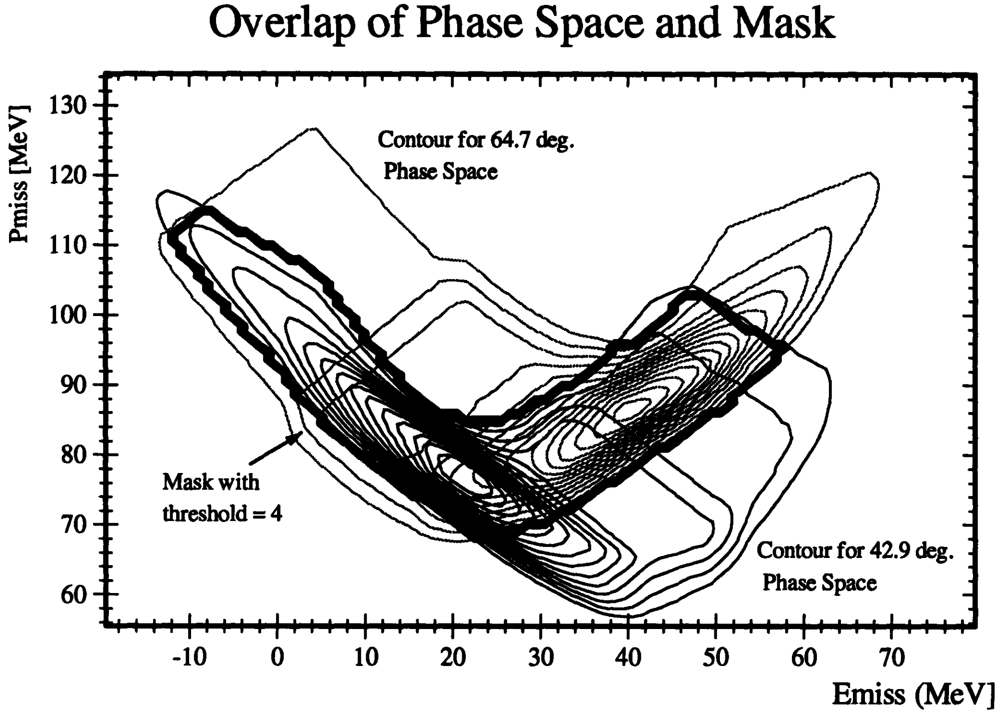

Figure 5.1 Contour histogram of the mask, overlaid on the two phase space histograms. The mask, indicated by the heavy black line, is used to enforce the overlap between the $\phi_{pq} = 0$ and $\phi_{pq} = \pi$ data. The mask does not extend beyond 55 MeV in missing energy. As a result the masked data sets do not sample in missing energy beyond 55 MeV, and no R_{LT} value can be extracted for that region.

obtained with a threshold of 4 (counts·Mev^{2}sr^2/nbarn)[1]. A smaller number causes unreasonably large error bars for the low phase-space regions, while a larger threshold would unnecessarily exclude more data.

- The two resulting histograms are multiplied together to create the final masking histogram, see figure 5.1.

To obtain a perfect overlap between the two sets of runs, the final cross-section histograms are each multiplied by the masking histogram. Notice that a considerable amount of data has to be rejected in order to obtain a proper overlap. The 42.9° and 64.7° acceptance volumes are reduced to 61% and 55% of their unmasked volume respectively. The mask does not extend beyond 55 MeV in missing energy. As a result

---

[1] These are the units for the final phase-space histogram. The counts histogram divided by this phase-space histogram gives a cross-section histogram in nbarn/MeV^2/sr^2.

the masked data sets do not sample in missing energy beyond 55 MeV, and no R_{LT} value can be extracted for that region.

The variable sets $\{q,\omega,E_m,P_m\}$ and $\{q,\omega,E_m,\theta_{pq}\}$ can both describe the kinematics equally well (see also section 3.1). Thus there is a direct transformation between P_m and θ_{pq}, which is given by:

$$\vec{P}_m = \vec{q} - \vec{p}_f \Rightarrow \cos(\theta_{pq}) = \frac{q^2 + p_f^2 - P_m^2}{2qp_f} \tag{5.1}$$

where P_m is the missing momentum and q is the momentum transfer. The variable p_f is the proton momentum. Its dependence on the $\{q,\omega,E_m,P_m\}$ variable set is derived from the definition of E_m (see equation 1.7):

$$\begin{aligned} p_f(\omega,E_m,P_m) &= \sqrt{(\omega + M_p - E_m - T_R)^2 - M_p^2} \\ T_R &= \sqrt{P_m^2 + M_R^2} - M_R \end{aligned} \tag{5.2}$$

The overlap of θ_{pq} between the two data sets is important because the extraction of R_{LT} depends on $\cos(\theta_{pq})$. Since the electron kinematics (q and ω) remained fixed for both sets of runs, it would be expected that θ_{pq} also has a perfect overlap on the masked histograms. This point is illustrated in the contour plot of figure 5.2, which is identical for both the zero and π side of the q-vector. Because θ_{pq} depends on ω, however, this overlap is only obtained if the acceptance in ω is sufficiently small, and does not vary much between the two data sets for each (E_m, P_m) bin. Since the actual problem of extracting R_{LT} is four dimensional (e.g. in $\{q,\omega,E_m,P_m\}$) a truly perfect overlap can only be obtained with a four dimensional analysis of the data. Such an analysis is not possible with the limited statistics of most experiments.

5.1.2 Extraction Point.

The final results of the experiment are an average over the acceptance. There are two possible methods to compare these results with theoretical calculations. The first method averages the results of a theoretical computation over the same acceptance as the experiment, so that a direct comparison is possible. This method is computationally very intensive and must be repeated for each theoretical calculation that is to be

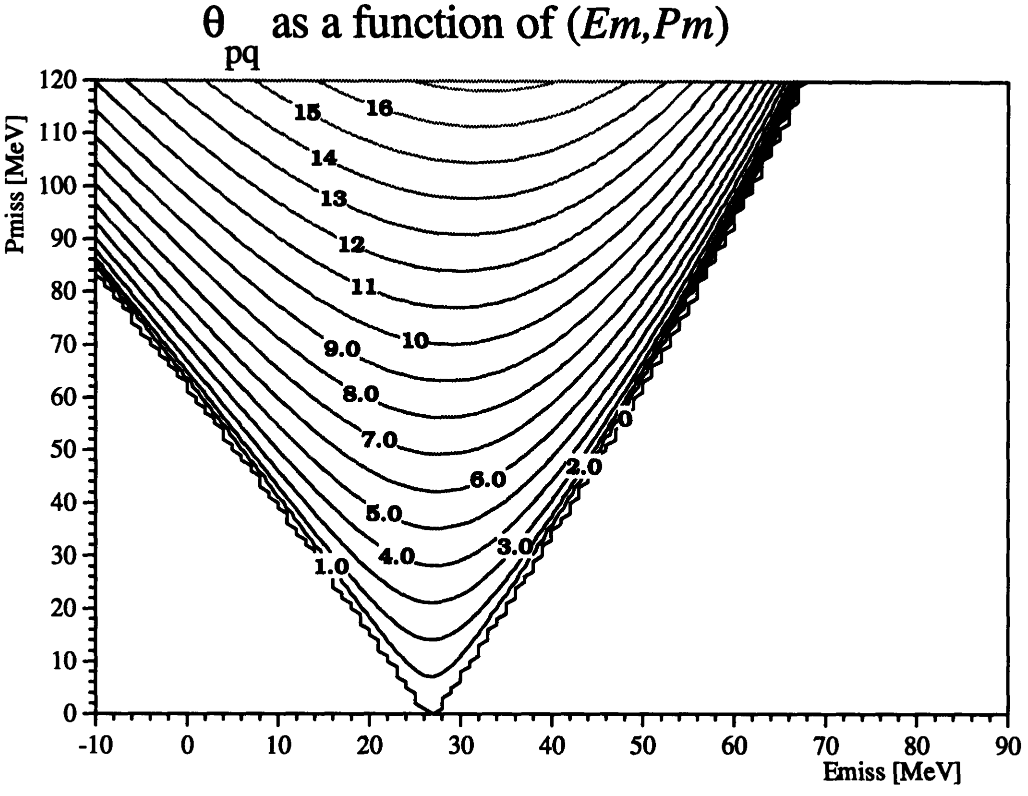

Figure 5.2 Contour plot of θ_{pq} as a function of (Em,Pm). This plot is identical for $\phi_{pq} = 0$ and $\phi_{pq} = \pi$. It can be used to determine the available kinematic region at a specific θ_{pq}. The numbers on the contour lines indicate the value of θ_{pq} in degrees.

compared with the data. Usually such computations are not available. A different method of comparison is to calculate an extraction point for the experimental data, which can be compared directly with theory.

The extraction point is the average of the kinematical variables over the acceptance. It is calculated by the ***Acceptance*** Monte Carlo program. The result of this calculation is presented in table 5.2, which contains four such points. The first two points are for the entire θ_p= 64.7° and θ_p= 42.9° acceptance, and the next two sets are for the masked region of this acceptance. It is important to distinguish the variables that depend on E_m or P_m (shaded in the table) from those that don't. The variables that don't depend on E_m or P_m are averaged over the entire acceptance in q and ω during the data analysis, while the variables that depend on E_m and/or P_m are averaged over only one bin of the (E_m, P_m) histogram for their E_m and/or P_m dependence. From the table it can be seen that the choice of representation in (E_m, P_m) is appropriate for the extraction of R_{LT}, since only E_m and P_m, and the variables that depend on them, vary significantly between the two

Table 5.2 Experimental Extraction Point

Variable	42.9°	64.7°	Masked 42.9°	Masked 64.7°
q	403.6 MeV/c	403.6 MeV/c	403.8 MeV/c	403.7 MeV/c
ω	111.9 MeV	111.9 MeV	110.1 MeV	110.1 MeV
E_m	28.01 MeV	27.94 MeV	18.36 MeV	28.70 MeV
P_m	86.36 MeV/c	95.37 MeV/c	87.17 MeV/c	87.88 MeV/c
P_{prot}	401.7 MeV/c	401.9 MeV/c	422.2 MeV/c	396.7 MeV/c
θ_e	-44.00°	-44.00°	-44.00°	-43.99°
θ_p	42.90°	64.70°	42.88°	64.68°
θ_{pq}^*	10.15°	-11.65°	10.42°	-11.38°
Jacobian	0.9998	1.0003	1.0052	0.9995
v_L	0.8518	0.8518	0.8566	0.8564
v_T	0.6247	0.6247	0.6260	0.6259
v_{LT}	-0.6801	-0.6801	-0.6829	-0.6827
v_{TT}	-0.4614	-0.4614	-0.4627	-0.4627
σ_{Mott}	6.83E-05	6.83E-05	6.83E-05	6.83E-05
F_{recoil}	1.0004	0.9999	0.9950	1.0006
C_{Bofli}	10.57	10.57	11.18	10.40
C_{kin}	0.03582	0.03582	0.03763	0.03536
σ_{ep} CC1	3.14E-05	4.30E-05	3.10E-05	4.30E-05

The shaded rows represent quantities that have a dependence on the missing energy or missing momentum. Their variation over a bin in the (E_m,P_m) histograms is much less. See chapter 1 for more information on the definitions of the variables.

* θ_{pq} has the sign convention of + when $\phi_{pq} = 0$, and - when $\phi_{pq} = \pi$, see figure 1.4

proton angle settings. For other experiments a different representation may be needed, for instance, (E_m,ω) for an R_L - R_T separation.

Due to the complicated nature of the phase space, it is not sufficient only to check whether the two data sets overlap when integrating over the entire phase space. It is still possible that the overlap is not perfect on a bin by bin basis. This is illustrated by table 5.3, which presents the same averages as table 5.2 for a single bin at $(E_m, P_m) = (24.5 MeV, 77.5 MeV/c)$ with a size of 1 MeV by 1 MeV/c. The variation of q between the two bins is 0.4%, and can be neglected. The variation of ω is 2.9%, which causes differences in the kinematic variables that depend on the electron kinematics. Several such variables, such as C_{kin} and v_{LT}, enter directly into the computation of R_{LT} (see section 5.1.4). Therefore the differences of these variables between the two data sets will affect the accuracy of the R_{LT} computation. This effect will be taken into account with the systematic uncertainties in section 5.1.5.

Table 5.3 Kinematic variables averaged over one bin.

Variable	64.7°	42.9 °
q	402.72	404.51
ω	109.84	106.66
E_m	24.50	24.50
P_m	77.50	77.50
P_{prot}	408.28	400.36
θ_e	-43.86	-44.04
θ_p	42.67	64.74
θ_{pq}^*	10.68	-10.96
Jacobian	1.00	1.00
v_L	0.8562	0.8657
v_T	0.6248	0.6288
v_{LT}	-0.6823	-0.6881
v_{TT}	-0.4627	-0.4652
σ_{Mott}	$6.915*10^{-5}$	$6.804*10^{-5}$
F_{recoil}	0.997	0.999
C_{pv5ff}	10.732	10.489
C_{kin}	0.0364	0.0357
σ_{ep} cc1	$3.155*10^{-5}$	$4.275*10^{-5}$

The variation of ω over the acceptance is shown in figure 5.3. These contour plots show that ω is not entirely independent of (E_m, P_m). The variation of ω is similar but not identical for the two proton angle settings. An investigation of the cross-section dependence on ω is presented in the next section.

5.1.3 ω dependence

The ω dependence of the data was studied by analyzing the data for three different cuts on the ω variable. The ranges for ω were [103 MeV, 110 MeV] for the low ω side, [108 MeV, 114 MeV] for the middle and [113 MeV, 120 MeV] for the high ω side. For each of these analysis runs a separate set of phase space volumes was calculated with the ***Acceptance*** Monte Carlo program. This ensures that these volumes correctly reflect the reduced ω acceptance. The masked data set for the high ω range could not be used, since there is zero phase-space overlap after the ω cut. The data was corrected for all normalizations, but no radiative corrections

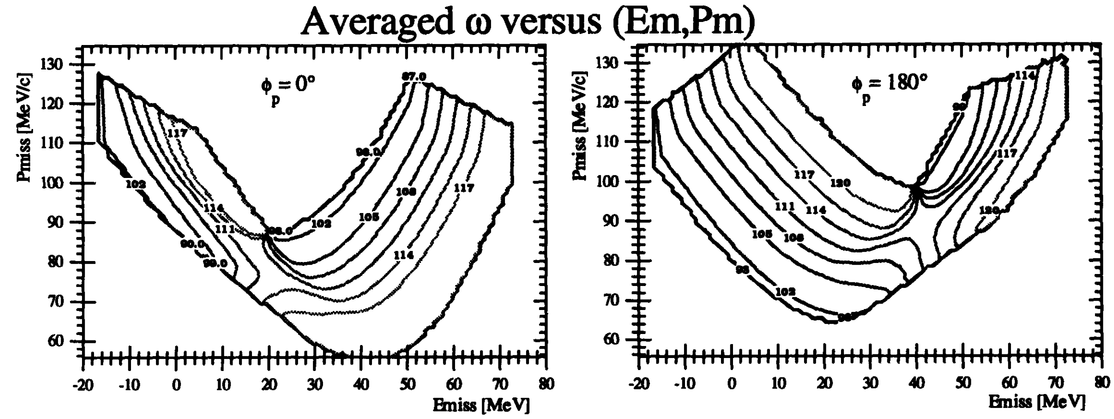

Figure 5.3 Contour plot of the average ω versus (E_m,P_m). The numbers on the contour lines indicate the value of ω, in MeV.

were applied. The cut on ω caused a width reduction in P_m for the (E_m, P_m) data histogram, which became too small for successful extrapolation of the data in RADC.

The results of this study for the full data set are plotted in figure 5.4 and the integrated cross-sections for both the masked and the full data set are tabulated in table 5.4. For the p-shell the data was integrated over a missing energy range from 13 MeV to 28 MeV, and for the s-shell it was integrated from 28 MeV to 50 MeV[2]. The table no significant variation in the cross-section with increasing ω. This can be expected since the kinematics on top of the quasielastic peak, where the variation of the cross-section with ω is small. The center of the quasielastic peak is at about $Q^2/2M_p + \varepsilon_x = 96MeV$. The three curves on the plots fall within 2 standard deviations (2σ) of the statistical error of each other, and have nearly identical shapes. The high ω data extends a little further in missing energy, as would be expected from the definition: $E_m \equiv \omega - T_p - T_R$.

In general it can be concluded that that the ω dependence of the data is small, and does not warrant special treatment. The final results can be averaged over the entire ω region without this affecting the final results significantly.

---

[2] The integration region for the s-shell corresponds to the extent of the longitudinal s-shell region, see P. Ulmer, Ph. D. thesis, MIT 1981.

Table 5.4 Integrated cross-sections for several cuts on ω.

	ω cut low [MeV]	ω cut high [MeV]	42.9° σ ± Δσ [nbarn/MeV Sr²] Full Data Set		64.7° σ ± Δσ [nbarn/MeV Sr²] Full Data Set		42.9° σ ± Δσ [nbarn/MeV Sr²] Masked Data Set		64.7° σ ± Δσ [nbarn/MeV Sr²] Masked Data Set	
P-Shell	103	120	6.58	0.18	10.87	0.21	6.65	0.19	10.11	0.3
low-ω	103	110	6.11	0.27	9.83	0.30	6.20	0.28	9.74	0.33
mid-ω	108	114	7.11	0.32	11.26	0.36	6.76	0.54	10.94	0.81
high-ω	113	120	6.95	0.31	11.92	0.36	-	-	-	-
S-Shell	103	120	3.58	0.17	5.52	0.18	3.32	0.28	5.59	0.20
low-ω	103	110	3.45	0.30	5.61	0.32	3.35	0.36	5.74	0.40
mid-ω	108	114	3.87	0.30	5.17	0.30	3.61	0.54	5.50	0.53
high-ω	113	120	3.83	0.25	5.58	0.26	-	-	-	-

All normalizations are included, but no radiative corrections were applied. The uncertainties are statistical only. No cross-sections can be computed for the high-ω masked data set, since there is no overlap in the phase-space.

5.1.4 R$_{LT}$ Extraction.

For an un-polarized beam and target, the equation for the cross-section is given by (see equation 1.27):

$$\frac{d^5\sigma(q,\omega,E_m,P_m)}{dE_f d\Omega_e d\Omega_p} = \frac{1}{(2\pi)^3} C_{kin}\sigma_{mott}\, f_{rec}^{-1} \left\{ \begin{matrix} v_L W_L + v_R W_R + \\ v_{TT} W_{TT} \cos(2\phi_{pq}) + \\ v_{LT} W_{LT} \cos(\phi_{pq}) \end{matrix} \right\} \tag{5.3}$$

The electron kinematic factors, v_{XX} depend only on q and ω. The structure functions W_{XX} depend also on E_m and P_m, but their dependence on the rotation around the q-vector is entirely contained in the $\cos(\phi_{pq})$ terms. The structure function W_{LT} is obtained from the data using this dependence. Subtracting two cross-sections with $\{q,\omega,E_m,P_m\}$ held constant, and $\phi_{pq} = 0°$ $(\cos(\phi_{pq}) = 1)$ for one and $\phi_{pq} = 180°$ $(\cos(\phi_{pq}) = -1)$ for the other, W_{LT} is found from:

$$W_{LT} = \frac{1}{2v_{LT}} \frac{(2\pi)^3}{C_{kin}\sigma_{Mott}\, f_{rec}^{-1}} \left\{ \frac{d^5\sigma(\phi_p = 0°)}{d\omega d\Omega_e d\Omega_p} - \frac{d^5\sigma(\phi_p = 180°)}{d\omega d\Omega_e d\Omega_p} \right\} \tag{5.4}$$

All the other $v_{XX}W_{XX}$ terms cancel because they are equal for the two measurements. The structure function R_{LT} is found from:

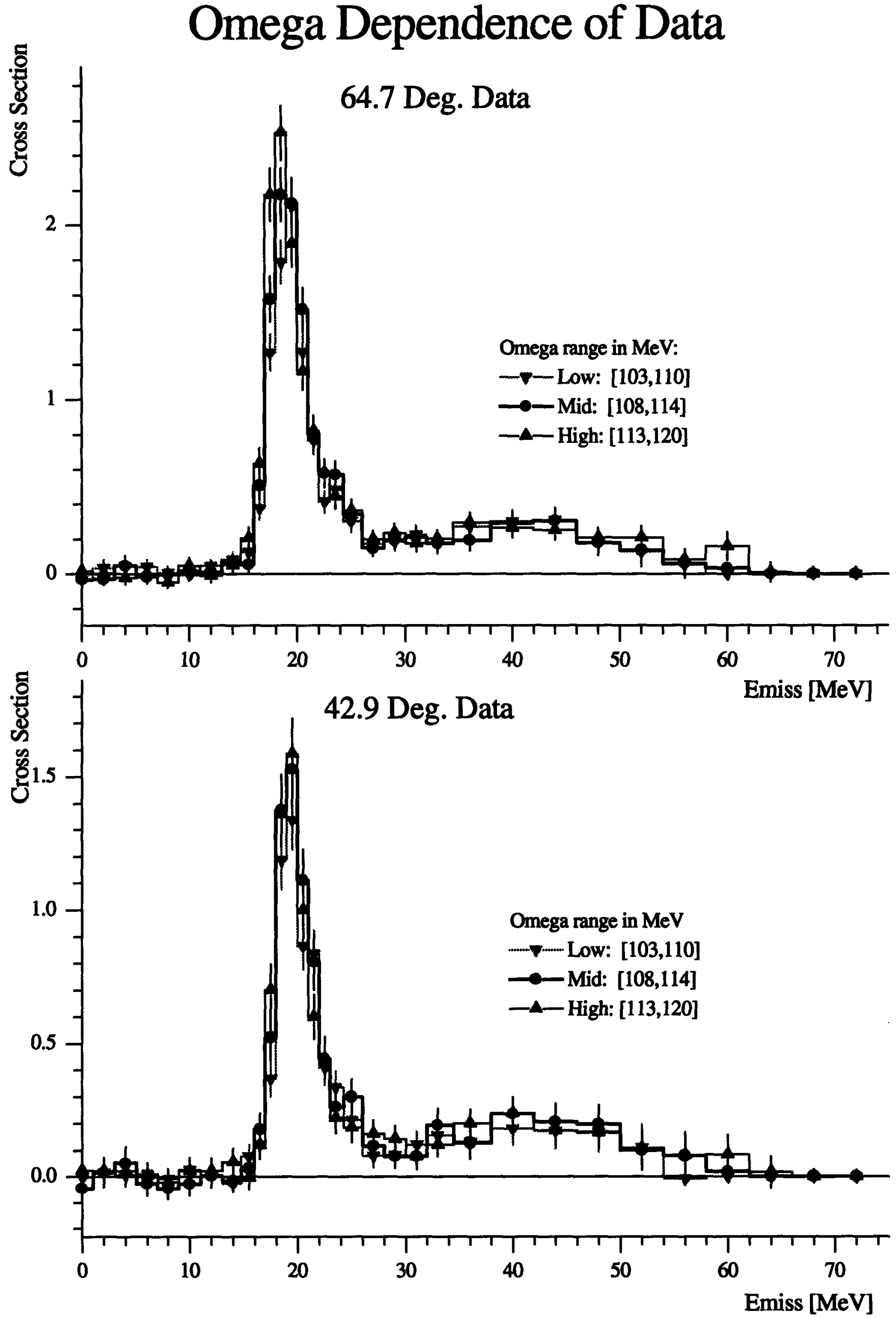

Figure 5.4 Histograms of the cross-section for different cuts on ω. The data for these histograms is not masked.

$$R_{LT} = W_{LT}\cos(\phi_p) \tag{5.5}$$

Notice that $\sigma(\phi_{pq} = 180°) > \sigma(\phi_{pq} = 0°)$ and $v_{LT} < 0$, so that W_{LT} is a positive quantity, and R_{LT} is positive on the $\phi_{pq} = 0°$ side. In this thesis all the plots of R_{LT} are for $\phi_{pq} = 0°$, where it is equal to W_{LT}.

It is also possible to take the sum of the two cross sections, and divide this by the same factors used for the extraction of R_{LT}. This quantity contains the information of the remaining parts of the structure functions, and in this thesis will be referred to as "*not-*R_{LT}". It is found from the formula:

$$\begin{aligned} not\ R_{LT} &= v_L R_L + v_T R_T + v_{TT} R_{TT} \\ &= \frac{1}{2}\frac{(2\pi)^3}{C_{kin}\sigma_{Mott}\,f_{rec}^{-1}}\left\{\frac{d^5\sigma(\phi_p = 0°)}{d\omega d\Omega_e d\Omega_p} + \frac{d^5\sigma(\phi_p = 180°)}{d\omega d\Omega_e d\Omega_p}\right\} \end{aligned} \tag{5.6}$$

The *not-*R_{LT} values are tabulated in the data tables for comparison with the R_{LT} values.

For this experiment the value for R_{LT} is computed for each bin of a two dimensional (E_m, P_m) cross-section histogram. This computation is performed by a set of UNIX shell scripts which call histogram manipulation programs. The following steps are taken:

1. **Addcross** is run to collect all the data in two 2-dimensional (E_m,P_m) cross-section histograms.
2. A mask is made from the acceptance volume histograms. (see section 5.1.1)
3. Each cross-section histogram is multiplied with the mask histogram. This creates two cross-section histograms that have the exact same shape in (E_m,P_m). (It was separately verified that these histograms are identical to histograms that are created by masking the data before collecting all the runs with **Addcross**.)
4. The histograms are rebinned so that they have an optimal size for **RADC**. The **RADC** program is limited to 16 bins in P_m, so a bin size of 5 MeV/c in P_m was needed.

5. Each masked cross-section histogram is radiatively corrected with **RADC**. (see section 3.6)
6. The histograms are each divided by histograms containing $(2\pi)^{-3}C_{kin}\sigma_{Mott}\,\mathrm{f}_{rec}^{-1}$ for each bin. These histograms were computed by the **Acceptance** program.
7. The resulting 64.7° histogram is subtracted from the 42.9° histogram, and the result is multiplied by $1/2v_{LT}$. This gives a two dimensional (E_m,P_m) R_{LT} histogram.
8. The two dimensional R_{LT} histogram is projected onto the missing energy.

The procedure for the last step is not obvious. There are two methods by which the R_{LT} projection onto the missing energy can be calculated. The first method takes the projected cross-sections from step 5, and then calculates R_{LT} following steps 6 and 7. The problem with this, is that it does not guarantee a proper weighting in the subtraction of the 64.7° histogram from the 42.9° histogram. The second method follows a more complicated procedure. Starting with equation 5.4 the experimental two dimensional R_{LT} histogram is given by:

$$R_{LT}(Em,Pm)=\frac{(2\pi)^3}{2v_{LT}}\left(\frac{\sigma_0(Em,Pm)}{C_{kin,0}\,\mathrm{F}_{rec,0}^{-1}\,\sigma_{Mott,0}}-\frac{\sigma_\pi(Em,Pm)}{C_{kin,\pi}\,\mathrm{F}_{rec,\pi}^{-1}\,\sigma_{Mott,\pi}}\right) \tag{5.7}$$

where the kinematic constants are evaluated for each bin. To find out how to project this histogram the cross-sections are written as the ratio $\mathcal{N}/\mathcal{V}$ as in equation 3.36, where $\mathcal{N}$ is the summed counts and $\mathcal{V}$ is the summed volume (acceptance phase-space). Dropping the bin labels, and simplifying the kinematic constant with $C_f=(2\pi)^{-3}C_{kin,f}\,\mathrm{F}_{rec,f}^{-1}\,\sigma_{Mott,f}$, equation 5.7 becomes:

$$\begin{aligned}R_{LT}&=\frac{1}{2v_{LT}}\left(\frac{\mathcal{N}_0}{C_0\mathcal{V}_0}-\frac{\mathcal{N}_\pi}{C_\pi\mathcal{V}_\pi}\right)\\&=\frac{1}{2v_{LT}}\left(\frac{\mathcal{N}_0C_\pi\mathcal{V}_\pi-\mathcal{N}_\pi C_0\mathcal{V}_0}{C_0\mathcal{V}_0C_\pi\mathcal{V}_\pi}\right)\end{aligned} \tag{5.8}$$

This can now be projected with a summation over P_m as was described in section 3.5:

$$R_{LT}(E_m) = \frac{1}{2v_{LT}} \left[\frac{\sum\limits_{P_m} \left(\mathcal{N}_0(E_m,P_m) C_\pi \mathcal{V}_\pi(E_m,P_m) - \mathcal{N}_\pi(E_m,P_m) C_0 \mathcal{V}_0(E_m,P_m) \right)}{\sum\limits_{P_m} C_0 \mathcal{V}_0(E_m,P_m) C_\pi \mathcal{V}_\pi(E_m,P_m)} \right] \tag{5.9}$$

where the (E_m, P_m) bin label was dropped from the kinematic constants for brevity. The result is a histogram of R_{LT} versus missing energy (see section 5.2.1, figure 5.6). The computation can be somewhat simplified using the identity $\mathcal{N} = \mathcal{V}\sigma$, the formula for R_{LT} (equation 5.7), and approximating $f^{-1}_{rec,0}\,\sigma_{Mott,0} \approx f^{-1}_{rec,\pi}\,\sigma_{Mott,\pi}$:

$$\begin{aligned} R_{LT}(E_m) &= \frac{1}{2v_{LT}} \left[\frac{\sum\limits_{P_m} \left(\sigma_0 \mathcal{V}_0 C_\pi \mathcal{V}_\pi - \sigma_\pi \mathcal{V}_\pi C_0 \mathcal{V}_0 \right)}{\sum\limits_{P_m} C_0 \mathcal{V}_0 C_\pi \mathcal{V}_\pi} \right] \\ &\cong \left[\frac{\sum\limits_{P_m} R_{LT}(E_m,P_m) \mathcal{V}_0 C_0 \mathcal{V}_\pi C_\pi}{\sum\limits_{P_m} C_0 \mathcal{V}_0 C_\pi \mathcal{V}_\pi} \right] \end{aligned} \tag{5.10}$$

For these data the two methods for projecting R_{LT} give nearly identical results. The second method was used the R_{LT} extraction.

The difficulty in the extraction of R_{LT} stems from the requirement for equation 5.4 that the variables $\{q, \omega, E_m, P_m\}$ are held constant while only $\cos(\phi_x)$ changes sign. As was shown in section 5.1.2, this constraint can not be perfectly satisfied, even on a bin by bin basis. This is taken into account as a systematic uncertainty in the next section.

5.1.5 Systematic Uncertainties.

The uncertainties in the calibrations of the equipment contribute to an overall systematic uncertainty in the analysis. This section describes the sources of these uncertainties, and how they affect the data analysis and ultimately the final results. Note that all the error bars on graphs in this thesis only include the statistical uncertainties.

The systematic uncertainties for this experiment originate from the following sources:

- The uncertainty in the beam energy: 576 ± 0.85 MeV.

- The uncertainty in the amount of charge on target: 0.3 %
- Uncertainty in the spectrometer angles: ELSSY $\theta_e = 44.0 \pm 0.05°$, OOPS $\theta_p = 64.7 \pm 0.1°$ and $\theta_p = 42.9 \pm 0.1°$
- Uncertainty in the central momentum of the spectrometers: ELSSY $k_f = 470.0 \pm 0.1$ MeV/c, OOPS $p_f = 440, 405, 373, 343 \pm 1.$ MeV/c. Because of the central momenta of the spectrometers were calibrated using the measured beam energy, these uncertainties are linked to the uncertainty in the beam energy.
- Uncertainty in the normalizations of the spectrometers, including spectrometer acceptances.
- Uncertainty in the extraction of R_{LT}, due to the difference in θ_{pq} between a bin of the 42.9° data and one from the 64.7° data. This difference is estimated to be 0.5° (see section 5.1.2)
- Uncertainty in the target thickness and angle are estimated to be accurate to better than 0.1%.

These uncertainties directly affect the accuracy of the analysis of the data. They also determine the precision of the separation points, which are needed for the comparison of the final results with theoretical predictions. The uncertainty in the separation points should therefore be reflected in the systematic error of the final results.

The data analysis depends on the uncertainties in the following manner:

- The calculation of the acceptance volume depends on the beam energy, the spectrometer angles and the spectrometer central momenta.
- The corrections to the data depend on the normalizations.
- The computation of the cross-sections depends on the amount of charge on target, the acceptance volume and the normalization corrections.
- The computation of R_{LT} depends on the cross-sections and the kinematic constants, which depend on the beam energy, the spectrometer angles and the spectrometer central momenta.

It would be very difficult to unravel these dependencies analytically. Instead, the approach taken here is mostly numerical. By changing one of the input variables to the analysis by the value of its uncertainty, the dependence of the final result on this uncertainty is obtained.

The uncertainty in the normalizations stem from two sources: the determination of the efficiencies of the detectors, and the overall trigger normalization of the spectrometers. The detector efficiency is calculated from the scalers and test values (see section 4.2.2 and section 4.3.2), and is therefore partially statistical in nature. It is added to the statistical uncertainty by the ***Addcross*** program. Any systematic error in the detector efficiencies is part of the trigger normalization. The ELSSY trigger efficiency was determined from the H(e,e') calibration runs by comparing the experimental cross-section with the MAINZ fit. The evaluation of the MAINZ prediction has an uncertainty of 0.45% due to the uncertainty in the beam energy and 0.51% due to the uncertainty of the electron scattering angle. Adding these in quadrature $\left(\sqrt{\sigma_1^2+\sigma_2^2+\cdots}\right)$ with the statistical error of the calibration (0.2%), the overall uncertainty for the ELSSY normalization is 0.7%. The OOPS trigger efficiency was determined from the H(e,e'p) comparison with ***REVMOC***, which had a 1% accuracy. It should be noted that these normalizations also calibrate the solid angle acceptance of the spectrometers, so no additional uncertainty is needed to account for uncertainty in the solid angles.

The amount of charge that was deposited on the target was measured by two current integrators. These integrators were calibrated before the experiment to an accuracy of 0.2% for ST4 and 0.1% for ST5. However, there was a discrepancy of up to 1% between these two instruments, which was attributed to the beam halo. The value of ST4, which is closer to the target, was used for the computation of the cross-sections. The uncertainty in the amount of charge on target is estimated at 0.3%. The uncertainty in the luminosity is the combination of the uncertainty in the amount of charge and the target thickness (0.1%), and is determined to be 0.3%.

The effects of the uncertainties in the acceptance volume and kinematics were studied by re-analyzing the entire data set with modified input parameters. For each run a single variable (e.g. the beam energy) was shifted by its uncertainty and a new set of acceptance volumes was calculated. The data were then analyzed with the same shift, and cross-sections were calculated. The value for R_{LT} was computed from the difference of the two cross-sections divided by the shifted kinematical constants. The results of this study is presented in table 5.5 as a percentage of the change in the cross-sections and

Table 5.5 Systematic uncertainties due to acceptance and kinematics shifts.

	P-Shell			S-Shell		
Variable	42.9° Δσ	64.7° Δσ	R_{LT}	42.9° Δσ	64.7° Δσ	R_{LT}
Ebeam	0.66%	0.42%	0.42%	0.83%	0.80%	0.32%
Kf	0.24%	0.53%	1.11%	0.10%	0.09%	0.06%
θ_e	0.03%	0.12%	0.79%	0.19%	0.38%	0.31%
Poops	0.66%	0.42%	0.29%	0.83%	0.80%	1.03%
θ_p	0.03%	0.11%	0.37%	0.16%	0.29%	1.07%
Total	0.97%	0.82%	1.52%	1.20%	1.24%	1.55%

R_{LT}. It should be noted that there is an uncertainty of ±2% in these values, which is due to statistical uncertainties.

There is some measure of coherence in the shifts of the acceptance volume and the data: e.g. when the acceptance shifts due to a change in beam energy, the data shift similarly. The error that is introduced by such shifts mostly affects the edges of the acceptance where the volume has steep slopes. Since the statistical error in these regions is also larger, an increased systematic error is not as noticeable. The overall shape of the cross-section versus missing energy did not change significantly by these shifts. These systematic uncertainties were added in quadrature, giving a combined systematic uncertainty of about 1% for the p-shell and 1.2% for the s-shell cross-sections. The R_{LT} values have a combined systematic uncertainty due to these shifts of about 1.5%.

A different aspect of the shift in the kinematic variables is the resulting shift of the separation point. A shift of the separation point causes an inaccuracy that is introduced when the data are compared with theoretical predictions. This effect was studied by calculating the DWIA predicted cross-sections and R_{LT} values for each of the shifted variables. The calculations were done with the ***PV5FF*** program[3], with the optical model of Schwandt et al.[4] to compute the distortions on the out-going proton (see section 5.3). The results of these calculations are presented in table 5.6. The largest

---

[3] S. Boffi, C. Giusti and F. D. Pacati, Nuc. Phys. **A435** (1985) 697.
Later calculations in this thesis are all performed with DWEEPy instead of PV5FF, since the PV5FF code gave erroneous results for the s-shell predictions. However, the error was in the normalization of the computed cross sections, and should not affect the percentages computed in table 5.6.

[4] Schwandt et al., Phys. Rev. **C26** (1981) 55.

Table 5.6 Systematic uncertainties due to shifts in the separation point.

		P-shell			S-shell		
Variable	**ΔVar.**	**64.7° Δσ**	**42.9° Δσ**	**R_{LT}**	**64.7° Δσ**	**42.9° Δσ**	**R_{LT}**
E_{beam}	0.85 MeV	0.26 %	0.29 %	0.10 %	0.04 %	0.57 %	1.73 %
θ_e	0.05°	0.48 %	0.53 %	0.05 %	0.29 %	0.21 %	0.35 %
K_f	0.50 MeV	0.36 %	0.43 %	0.01 %	0.02 %	0.38 %	1.30 %
E_m	0.20 MeV	0.17 %	0.19 %	0.01 %	0.04 %	0.11 %	0.52 %
θ_{pq}	0.50°	3.15 %	1.87 %	5.89 %	6.78 %	2.87 %	3.96 %
θ_{pq}	0.10°	0.66 %	0.41 %	1.19 %	1.37 %	0.60 %	0.74 %
Total ($\Delta\theta_{pq}$= 0.5°)		(3.22 %)	(2.02 %)	5.89 %	(6.79 %)	(2.96 %)	4.56 %
Total ($\Delta\theta_{pq}$= 0.1°)		0.94 %	0.87 %	(1.20 %)	1.40 %	0.94 %	(2.37 %)

contributions to the theoretical systematic uncertainties come from the pointing errors of the spectrometers. For this study two values for the uncertainty in θ_{pq} were used. The first value of ± 0.5° includes the uncertainty that is introduced due to the differences in θ_{pq} between a bin of the 42.9° data and a bin of the 64.7° data. This difference only affects the calculation of R_{LT}. For the uncertainty in the cross-sections the smaller value of ± 0.1° is used, which comes from the pointing error of the OOPS spectrometer.

The radiative unfolding program ***RADC*** increases the error bars of the corrected histogram to include the uncertainty introduced by the unfolding procedure (see section 3.6.2). There remains, however, some uncertainty about the accuracy of the unfolding procedure itself, which depends on the accuracy of the data extension. This uncertainty was studied by running the ***RADC*** program with different settings for the order to which it will attempt to fit a polynomial, and by using different bin sizes for the (E_m,P_m) histograms. This fit is somewhat compromised by the few channels that are available in P_m for any given slice in E_m (the data are narrow in the P_m direction). It was found that the p-shell cross-section was not sensitive to the order of the fit, the integrated cross-sections for the p-shell would change by less than 0.1% for the worst case. The s-shell cross-section however is much more sensitive. Radiative tails from the p-shell, and extended p-shell region, extend into the s-shell region. Since the p-shell has more strength than the s-shell, the subtraction of these tails has a significant effect on the s-shell cross-section.

This effect was tested by using a zero-th order fit (straight horizontal line) and a first order fit (straight line with slope) for the full data set. The difference in cross-section

Table 5.7 Combined systematic uncertainties.

	P-shell			S-shell		
Source	**64.7° $\Delta\sigma$**	**42.9° $\Delta\sigma$**	**R_{LT}**	**64.7° $\Delta\sigma$**	**42.9° $\Delta\sigma$**	**R_{LT}**
Luminosity	0.3 %	0.3 %	0.4 %	0.3 %	0.3 %	0.4 %
H(e,e') Norm	0.7 %	0.7 %	0.7 %	0.7 %	0.7 %	0.7 %
H(e,e'p) Norm	1.0 %	1.0 %	1.0 %	1.0 %	1.0 %	1.0 %
Acceptance	1.0 %	0.8 %	1.5 %	1.2 %	1.2 %	1.6 %
RADC	0.1 %	0.1 %	0.1 %	1.0 %	1.0 %	1.4 %
Theory Sep.	0.9 %	0.9 %	5.9 %	1.4 %	0.9 %	4.6 %
Total	1.9 %	1.7 %	6.2 %	2.4 %	2.2 %	5.2 %

between the results of these corrected data sets was 1%, which is taken as the uncertainty in the s-shell radiative correction. Note that the order for the fit, n, must be equal or smaller than the available number of bins, n_b, in the P_m direction, or the data extension is not performed. Thus for the masked data set, where n_b is 2 for some slices of E_m, this extension procedure becomes very unreliable. All radiative corrections for this experiment were done with a zero-th order extension of the data, unless noted otherwise.

The systematic errors from all these different sources are combined by adding them in quadrature. The result is presented in table 5.7. The uncertainty for the cross-sections includes the contribution for $\Delta\theta_{pq}$= 0.1°, while the uncertainty for R_{LT} includes the contributing for $\Delta\theta_{pq}$ = 0.5°. Notice that the normalizations of the spectrometers affect the computation of R_{LT} is a coherent linear manner, e.g. if the OOPS normalization is off by +0.5%, both the 42.9° and the 64.7° cross-sections are off by +0.5%, and thus R_{LT} is also off by +0.5%. However, the accuracy of the charge on target depends on the beam quality, which is not coherent, and therefore these uncertainties are added in quadrature for R_{LT}. The final systematic errors are better than 2.4% for the cross-sections and 6.2% for R_{LT}.

5.2 Results.

The final results of this experiment are presented in a set of graphs of the cross-sections and R_{LT} values versus missing energy and tables of integrated cross-sections and R_{LT} values. The projection of the cross-sections onto the missing momentum axis does not provide meaningful results for these data, because there is insufficient phase space (width) in P_m on the two dimensional (E_m,P_m) histograms. Also, the phase space has slopes in the P_m direction that are too steep to accurately extract a cross-section versus missing momentum.

Figure 5.5 presents the graph of the cross-section versus missing energy for the full data set. The data were corrected for all normalizations and for radiative processes. This data were not masked, so R_{LT} values could not be extracted reliably. The cross-section is differential in $d^6\sigma/d\omega dE_m d\Omega_e d\Omega_p$. The bin size is adjusted from 1 MeV/bin in the p-shell region (10 to 29 MeV) to 2 and 4 MeV/bin in the s-shell region (29 to 39 MeV with 2 MeV/bin, 39 and higher with 4 MeV/bin) to average over statistical fluctuations.

The graph shows a clear separation between the p and s-shell regions. The p-shell region, from about 14 MeV up to 28 MeV, is known to contain several excited states of the ^{11}B residual nucleus[5]. The resolution in this experiment is not high enough to distinguish these states, although there is some indication of the peak corresponding to an excited state at about 24 MeV (8 MeV in excitation energy for the ^{11}B residual nucleus) . A similar peak was observed by Ulmer et al. at similar kinematics[6]. The strength of these peaks is expected to be less than 20% of the ground state strength at the kinematics of this experiment. The integrated cross-sections are computed by integrating over the entire p-shell region from 13 MeV to 28 MeV. The results are $8.2 \pm 0.2 \pm 0.1$ and $13.5 \pm 0.3 \pm 0.3$ nbarn/MeV/sr^2 for the 42.9° and the 64.7° data respectively. These results are not very sensitive to the integration limits. The lower limit can be moved between 12 and 15 MeV with less that 1% variation in the integrated cross-section, which is less than the statistical error. The upper limit is more sensitive, but still allows for a shift of about 1 MeV without a significant change in the cross-sections.

The s-shell region ranges from 28 MeV up to 50 MeV in missing energy. This upper limit was established by Ulmer[6], who found that the longitudinal part of the cross-section extends only to 50 MeV, while the transverse part extends further. The integrated s-shell cross-section is $3.8 \pm 0.2 \pm 0.1$ nbarn/MeV/sr^2 for the 42.9° data and $5.7 \pm 0.2 \pm 0.1$ nbarn/MeV/sr^2 for the 64.7° data. These results are fairly sensitive to the

---

[5] G. van der Steenhoven et al. , Nucl. Phys. **A484** (1988) 445.

[6] Paul Ulmer, Ph.D. thesis, MIT (1987) unpublished.

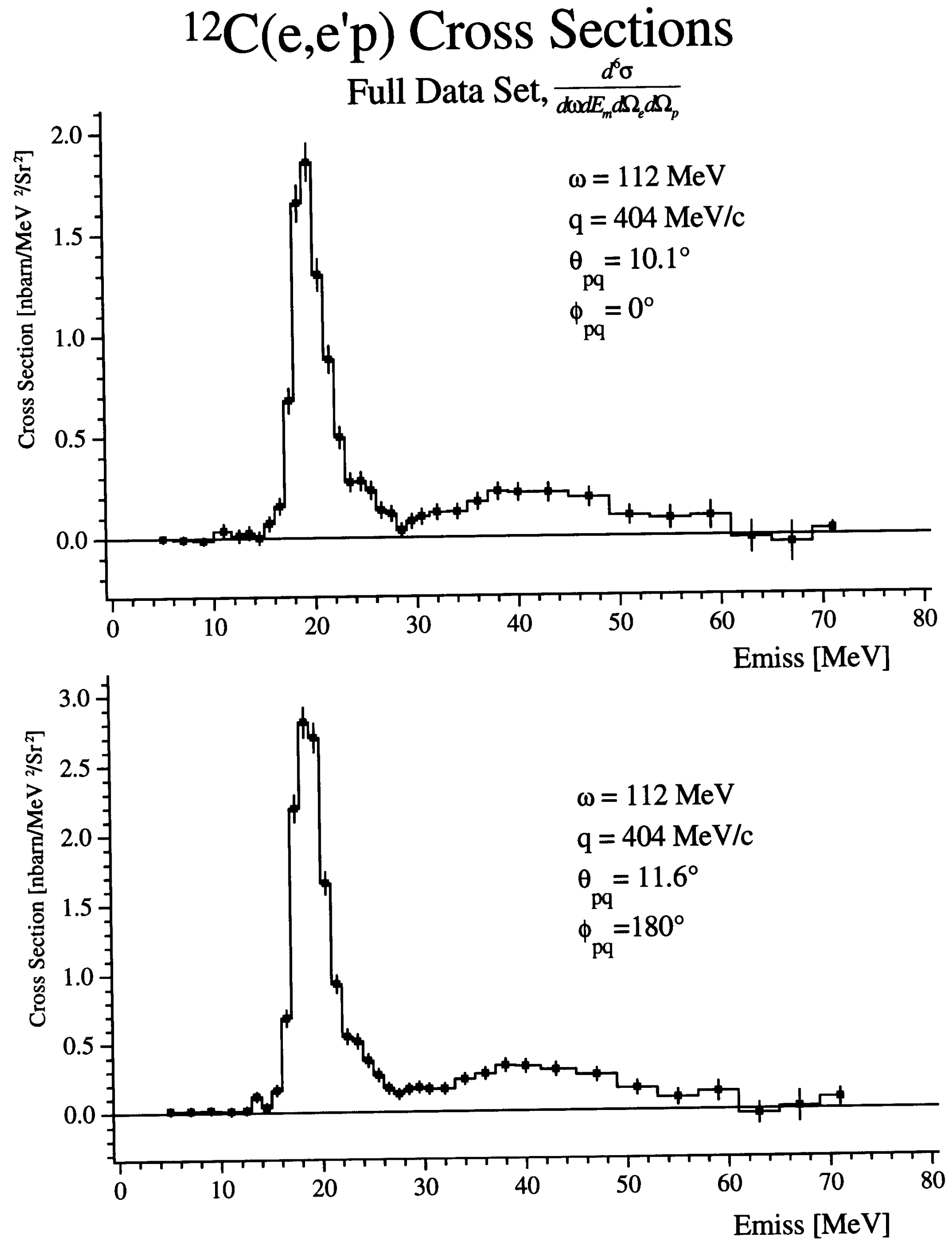

Figure 5.5 Cross-section versus missing energy for the full data set.

upper integration limit, varying by about 0.2 nbarn/MeV/sr^2 for each additional MeV increase of the upper integration limit. The integrated cross-section in the region from 50 MeV to 75 MeV, is 0.8 ± 0.3 nbarn/MeV/sr^2 for the 42.9° data and 1.7 ± 0.4 nbarn/MeV/sr^2 for the 64.7° data. These cross-sections are summarized in table 5.8. (For the details of the other entries in this table, see the next paragraphs.)

For the extraction of R_{LT} the data were masked to create an (E_m, P_m) overlap between the $\phi_{pq} = 0°$ and the $\phi_{pq} = 180°$ data. The results are presented in figure 5.6. The cross-section histograms look very similar to those for the full data set, except that the data extend only to about 55 MeV in missing energy. There was no overlap between the two data sets for missing energies higher than 55 MeV, which can also be seen in figure 5.1. The integrated cross-sections for the p-shell are slightly lower than in the full data set for the 64.7° data, and slightly higher for the 42.9° data; for the s-shell the opposite is true. This reflects the small shift in the extraction point that occurs when the data are masked. The cross-sections for the masked data can be found in table 5.8.

The extracted R_{LT} versus missing energy is also shown in figure 5.6. In the p-shell region the main p-shell peak stands out clearly. The smaller peak at 24 MeV now seems to be more clearly present, although it is only one bin, and can not be considered significant. The s-shell region is less clear due to the poor statistics. The R_{LT} strength is consistent with zero for missing energies higher than 42 MeV. It is identical to zero at $E_m = 55$ MeV, but this last bin should be interpreted with caution. This result is consistent with the findings by Ulmer[6] that the longitudinal component of the cross-section vanishes at a missing energy of 50 MeV. The R_{LT} strength for the continuum could not be measured because the data do not extend far enough in missing energy. The integrated R_{LT} values for the three regions are also presented in table 5.8.

These integrated cross-sections can be compared with theory (see section 5.3), using the separation point of table 5.2, but with an average value for the missing momentum, $\langle P_m \rangle$, that reflects the integration region. These values for $\langle P_m \rangle$ are given in table 5.8 along with the cross-sections. They were calculated by computing the weighted average of the missing momentum of each bin of the (E_m, P_m) acceptance histogram, for the p-shell or s-shell region. In this calculation the weighting factor for each bin is the acceptance volume for that bin. The following equation was used:

$$\langle P_m \rangle = \frac{\sum_{P_m} P_m \left(\sum_{E_m = E_m^{low}}^{E_m^{high}} \mathcal{V}(E_m, P_m) \right)}{\sum_{P_m} \left(\sum_{E_m = E_m^{low}}^{E_m^{high}} \mathcal{V}(E_m, P_m) \right)} \tag{5.11}$$

Table 5.8 Cross-Sections for 12C(e,e'p) data.

Data Set	P-shell	S-shell	Continuum
Integration Range E_m	13 - 28 MeV	28 - 50 MeV	50 - 75 MeV
$<P_m>$ 42.9°	77.5 ± 0.6	75.7 ± 5.0	90.7 ± 4.9
Full 42.9° (ϕ_{pq} =0)	8.2 ± 0.2 ± 0.1	3.8 ± 0.2 ± 0.1	0.8 ± 0.3
$<P_m>$ 64.7°	85.9 ± 2.9	86.9 ± 3.5	103.9 ± 10.0
Full 64.7° (ϕ_{pq}= π)	13.5 ± 0.3 ± 0.3	5.7 ± 0.2 ± 0.1	1.7 ± 0.4
$<P_m>$ Masked 42.9°	77.6 ± 0.4	83.1 ± 4.0	-
Masked 42.9° (ϕ_{pq} =0)	8.3 ± 0.2 ± 0.1	3.5 ± 0.2 ± 0.1	-
$<P_m>$ Masked 64.7°	78.8 ± 0.7	86.1 ± 0.4	
Masked 64.7° (ϕ_{pq}= π)	13.1 ± 0.4 ± 0.3	5.9 ± 0.2 ± 0.1	-
Masked R_{LT}	25. ± 2. ± 2.	14. ± 2. ± 1.	-

All cross-sections are for the $d^4\sigma / d\omega dE_e d\Omega_e d\Omega_p$ differential, in nbarn/MeV/sr^2, and integrated over E_m,. The values for R_{LT} are in fm^3. Uncertainties are quotes as ± statistical ± systematic. The values for $<P_m>$ are the weighted average of P_m over acceptance (see next paragraph).

where $\mathcal{V}$ is the phase-space histogram for the sum of all runs as calculated by ***Addcross*** (see equation 3.36), and E_m^{low}, E_m^{high} are 13 MeV, 28 MeV respectively, for the p-shell, and 28 MeV, 50 MeV respectively, for the s-shell. The summation over P_m is over the entire accessible region. For the masked data the calculation is performed using the corresponding masked phase-space histogram. It can be noted that this average value for the missing momentum would be identical to the value for P_m in table 5.2, if the summation over E_m is over the entire volume, instead of the p- or s-shell region. The uncertainty for $<P_m>$ is taken to be the difference between the value calculated with equation 5.11, and the value that is obtained if the averaging is over the cross-section instead of the phase-space volume. This uncertainty is a measure of the width in P_m of the region and the variation of the phase-space volume in this region.

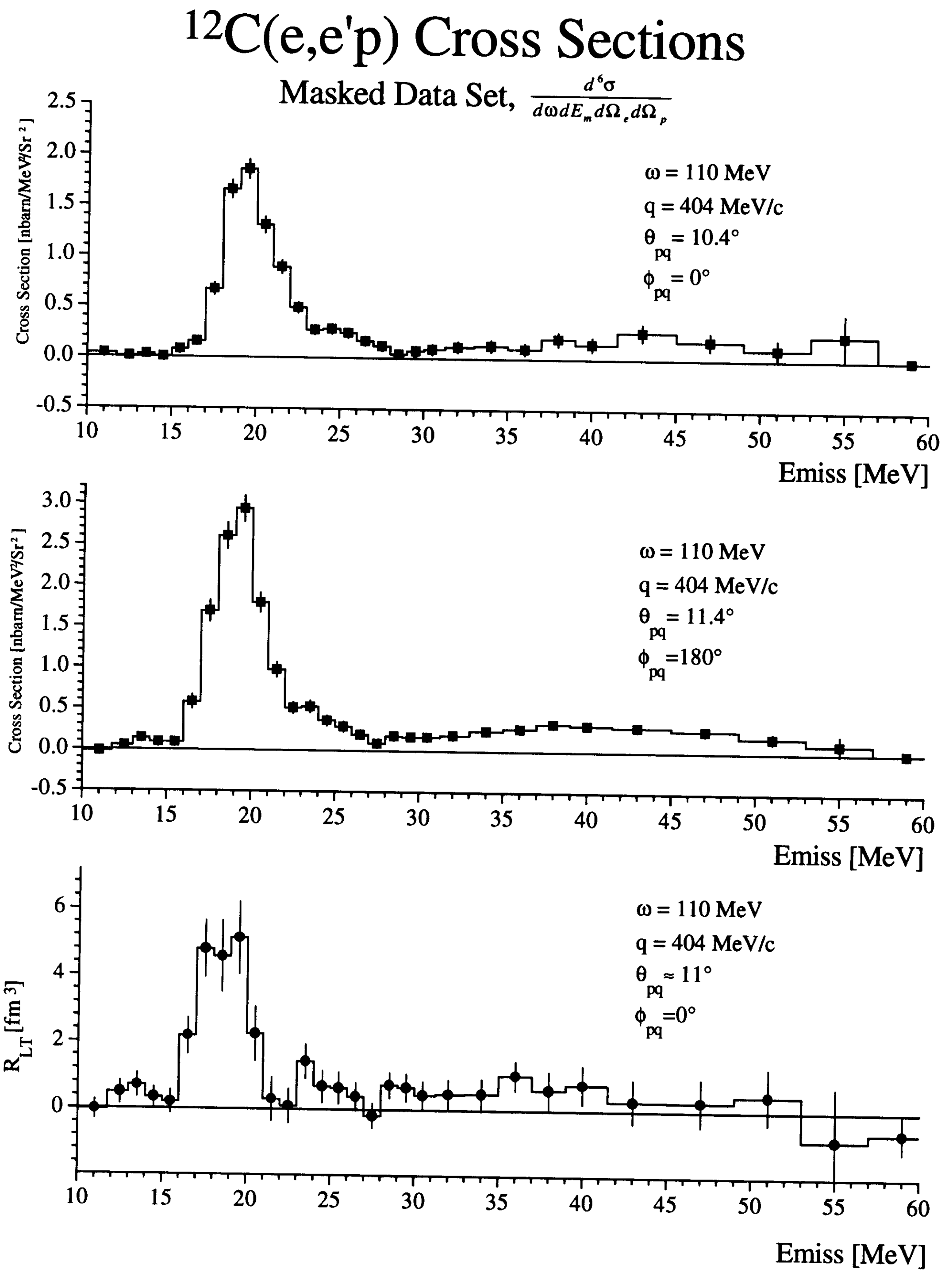

Figure 5.6 Histograms of the cross-sections and R_{LT} for the masked data set.

5.3 Comparison with Theory.

This section will present the results of the theoretical calculations that were performed with the ***DWEEPy*** (Distorted Wave (e,e'p)) program[7]. This program is based upon the work by the Pavia group[8,9] and the program ***PV5FF***[10]. It calculates the bound state wave function of the proton for a particular bound state (for carbon: $p_{\frac{3}{2}}$ and $s_{\frac{1}{2}}$) by solving the Schrödinger equation including a spin orbit term:

$$\frac{-\hbar}{2m}\nabla^2\psi + V_c(r)\psi + V_{so}(r)\mathbf{L}\cdot\mathbf{S}\psi = E_b\psi \qquad \textbf{(5.12)}$$

The potential wells V_c and V_{so} are of the Wood-Saxon form:

$$V(r) = \frac{-V_0}{\left(1+e^{(r-r_0)/a}\right)} \qquad \textbf{(5.13)}$$

where V_0 is the well depth, r_0 is the radius, and a is the diffuseness parameter. The program will solve for the depth of the potential V_0, given the desired binding energy of the state E_b. This is done for several settings of the radius parameter r_0, until the root mean square (RMS) charge radius, r_{RMS}, agrees with the radius obtained from magnetic elastic electron scattering. The parameters that were used in these computations are given in table 5.9. The RMS charge radius was obtained from ref. 11, but includes a correction for coupled-channel effects[12]. The diffuseness parameter is taken from ref. 12, and the spin-orbit well depth, V_{so}, is the same as was used for that study[13].

---

[7] The ***DWEEPy*** program was obtained from NIKHEF, the version used for this work is ***dweepy2c*** (1993), which has several bug fixes. A predecessor of this program was called ***PEEPSO***.

[8] S. Boffi et. al. Nucl. Phys. **A336**, 416,437 (1980). **A386**, 599 (1982), **A435**, 697 (1985).

[9] C. Giusti and F. D. Pacati, Nucl. Phys. **A336**, 427 (1980), **A473**, 717 (1987) and **A485**, 461 (1988).

[10] ***PV5FF*** was also used for some of the calculations, however, it did not calculate reliable cross-sections for the s-shell, which prompted the switch to the ***DWEEPy*** code. P-shell calculations were consistent between the two programs.

[11] T. W. Donnelly and I. Sick, Rev. Mod. Phys. **56**, 461 (1984), as quoted in ref. 12.

[12] D. G. Ireland and G. van der Steenhoven, Phys. Rev. **C49 N4**, 2182 (1994)

[13] G. van der Steenhoven, private communication.

Table 5.9 Wood Saxon parameters for the computation of the Bound State Wave Functions.

	P-shell	S-shell
Binding Energy: E_b	15.95 MeV	36 MeV
Well Depth V_c	56.62 MeV	63.82 MeV
Radius r_0	3.06 fm	3.06 fm
Diffuseness a	0.65 fm	0.65 fm
Spin-Orbit Well Depth V_{so}	25.0 MeV	25.0 MeV
RMS radius: r_{rms}	2.804 fm	2.059 fm

The radii quoted here include the $A^{1/3}$ term which is frequently divided out.

The ***DWEEPy*** program uses these bound state wave functions to obtain the non-relativistic, un-factorized plane wave impulse approximation (PWIA) and distorted wave impulse approximation (DWIA) cross-sections. A partial wave expansion is used to calculate the distortions of the outgoing proton wave using a non-relativistic optical-model potential. The optical-model potentials are derived by fitting a phenomenological potential shape to a coupled-channel analysis of elastic proton scattering from ^{12}C. It would have been preferable to use an optical model derived from ^{11}B(p,p'), but such a study is not available. The form of the potential is given by:

$$\begin{aligned} U(r) &= V_c + Vf(r) + iWf(r) + iW_s \frac{d}{dr} f(r) \\ &+ \frac{1}{r}\left[V_{so} \frac{d}{dr} f_{so}(r) + iW_{so} \frac{d}{dr} f_{so}(r) \right] \mathbf{L} \cdot \mathbf{S} \end{aligned} \qquad \textbf{(5.14)}$$

where the f terms are Wood-Saxon potential shapes (see equation 5.13). The V_c term is the Coulomb potential, and the V, V_s, V_{so} and W, W_s, W_{so} are the real and imaginary strengths for the main potential shape, the surface term, and the spin-orbit term, respectively. These parameters are published for different values of the outgoing proton kinetic energy. The values used for the calculations presented here are presented in table 5.10, and were interpolated from the published values. The designators are: Comfort for ref. 14, Jackson for ref. 15, and Schwandt for ref. 16.

---

[14] J. R. Comfort and B. C. Karp, Phys. Rev. **C21**, 2162 (1980)

[15] D. F. Jackson and I. Abdul-Jalil, J. Phys. **G6**, 481 (1980)

[16] Schwandt et al., Phys. Rev. **C26**, 55 (1981)

Table 5.10 Optical Model Parameters.

		Main			Surf.			Spin-Orbit		
Tp=92		**r**	**a**	**V**	**r**	**a**	**V**	**r**	**a**	**V**
Comfort	Real	2.669	0.633	23.65	0	0	0	2.002	0.5	5.812
	Im.	3.009	0.643	8.903	0	0	0	0	0	0
Jackson	Real	3.234	0.554	16.69	3.234	0.554	1.939	1.875	0.225	2.03
	Im.	2.073	0.612	16.93	0	0	0	2.72	0.64	-2.421
Schwandt	Real	2.624	0.704	30.31	0	0	0	2.135	0.656	4.559
	Im.	3.078	0.554	7.29	0	0	0	2.068	0.62	-0.986
Tp=72										
Comfort/	Real	2.669	0.625	29.32	0	0	0	2.002	0.5	5.696
Karp	Im.	3.069	0.662	8.059	0	0	0	0	0	0
Jackson	Real	3.225	0.554	18.28	3.225	0.612	3.69	1.746	0.225	2.41
	Im.	2.073	0.612	9.281	0	0	0	3.002	0.64	-1.605
Schwandt	Real	2.58	0.698	34.31	0	0	0	2.135	0.68	5.304
	Im.	3.18	0.504	6.65	0	0	0	2.068	0.62	-0.515

The results for the PWIA calculation and the DWIA calculations are presented with the data in table 5.11, and figures 5.7 and 5.8. The data are integrated over the missing energy range of 13 to 28 MeV for the p-shell, and 28 to 50 MeV for the s-shell. The same values and uncertainties for $<P_m>$ were used as in table 5.8. These uncertainties are reflected in the horizontal error bars. The calculations assume a shell occupancy of 4 protons for the p-shell, and 2 protons for the s-shell (full occupancy). The theoretical cross-sections were evaluated for the exact $<P_m>$ value by interpolating the calculated points of a table. These calculations are all performed at the extraction point, and are not averaged over the acceptance.

The three optical models that were used in these calculations give fairly similar results. The spread in these results can be taken as the uncertainty in the optical model potentials. Additional uncertainties in the theoretical predictions arise from uncertainties in the off-shell proton form factor (σ^{CC1}), and uncertainties in the bound state wave functions. These additional uncertainties are not included in the total systematic uncertainty, since they are difficult to quantify. The theoretical values for R_{LT} were calculated from the DWIA cross-sections using equation 5.6. The comparison with data for R_{LT} is plotted in figure 5.9.

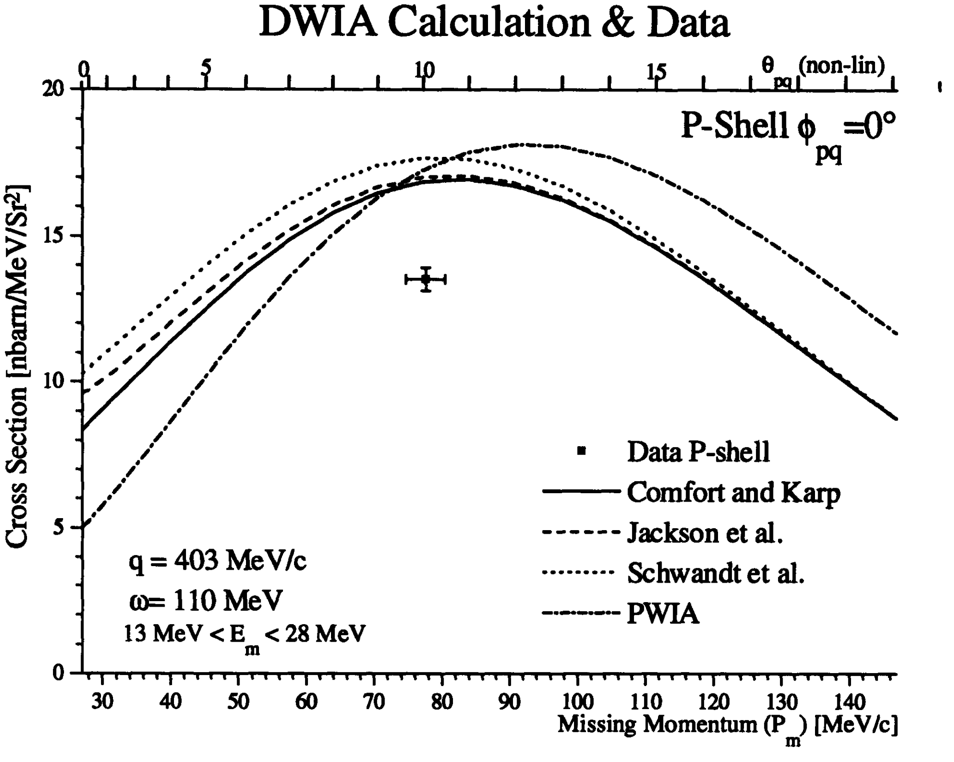

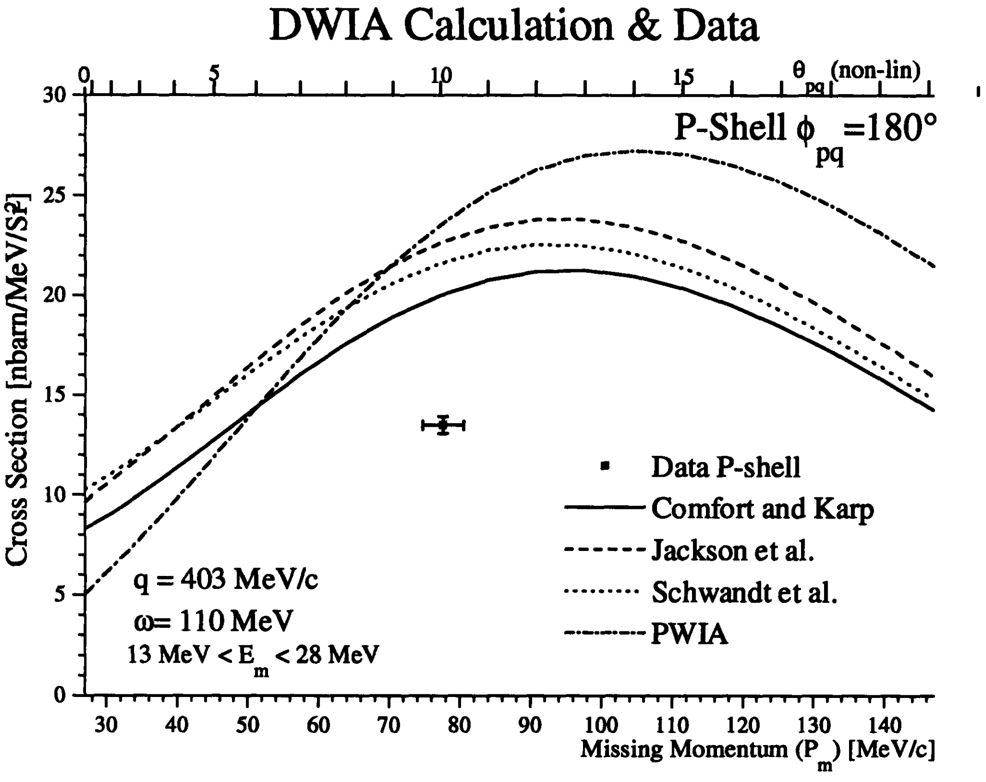

Figure 5.7 Comparison of DWIA calculations with data for the P-shell.

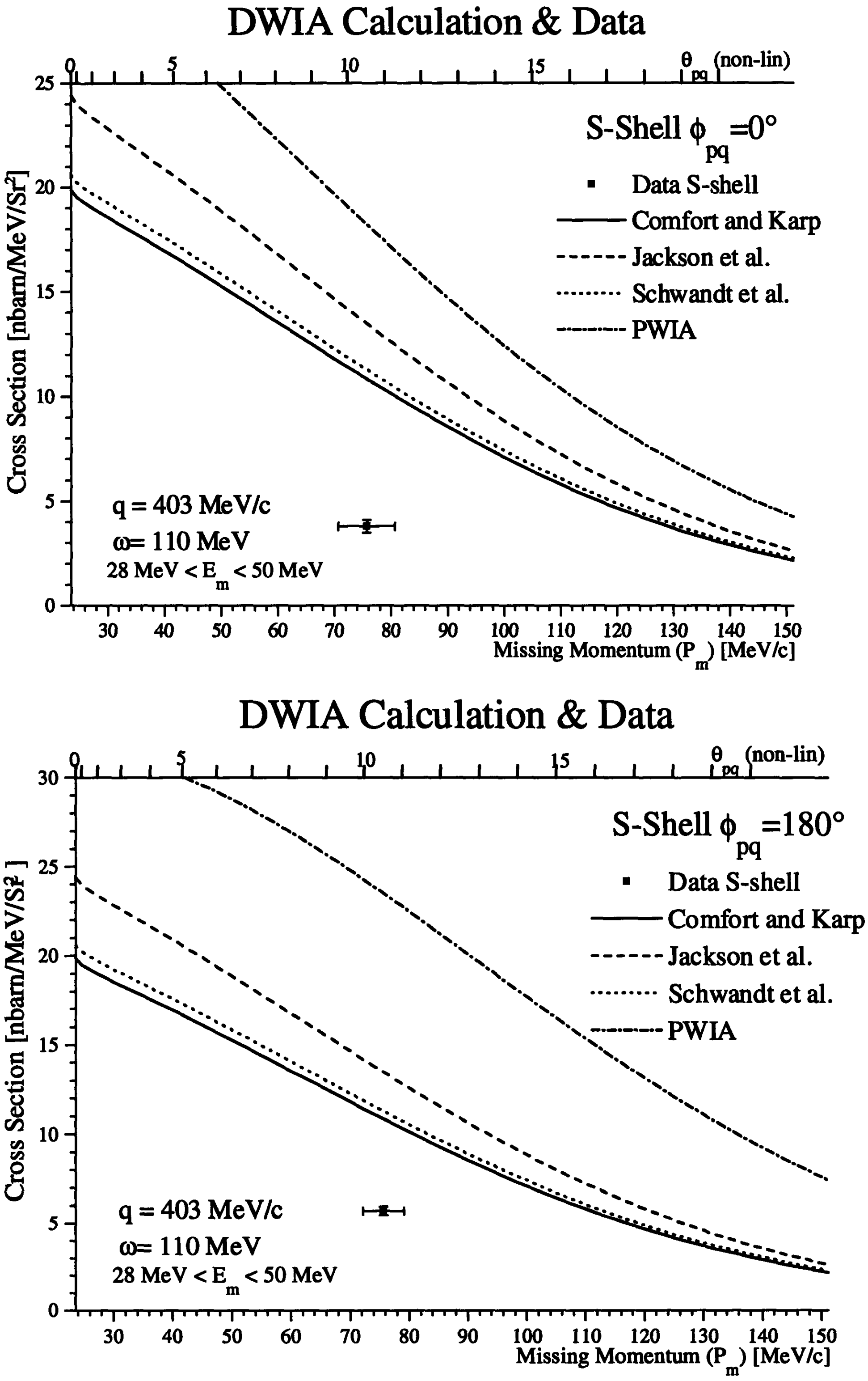

Figure 5.8 Comparison of DWIA calculations with data for the S-shell

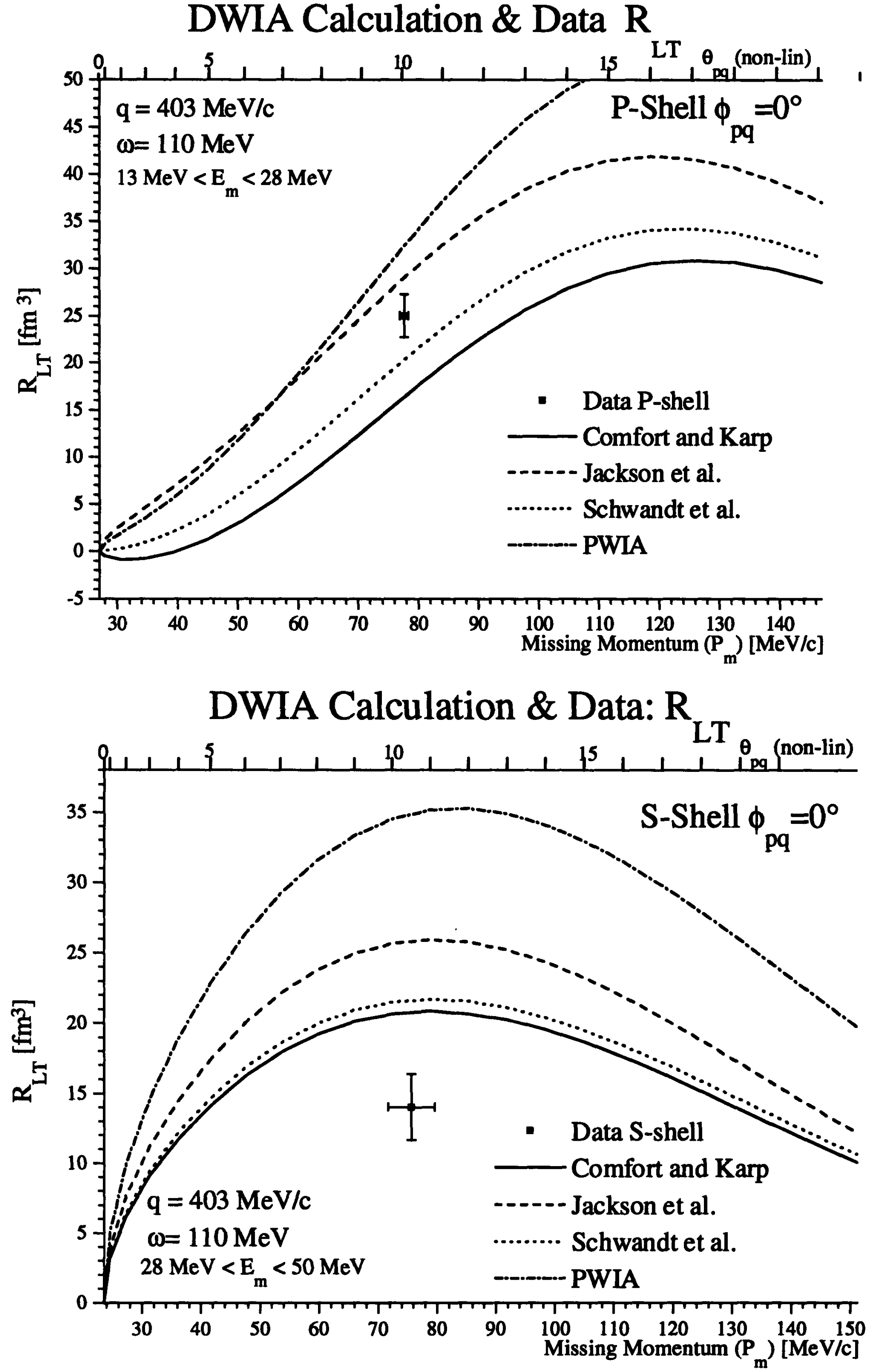

Figure 5.9 Comparison of the theory predicted R_{LT} values and data.

Table 5.11 Data compared with theory. [illegible]

$d^5\sigma / d\omega d\Omega_e d\Omega_p$	$<P_m>$	Data		DATA		PWIA	DWIA	DWIA	DWIA
		No-RADC		RADC			Comfort	Jackson	Schwandt
P-shell		nbarn/MeV/sr^2	±	nbarn/MeV/sr^2	±	nbarn/MeV/sr^2	nbarn/MeV/sr^2	nbarn/MeV/sr^2	nbarn/MeV/sr^2
42.9	77.5	6.80	0.17	8.16	0.22	17.17	16.76	16.91	17.57
64.7	85.9	11.19	0.20	13.31	0.25	25.69	21.09	23.73	22.54
Masked 42.9	77.6	6.87	0.18	8.23	0.23	17.19	16.76	16.91	17.57
Masked 64.7	78.8	10.74	0.28	12.90	0.36	23.83	20.12	22.74	21.68
R_{LT}	78.2	20.00	1.74	24.90	2.20	34.01	17.20	29.87	21.06
Not-R_{LT}	78.2	61.51	1.17	108.22	1.48	210.05	188.88	203.11	201.01
S-shell		nbarn/MeV/sr^2	±	nbarn/MeV/sr^2	±	nbarn/MeV/sr^2	nbarn/MeV/sr^2	nbarn/MeV/sr^2	nbarn/MeV/sr^2
42.9	75.7	3.63	0.16	3.73	0.20	18.20	10.846	13.474	11.287
64.7	86.9	5.49	0.17	5.49	0.21	21.55	12.61	15.70	13.15
Masked 42.9	83.1	3.50	0.28	3.51	0.34	16.38	9.66	12.01	10.06
Masked 64.7	86.1	5.81	0.18	5.64	0.22	21.74	12.747	15.863	13.281
R_{LT}	84.6	13.33	1.97	13.58	2.44	30.83	17.78	22.16	18.55
NOT-R_{LT}	84.6	53.52	1.17	52.64	1.43	219.24	128.81	160.27	134.19

There is a significant discrepancy between the DWIA calculations and the data for both the p-shell and the s-shell cross-sections. This discrepancy is often expressed as a "spectroscopic factor", which is defined as the ratio of the experimental cross-section to the "one-proton" predicted cross-sections:

$$F_{spectroscopic} = \frac{\sigma_{data}(e,e'p)}{\sigma_{theory}^{1-proton}(e,e'p)} \tag{5.15}$$

The one-proton cross-section, $\sigma_{theory}^{1-proton}$, is calculated assuming a single proton in the shell, instead of 4 protons for the p-shell, or 2 protons for the s-shell. These values are obtained from the values in table 5.11 by dividing the p-shell cross-sections by 4 and the s-shell cross-sections by 2. The calculated spectroscopic factors are found in table 5.12 for each of the optical potentials and the PWIA calculation. The averages of these values are given in the last column with the total uncertainty (Tot Err). The total uncertainty includes the statistical and systematic uncertainty in the experimental cross-sections, and a theoretical uncertainty which is taken to be the standard deviation of the spectroscopic factors for the DWIA calculations.

Table 5.12 Spectroscopic Factors

$\sigma_{data}/\sigma_{DWIA}$(1proton)	PWIA	DWIA	DWIA	DWIA	DWIA	
		Comfort	Jackson	Schwandt	Average	Tot Err
P-shell						
42.9 °	1.90	1.95	1.93	1.86	1.91	0.06
64.7 °	2.07	2.52	2.24	2.36	2.38	0.12
Masked 42.9°	1.92	1.96	1.95	1.87	1.93	0.07
Masked 64.7°	2.17	2.56	2.27	2.38	2.40	0.14
R_{LT}	2.93	5.79	3.33	4.73	4.62	1.09
NOT-R_{LT}	2.06	2.29	2.13	2.15	2.19	0.07
S-shell						
42.9 °	0.41	0.69	0.55	0.66	0.63	0.07
64.7 °	0.51	0.87	0.70	0.84	0.80	0.08
Masked 42.9°	0.43	0.73	0.59	0.70	0.67	0.09
Masked 64.7°	0.52	0.88	0.71	0.85	0.82	0.08
R_{LT}	0.88	1.53	1.23	1.46	1.41	0.28
NOT-R_{LT}	0.48	0.82	0.66	0.78	0.75	0.07

The averaged value for the spectroscopic function does not include the PWIA spectroscopic factor. The Tot Err column contains the full uncertainty on the spectroscopic factors, including an estimated theoretical uncertainty which is taken to be the standard deviation of the DWIA spectroscopic factors, and the systematic and statistical uncertainties of the experimental cross-sections.

The spectroscopic factors that are found in this experiment are consistent with those found in previous experiments on ^{12}C(e,e'p), which fall in a range of 2.2 to 3 for the p-shell, and 0.6 to 1.2 for the s-shell[17]. However, this measurement is on the low side of both those ranges. This could be caused by uncertainties in the exact treatment of the DWIA calculation, which, especially for the s-shell, is still somewhat uncertain[18], or it could be due to the optical potentials used.

A more surprising result is the good agreement of the R_{LT} structure function between data and calculation. The p-shell R_{LT} value agrees with the DWIA calculations, and the s-shell value is less than two standard deviations (2σ) from the calculation. This is unexpected, since R_{LT} is a difference between the $\phi_{pq} = 0$ and $\phi_{pq} = \pi$ cross-sections, and is thus expected to scale with the same spectroscopic factor. Instead the spectroscopic factors for the R_{LT} component of the wave function are consistent with

---

[17] S. Penn, Ph.D. thesis. (1993) unpublished.

[18] S. Boffi private communication, G. van der Steenhoven, private communication.

occupation numbers of 4 for the p-shell and 2 for the s-shell. However, the DWIA calculations are not accurate enough to draw conclusions from this.

To investigate the sensitivity to the slight difference in θ_{pq} between the two data sets (see section 5.1.2 and 5.1.5), the theoretical R_{LT} values were re-computed taking this shift into account. The difference in θ_{pq} for a single bin in the data was 0.3°, and the uncertainty in the OOPS pointing angle about 0.5°. The shifted R_{LT} values were computed with a slight modification of equation 5.4:

$$R_{LT}(\theta_{pq}) = \frac{1}{2v_{LT}} \frac{(2\pi)^3}{C_{kin}\, f_{rec}^{-1}\, \sigma_{Mott}} \left\{ \frac{d\sigma(\phi_{pq}=0,\theta_{pq})}{d\omega d\Omega_e d\Omega_p} - \frac{d\sigma(\phi_{pq}=\pi,\theta_{pq}+1^\circ)}{d\omega d\Omega_e d\Omega_p} \right\} \quad (5.16)$$

which takes into account that the $\phi_{pq} = \pi$ data was taken at a 1° larger θ_{pq}, which is an over estimation of the uncertainty in θ_{pq}. The results are plotted in figure 5.10, which shows a band between the shifted (lower curves at small P_m) and the un-shifted R_{LT} predictions. The graph shows that at θ_{pq}= 11°, the p-shell value is not very sensitive to these shifts, while the agreement with the data improves for the s-shell value.

The s-shell strength is distributed over a range in missing energy in a particular way. To account for this a spectral function can be introduced, which describes how the s-shell strength is distributed as a function of missing energy. This can be thought of as an energy dependent spectroscopic factor. A calculation of the cross section using this spectral function, is shown with the data in figure 5.11[19]. The shape of the spectral function is a Lorentzian curve with an energy dependent width of the form[20,21]:

$$S_{s\frac{1}{2}}(E_m) = \frac{1}{\pi} \frac{W(E_m - \varepsilon_F)}{\left(E_m - \varepsilon_F - |\varepsilon_h - \varepsilon_F|\right)^2 + \left[W(E_m - \varepsilon_F)\right]^2} \quad (5.17)$$

---

[19] J. Ryckebusch, private communication.

[20] J. Ryckebusch et al. Phys. Rev. **C49 N5**, 2704 (1994)

[21] C. Mahaux et al. Phys. Rep. **120**, 1 (1985)

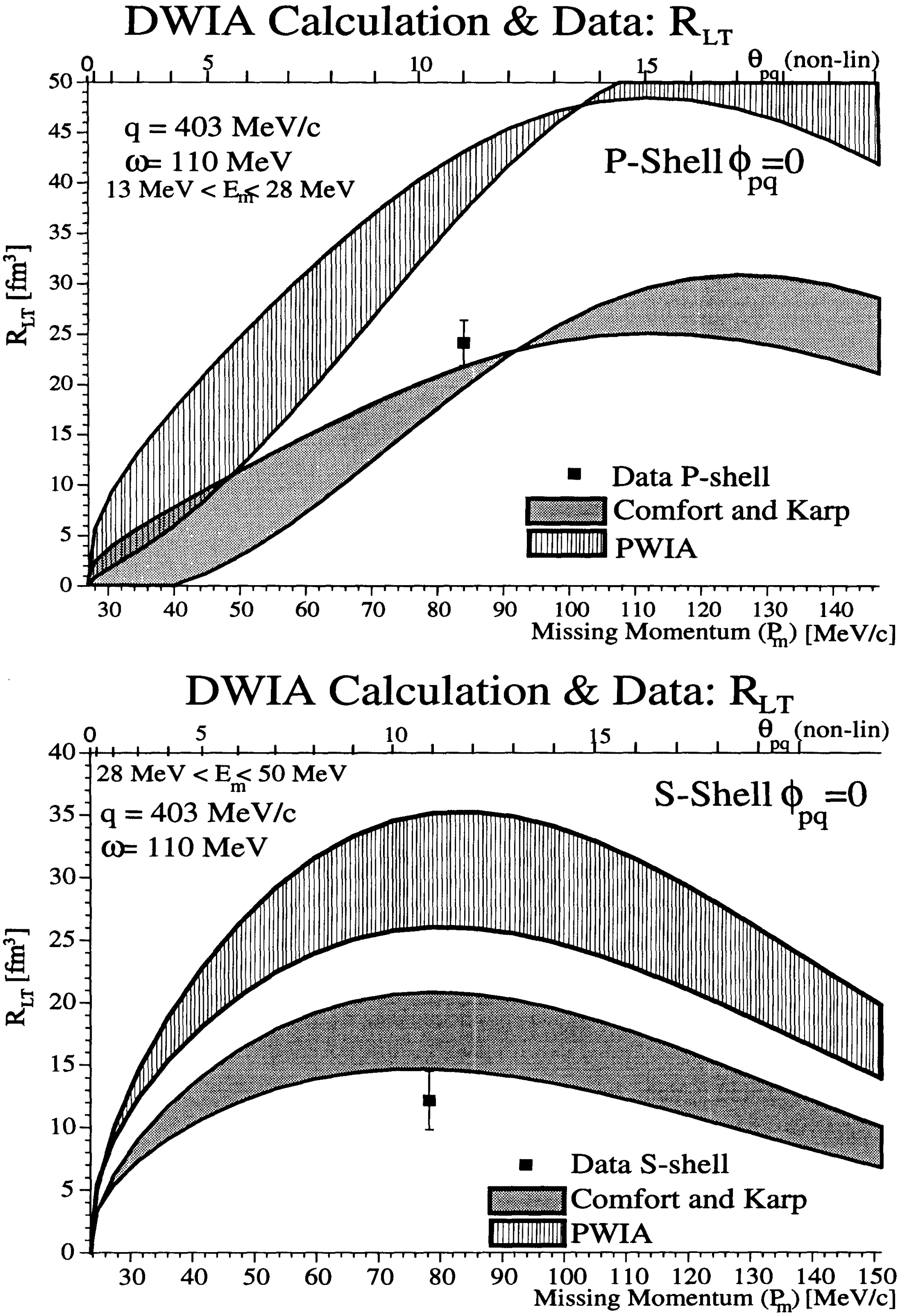

Figure 5.10 Predictions for RLT, taking into account a 1° shift in θ_{pq} between the $\phi_{pq} = \pi$ and $\phi_{pq} = 0$ sides.

where ε_h is the energy needed to remove a proton from the s-shell and ε_F is the Fermi energy ($\varepsilon_F \approx 18\,\mathrm{MeV}$, $|\varepsilon_h - \varepsilon_F| \approx 23\,\mathrm{MeV}$ for a ^{12}C $1s_{1/2}$ proton). For the energy dependent width, *$W(E_m)$*, the imaginary part of an optical potential parametrization was used of the form:

$$W(E) = \frac{9E^4}{E^4 + (13.27)^4}[\mathrm{MeV}] \qquad \textbf{(5.18)}$$

which was obtained from compilations of experimental data[22]. The strength for each point of the spectral function was obtained from a self-consistent Hartree-Fock Random Phase Approximation (HF-RPA), which is multiplied by a factor of 0.3 to account for the spectroscopic factor for the total 1s strength[23]. The same spectroscopic factor is used for both the $\phi_{pq} = 0$ and $\phi_{pq} = \pi$ side. The result is a cross section as a function of missing energy given by:

$$\sigma_{1s_{\frac{1}{2}}}(E_m) = 0.3 \cdot S(E_m)\sigma_{1s_{\frac{1}{2}}}^{\mathrm{HF-RPA}} \qquad \textbf{(5.19)}$$

The resulting curve is in good agreement with the both the $\phi_{pq} = 0$ and $\phi_{pq} = \pi$ s-shell data, and also with the extracted R_{LT}. Thus for the HF-RPA calculation, the missing strength affects R_{LT} in a similar manner as it affects the cross sections. Unfortunately the statistical uncertainty in the data is too large to make a precise comparison. Since this measurement was performed with a mostly longitudinal photon polarization ($\theta_e = 44°$), little strength is expected in the continuum. The spectral function calculation agrees with the data for the entire s-shell.

A different picture is obtained when a similar curve is compared with the separated R_L and R_T structure functions of Ulmer et al. These curves are displayed with the data in figure 5.12. They used a spectroscopic factor of 0.4, which normalized the calculation to the R_L data. Here the agreement with the shape of the R_L structure function is very good, but the R_T calculation underestimates the data significantly at higher missing energies. This extra strength can not be explained with a two-nucleon knockout calculation (dashed line in figure 5.12).

---

[22] J. P. Jeukenne and C. Mahaux, Nucl. Phys. **A394**, 445 (1983)

[23] This much smaller spectroscopic factor may be caused by the absence of an imaginary part of the optical potential for this calculation.

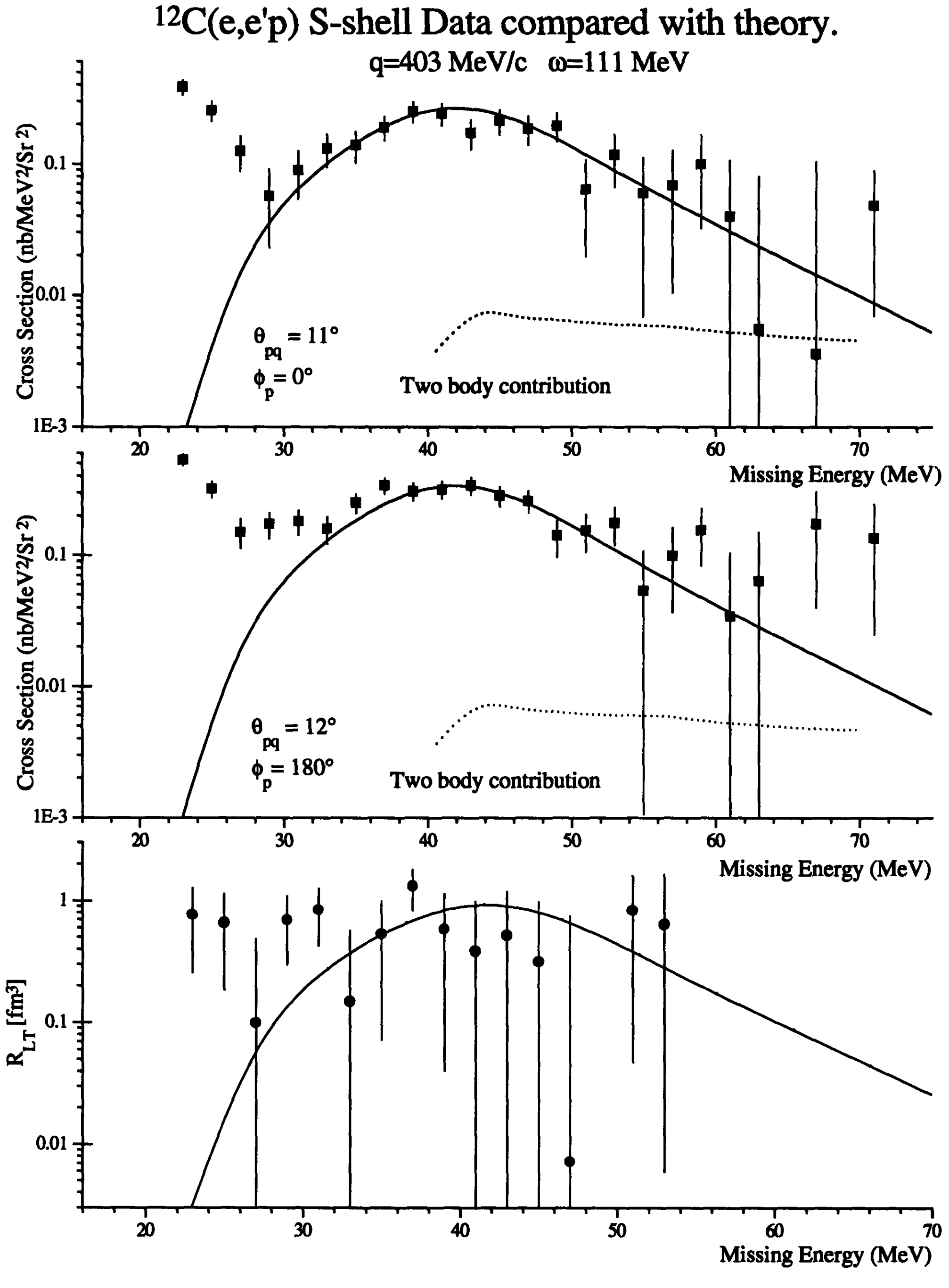

$^{12}C(e,e'p)$ S-shell Data compared with theory.

q=403 MeV/c ω=111 MeV

Figure 5.11 Comparison of the s-shell data with an HF-RPA calculation using a spectroscopic function to model the shape of the s-shell.

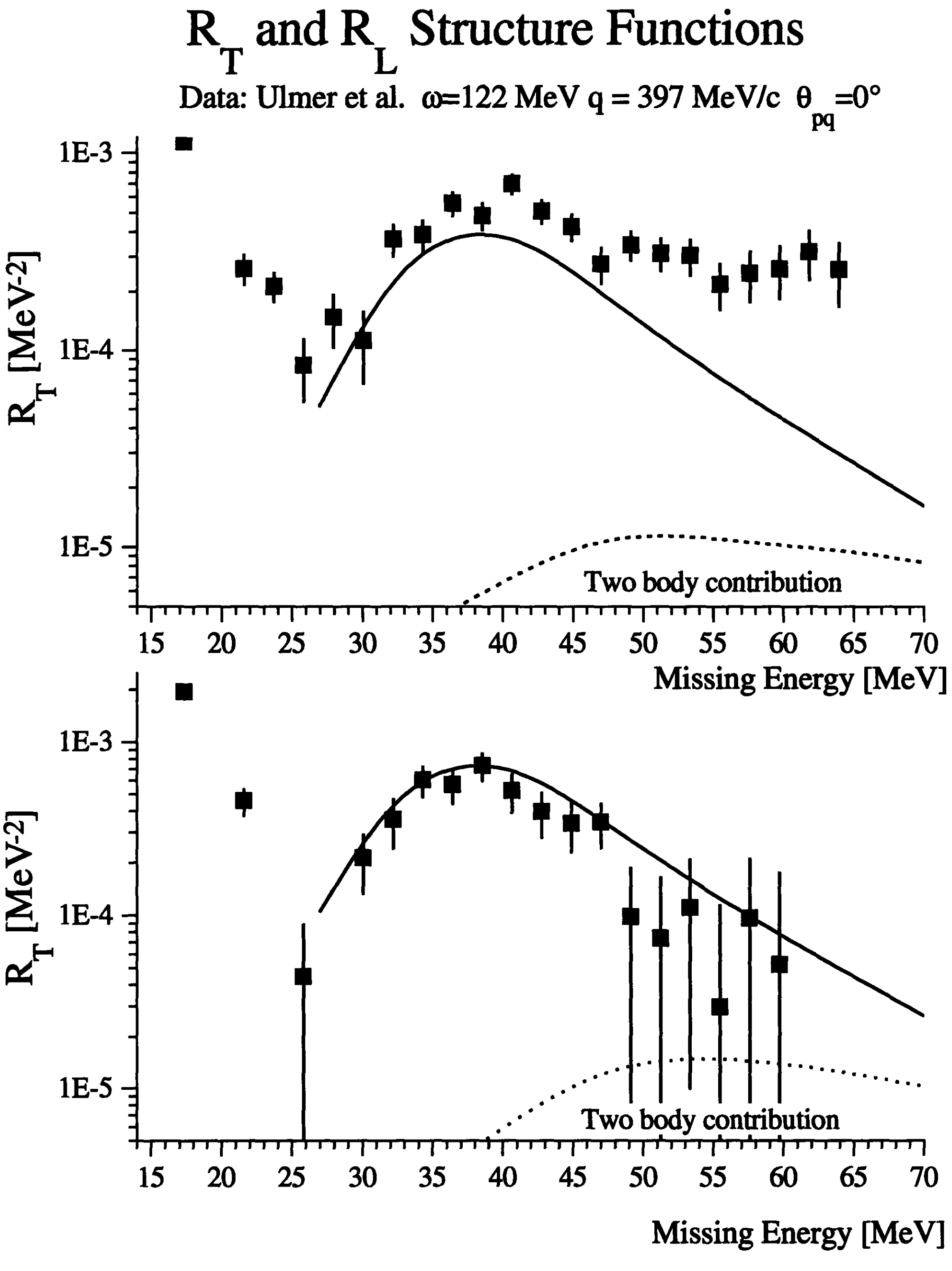

Figure 5.12 Comparison of the separated R_L and R_T structure functions from Ulmer et al., with an HF-RPA calculation using an s-shell spectroscopic function. Also indicated is the two-nucleon knockout contribution to the structure functions (dashed line).

It should be noted that these HF-RPA calculations (with s-shell spectroscopic function) do not fold the theory over the acceptance. The calculation follows a constant line of fixed θ_{pq} through the available phase-space (see figure 5.2 for examples of such lines).

The same Mahaux spectroscopic function was also used to calculate the s-shell shape of the cross section in a 2-dimensional (Em,Pm) histogram. In this calculation the shape in the P_m direction is given by the DWIA calculation at a fixed potential well depth of 68.3 MeV (this corresponds to a state with E_m = 36 MeV). The shape in the E_m direction is given by equation 5.17. The cross-section for each bin is then given by:

$$\sigma(E_m,P_m) = S(E_m)\cdot\sigma_{s-shell}^{DWIA}(P_m) \tag{5.20}$$

where the DWIA cross section is calculated assuming an occupation of 2 protons in the s-shell. The results for the Comfort and Karp optical potential are shown in figure 5.13, which shows the shape of the entire region. From these results R_{LT} was calculated using equation 5.6. This result is plotted in figure 5.14. The shape of the cross-sections does not vary dramatically over the acceptance region.

DWIA "counts" histograms can be obtained by multiplying these 2-dimensional DWIA cross-section histograms with the phase-space volume, using the same method as was used to project the de-radiated cross-sections (see section 3.6) These DWIA "counts" histograms can then be projected and integrated using the exact same method as was used for the data. The result is a DWIA cross-section that is properly averaged over the acceptance. These results are presented in table 5.13. The spectroscopic function that was used for the p-shell was a simple Gaussian shape, centered at 18 MeV, with a width parameter of 2 MeV.

From table 5.13 it can be seen that the p-shell cross-sections and spectroscopic factors are not very sensitive to the averaging procedure, changing by less than 10%. The R_{LT} value appears high, but is was also high for the not averaged DWIA cross-sections in table 5.11. This seems to be a result of the Comfort and Karp optical potential. The s-shell cross-sections are much more sensitive to this averaging procedure, which results in cross-sections that are almost 30% smaller. This can be explained by the Mahaux spectroscopic function, which does not integrate to 1 for missing energies between 28 and 50 MeV. The difference between the spectroscopic factors for the cross-sections and the spectroscopic factors for the R_{LT} values can not be explained by folding an s-shell shape into the DWIA calculation.

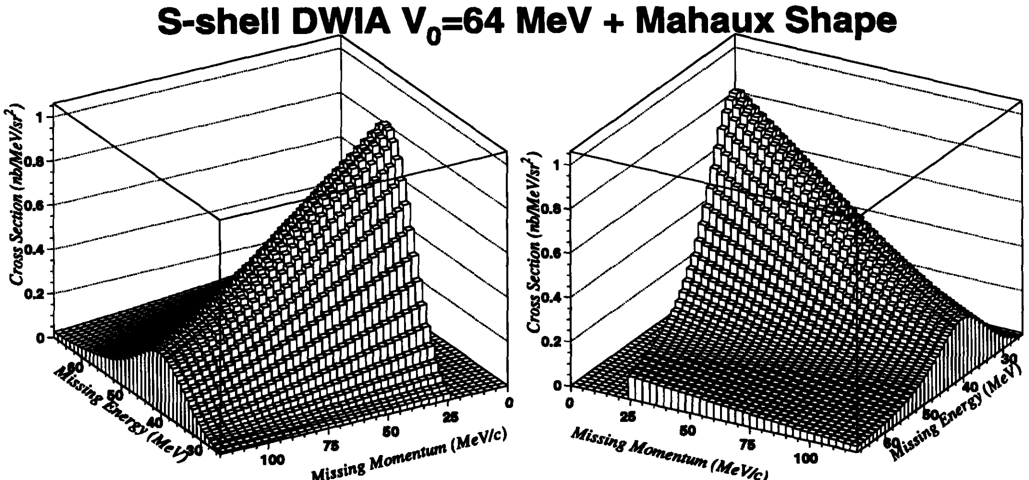

S-shell DWIA, $\phi_{pq} = 0$

S-shell DWIA, $\phi_{pq} = 0$ (reversed)

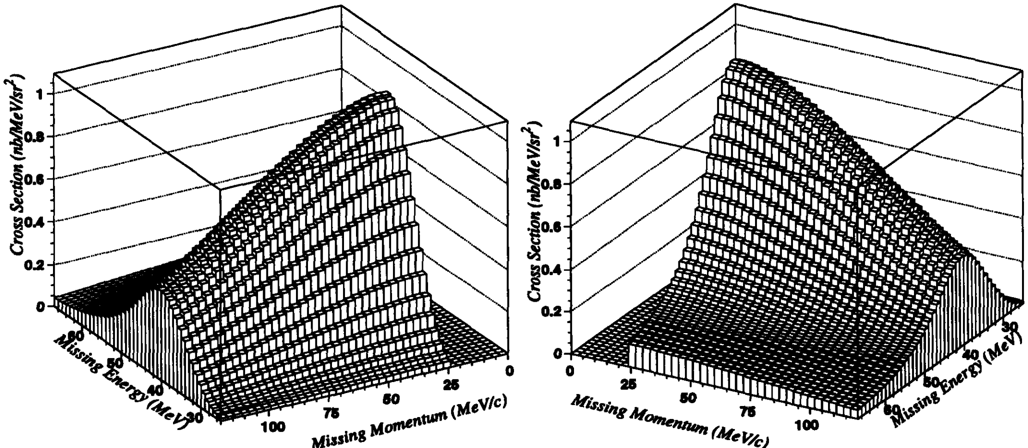

S-shell DWIA, $\phi_{pq} = \pi$

S-shell DWIA, $\phi_{pq} = \pi$ (reversed)

Figure 5.13 Three dimensional perspective plot of the DWIA cross-section.

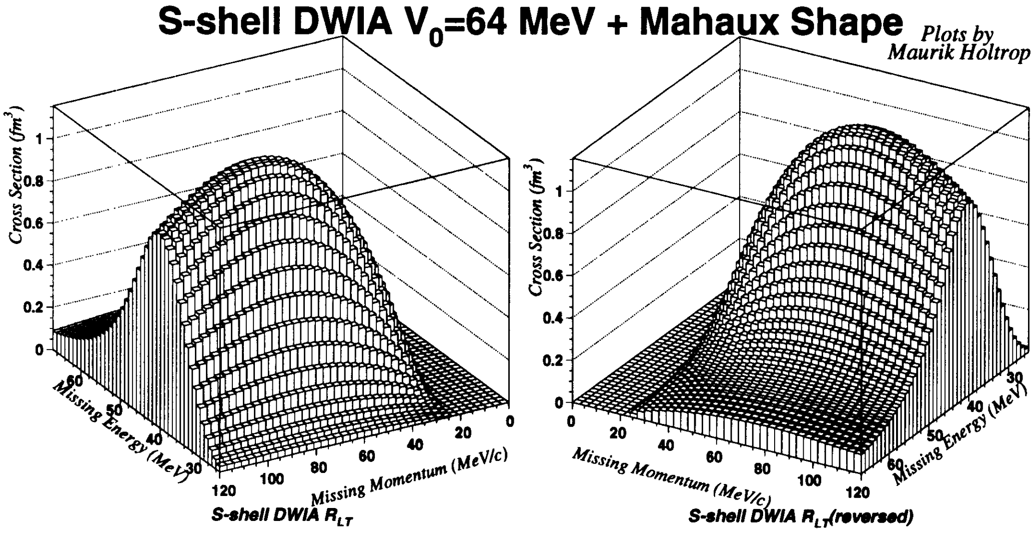

Figure 5.14 Three dimensional perspective plot of the DWIA R_{LT} results.

Table 5.13 DWIA cross-sections averaged over the acceptance phase-space.

	PWIA	DWIA	PWIA	DWIA	Tot Err.
P-shell	Cross Section	Cross Section	Spect. Factor	Spect. Factor	
42.9 °	16.89	16.43	1.93	1.99	0.07
64.7 °	24.06	19.80	2.21	2.69	0.13
Masked 42.9°	17.08	16.62	1.93	1.98	0.07
Masked 64.7°	23.37	19.81	2.21	2.60	0.14
R_{LT}	31.85	16.17	3.13	6.16	1.14
NOT-R_{LT}	207.18	186.59	2.09	2.32	0.08
S-shell					
42.9 °	16.02	8.33	0.47	0.90	0.08
64.7 °	19.99	9.77	0.55	1.12	0.09
Masked 42.9°	14.22	7.29	0.49	0.96	0.11
Masked 64.7°	19.56	10.02	0.58	1.13	0.09
R_{LT}	29.61	16.15	0.92	1.68	0.33
NOT-R_{LT}	194.24	99.53	0.54	1.06	0.07

The Tot Err. values are calculated in the same manner as for table 5.12, using the same uncertainty in the DWIA calculation as was used in table 5.12.

5.4 Summary and Conclusions.

In this experiment the cross-section of the ^{12}C(e,e'p) reaction was measured in the quasi-elastic region, at an energy transfer, ω, of 110 MeV, and a momentum transfer, q, of 404 MeV/c, at two proton angles: 42.9° and 64.7°. The beam energy was 576 MeV and the electron scattering angle, θ_e, was 44°. From these measurements the R_{LT} structure function was extracted. This experiment is one of the first to extract R_{LT} for the carbon nucleus.

The results can be summarized as follows:

- The cross-sections for the p and s-shell agree with previous measurements and are found to be significantly lower than the DWIA predictions, giving spectroscopic factors of 1.9 ± 0.2 and 2.4 ± 0.3 for the p-shell and 0.6 ± 0.2 and 0.8 ± 0.2 for the s-shell at θ_p= 42.9° and 64.7°, respectively.
- The measured R_{LT} structure function agrees well with the DWIA predicted values for both the p and s-shell, giving spectroscopic factors for the R_{LT} part of the cross-section of 4.0 ± 0.8 for the p-shell and 1.7 ± 0.2 for the s-shell. These values are consistent with full occupation of 4 protons in the p-shell and 2 protons in the s-shell.
- An HF-RPA calculation with an energy dependent spectral function from Mahaux et al. agrees well with the shape of the s-shell cross-section as a function of missing energy. This agreement is obtained with the same spectroscopic factor for both the $\theta_p = 42.9°$ and $\theta_p = 64.7°$ cross-sections, as well as the extracted R_{LT} values. This differs from the DWIA calculation where different spectroscopic factors were found.
- The R_{LT} structure function is consistent with zero for missing energies larger than 50 MeV. This finding is consistent with the results of Ulmer et al.[6]
- The prototype OOPS spectrometer performed well in this first series of coincidence experiments in the North Hall of the Bates laboratory, showing that this device is capable of taking high quality data. With these experiments the OOPS program is successfully launched, and four more OOPS spectrometers are now being commissioned for data taking in the South Hall at Bates.

This experiment demonstrates that knowledge of the R_L and R_T structure functions is not sufficient to predict the R_{LT} interference structure function. This reflects the complicated nature of the nuclear current, which is composed of six independent components: the real and imaginary parts of $\rho(\vec{q}), J(\vec{q};+1), J(\vec{q};-1)$, which can be combined to form six structure functions (see table 1.2). In order to fully determine all the components of the nuclear current, all six structure functions should be measured.

This single measurement of R_{LT} has provided an interesting result: the spectroscopic factor for R_{LT} is not consistent with the spectroscopic factor for the cross-sections. Without further experimental data on R_{LT} it is not possible to determine what may be the cause of this difference. Additional information might also be extracted from the R_{TT} and $R_{LT'}$ structure functions.

Appendix A The ELSSY Matrix Elements

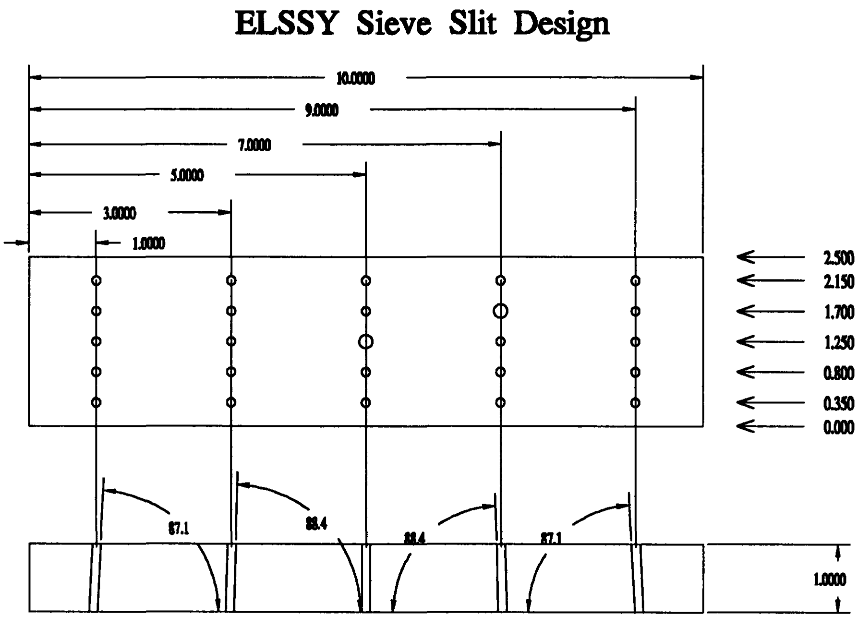

Figure A.1 Sieve slit design. The sieve slit was positioned 2 meters from the target. Dimensions are in inches and degrees.

This appendix summarizes the results of the study of the ELSSY matrix elements. The experiment ran for about 7 hours, with a beam energy of 250 MeV, and a current between 14 and 25 μA. ELSSY was positioned at an angle of 45.9 degrees. We used a 71 mg BeO target and two Carbon targets of 69 mg and 35 mg each. We also attempted to use a 1 mm Carbon pencil target, but found that 1 mm was too small to give us a significant event rate.

The sieve slit we used had two larger holes of 1.5 mm radius and 23 smaller holes of 0.75 mm radius. The larger holes served to unambiguously establish the orientation of the sieve slit. The holes are separated in the ϕ direction by 5.73 mr, and in the θ direction by 25.44 mr. They are angled in such a way that they point towards a single point on the target (see figure A.1.)

It is important to realize that the matrix elements that are found through an experiment are directly coupled to the method that was used to analyze the experimental data. It is possible to find matrix elements that give the correct target coordinates based on incorrectly calculated focal plane coordinates, as long as this is done consistently. On the other hand, if one uses the matrix elements from some theoretical model, such as those found by Transport or Raytrace, it is very important to interpret the detector information correctly so that one calculates the actual angles and position of each particle track. See Chapter 3 for our method of analyzing the detector information.

We fit the data using two different methods. The first method we tried was ray writing, the next method we tried was fitting the individual peaks. Each method has its own advantages and disadvantages, but the results of the two methods agreed to a high degree of accuracy. The results published here are from the peak fitting, because this method gives full errors for the matrix elements.

A.1 The Ray Writing Method

We used the ray writing method to analyze the data by writing a large number of "rays" to a disk file. From the histogram of θ versus Y we can determine which hole in the sieve slit the ray most likely came from. This was done by setting a logical box around the centroid of each peak in this histogram (see figure A.2). For each ray that goes through a specific box we write the focal plane coordinates X, θ, Y, ϕ and the coordinates of the hole in the sieve slit (θ_t ,ϕ_t). This procedure is repeated separately for a number of different peaks in the X spectrum. We needed to look at specific values of X in order to remove the variation of θ_f with respect to X. All this data is accumulated in a single file and is then fitted to a polynomial by minimizing χ^2. Note that we do not include the uncertainties in the measured focal plane coordinates. The computer code for this fitting was written by Joe Mandeville. It minimizes the following equation:

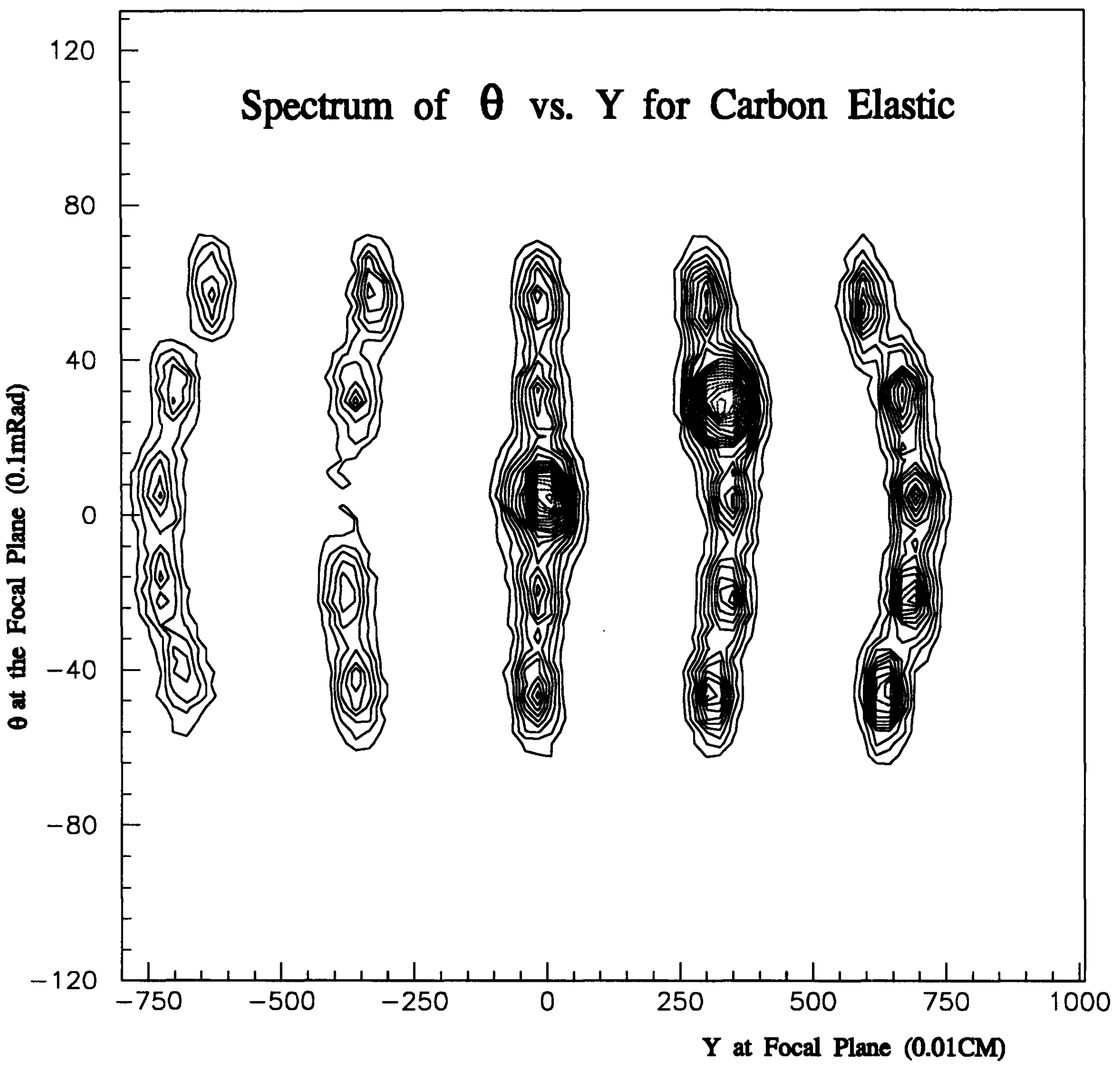

Figure A.2 A contour plot of θ versus Y at the focal plane for the Carbon elastic peak. Each of the sieve slit holes forms a peak in this spectrum, around which a logical box is set. This is the best picture, others looked less clear because they had less data

$$\chi_\phi^2 = \sum_e \left[\frac{\sum_{ijkl} \left[\Phi_{ijkl} \cdot (x_f)^i \cdot (\theta_f)^j \cdot (y_f)^k \cdot (\phi_f)^l \right] - \phi_t^e}{\sigma_\phi} \right]^2 \Bigg|_e \tag{A.1}$$

where

$$\Phi_{ijkl} = \left\langle \phi_t \middle| x_f^i \theta_f^j y_f^k \phi_f^l \right\rangle \tag{A.2}$$

and σ_ϕ is the uncertainty associated with the size of each hole. The sum over *e* is over all rays in the file. We ran the code several times on the same data set, eliminating those rays that are more than 2 sigma outside the expected value. We)followed this same procedure for the fitting of θ, with ϕ_t replaced by θ_t in equations A.1 and A.2.

The biggest problem associated with this method is the proper identification of the peaks, and the correct placement of the logical boxes around each peak. It was found that it was difficult to place each box accurately in the θ direction because the peaks were not separated well enough. If a box is not centered around a peak there will be more rays from one side than the other, and the peak position becomes effectively skewed. To avoid this problem each peaks centroid was fitted using a Gaussian, and the centroids of these gaussians were used to center the logical box.

Another disadvantage of this method is that it does not always treat uncertainties correctly. The peaks are not necessarily weighted according to the accuracy of the known position, and the uncertainty of measurement by the detector is ignored. The method also does not provide uncertainties for the fitted matrix elements, making it more difficult to determine which matrix elements are important. The method used here to determine which matrix elements are kept and which elements are tossed, was solely based on how much each element reduced the χ^2, which can not always distinguish the poorly determined matrix elements from the well determined ones.

An advantage of this method could be that the actual peak width of the calculated target peaks is reduced by including aberrative corrections that contribute to the widening of the peaks. We found, however, that the width of the peaks is dominated by multiple scattering, and no reduction of peak width was observed. Another advantage of this method could be that it includes ϕ_f properly, even though no peaks are seen in the ϕ_f histogram, but we found that there was no significant dependence on ϕ_f.

A.2 The Peak Fitting Method

The peak fitting method can be broken down into the following steps, which are detailed later in this chapter:

1. 1. We made one dimensional projections for each peak in x from the two dimensional histogram of θ versus y (see figure A.2 .) We then projected 5 slices in both θ and y, one for each row of holes.

2. 2. We fitted asymmetric gaussians to each of the peaks in the y slices, and fitted symmetric gaussians with linked widths to the peaks in the θ slices. We extracted the position, uncertainty in the position and the width of each peak.
3. 3. We then used the positions found in step 2 to fit for the matrix elements by minimizing χ^2.
4. In step 1 we create a histogram of θ_f versus y_f for each of the peaks found in x_f for the two different targets. We then projected slices of these histograms onto the θ axis. The bands in y for these projections are clearly separated, so the limits for the bands could be set by eye. Next we found the centroids of the peaks in these θ slices in a first pass fit. We then used these centroids to determine which limits of the bands in θ were appropriate for the projections onto the y axis.

In step 2 we fitted these projections, using the fitting capabilities of the PAW data analysis package. We fit the slices in θ by symmetric gaussians with linked widths. We minimized the equation:

$$\chi^2 = \sum_i \left[\frac{\left(\sum_{j=1}^{5} \mathrm{F}_j(x_i) \right) - N_i}{\sqrt{N_i}} \right]^2 \tag{A.3}$$

where the sum over i is over the channels of the histogram, x_i is the channel in the histogram and N_i is the number of counts in the channel. The function F_j is the Gaussian fit function. For the θ fit, F_j is given by:

$$F_j(x) = h_j \cdot e^{-\frac{1}{2}\left(\frac{p_j - x}{w}\right)^2} \tag{A.4}$$

where h_j is the height of the peak, p_j is the position of the peak and w is the common width. An example of a fit is shown in figure A.3. We had to fit with a common width because the peaks do not stand out cleanly enough to establish their widths on an individual basis. Since the peak width is predominantly determined by the angular resolution of the VDC, it is reasonable to assume that all the peaks have the same width. Typical widths were around 8 mr.

For the y slices we used the same method of fitting, but with a different function F_j. We used an asymmetric Gaussian shape, given by:

$$F_j(x)=\begin{cases} h_j\cdot e^{-\frac{1}{2}\left(\frac{p_j-x}{w_j(1-\alpha_j)}\right)^2} & ,x<p_j \\ h_j\cdot e^{-\frac{1}{2}\left(\frac{p_j-x}{w_j(1+\alpha_j)}\right)^2} & ,x\geq p_j \end{cases} \qquad \textbf{(A.5)}$$

where w_j is now the individual peak width and α_j is the asymmetry. The peaks in y are well enough separated that we could fit each peak individually. We found widths of around 0.2 to 0.3 cm and asymmetries between -0.3 to 0.3, usually small.

In step 3 we found the matrix elements by minimizing χ^2 in equation A.6:

$$\chi_\phi^2=\sum_e\left[\frac{\left(\sum_{ijk}\Phi_{ijk}\cdot(x_f)^i\cdot(\theta_f)^j\cdot(y_f)^k-\phi_t^e\right)^2}{\sigma_\phi^2+F_\sigma^2(x_f,\theta_f,y_f)}\right] \qquad \text{(A.6)}$$

where Φ_{ijk} is the same as in equation A.2 with $l = 0$, and where F_σ is given by:

$$\begin{aligned} F_\sigma^2 = &\left[\frac{\partial}{\partial x_f}\left(\sum_{ijk}\Phi_{ijk}\cdot(x_f)^i\cdot(\theta_f)^j\cdot(y_f)^k\right)\right]^2\cdot\sigma_{x_f}^2+ \\ &\left[\frac{\partial}{\partial \theta_f}\left(\sum_{ijk}\Phi_{ijk}\cdot(x_f)^i\cdot(\theta_f)^j\cdot(y_f)^k\right)\right]^2\cdot\sigma_{\theta_f}^2+ \\ &\left[\frac{\partial}{\partial y_f}\left(\sum_{ijk}\Phi_{ijk}\cdot(x_f)^i\cdot(\theta_f)^j\cdot(y_f)^k\right)\right]^2\cdot\sigma_{y_f}^2 \end{aligned} \qquad \text{(A.7)}$$

x is the VDC peak position and the variables θ and y are the fitted values from step 2. Notice that there is no dependence on ϕ anywhere since ϕ is approximately zero. The error function F depends on the matrix elements themselves, and thus has to be updated

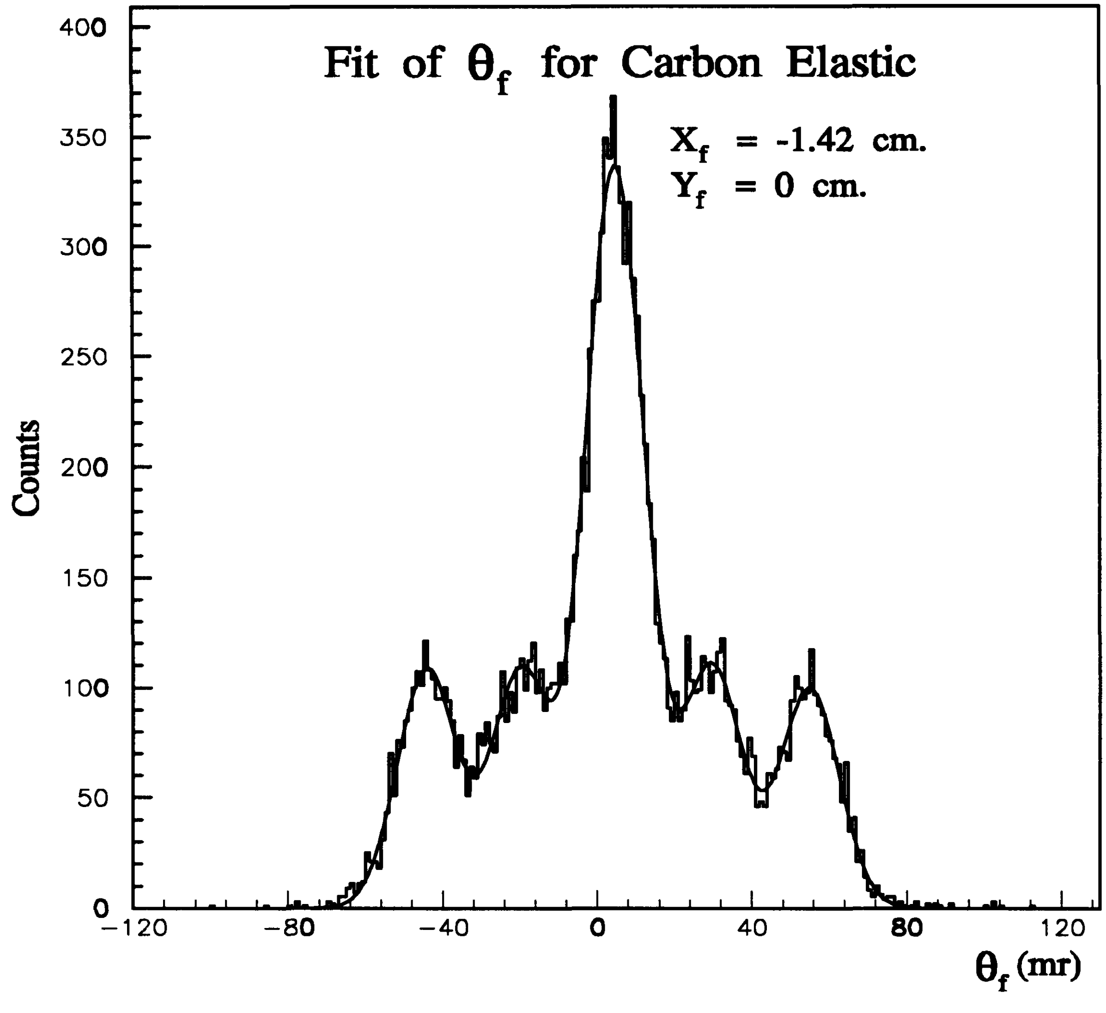

Figure A.3 A typical fit of θ at the focal plane, for the center slice in Y. The data is from the carbon elastic peak. Notice that the central hole has more counts because it was larger than the other holes.

every time the matrix elements change during the fit. The fitting code uses the MINUIT package from the CERN libraries to minimize equation A.6, which returns a full error matrix for the fitted parameters (here the matrix elements). This procedure was repeated for θ.

The biggest advantage of this method is that it gives the correct uncertainty for the matrix elements, and thus gives a good handle on how important a certain term is. We eliminated all terms that are consistent with zero from the fit. A disadvantage of this method is that it depends on a good fit for the individual peaks, which can be very difficult if there is little data available and the peaks are not well separated. Also we could not fit for ϕ since no peaks show up on the ϕ_f histogram.

Another difference between the two methods is that the ray writing method finds the mean value of a peak, because it averages all the rays over the size of a box. The asymmetric peak fitting method finds the mode of peak. These differ slightly, resulting in slightly different matrix elements. As a result of this we found that in a direct comparison, event by event, of the two sets of matrix elements, there was a difference in the target angles calculated. The difference was less than 0.2 mr. On the whole, the two methods resulted in matrix elements that agreed with each other.

A.3 Results

Table 1 and 2 list the matrix elements we found. Most matrix elements that are consistent with zero were omitted, but some are left in the table for ϕ_t because they straightened the curvature of the bands in θ. This set of matrix elements can be used to calculate the target angles for each event. In doing this for the sieve slit data we can reconstruct an image of the sieve slit (see figure A.2) and check how well we did in this reconstruction. By fitting peaks to the sieve slit reconstruction we found that for θ_t the centroids of the peaks were on average less than 1.5 mr from the expected value (where the uncertainty in the peak position was about 0.8 mr). The peak width was about 8.3 mr (σ). For ϕ_t the centroids were less than 0.2 mr from the expected value (where the uncertainty in the peak position was about 0.01 mr), and the average peak width was 0.5 mr (σ). Note that the size of the small holes would cause a peak width of 0.375 mr for perfect resolution. The resolution in θ is dominated by multiple scattering and by the resolution of the measurement of θ_f.

It is difficult to compare these matrix elements directly with the design values for the spectrometer, because those values are found as the inverse of the matrices found here. Bill Schmitt made an attempt to invert the matrices published in the original design (see tables 3 and 4). He did not consider terms for y in the θ_t matrix, and did include ϕ_f in the ϕ_t matrix. This difference can account for some of the discrepancy between the values in tables 1 and 2 with tables 3 and 4. A larger contribution to the difference is most likely due to the "sag" of the VDC, which will affect all terms involving θ_f.

Table A.1 Measured Theta Target Matrix Elements.

Matrix Element	**Value**	**Uncertainty**
Constant	+5.200	0.190
$< \theta \mid \theta >$	-1.022	0.003
$< \theta \mid x >$	$+8.618 \cdot 10^{-1}$	$0.141 \cdot 10^{-1}$
$< \theta \mid y >$	$-2.484 \cdot 10^{-1}$	$0.182 \cdot 10^{-1}$
$< \theta \mid y^2 >$	$+3.882 \cdot 10^{-2}$	$0.475 \cdot 10^{-2}$
$< \theta \mid x\theta >$	$-1.109 \cdot 10^{-3}$	$0.273 \cdot 10^{-3}$
$< \theta \mid xy >$	$-1.530 \cdot 10^{-2}$	$0.185 \cdot 10^{-2}$
$< \theta \mid xy^2 >$	$+1.394 \cdot 10^{-3}$	$0.491 \cdot 10^{-3}$
$< \theta \mid \theta^2 >$	$+2.483 \cdot 10^{-4}$	$0.867 \cdot 10^{-4}$

Table A.2 Measured Phi Target Matrix Elements.

Matrix Element	**Value**	**Uncertainty**
Constant	$+4.734 \cdot 10^{-2}$	$6.46 \cdot 10^{-2}$
$< \phi \mid y >$	+1.636	0.020
$< \phi \mid \theta^2 y >$	$+7.397 \cdot 10^{-5}$	$1.329 \cdot 10^{-5}$
$< \phi \mid x\theta y >$	$-1.781 \cdot 10^{-4}$	$0.428 \cdot 10^{-4}$
$< \phi \mid \theta y >$	$-5.005 \cdot 10^{-5}$	$48.100 \cdot 10^{-5}$
$< \phi \mid xy >$	$-9.983 \cdot 10^{-3}$	$1.286 \cdot 10^{-3}$

Table A.3 Theta Target found by inverting design values.

Matrix Element	**Value**	**Uncertainty**
$< \theta \mid \theta >$	-1.000	0.000
$< \theta \mid x >$	+1.229	0.000
$< \theta \mid x^2 >$	$-3.756 \cdot 10^{-3}$	$0.004 \cdot 10^{-3}$
$< \theta \mid x\theta >$	$+2.034 \cdot 10^{-4}$	$0.001 \cdot 10^{-4}$
$< \theta \mid \theta^2 >$	$+5.360 \cdot 10^{-4}$	$0.003 \cdot 10^{-4}$
$< \theta \mid x^3 >$	$+1.898 \cdot 10^{-5}$	$0.033 \cdot 10^{-5}$

Table A.4 Phi target found by inverting design values.

Matrix Element	Value	Uncertainty
$< \phi \mid y >$	$+1.621$	0.000
$< \phi \mid xy >$	$-9.474 \cdot 10^{-3}$	$0.006 \cdot 10^{-3}$
$< \phi \mid x\phi >$	$1.644 \cdot 10^{-3}$	$0.003 \cdot 10^{-3}$
$< \phi \mid \theta y >$	$7.269 \cdot 10^{-4}$	$0.032 \cdot 10^{-4}$
$< \phi \mid \theta\phi >$	$-9.554 \cdot 10^{-4}$	$0.015 \cdot 10^{-4}$
$< \phi \mid x^2y >$	$1.371 \cdot 10^{-4}$	$0.011 \cdot 10^{-4}$
$< \phi \mid x\theta y >$	$-2.350 \cdot 10^{-4}$	$0.004 \cdot 10^{-4}$
$< \phi \mid \theta^2y >$	$1.022 \cdot 10^{-4}$	$0.001 \cdot 10^{-4}$
$< \phi \mid x^3y >$	$-4.095 \cdot 10^{-6}$	$0.178 \cdot 10^{-6}$
$< \phi \mid x^3\phi >$	$1.313 \cdot 10^{-6}$	$0.128 \cdot 10^{-6}$
$< \phi \mid x^2\theta y >$	$4.910 \cdot 10^{-6}$	$0.182 \cdot 10^{-6}$
$< \phi \mid x^2\theta\phi >$	$-1.792 \cdot 10^{-6}$	$0.111 \cdot 10^{-6}$
$< \phi \mid x\theta^2y >$	$-1.517 \cdot 10^{-6}$	$0.053 \cdot 10^{-6}$
$< \phi \mid x\theta^2\phi >$	$5.624 \cdot 10^{-7}$	$0.501 \cdot 10^{-7}$

A.4 Summary and Conclusion

The matrix elements for ELSSY have been fairly accurately established in this experiment for a central momentum around 225 MeV/c and the dipoles powered from the same power supply. It is important to realize that these results are only accurate if the experimental conditions are closely matched to the conditions in which this experiment was conducted. For any other configuration the experiment should be repeated. This is needed because one would find it difficult to correct for effects like the sag in the VDC in any other way.

In conclusion we would like to remark that a number of things could be improved significantly in order to fully understand the optical properties of ELSSY:

1. This experiment should be repeated with several settings for the central momentum of ELSSY so that the dependence of field settings can be included.
2. When the experiment is repeated, enough time should be allotted to fully tune the beam line for maximum resolution in dispersion matching mode.

3. It would be advisable to use a sieve slit with larger holes, that have a larger separation by alternating them like the "5" on dice. Also the sieve slit could be constructed with flanges that latch on to the solid angle defining slits of ELSSY. This will simplify the procedure of mounting the slit.
4. It would be nice to have a pencil target made of carbon, with a diameter larger than 1 mm, to allow data to be taken without the x_t dependence, but with a high enough rate.
5. The detector package in ELSSY should be extended to include two fully instrumented VDCs. The actual chambers exist, but they can not currently be fully instrumented. It would be preferable to have them instrumented with four delay lines per VDC, or better yet, with one TDC per wire. This would greatly enhance the readout capabilities of the spectrometer and greatly increase the resolution of θ_f.
6. Noise in the Transverse Arrays should be greatly reduced.

The ELSSY spectrometer is a very high resolution device, and currently the only spectrometer at BATES capable of attaining such high resolutions. These resolutions are important for certain measurements, and for determination of the beam energy. It would be unfortunate if its capabilities could not be fully exploited.

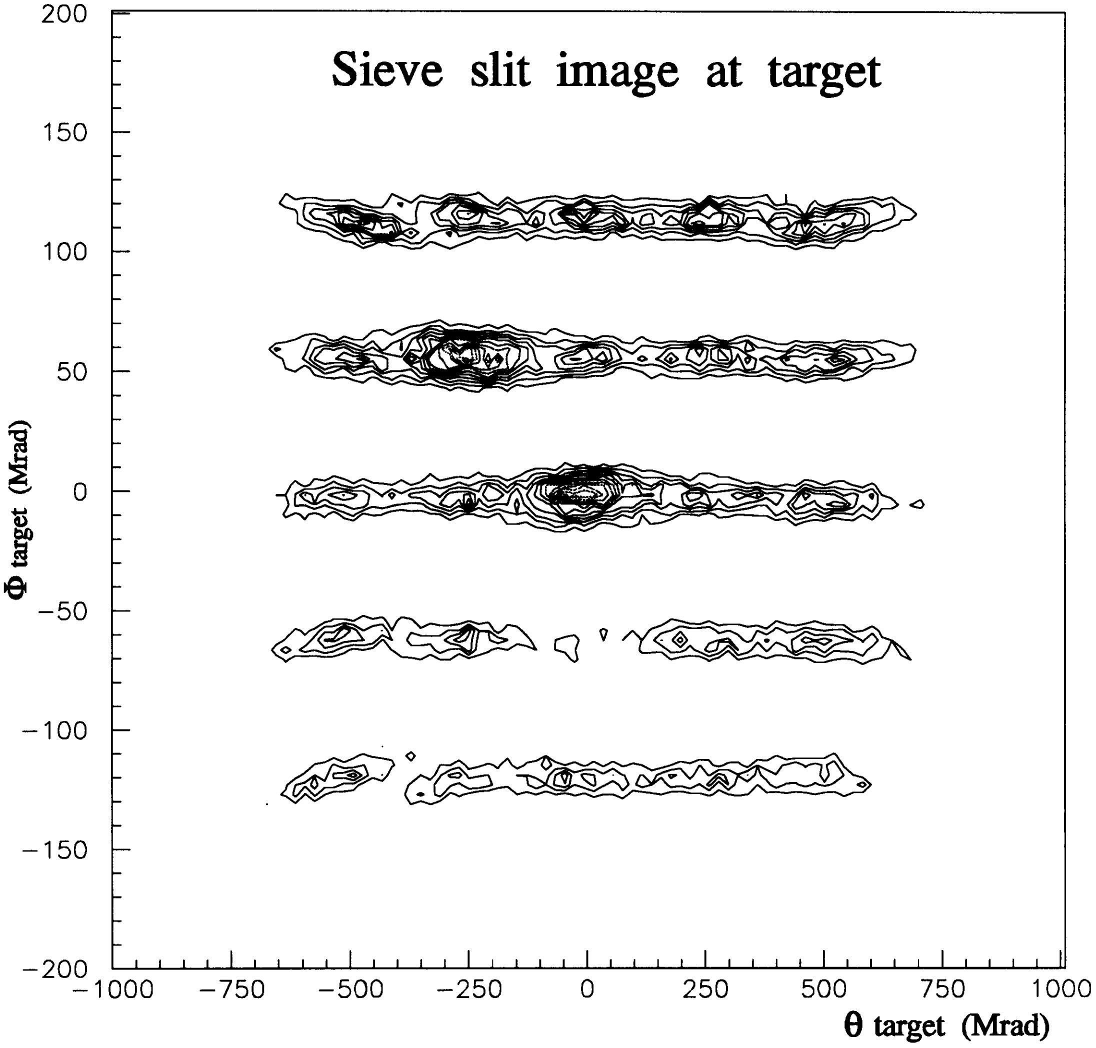

Figure A.3 A histogram of ϕ_t versus θ_t for the carbon data. The image was calculated using the matrix elements of tables 1 and 2.

Appendix B Nucleon Form Factors

This appendix will describe the nucleon form factors for the proton that were used to compute the hydrogen cross section for the H(e,e') normalization of the ELSSY spectrometer, and the half-off-shell single-nucleon cross-section that is used for PWIA and DWIA calculations. Some of the definitions for the kinematics can be found in chapter 1.

The cross-section for elastic scattering from a single nucleon can be described with the Born approximation, or one-photon approximation. For a particle without structure, this would simply result in the Mott cross-section, times a factor for the kinematics. For elastic scattering from a nucleon, the cross section can be described with two form factors:

$$\frac{d\sigma}{d\Omega_e} = \frac{E_f}{E_b}\sigma_{Mott}\left\{A(Q^2) + B(Q^2)\tan^2(\theta/2)\right\} \tag{B.1}$$

where E_f is the final electron energy and E_b is the beam energy, and A and B are two form factors that only depend on the square of the momentum transfer. Notice that the kinematic term is equivalent to the recoil factor:

$$f_{rec}^{-1} = \left[1 + \frac{2E_b}{M}\sin^2(\theta_e)\right] = \left[1 + \frac{-q_\mu^2}{2ME_f}\right] = \frac{E_b}{E_f} \tag{B.2}$$

A different set of form factors can be derived from the ones in equation B.1, known as the Sachs form factors:

$$\begin{aligned} A(Q^2) &= \left\{G_E^2(Q^2) + \tau G_M^2(Q^2)\right\}/(1+\tau) \\ B(Q^2) &= 2\tau G_M^2(Q^2) \end{aligned} \tag{B.3}$$

with $\tau = Q^2/(4M_N^2)$ and M_N is the nucleon mass.

These form factors were measured in an experiment at Mainz[1] for a range of q values from 72 MeV/c to 233 MeV/c (q^2 between 0.13 fm^{-2} and 1.4 fm^{-2}). The result was fit with the function:

$$G(q^2)=\sum_{n=1}^{4}\frac{a_n}{1+q_\mu^2/m_n^2} \qquad \sum_{n=1}^{4}a_n=1 \tag{B.4}$$

the coeficients are given in table **B.1**

Table B.1 Best fit coeficients for GEP and GMP.

	a1	a2	a3	a4	m1	m2	m3	m4
GEP	0.312	1.312	-0.709	0.085	6.0	15.02	44.08	154.2
GMP/μ	0.694	0.719	-0.418	0.005	8.5	15.02	44.08	355.4

Figure 2.1 plots the ratio of the hydrogen cross section computed with the Mainz fit to cross sections obtained from three other fits. The dipole fit is obtained by modeling the proton as a dipole:

$$G_D=\frac{1}{\left(1+\left|Q^2\right|/(4.28)^2\right)} \tag{2.5}$$

The Jansen fit is found in ref. 2.

These form factors can be used to obtain a half-off-shell electron nucleon cross-section. The most frequently used prescription for this is called σ_{np}^{CC1}, which is due to De Forest[3]. There are, however, several other prescriptions (CC1(0), CC1(3), CC2(0), CC2(3), NCC1, NCC2...). These various prescriptons can be found in ref. 4. The program **DWEEPy** uses the CC1 prescription, which is used also for all calculations in

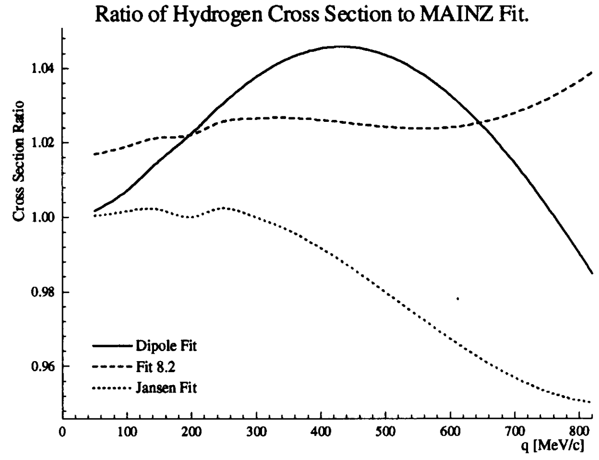

Figure 2.1 Ratio of other fits to the Mainz fit.

---

[1] G. G. Simon et al., Nuclear Physics **A333**, (1980) 381

[2] T. Janssen et al. , Phys. Rev. **142,** (1966) 942

[3] T. De Forest, Nuclear Physics **A392**, (1983) 232

[4] J. A. Caballero, T. W. Donnelly, and G. I. Poulis, Nuclear Physics **A555** (1993) 709

this thesis.

The CC1 prescription can be computed from the following formulas (details can be found in ref. 4):

$$\sigma_{eN}^{CC1} = \frac{M_N^2}{\overline{E}E_N}\sigma_{Mott}\left\{v_L R_L + v_T R_T + v_{TT} R_{TT} + v_{LT} R_{LT}\right\} \qquad \textbf{(B.6)}$$

where $\overline{E} = \sqrt{P_m^2 + M_N^2}$ is the "on-shell" energy of the struck nucleon (PWIA approx: P_m is the missing momentum), and E_N is the energy of the measured out-going nucleon. Similar "on-shell" quantities can be defined: $\overline{P}^\mu = \left(\overline{E}, P_m\right)$, $\overline{Q}^\mu = P_N^\mu - \overline{P}^\mu = (\overline{\omega}, \vec{q})$ with $\overline{\omega} = E_N - \overline{E}$. The structure functions for equation B.6 can then be found from:

$$\begin{aligned}
R_L &= \frac{\kappa^2}{\overline{\tau}}\left\{\chi^2\left[F_1^2 + \overline{\tau}F_2^2\right] + \left[F_1 - \overline{\tau}F_2\right]^2\right\} \\
R_T &= \chi^2\left[F_1^2 + \overline{\tau}F_2^2\right] + 2\overline{\tau}\left[F_1 + \overline{\tau}F_2\right]^2 \\
R_{TT} &= -\chi^2\left[F_1^2 + \overline{\tau}F_2^2\right]\cos(2\phi) \\
R_{LT} &= 2\sqrt{2}\xi\chi\left[F_1 + \overline{\tau}F_2\right]\cos(\phi)
\end{aligned} \qquad \textbf{(B.7)}$$

with

$$\begin{aligned}
\chi &= \frac{P_N}{M_N}\sin\left(\theta_{Nq}\right) \\
\overline{\tau} &= \left|\overline{Q}^2\right|/4M_N^2 = \left(q^2 - \overline{\omega}^2\right)/4M_N^2 \\
\xi &= \frac{\overline{E} + E_N}{2M_N}
\end{aligned} \qquad \textbf{(B.8)}$$

and[5]

$$\begin{aligned}
F_1 &= \left[G_E + \tau G_M\right]/(1+\tau) \\
F_2 &= \left[G_M - G_E\right]/(1+\tau)
\end{aligned} \qquad \textbf{(B.9)}$$

---

[5] Notice: ref 4 equation 48 switched F_1 and F_2

Appendix C Data Tables

Table C.1 Cross-section versus E_m for $\theta_p = 42.9°$ data.

E_m (MeV)	Full Data	±error	Masked Data	±error
5	-0.00142	0.001687	-0.00202	0.002382
7	-0.00678	0.00182	-0.00388	0.002063
9	-0.01218	0.016296	-0.01567	0.016463
11	0.035756	0.034292	0.036703	0.035073
12.5	0.011142	0.031004	0.007059	0.031392
13.5	0.025306	0.031628	0.028155	0.032245
14.5	2.47E-06	0.031557	0.0026	0.032283
15.5	0.070984	0.035052	0.075126	0.035644
16.5	0.156716	0.039527	0.152523	0.039833
17.5	0.677706	0.061726	0.669903	0.062024
18.5	1.65081	0.089362	1.65735	0.090526
19.5	1.85286	0.091675	1.8586	0.092565
20.5	1.29903	0.077813	1.30482	0.078423
21.5	0.880608	0.06547	0.888494	0.066189
22.5	0.494417	0.053152	0.492917	0.053432
23.5	0.272079	0.044547	0.273335	0.04526
24.5	0.277914	0.044814	0.282703	0.047428
25.5	0.231301	0.042881	0.243225	0.046968
26.5	0.133594	0.037607	0.166233	0.043476
27.5	0.116513	0.036749	0.116205	0.042437
28.5	0.034326	0.032924	0.040429	0.041981
29.5	0.079147	0.034749	0.073121	0.045736
30.5	0.100804	0.036906	0.088258	0.050482
32	0.122195	0.036425	0.112554	0.052683
34	0.124094	0.03659	0.125528	0.057123
36	0.172534	0.03881	0.09708	0.057858
38	0.22126	0.041529	0.198108	0.067804
40	0.216381	0.042876	0.147138	0.067291
43	0.215455	0.045065	0.266873	0.08399
47	0.189595	0.046247	0.181728	0.085522
51	0.100685	0.045842	0.103421	0.105504
55	0.085221	0.054333	0.241278	0.217458
59	0.095518	0.066408	0	0
63	-0.01416	0.076454	0	0
67	-0.03948	0.095925	0	0
71	0.027742	0.026372	0	0

Table C.2 Cross-section versus E_m for θ_q = 64.7° data and R_{LT}.

E_m (MeV)	Full Data	±error	Masked Data	±error	R_{LT}	± error
5	0.016686	0.002449	0.032593	0.005391	0.118272	0.031853
7	0.015771	0.002005	0.018663	0.003867	0.110377	0.020329
9	0.017834	0.016409	0.031873	0.024597	0.050404	0.018312
11	0.01281	0.027974	-0.02376	0.035546	-0.02654	0.253747
12.5	0.016383	0.027791	0.048674	0.04261	-0.05641	0.267651
13.5	0.118255	0.033968	0.139226	0.049909	0.207423	0.263692
14.5	0.03919	0.029787	0.090412	0.049968	0.556233	0.297472
15.5	0.163217	0.037683	0.091017	0.049094	0.441971	0.299347
16.5	0.68392	0.059594	0.584129	0.085954	0.080654	0.306718
17.5	2.19338	0.097511	1.68823	0.130918	2.19422	0.481902
18.5	2.81182	0.107685	2.60478	0.156257	5.20566	0.74318
19.5	2.70133	0.103842	2.9382	0.155929	4.87049	0.934196
20.5	1.65578	0.082026	1.79339	0.117754	5.57878	0.944683
21.5	0.931586	0.064384	0.979012	0.091571	2.53895	0.738326
22.5	0.547613	0.053259	0.516625	0.071412	0.476161	0.591048
23.5	0.513214	0.052229	0.533901	0.071157	0.126785	0.468117
24.5	0.372409	0.047012	0.363946	0.063217	1.37437	0.444885
25.5	0.266584	0.043439	0.289903	0.059234	0.431809	0.418939
26.5	0.172507	0.038871	0.19674	0.051682	0.249826	0.402733
27.5	0.128726	0.036279	0.088516	0.044179	0.164101	0.361633
28.5	0.165959	0.038319	0.181069	0.048172	-0.14847	0.329845
29.5	0.178113	0.038839	0.169073	0.045875	0.762051	0.346075
30.5	0.165378	0.037801	0.171065	0.045181	0.523014	0.352759
32	0.165345	0.037595	0.187883	0.043611	0.762936	0.369318
34	0.233215	0.04019	0.24321	0.044337	0.168996	0.387841
36	0.271292	0.042414	0.275237	0.044596	0.71273	0.412425
38	0.329317	0.04566	0.336458	0.046625	1.29716	0.438849
40	0.322653	0.046724	0.32277	0.046978	0.912936	0.455558
43	0.297487	0.048125	0.302627	0.048683	0.322347	0.570688
47	0.257469	0.049248	0.266317	0.05084	0.542908	0.580618
51	0.158509	0.049691	0.184159	0.060313	0.345324	0.69168
55	0.08889	0.055325	0.106126	0.118237	-0.07525	1.274486
59	0.129932	0.071169	0	0	-0.63188	0.549818
63	-0.03113	0.073293	0	0	0	0
67	0.016542	0.107494	0	0	0	0
71	0.079842	0.060152	0	0	0	0

Bibliography

1.1 S. M. Dolfini et al., Nuclear Instruments and Methods (1993)
1.2 To be published
1.3 J. Mandeville and the OOPS collaboration, Nuclear Instruments and Methods (1993)
1.4 M. Holtrop et al., The ELSSY Matrix Elements, BATES Internal Report, (1992)
1.5 P. Ulmer et al., Phys. Rev. Lett. 59, 2259 (1987)
1.6 R. Lourie et al., Phys. Rev. Lett. 56, 2364 (1986)
1.7 H. Baghaei et al., Phys. Rev. C39, 177 (1989)
1.8 L. Weinstein et al., Phys. Rev. Lett. 64, 1646 (1990)
1.9 J. Morrison, Ph.D. Thesis, MIT, unpublished. (1993)
1.10 S. Penn, Ph.D. Thesis, MIT, unpublished. (1993)
1.11 D. Jordan, Ph.D. Thesis, MIT, unpublished. (1994)
1.12 T. McIlvain, Ph.D. Thesis, MIT, unpublished. (1995)
1.13 J. S. O'Connell et al., Phys. Rev. Lett., 53, 1627 (1984); Phys Rev, C35, 1063 (1987)
1.14 K. Y. Horikawa, F. Lenz and N. C. Mukhopadhyay, Phys. Rev. C22 1680 (1980)
1.15 R. R. Whitney, I. Sick, J. R. Ficenec, R. D. Kephart, and W. P. Trower, Phys. Rev, C9 2230 (1974).
1.16 T. De Forest, Jr. , in "Effets Mésoniques dans les Noyoux et Diffusion d'Electrons à Energy Intermédiaire", Saclay, CEA DPHN p. 223, (1975) as noted in S. Frullani and J. Mougey, Advances in Nuclear Physics Vol 14, ed. by J. W. Negele and E. Vogt, Plenum Press, New York (1984)
1.17 J. M. Finn, R. W. Lourie, B. H. Cottman, Phys. Rev. Lett 49, 1016 (1982)
1.18 P. Barreau et al. , Nucl. Phys. A402, 515 (1983)
1.19 R. Altemus et al. , Phys. Rev. Lett. 44, 965 (1980)
1.20 T. W. Donnelly, Nucl. Phys. A555, (1993) and "Polarization in Lepton-induced Reactions" presented at the NATO Advanced Study Institute on Perspectives in the Structure of Hadronic Systems, Dronten, The Netherlands, 1993
1.21 J. D. Bjorken and S. D. Drell, "Relativistic Quantum Mechanics," McGraw-Hill, New York (1964)
1.22 First introduced in Day, McCarthy,Donnelly and Sick, Ann. Rev. Nucl. Part. Sci.. 40, 357 (1990)
1.23 T. W. Donnelly and J. D. Walecka, Annual Review of Nuclear Science, 25, 329 (1975)
1.24 S. Frullani and J. Mougey, "Single Particle Properties of Nuclei Through (e,e'p) Reactions," in Advances in Nuclear Physics, Vol 14, edited by J. W. Negele and E. Vogt, Plenum Press, New York (1984)
1.25 A. S. Raskin and T. W. Donnelly, Annals of Physics, 191, 78-142 (1989)
1.26 S. Boffi, C. Giusti and F. D. Pacati, Phys. Rep. 226, (1993)
1.29 Sylvester, Camb. & Dubl. Math Journal, (1852)
1.30 T W Donnelly and A. S. Raskin, Ann. Phys., 169 (1986),247
1.32 S. Boffi, C. Giusti and F. D. Pacati, Nucl. Phys. A435, 697
1.33 J. A. Caballero, T. W. Donnelly and G. I. Poulis, Nucl. Phys. A555, 709 (1993),
1.34 T. De Forest, Nucl. Phys., A392 (1983) 232
1.35 S. Frullani and J. Mougey, "Single Particle Properties of Nuclei Through (e,e'p) Reactions," in Advances in Nuclear Physics, Vol 14, edited by J. W. Negele and E. Vogt, Plenum Press, New York (1984)
1.36 S. Boffi, C. Giusti and F. D. Pacati, Nucl. Phys., A319, 461 (1979)
2.4 W. Bertozzi *et. al.*, Nuclear Instruments and Methods **162**, 211 (1979) and **141**, 457 (1977).

2.5 K. L. Brown *et. al.*, **Transport**, SLAC (unpublished)

2.6 M. Holtrop *et. al.*, Internal Report B/IR 92-04, Bates Linear Accelerator Center (unpublished).

2.8 Bill Schmitt, *Ph. D. thesis*, MIT, unpublished (1993).

2.9 W. Bertozzi *et. al.* Nuclear Instruments and Methods, **141**, 457 (1977)

2.10 Often VDC chambers have 4 or more delay lines, and sometimes even a TDC per delay line. This increases the accuracy of the VDC and the maximum count rate.

2.11 J. B. Mandeville *et. al.*, Nuc. Inst. & Methods **A344** (1994) 571

2.12 S. M. Dolfini *et. al.*, Nuc. Inst. & Methods **A344** (1994) 583

2.13 S. M. Dolfini *et. al.*, Internal report, University of Illinois at Urbana-Champaign (unpublished)

2.14 J. B. Mandeville *et. al.*, Internal report, University of Illinois at Urbana-Champaign (unpublished)

2.15 L. G. Atencio, J. F. Amann, R. L. Boudrie and C. L. Morris, Nuclear Instruments an Methods **187**, 381 (1981)

2.16 David A. Toback, B. S. Thesis (unpublished)

3.3 W. Bertozzi *et al.*, Nuclear Instruments and Methods **162**, 211 (1979)

3.4 D. Jordan, M. Holtrop, B. Schmitt, *Understanding the ELSSY VDC*, BATES INTERNAL REPORT B/IR 92-03.

3.5 Los Alamos Meson Physics Facility, MP10 group. DRT is part of the Q system.

3.6 see Leo, *Techniques for Nuclear and Particle Physics Experiments*, Springer-Verlag (1987) or *Particle Physics Booklet,* Particle Data Group, Phys Rev **D50**, 1173

3.7 See David A. Toback, B. S. Thesis (unpublished)

3.8 J. B. Mandeville *et al.*, Internal Report, University of Illinois at Urbana-Champaign (unpublished)

3.11 Sylvester, *Camb. & Dubl. Math Journal,* (1852)

3.13 E. Quint, "Limitations of the Mean-Field Description of Nuclei in the Pb-Region, Observed with the (e,e'p) Reaction", Ph.D. Thesis (1988), unpublished.

3.14 J. Schwinger, Phys. Rev. **76**, 760 (1949)

3.15 L. W. Mo and Y. S. Tsai, Reviews of Modern Physics **122**, 1898 (1961)

3.16 S. Penner, Nuclear Structure Physics, Proceedings of the 18th Scottish Univ. Summer School in Physics, page 284 (1977)

3.17 L. W. Mo and Y. S. Tsai, Reviews of Modern Physics, **41**, 208 (1969)

3.18 J. Schwinger, Phys. Rev. **75**, 898 (1949)

3.20 N. Makins, "Measurement of the Nuclear Dependence and Momentum Transfer Dependence of the Quasielastic (e,e'p) Scattering at Large Momentum Transfer", Ph.D. Thesis 1994, unpublished, and D. Wasson private communications.

3.21 J. Friedrich, Nuclear Instruments and Methods, **129**, 505 (1975)

3.22 Y. S. Tsai, Rev. Mod. Phys. **46** (1974) 815

3.23 H. A. Bethe and W. Heitler, Proc. Roy. Soc. **A146** (1934) 83

3.24 D. J. S. Findlay and A. R. Dusautoy, Nucl. Instr. and Meth. **174**, 531 (1980)

3.25 L. C. Maximon, Reviews of Modern Physics, **41**,193 (1969)

3.26 This was first suggested by H. Crannell, Nucl. Inst. and Meth. **71**, 208 (1969)

4.5 J. Kelly, *Ph.D. Thesis, MIT*, unpublished (1981).

4.6 Steve Penn, *Ph.D. Thesis, MIT,* unpublished (1993),
Paul Ulmer, *Ph.D. Thesis, MIT,* unpublished (1987)

4.7 C. G. Simon et. al., *Nucl. Phys.* **A333** (1980) 381.

4.9 C. Kost and P. Reeve, Technical Report No. TRI-DN-82-28, TRIUMF (unpub.)

4.10 More detail can be found in: D. Jordan, *Ph.D. Thesis, MIT,* unpublished (1994), and V. Bushan, *S.M. Thesis, MIT* (1992).

5.2 The integration region for the s-shell corresponds to the extent of the longitudinal s-shell region, see P. Ulmer, Ph. D. thesis, MIT 1981.

5.3 S. Boffi, C. Giusti and F. D. Pacati, Nuc. Phys. **A435** (1985) 697.

5.4 Schwandt et al., Phys. Rev. **C26** (1981) 55.

5.5 G. van der Steenhoven et al. , Nucl. Phys. **A484** (1988) 445.

5.6 Paul Ulmer, Ph.D. thesis, MIT (1987) unpublished.
5.8 S. Boffi et. al. Nucl. Phys. **A336**, 416,437 (1980). **A386**, 599 (1982), **A435**, 697 (1985).
5.9 C. Giusti and F. D. Pacati, Nucl. Phys. **A336**, 427 (1980), **A473**, 717 (1987) and **A485**, 461 (1988).
5.10 T. W. Donnelly and I. Sick, Rev. Mod. Phys. **56**, 461 (1984), as quoted in ref. 12.
5.11 D. G. Ireland and G. van der Steenhoven, Phys. Rev. **C49 N4**, 2182 (1994)
5.12 G. van der Steenhoven, private communication.
5.13 J. R. Comfort and B. C. Karp, Phys. Rev. **C21**, 2162 (1980)
5.14 D. F. Jackson and I. Abdul-Jalil, J. Phys. **G6**, 481 (1980)
5.15 Schwandt et al., Phys. Rev. **C26,** 55 (1981)
5.16 S. Penn, Ph.D. thesis. (1993) unpublished.
5.17 S. Boffi private communication, G. van der Steenhoven, private communication.
5.18 J. Ryckebusch, private communication.
5.19 J. Ryckebusch et al. Phys. Rev. **C49 N5**, 2704 (1994)
5.20 C. Mahaux et al. Phys. Rep. **120**, 1 (1985)
5.21 J. P. Jeukenne and C. Mahaux, Nucl. Phys. **A394**, 445 (1983)
B.1 G. G. Simon et al., Nuclear Physics **A333**, (1980) 381
B.2 T. Janssen et al. , Phys. Rev. **142,** (1966) 942
B.3 T. De Forest, Nuclear Physics **A392**, (1983) 232
B.4 J. A. Caballero, T. W. Donnelly, and G. I. Poulis, Nuclear Physics **A555** (1993) 709

Acknowledgments

This thesis would not have been possible without the help and support of many people, both inside and outside the physics community.

First I would like to thank my supervisor, Bill Bertozzi, who has been a constant source of support throughout this project. Bill has always been most generous with his time, attention and patience, and his insight into physics problems has taught me much. He has always been the driving force behind the high quality of work in his research group, without which this project would never have happened. But beyond this he has been a most caring person who is as deeply concerned about humanity as he is with physics. One of his many great contribution was hiring such an excellent group of post-docs and research scientists to help with every aspect of this thesis.

Much gratitude goes to Shalev Gilad, with whom I have had so many great conversations and problem solving sessions. His editing work on this thesis has made all the difference, and his support through the final months of analysis was invaluable.

I would also like to thank Adam Sarty, for all his help and suggestions, his friendship and the many trips to get a cappuccino. Without his companionship and his confidence in me this thesis would never have been completed.

I would like to thank my readers, Bill Donnelly and June Mathews for their time and efforts in editing and advise. They have greatly improved this thesis.

I would like to acknowledge Dan Dale for all his efforts in this long project, and for the trips to the mountains, the climbing wall and the brew house. Also I would like to thank Larry Weinstein for all his help, his optimism, and his friendship, and Werner Boeglin for all the work on the wire chambers. The efforts of Jiang-Ping Chen and Jeff Templon are also much appreciated.

Many thanks go to my fellow graduate students on the OOPS project. To Dave Jordan for his ability to keep going even after long shifts in the counting bay or long days of data analysis, and for his original, humorous look on life. To Steve Dolfini, who produced all of the autocad drawings in this thesis, and who has been a fun companion on many occasions, to Joe Mandeville for all his programming efforts and to Tom McIlvain for his hard work. I would also like to thank all the other students, who weren't involved with OOPS but made life at MIT a lot more fun: Steve Penn, Dave Toback, John Morrison, Marla Dowell, John Perkins, John Dawe, Vipul....and many more who have helped in one sense or another.

I would like to thank the Bates crew for making the experiment a success, especially the efforts of Dan Tieger, Karen Dow, Scott Otaway, the beam operators and the mechanical crew. Many thanks go to George Setchen for introducing me to the fine skills of machining

I would also like to thank Gerard van der Steenhoven and Jan Ryckebusch, who have been most helpful with the theoretical calculations, and Louk Lapikas for introducing me to RADC.

My deepest gratitude goes out to my family and my friends, who have supported me throughout this period, and who have been an invaluable source of energy, fun and life. With them I have explored many other aspects of being, and have lived a much richer life because of it. I would like to thank David for the many long and wild trips, introducing me to great outdoors adventures in wild places, and for being such a compassionate friend. I would also like to thank my friends: James, Amy, Carol, John, Susan, Denise, Craig, Louise, Oury, John, David, Heather, Katherine, Brooke...all the other people who have touched my life; all my friends and teachers at the Cambridge Zen Center who have showed me a different approach to the questions of life, and the members of Catherine's Dance Company, and Beth Soll, who have introduced me to the world of dance. I would like to thank Rebecca for all her help, love and support in the final and most difficult months.